IRREGULAR WAVE INTERACTION WITH PERMEABLE SLOPES OF COASTAL STRUCTURES

by

Andojo Wurjanto

and

Nobuhisa Kobayashi

RESEARCH REPORT NO. CACR-92-03

July 1992

CENTER FOR APPLIED COASTAL RESEARCH

Department of Civil Engineering
University of Delaware
Newark, Delaware 19716

ACKNOWLEDGEMENTS

This study was partially funded by the National Science Foundation under grant CTS-8900640.

TABLE OF CONTENTS

LIST OF FIGURES vii
LIST OF TABLES xiii
ABSTRACT xv

Chapter

1 INTRODUCTION **1**

1.1 Previous Work for Thin Permeable Underlayer 2
1.2 Previous Work for Impermeable Slopes 4
1.3 Other Analytical and Numerical Models for Permeable Structures 6
1.4 Background for Adopted Numerical Methods 9
1.5 Objectives and Outline of the Present Work 10

2 APPROXIMATE TWO-DIMENSIONAL EQUATIONS **13**

2.1 Flow over Rough Slope 13
2.2 Flow inside Permeable Underlayer 18

3 APPROXIMATE ONE-DIMENSIONAL EQUATIONS **23**

3.1 Introduction 23
3.2 Flow over Rough Slope 23
3.3 Flow inside Permeable Underlayer without Free Surface 31
3.4 Flow inside Permeable Underlayer with Free Surface 35

4 NUMERICAL METHODS **39**

4.1 Introduction 39
4.2 Lax-Wendroff Method without Dissipation 42
4.3 Lax-Wendroff Method with Dissipation 53
4.4 A Discussion on the MacCormack Method 58

5 ONE-DIMENSIONAL ENERGY EQUATIONS 63

5.1 Energy Equation for Region 1 63
5.2 Energy Equation for Region 2 68
5.3 Energy Equation for Region 3 71
5.4 Time-Averaged Energy Equations 73

6 COMPARISON BETWEEN NUMERICAL MODEL AND EXPERIMENT 77

6.1 Experiment on Irregular Wave Run-up and Reflection 77
6.2 Summary of Input to Numerical Model 78
6.3 Comparison Between Measured and Computed Reflected Waves 84
6.4 Comparison Between Measured and Computed Waterline Oscillations . 95
6.5 Computed Time-Dependent Flow Fields 105
6.6 Time-Averaged Mass Balance 125
6.7 Time-Averaged Energy Balance 130
6.8 Sensitivity of Computed Results to Finite Difference Grid 137

7 COMPARISON BETWEEN PERMEABLE AND IMPERMEABLE SLOPES 139

7.1 Introduction 139
7.2 Irregular Wave Reflection 140
7.3 Irregular Wave Run-up 146
7.4 Irregular Wave Energy Dissipation 158
7.5 Hydraulic Stability of Armor Units 161
7.6 Spectral Evolution of Surface Elevation 167

8 CONCLUSIONS 171
REFERENCES 173

LIST OF FIGURES

2.1 Definition sketch for flow over rough slope and inside permeable underlayer. 14

2.2 Surface stresses acting on fluid element near free surface. 18

3.1 One-dimensional model for flow over rough slope and inside permeable underlayer. 24

3.2 Vertical distribution of horizontal fluid velocity u_1 assumed by Svendsen and Madsen (1984). 30

3.3 Momentum correction coefficient C_m computed as a function of b/h and u_s/u_o for vertical distribution of horizontal fluid velocity u_1 assumed by Svendsen and Madsen (1984). 30

4.1 Three regions for computation of flow fields. 40

5.1 Energy correction coefficient C_e computed as a function of b/h and u_s/u_o for vertical distribution of horizontal fluid velocity u_1 assumed by Svendsen and Madsen (1984). 67

6.1 Permeable slope geometry specified as input to numerical model. . . . 79

6.2 Measured and computed reflected wave trains at x=0 for Run P1. . . 88

6.3 Measured and computed reflected wave trains at x=0 for Run P2. . . 89

6.4 Measured and computed reflected wave trains at x=0 for Run P3. . . 90

6.5 Measured and computed reflected wave spectra shown relative to incident wave spectrum at x=0 for three runs. 91

6.6 Measured and computed reflection coefficient, coherence and phase between incident and reflected waves at x=0 for Run P1. 92

6.7 Measured and computed reflection coefficient, coherence and phase between incident and reflected waves at $x=0$ for Run P2. 93

6.8 Measured and computed reflection coefficient, coherence and phase between incident and reflected waves at $x=0$ for Run P3. 94

6.9 Measured and computed waterline oscillations on upper slope for Run P1. 98

6.10 Measured and computed waterline oscillations on upper slope for Run P2. 99

6.11 Measured and computed waterline oscillations on upper slope for Run P3. 100

6.12 Measured and computed spectra of waterline oscillations on upper slope as well as coherence and phase between incident waves and waterline oscillations on upper slope for Run P1. 101

6.13 Measured and computed spectra of waterline oscillations on upper slope as well as coherence and phase between incident waves and waterline oscillations on upper slope for Run P2. 102

6.14 Measured and computed spectra of waterline oscillations on upper slope as well as coherence and phase between incident waves and waterline oscillations on upper slope for Run P3. 103

6.15 Measured and computed exceedance probability of run-up as compared with Rayleigh distribution for three runs. 104

6.16 Computed waterline oscillations on lower slope for Run P2. 112

6.17 Portions of time series of surface elevation $\eta(x,t)$ at $x = 0.31$, 0.61, and 0.92 for Run P2. 113

6.18 Instantaneous spatial variations of free surface elevation η and depth-averaged horizontal velocity u for Run P2. 114

6.19 Instantaneous spatial variations of volume influx q_b and horizontal velocity u_b for Run P2. 115

6.20 Instantaneous spatial variations of vertically-averaged discharge velocity u_p and discharge m_p for Run P2. 116

6.21 Mean, maximum, and minimum values of free surface and water table elevation η for Run P2. 117

6.22 Mean, maximum, and minimum values of depth-averaged horizontal velocity u for Run P2. 117

6.23 Mean, maximum, and minimum values of horizontal volume flux m for Run P2. 118

6.24 Mean, maximum, and minimum values of volume influx q_b for Run P2. 118

6.25 Mean, maximum, and minimum values of vertically-averaged discharge velocity u_p for Run P2. 119

6.26 Mean, maximum, and minimum values of discharge m_p for Run P2. . . 119

6.27 Mean, maximum, and minimum values of depth-averaged horizontal velocity u for Run P2 from two computations with different values of maximum allowable time step Δt. 120

6.28 Mean, maximum, and minimum values of depth-averaged horizontal velocity u for Run P3 from two computations with different values of maximum allowable time step Δt. 121

6.29 Computed spectra of upper and lower waterline oscillations for Runs P2 and P3. 122

6.30 Spectra, coherence, and phase of incident waves and computed waterline oscillations on lower slope for Run P2. 123

6.31 Computed spectra, coherence, and phase of waterline oscillations on upper and lower slopes for Run P2. 124

6.32 Mass balance for Region 1 for Run P2. 128

6.33 Mass balance for Regions 2 and 3 for Run P2. 128

6.34 Time-averaged volume fluxes for Runs P2 and P3. 129

6.35 Time-averaged energy quantities for Region 1 for Run P2. 133

6.36 Time-averaged energy quantities for Regions 2 and 3 for Run P2. . . . 133

6.37 Energy balance for Regions 2 and 3 for Runs P2 and P3. 134

6.38 Time-averaged energy quantities for Region 1 for Run P1 from two computations with $\epsilon_1=\epsilon_2=1$ and $\epsilon_1=\epsilon_2=3$. 135

6.39 Time-averaged energy quantities for Region 1 for Run P1 from two computations with $\epsilon_1=\epsilon_2=1$ and $\epsilon_1=\epsilon_2=0$. 136

6.40 Mean, maximum, and minimum values of free surface and water table elevation η for Run P1 from three computations with different values of Δx. 138

7.1 Computed reflected wave spectra at $x=0$ for six runs. 143

7.2 Computed reflection coefficient, coherence and phase between incident and reflected waves at $x=0$ for Runs P1 and I1. 144

7.3 Computed reflection coefficient, coherence and phase between incident and reflected waves at $x=0$ for Runs P3 and I3. 145

7.4 Computed spectra of waterline oscillations on 1:3 slope as well as coherence and phase between incident waves and waterline oscillations for Runs P1 and I1. 149

7.5 Computed spectra of waterline oscillations on 1:3 slope as well as coherence and phase between incident waves and waterline oscillations for Runs P3 and I3. 150

7.6 Instantaneous spatial variations of free surface elevation η for Runs P1 and I1. 151

7.7 Instantaneous spatial variations of depth-averaged horizontal velocity u for Runs P1 and I1. 152

7.8 Instantaneous spatial variations of free surface elevation η for Runs P3 and I3. 153

7.9 Instantaneous spatial variations of depth-averaged horizontal velocity u for Runs P3 and I3. 154

7.10 Mean, maximum, and minimum values of free surface elevation η and depth-averaged horizontal velocity u for Runs P1 and I1. 155

7.11 Mean, maximum, and minimum values of free surface elevation η and depth-averaged horizontal velocity u for Runs P3 and I3. 156

7.12 Computed exceedance probability of run-up as compared with Rayleigh distribution for six runs. 157

7.13 Time-averaged energy quantities for Runs P1 and I1. 159

7.14 Time-averaged energy quantities for Runs P3 and I3. 160

7.15 Spatial variations of local stability number N_{sx} for six runs. 164

7.16 Flow conditions at time of minimum armor stability for Runs P1 and I1. 165

7.17 Flow conditions at time of minimum armor stability for Runs P3 and I3. 166

7.18 Evolution of spectra of surface elevation for Runs P1 and I1. 168

7.19 Evolution of spectra of surface elevation for Runs P3 and I3. 169

LIST OF TABLES

6.1 Three test runs compared with numerical model. 81

6.2 Computation parameters specified as input to numerical model. 83

6.3 Effective range of normalized frequency domain. 85

6.4 Measured and computed values of average reflection coefficient $\overline{r}$, wave set-up $\overline{Z_r^U}$, significant swash height h_s^U, significant run-up R_s^U, and maximum run-up R_{max}^U on the upper slope. 87

6.5 Largest absolute values of R_h, R_E, and R_{E_P}. 127

7.1 Computation parameters specified as input to computations for Runs I1, I2, and I3. 141

7.2 Computed values of average reflection coefficient $\overline{r}$, wave set-up $\overline{Z_r^U}$, significant swash height h_s^U, significant run-up R_s^U, and maximum run-up R_{max} for permeable (P) and impermeable (I) slopes. 142

7.3 Computed values of critical stability number N_{sc}, time t_{sc}, and coordinates (x_{sc},z_{sc}) of minimum stability for permeable (P) and impermeable (I) slopes, together with stability number N_s for each test run. 163

ABSTRACT

A one-dimensional, time-dependent numerical model is developed to simulate the flow on a rough slope of arbitrary geometry and the flow inside a permeable underlayer of arbitrary thickness for specified normally-incident irregular waves. The continuity and momentum equations are used to solve the flow fields, whereas the energy equation for each flow field is utilized to estimate energy fluxes and dissipation rates. The derivations of these equations and adopted finite difference methods are presented to clarify the approximations and assumptions made in the numerical model.

The comparison with three test runs shows that the model can predict the time series and spectral characteristics of the reflected waves and waterline oscillations on a 1:3 rough slope with a thick permeable underlayer. The examination of the computed energy balance shows that the incoming wave energy is dissipated little over the rough slope but is transmitted mostly into the permeable underlayer to be dissipated locally by the turbulent and viscous flow resistance. The 1:3 permeable slope tends to reflect low-frequency wave components and dissipate high-frequency wave components. The average reflection coefficient increases with the increase of the surf similarity parameter. The degree of the waterline oscillation on the 1:3 slope also increases as the surf similarity parameter is increased. The low-frequency components in the waterline oscillations on the 1:3 slope are very small unlike shoreline oscillations on sand beaches. The probability distribution of individual run-up heights tends to follow the Rayleigh distribution, except for very small exceedance probability. Moreover, the circulation of time-averaged mass flux is as follows: into the permeable underlayer above the still water level (SWL), out of the underlayer below SWL, landward above the rough slope, and seaward inside the underlayer.

The computed results for the 1:3 rough permeable slope and the corresponding impermeable slope are also compared to quantify the differences caused solely by the thick permeable underlayer. The thick permeable underlayer is shown to reduce the wave reflection and run-up noticeably and increase the stability of armor units considerably. The thick permeable underlayer is effective in dissipating the high-frequency wave components.

Chapter 1

INTRODUCTION

Quantitative understanding of the interaction of irregular waves with permeable slopes is essential for the design of breakwaters with S-shape profiles (Bruun and Johannesson 1976), berm breakwaters (Baird and Hall 1984), reef breakwaters (Ahrens 1989), dynamic revetments (Ahrens 1990), and bermed revetments (Ahrens and Ward 1991). Viscous effects inside permeable slopes are normally not in similitude between small-scale physical models and prototypes (Johnson, Kondo, and Wallihan 1966; Delmonte 1972; Wilson and Cross 1972; Hall 1991; Bruun 1992). Alternatively, numerical models may be calibrated using model tests and applied to simulate the viscous and turbulent flow resistance inside the permeable slope. Furthermore, numerical models yield quantitative information, some of which is difficult or impossible to measure, with high spatial and temporal resolutions. The quantitative understanding of the hydrodynamic processes involved with irregular wave interaction with permeable slopes is still rudimentary, although extensive hydraulic model tests have been performed.

The existing computer programs developed by Kobayashi and Wurjanto (1989a) and Wurjanto and Kobayashi (1991) are applicable only to impermeable structures and beaches. As a result, they can not be applied to the highly permeable structures mentioned above. An initial attempt to include the permeability effect was made by Kobayashi and Wurjanto (1990) by assuming a thin permeable underlayer. The assumption of the thin permeable underlayer allows one to neglect the region landward of the waterline on the rough slope and the inertia terms in the horizontal momentum equation for the flow inside the thin permeable underlayer. However, this previous numerical model has turned out to be of limited practical use since the permeability effects of the thin permeable underlayer have been found to be minor or negligible. The previous numerical model and computed results based on the assumption of the thin permeable underlayer are summarized in the next section, whereas different models for permeable breakwaters developed by other researchers is reviewed in Section 1.3.

An improved numerical model for a permeable slope with a thick permeable underlayer is described in detail herein. The improved numerical model eliminates most of the shortcomings of the previous models. Finite difference equations based on the numerical methods of Lax and Wendroff (1960) and MacCormack (1969) are developed from the governing equations. Section 1.4 provides a background for the adoption of these numerical methods. The performance of the improved numerical model is then examined and the computed results are interpreted physically. An outline of the presentation of the present work is given in Section 1.5.

The numerical model developed by Wurjanto and Kobayashi (1991) is also used in Chapter 7 to simulate the flow field on the corresponding impermeable slope to quantify the permeability effects. A summary of the previous work related to this model for impermeable slopes is provided in Section 1.2 since it is not explained in Chapter 7 and the present numerical model is an extension of this previous model.

1.1 Previous Work for Thin Permeable Underlayer

Kobayashi and Wurjanto (1990) developed a numerical model to predict the flow and armor response on a rough permeable slope as well as the flow in a thin permeable underlayer for a normally-incident wave train. In addition to the continuity and momentum equations used to compute the flow fields, an equation of energy was used to estimate the rate of energy dissipation due to wave breaking. Computation was made for six test runs to examine the accuracy and capability of the numerical model for simulating the fairly detailed hydrodynamics and armor response under the action of regular waves. The computed critical stability number for initiation of armor movement was compared with the measured stability number corresponding to the start of the damage under irregular wave action to quantify the limitations of the regular wave approximation. The computed wave run-up, run-down, and reflection coefficients were shown to be in qualitative agreement with available empirical formulas based on regular wave tests. Kobayashi and Wurjanto (1989b) applied the developed numerical model to hypothetical permeable slopes corresponding to available impermeable slope tests. The computed results with and without a permeable underlayer indicated that the permeability effects would increase the hydraulic stability of armor units noticeably and decrease wave run-up and reflection slightly. The computed results were qualitatively consistent with available data although they were not extensive and limited to regular waves only.

Kobayashi, Wurjanto, and Cox (1990a) applied the developed numerical model to compute the irregular wave motion on a rough permeable slope. The normally-incident irregular wave train characterized by its spectral density at the toe of the slope was generated numerically for six test runs. The computed critical stability number for initiation of armor movement under the computed irregular wave motion was shown to be in fair agreement with the measured stability number corresponding to the start of the damage (Van der Meer 1988). The comparison of the computed armor stability for the incident regular and irregular waves indicated that the armor stability would be reduced appreciably and vary less along the slope under the irregular wave action. On the other hand, the comparison between the computed reflected wave spectrum and the specified incident wave spectrum indicated the reflection of Fourier components with longer periods and the dissipation of Fourier components with shorter periods, while the average reflection coefficient increased with the increase of the surf similarity parameter. The computed waterline oscillations were examined using spectral and time series analyses. The computed spectra of the waterline oscillations showed noticeable low-frequency components, which increased with the decrease of the surf similarity parameter. The statistical analysis of individual wave run-up heights indicated that the computed run-up distribution followed the Rayleigh distribution fairly well for some of the six test runs. The computed maximum wave run-up was in agreement with the empirical formula based on irregular wave run-up tests.

Furthermore Kobayashi, Wurjanto, and Cox (1990b) analyzed the computed results for the six test runs to examine the critical incident wave profile associated with the minimum rock stability for each run. The minimum rock stability computed for the runs with dominant plunging waves on gentle slopes was caused by the large wave with the maximum crest elevation during its up-rush on the slope. The minimum rock stability computed for the runs with dominant surging waves on steeper slopes was caused by the down-rushing water with high velocities resulted from a large zero-upcrossing wave with a high crest followed by a deep trough. These computed results may eventually allow one to quantify incident design wave conditions more specifically than the simple approach based on the representative wave height and period. In addition, a simplified model was proposed to predict the eroded area due to the movement and dislodgement of rock units using the probability of armor movement computed by the numerical model. This model was shown to be in qualitative agreement with the empirical formula for the damage level proposed by Van der Meer (1988).

The numerical model based on the assumption of a thin permeable underlayer was found to be inapplicable to three test runs conducted for a 1:3 rough permeable slope with a thick permeable underlayer (Kobayashi, Cox, and Wurjanto 1991). The computed results did not satisfy the time-averaged equation of mass conservation mainly because the previous model did not account for water storage in the region landward of the waterline on the slope.

1.2 Previous Work for Impermeable Slopes

Kobayashi and Wurjanto (1989a) developed a computer program called IBREAK, which may be used for the design of rough or smooth impermeable coastal structures of arbitrary geometry against normally-incident monochromatic or transient waves. IBREAK had been extensively examined for regular waves. A summary of the previous work related to IBREAK is given in Wurjanto and Kobayashi (1991). Attempts have been made to simulate irregular waves on the slope of a coastal structure using IBREAK since any incident wave train can be specified as input to IBREAK at the seaward boundary of the computation domain. However, the irregular waterline oscillation on the slope was found to cause numerical difficulties and stoppage during the computation of a sufficient duration for a stationary random sea. The constant time step size Δt for the explicit finite difference method used in IBREAK was reduced to overcome the numerical difficulties. This increased the computation time considerably but did not always work.

Wurjanto and Kobayashi (1991) developed a computer program called RBREAK, which is an improved version of IBREAK with an automated adjustment procedure. The adjustment procedure reduces the time step size Δt for portions of the computation with numerical difficulties. Since the portions with numerical difficulties are not known in advance, the time-marching computation needs to be reversed to an earlier time level before the initiation of the current numerical difficulty and then resumed from the reversed time level using a smaller value of Δt. To reduce the computation time, the value of Δt needs to be increased after overcoming the current numerical difficulty. This automated adjustment procedure has been essential for making successful computations for incident random waves of sufficient durations in an efficient manner. The subroutines required for the spectral and time series analyses for random waves were reported separately by Cox, Kobayashi, and Wurjanto (1991).

Kobayashi, Cox, and Wurjanto (1990) showed that RBREAK could predict the time series and spectral characteristics of irregular wave reflection and run-up on a 1:3 rough impermeable slope. Kobayashi and Wurjanto (1992) showed that RBREAK could also be used to predict shoreline oscillations on natural beaches, which are normally dominated by low-frequency wave components (Guza and Thornton 1982, Holman and Sallenger 1985). On the other hand, Wise, Kobayashi, and Wurjanto (1991) attempted to predict the net cross-shore sediment transport in the surf and swash zones using the depth-averaged velocities computed by RBREAK. Their attempt has indicated that RBREAK will need to be expanded to account for the vertical variation of the horizontal fluid velocity, if it is to be applied to predict the net cross-shore sediment transport.

1.3 Other Analytical and Numerical Models for Permeable Structures

This section summarizes existing analytical and numerical models for permeable structures developed by other researchers so that the distinction of the present work from those of other researchers can be seen in a perspective.

Most analytical models for wave interaction with a permeable structure assumed a linear system forced by a simple harmonic wave motion from outside the structure to analyze the simple harmonic wave motion inside the permeable structure (Sollitt and Cross 1972, 1976; Kondo and Toma 1972; Madsen 1974; Madsen and White 1976; Madsen, Shusang, and Hanson 1978; Madsen 1983; Scarlatos and Singh 1987; Dalrymple, Losada, and Martin 1991). Massel and Butowski (1980) used a forcing in the form of a wind wave spectrum, but assumed a linear system. Dalrymple, Losada, and Martin (1991) considered obliquely-incident waves, while the others assumed normally-incident waves. For the analysis of wave transmission through porous breakwaters, Madsen and co-authors (1974, 1976, 1978) and Scarlatos and Singh (1987) adopted the long wave assumption for the reason that severe design wave conditions for breakwaters normally correspond to relatively long waves. Kondo and Toma (1972) and Madsen (1983) assumed long waves as well, probably because the long wave assumption simplifies the analysis considerably as demonstrated by Sollitt and Cross (1972, 1976) and Dalrymple, Losada, and Martin (1991). Except for Madsen, Shusang, and Hanson (1978) who dealt exclusively with trapezoidal breakwaters, the analytical solutions in the work mentioned above were developed for rectangular structures. Trapezoidal structures were treated by introducing a concept of an equivalent rectangular breakwater so that solutions developed for rectangular structures could be applied (Sollitt and Cross 1972, 1976; Madsen and White 1976; Massel and Butowski 1980). Energy losses on the seaward slope of a trapezoidal structure were taken into account in different ways. Sollitt and Cross (1972, 1976) considered energy loss due to wave breaking in an empirical manner. Madsen and co-authors (1976, 1978) assumed no wave breaking but took into account energy loss due to bottom friction.

There is no universally accepted formulation expressing the flow resistance inside the permeable structures. However, most of available expressions have the following form (*e.g.*, Bear 1979):

$$\delta \mathbf{F} = -\rho \left(a + b \left| \mathbf{v} \right| \right) \mathbf{v} \tag{1.1}$$

where ρ is the fluid density, $\delta \mathbf{F}$ is the resistance force per unit volume, $\mathbf{v}$ is the discharge velocity inside the permeable structure, a and b are coefficients associated with laminar and turbulent flow resistance, respectively. Eq. 1.1, which is also known as the Forchheimer relation in honor of its originator (Scheidegger 1960), is based on the widely accepted premise that laminar flow resistance follows the Darcy's law, whereas turbulent flow resistance varies approximately with the second power of velocity (Todd 1980). Hall (1992) compiled eleven different expressions for the coefficients a and b. For example, Sollitt and Cross (1972, 1976) and Dalrymple, Losada, and Martin (1991) used an expression similar to Ward (1964). Madsen and co-authors (1974, 1976, 1978) and Madsen (1983) utilized the expression introduced by Engelund (1953). Massel and Butowski (1980) adopted the approach of Arbhabhirama and Dinoy (1973). In the majority of studies mentioned above, the Lorentz' principle of equivalent work was applied to linearize the resistance force expressed by Eq. 1.1 in order to derive a linear equation of motion inside the permeable structure [*e.g.*, Madsen (1983)]. Sollitt and Cross (1972, 1976), and Dalrymple, Losada, and Martin (1991) applied a potential flow approach and presented their solutions in the form of eigenfunction expansions, whose leading term corresponded to the long wave assumption. Massel and Butowski (1980) also used the potential flow approach. Others assumed long waves in the first place and utilized various analytical methods to arrive at their solutions.

A numerical solution to the problem of wave reflection and transmission at permeable breakwaters was given by Sulisz (1985) using a boundary element method. The equation of motion was linear and forced by normally-incident simple harmonic waves. Thanks to the use of the boundary element method, this model could handle any vertically two-dimensional structure geometry. However, the model did not consider any energy dissipation mechanism on the seaward side of an inclined structure.

Another class of numerical models for wave interaction with permeable structures was developed by Hannoura and McCorquodale (1985), Barends and Holscher (1988), and Holscher and Barends (1990). These models utilized a hybrid of finite difference (FD) and finite element (FE) schemes. First, the water table elevation inside the permeable structure was computed by a one-dimensional FD scheme. Second, an FE scheme was then used to simulate the vertical flow field below the computed water table in the porous medium. The numerical models required the measured pressure distribution along the seaward side of the structure as a boundary condition. As a result, these models can not be used to predict the flow field inside a permeable structure for given normally-incident waves. This class of models dealt only with the interior processes inside permeable structures. Any kind of the boundary pressure distribution can be imposed, unlike the other models discussed in this section, which solved only the linear wave fields outside and inside the permeable structure.

In the present work, a numerical model in the time domain is developed to solve the flow fields inside and above a permeable slope for any incident wave train represented by its surface elevation. Energy losses due to bottom friction and wave breaking above the permeable slope are facilitated through the inclusion of a shear stress in the equation of motion as will be described in Chapter 2. In perspective, the present work on wave interaction with coastal structures may be seen as a milestone in the continuing efforts to develop realistic numerical models of practical use starting from IBREAK (Kobayashi and Wurjanto 1989a) and then RBREAK (Wurjanto and Kobayashi 1991). The wave hydrodynamics *above* the seaward slope of coastal structures have been extensively studied using IBREAK and RBREAK as summarized in the preceding sections. An attempt is made herein to simulate the nonlinear wave motion inside permeable coastal structures as well. The permeability effects are considered to be important for highly porous coastal structures. The present numerical model is the first model to simulate the nonlinear interaction of the flow fields above and inside a thick permeable underlayer.

1.4 Background for Adopted Numerical Methods

Used in present numerical model are proven numerical methods in similar problems. No attempt is made to compare different numerical methods in solving the problem at hand, although this may be done in a future work. Emphasis is placed on the application of proven numerical methods to show the feasibility of simulating the nonlinear wave interactions and gain an insight into the physical processes involved in the problem. This is an important first step since the nonlinear interaction of breaking or non-breaking waves with permeable slopes has never been computed previously.

The finite difference method introduced by Lax and Wendroff (1960) is adopted in the present work to solve the flow field above the permeable slope. Basically, a shock-capturing numerical method is needed to solve this flow field because of potential development of steep fronts of breaking and broken waves on the permeable slope. A recent review of numerical methods developed for flows with shocks was given by Moretti (1987). The Lax-Wendroff method has been used in our previous numerical models IBREAK and RBREAK because of its proven track record in solving problems involving bores on beaches (Hibberd and Peregrine 1979, Packwood 1980 and 1983). Moreover, the Lax-Wendroff method has a proven option to include numerical dissipation to damp high frequency oscillations which tend to appear on the rear of computed steep fronts (Richtmyer and Morton 1967).

The flow field inside the permeable slope, on the other hand, is solved using the MacCormack method (MacCormack 1969) for several reasons. First, the Lax-Wendroff method may not be applied easily because the Jacobian required in this method does not exist as will be described in Section 4.4. Second, the MacCormack method may be regarded as a simplified version of the Lax-Wendroff method without numerical dissipation, where physical dissipation is dominant inside the permeable slope as will be shown in Chapter 6. Third, the MacCormack method, besides being very popular in computational aerodynamics (Roache 1982), is also a very efficient method for unsteady open channel flow as shown by Fennema and Chaudhry (1986), who compared the MacCormack method against the Lambda method (Moretti 1979), Gabutti method (Gabutti

1983), and Preissmann method (Cunge, Holley, and Verwey 1980). It should be mentioned that Fennema and Chaudhry (1986) selected the first three methods, which are second order accurate, explicit finite difference methods, on the basis of their simplicity, robustness, and capability of capturing shocks. While the three methods performed comparably in those criteria, the MacCormack method fared the best in terms of CPU usage. The implicit Preissmann method was included to demonstrate the efficiency of explicit methods. The MacCormack method has been selected as a first choice in this study in the light of the findings of Fennema and Chaudhry (1986).

1.5 Objectives and Outline of the Present Work

The present work examines the time-dependent, one-dimensional flow fields above and inside a rough permeable slope. The rough permeable slope consists of a permeable underlayer resting on an impermeable slope and an armor layer covering the permeable underlayer. The upper boundary of the permeable underlayer separates the flow field above the rough slope and the flow field inside the permeable underlayer. The computer program called PBREAK, described in detail by Wurjanto and Kobayashi (1992), simulates this two-flow system. Hereafter, this user's manual by Wurjanto and Kobayashi (1992) will be referred to as *WK 92* and the numerical model described in WK 92 will be referred to as PBREAK for brevity.

The objectives of the present work are as follows:

1. To provide the derivations of the approximate governing equations and finite difference methods used in PBREAK.
2. To evaluate the performance of PBREAK by comparing it with available experimental results.
3. To examine the computed results to elucidate the hydrodynamic processes involved in the interaction of irregular waves with the highly permeable slope.

4. To compare the computed results using PBREAK with those for the corresponding impermeable slope in order to quantify the differences caused *solely* by the presence of the thick permeable underlayer.

WK 92 has presented the final results of the approximate governing equations for the two-flow system and the numerical methods of Lax and Wendroff (1960) and MacCormack (1969) without proof since it is a user's manual. The seaward and landward boundary conditions have been explained in detail, and the computational aspects including examples have been discussed extensively. In short, WK 92 provides information required to apply and modify PBREAK without knowing the detailed background of the governing equations and numerical methods.

The derivation of the governing equations for the flow over the rough slope and the flow inside the permeable underlayer starts in Chapter 2 where the two-dimensional continuity and momentum equations are discussed and simplified. The simplified two-dimensional equations obtained in Chapter 2 are further reduced to one-dimension in Chapter 3. The basic assumptions and approximations involved in the numerical model PBREAK are stated in these two chapters.

Chapter 4 derives the finite difference equations on the basis of the dissipative Lax-Wendroff method (Lax and Wendroff 1960) to solve the flow over the rough slope. The MacCormack method (MacCormack 1969) used to solve the finite difference equations for the flow inside the permeable underlayer is discussed in this chapter in relation with the Lax-Wendroff method.

Chapter 5 derives the one-dimensional energy equation for each flow field from the corresponding continuity and approximate momentum equations to estimate energy fluxes and dissipation rates.

The aspects of the numerical model PBREAK explained sufficiently in WK 92 are not repeated herein. These include the boundary conditions, numerical stability, and hydraulic stability of armor units. These aspects of the numerical model are explained only to the degree needed for interpreting the computed results.

The performance of PBREAK is evaluated in Chapter 6 by comparing it with the three laboratory test runs for irregular wave reflection and run-up on a rough permeable slope conducted by Cox (1989). The computed results are also examined to gain a better physical insight into the hydrodynamic processes.

Chapter 7 examines how permeable and impermeable slopes interact with identical incident irregular wave trains where use is made of the numerical model RBREAK developed by Wurjanto and Kobayashi (1991) to simulate the flow on the corresponding impermeable slope. The permeable and impermeable slopes are subjected to the identical incident irregular wave trains so that the differences on the computed results can be attributed solely to the presence of the thick permeable underlayer.

Chapter 2

APPROXIMATE TWO-DIMENSIONAL EQUATIONS

The physical analysis domain is depicted in Figure 2.1 where normally-incident waves interact with a thick layer of homogeneous permeable materials placed on top of an impermeable slope and protected by a primary cover layer. The seaward end of the analysis domain is at the location where the upper and lower boundaries of the permeable underlayer intersect and the water depth below the still water level (SWL) is d'_t. The symbols shown in Figure 2.1 are explained as they appear in the following analysis.

2.1 Flow over Rough Slope

Approximate governing equations for the flow over the rough slope due to normally-incident waves are derived from the two-dimensional continuity and Reynolds equations [*e.g.*, Panton (1984)]:

$$\frac{\partial u'_j}{\partial x'_j} = 0 \tag{2.1}$$

$$\frac{\partial u'_i}{\partial t'} + u'_j \frac{\partial u'_i}{\partial x'_j} = -\frac{1}{\rho}\frac{\partial p'}{\partial x'_i} - g\delta_{i2} + \frac{1}{\rho}\frac{\partial \tau'_{ji}}{\partial x'_j} \tag{2.2}$$

in which the prime indicates the physical variables and use is made of the summation convention with respect to repeated indices. The symbols involved in Eqs. 2.1 and 2.2 are explained in the following:

t' = time

x'_1 = horizontal coordinate taken to be positive landward

x'_2 = vertical coordinate taken to be positive upward with x'_2=0 at SWL

u'_1 = horizontal velocity

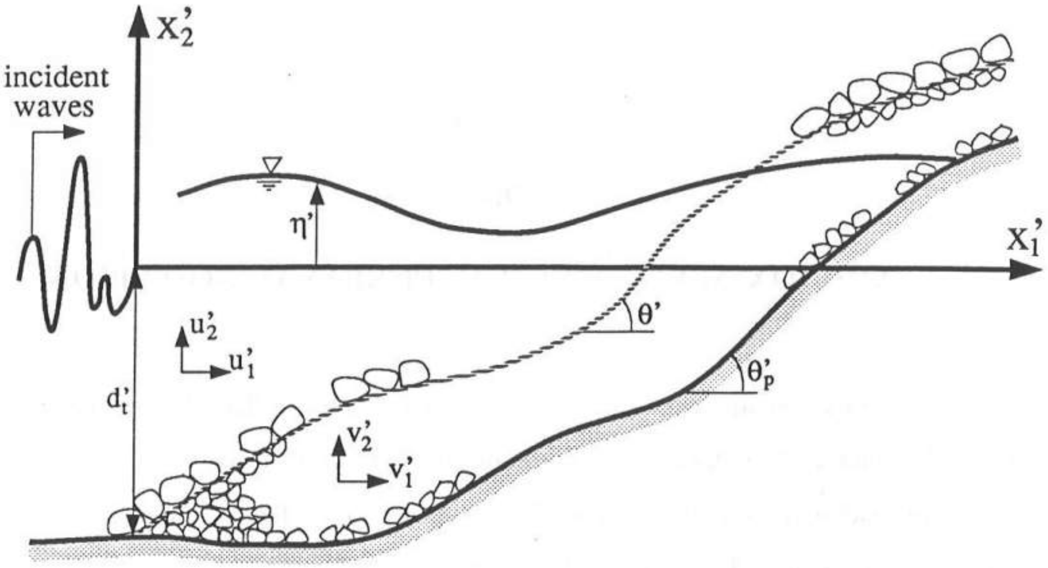

Figure 2.1: Definition sketch for flow over rough slope and inside permeable underlayer.

u_2' = vertical velocity
ρ = fluid density, which is assumed constant
p' = pressure
g = gravitational acceleration
δ_{i2} = Kronecker delta
τ_{ji}' = sum of turbulent and viscous stresses

The following dimensionless variables and parameters are introduced to normalize Eqs. 2.1 and 2.2:

$$t = \frac{t'}{T'} \quad ; \quad x_1 = \frac{x_1'}{T'\sqrt{gH'}} \quad ; \quad x_2 = \frac{x_2'}{H'} \quad ; \quad u_1 = \frac{u_1'}{\sqrt{gH'}} \quad ; \quad u_2 = \frac{T'u_2'}{H'} \tag{2.3}$$

$$p = \frac{p'}{\rho g H'} \quad ; \quad \tau_{ji} = \frac{T'\tau_{ji}'}{\rho H'\sqrt{gH'}} \quad ; \quad \sigma = T'\sqrt{\frac{g}{H'}} \tag{2.4}$$

where H' and T' are the characteristic wave height and period used for the normalization. It is obvious from Eq. 2.3 that the length scales used in this analysis are

$$L_1' = T'\sqrt{gH'} = \text{horizontal length scale} \tag{2.5}$$

$$L'_2 \quad = \quad H' \quad = \quad \text{vertical length scale} \tag{2.6}$$

The following explanation is intended to clarify the choice of the length scales given in Eqs. 2.5 and 2.6. Shallow water wave theories generally involve one horizontal length scale, λ_1, and two vertical length scales: λ_2 for wave height and λ_3 for water depth. The three length scales are normally reduced to the following two dimensionless parameters: Γ_1 representing the ratio $\frac{\lambda_3}{\lambda_1}$, and Γ_2 representing the ratio $\frac{\lambda_2}{\lambda_3}$ [*e.g.*, Mei (1983)]. In the present work, it is assumed that the water depth is on the same order as the characteristic wave height:

$$\frac{\lambda_3}{\lambda_2} = \bigcirc(1) \tag{2.7}$$

where the notation $\bigcirc(1)$ means the order of unity. This assumption is normally satisfied for breakwaters and revetments located in relatively shallow water during severe design wave conditions. This assumption leads to the single vertical length scale which is taken to be the characteristic wave height H' based on the premise that wave steepness is important to be represented by the resulting single dimensionless parameter. The parameter σ in Eq. 2.4 represents the ratio of the horizontal length scale L'_1 to the vertical length scale L'_2. Since L'_2 equals H', L'_1 may be regarded as a characteristic wavelength in shallow water and σ is then also a measure of wave steepness. For the uniform slope inclination θ', the parameter σ is directly related to the surf similarity parameter $\xi = \frac{\sigma}{\sqrt{2\pi}} tan\theta'$ (Battjes 1974) which has been used extensively to describe gross wave characteristics on uniform slopes.

For waves in shallow water, it may be assumed that the dimensionless variables t, x_1, x_2, u_1, u_2, and p are on the order of unity and the normalized stresses τ_{ji} are on the order of unity or less. The present analysis will be limited to the case where the following conditions are satisfied:

$$\sigma^2 \gg 1 \quad \text{and} \quad (\cot\theta')^2 \gg 1 \tag{2.8}$$

with $\tan\theta'$ being the characteristic slope in the analysis domain. The condition $\sigma^2 \gg 1$ in Eq. 2.8 may be appropriate for waves in shallow water although this condition may not be satisfied locally at the steep front of a breaking wave where the local horizontal length scale may become as small as the vertical length scale. The condition $(\cot\theta')^2 \gg 1$ in Eq. 2.8 is required since the horizontal and vertical length scales for a steep slope may be imposed by the slope geometry and $\cot\theta'$ may express the ratio between the horizontal and vertical length scales.

Substituting Eqs. 2.3 and 2.4 into Eqs. 2.1 and 2.2 yields

$$\frac{\partial u_j}{\partial x_j} = 0 \tag{2.9}$$

$$\frac{\partial u_1}{\partial t} + u_j\,\frac{\partial u_1}{\partial x_j} = -\frac{\partial}{\partial x_1}\left(p - \frac{\tau_{11}}{\sigma}\right) + \frac{\partial \tau_{21}}{\partial x_2} \tag{2.10}$$

$$\frac{1}{\sigma^2}\left(\frac{\partial u_2}{\partial t} + u_j\,\frac{\partial u_2}{\partial x_j} - \frac{\partial \tau_{12}}{\partial x_1}\right) = -\frac{\partial}{\partial x_2}\left(p - \frac{\tau_{22}}{\sigma} + x_2\right) \tag{2.11}$$

Adding the following terms, which are zero,

$$\frac{\partial}{\partial x_1}\left(\frac{\tau_{22}}{\sigma}\right) - \frac{\partial}{\partial x_1}\left(\frac{\tau_{22}}{\sigma}\right)$$

Eq. 2.10 is rearranged as follows:

$$\frac{\partial u_1}{\partial t} + u_j\,\frac{\partial u_1}{\partial x_j} = -\frac{\partial}{\partial x_1}\left(p - \frac{\tau_{22}}{\sigma}\right) + \frac{\partial \tau_{21}}{\partial x_2} + \frac{1}{\sigma}\,\frac{\partial}{\partial x_1}\left(\tau_{11} - \tau_{22}\right) \tag{2.12}$$

Furthermore, assuming that the stress difference $(\tau_{11} - \tau_{22})$ is on the order of $\frac{1}{\sigma}$ or less, the last term of Eq. 2.12 may be neglected under the assumption $\sigma^2 \gg 1$ in Eq. 2.8. Eq. 2.12 may thus be simplified as

$$\frac{\partial u_1}{\partial t} + u_j\,\frac{\partial u_1}{\partial x_j} = -\frac{\partial}{\partial x_1}\left(p - \frac{\tau_{22}}{\sigma}\right) + \frac{\partial \tau_{21}}{\partial x_2} \tag{2.13}$$

Also under the assumption $\sigma^2 \gg 1$ in Eq. 2.8, the normalized vertical momentum equation, Eq. 2.11, may be simplified by neglecting the terms on its left hand side:

$$\frac{\partial}{\partial x_2}\left(p - \frac{\tau_{22}}{\sigma} + x_2\right) = 0 \tag{2.14}$$

The symbol η' in Figure 2.1 represents the physical free surface elevation above SWL. Its normalized counterpart, η, is given by

$$\eta = \frac{\eta'}{H'} \tag{2.15}$$

where H' is the characteristic wave height. The dynamic boundary conditions at the free surface $x_2 = \eta$ are taken as zero normal and tangential stresses at the free surface, which result in

$$p - \frac{\tau_{22}}{\sigma} = 0 \quad ; \quad \tau_{21} = 0 \qquad \text{at} \quad x_2 = \eta \tag{2.16}$$

as explained in the following. Figure 2.2 shows the surface stresses acting on an infinitesimal fluid element bounded on one side by the free surface $x_2' = \eta'$. There is no stress at the free surface side because of the assumed dynamic boundary conditions thereat. For $\delta x_1' \rightarrow 0$ and $\dfrac{\delta x_2'}{\delta x_1'} \rightarrow \dfrac{\partial \eta'}{\partial x_1'}$, the vertical and horizontal force balances are expressed as

$$-p' + \tau_{22}' = \tau_{12}' \, \frac{\partial \eta'}{\partial x_1'} \qquad \text{at} \quad x_2' = \eta' \tag{2.17}$$

$$(-p' + \tau_{11}') \, \frac{\partial \eta'}{\partial x_1'} = \tau_{21}' \qquad \text{at} \quad x_2' = \eta' \tag{2.18}$$

Substituting Eqs. 2.3 and 2.4 into Eq. 2.17 yields

$$\begin{aligned} -p + \frac{\tau_{22}}{\sigma} &= \frac{1}{\sigma^2}\, \tau_{12} \, \frac{\partial \eta}{\partial x_1} \qquad \text{at} \quad x_2 = \eta \\ \text{Neglect term of order } \frac{1}{\sigma^2} &\quad \Downarrow \\ -p + \frac{\tau_{22}}{\sigma} &= 0 \qquad \text{at} \quad x_2 = \eta \end{aligned} \tag{2.19}$$

Substituting Eqs. 2.3, 2.4, and 2.19 into Eq. 2.18 yields

$$\begin{aligned} \frac{1}{\sigma^2}\, (\tau_{11} - \tau_{22}) \, \frac{\partial \eta}{\partial x_1} &= \frac{1}{\sigma}\, \tau_{21} \qquad \text{at} \quad x_2 = \eta \\ \text{Neglect terms of order } \frac{1}{\sigma^2} &\quad \Downarrow \\ \tau_{21} &= 0 \qquad \text{at} \quad x_2 = \eta \end{aligned} \tag{2.20}$$

Eqs 2.19 and 2.20 are identical to the dynamic boundary conditions given in Eq. 2.16.

Integrating Eq. 2.14 with respect to x_2 and employing Eq. 2.16, Eq. 2.14 yields

$$p = \eta - x_2 + \frac{\tau_{22}}{\sigma} \tag{2.21}$$

Eq. 2.21 will be substituted into Eq. 2.13 in Section 3.2.

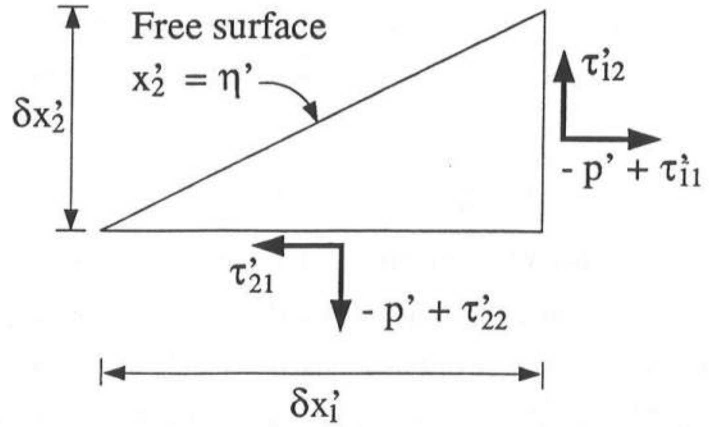

Figure 2.2: Surface stresses acting on fluid element near free surface.

2.2 Flow inside Permeable Underlayer

The major question in analyzing the flow inside the permeable underlayer is how to express the flow resistance. Since there are so many formulas in the literature as discussed in Section 1.3, any formula may be adopted provided empirical coefficients have been calibrated for similar problems.

The flow resistance formula of Engelund (1953) used by Madsen and White (1976) is particularly appealing since Madsen and White (1976) obtained a good agreement between their analytical model and the experiment on regular wave transmission conducted by Sollitt and Cross (1972) with little calibration of empirical coefficients. This flow resistance formula was also adopted by Madsen (1983) who compared his analytical model with the numerical model developed by Abbott, McCowan, and Warren (1981). It may be of interest to compare various resistance formulas but the empirical coefficients involved in these formulas may need to be calibrated for specific problems. The flow resistance formula of Engelund (1953) is adopted herein because it has been applied successfully to the closely related problems of wave reflection and transmission at permeable breakwaters.

Approximate governing equations for the flow inside the permeable underlayer may be derived from the the following two-dimensional continuity and momentum equations (Madsen and White 1976):

$$\frac{\partial v'_j}{\partial x'_j} = 0 \tag{2.22}$$

$$\frac{1}{n_p}\,\frac{\partial v'_i}{\partial t'} + \frac{1}{n_p^2}\,v'_j\,\frac{\partial v'_i}{\partial x'_j} = -\frac{1}{\rho}\,\frac{\partial p'}{\partial x'_i} - g\delta_{i2} - \left(\alpha' + \beta'\sqrt{v'_j v'_j}\right) v'_i \tag{2.23}$$

with

$$\alpha' = \frac{\alpha_o\,(1-n_p)^3\,\nu}{\left(n_p\,d'_p\right)^2} \tag{2.24}$$

$$\beta' = \frac{\beta_o\,(1-n_p)}{n_p^3\,d'_p} \tag{2.25}$$

in which

v'_1 = horizontal discharge velocity
v'_2 = vertical discharge velocity
n_p = porosity of the permeable underlayer
α' = coefficient expressing the laminar flow resistance
β' = coefficient expressing the turbulent flow resistance
ν = kinematic viscosity of the fluid
d'_p = characteristic stone diameter inside the permeable underlayer
α_o = empirical constant in the range $780 \leq \alpha_o \leq 1500$
β_o = empirical constant in the range $1.8 \leq \beta_o \leq 3.6$

It is noted that Madsen and White (1976) included the added mass terms in Eq. 2.23 but eventually neglected them since the added mass coefficients are not well established. The *seepage velocity concept* used in the standard analyses for flow in porous media [*e.g.*, Bear (1979)] is adopted in the following. The porosity and flow-resistance coefficients are assumed to be uniform throughout the porous medium. The horizontal and vertical seepage velocities of the pore fluid are given by $\frac{v'_1}{n_p}$ and $\frac{v'_2}{n_p}$, respectively. It is noted that the porosity n_p used herein is actually the *effective* porosity excluding the part of the voids of the porous medium where molecular and surface-tension forces hold fluid (Marino and Luthin 1982). To normalize Eqs. 2.22 and 2.23, the following dimensionless variables are introduced:

$$v_1 = \frac{v_1'}{p_q\sqrt{gH'}} \quad ; \quad v_2 = \frac{T' v_2'}{p_q H'} \quad ; \quad p_q = n_p p_u \tag{2.26}$$

The variables v_1 and v_2 are assumed to be on the order of unity. The dimensionless parameter p_q indicates the order of magnitude of $\frac{v_1'}{u_1'}$ and $\frac{v_2'}{u_2'}$. Accordingly, the dimensionless parameter p_u indicates the order of magnitude of $\frac{(v_1'/n_p)}{u_1'}$ and $\frac{(v_2'/n_p)}{u_2'}$ where $\frac{v_1'}{n_p}$ and $\frac{v_2'}{n_p}$ are the seepage velocities. The parameter p_u will be determined in the following analysis.

Substituting Eq. 2.26 together with Eq. 2.3 into Eq. 2.22 yields

$$\frac{\partial v_j}{\partial x_j} = 0 \tag{2.27}$$

The following equation is obtained by substituting Eq. 2.26 together with Eqs. 2.3 and 2.4 into the horizontal component of Eq. 2.23:

$$\begin{aligned} p_u \frac{\partial v_1}{\partial t} + p_u^2\, v_j \frac{\partial v_1}{\partial x_j} \;&=\; -\frac{\partial p}{\partial x_1} \\ &\quad - \left[\frac{\alpha_o (1-n_p)^2}{\beta_o\, p_u} \frac{\nu}{d_p' \sqrt{gH'}} + \sqrt{v_1^2 + \frac{1}{\sigma^2} v_2^2} \right] \cdot \\ &\quad \cdot \frac{\beta_o (1-n_p)}{n_p} \cdot \frac{T'\sqrt{gH'}}{d_p'}\, p_u^2\, v_1 \end{aligned} \tag{2.28}$$

To simplify the expression of Eq. 2.28, a new parameter μ is defined as

$$\mu = \frac{\alpha_o (1-n_p)^2}{\beta_o\, p_u} \cdot \frac{\nu}{d_p' \sqrt{gH'}} \tag{2.29}$$

whose significance will be discussed at the end of this section. Since v_1 and v_2 are assumed to be on the order of unity, under the assumption $\sigma^2 \gg 1$, the following approximation may be made:

$$\left(v_1^2 + \frac{1}{\sigma^2} v_2^2 \right) \simeq v_1^2 \tag{2.30}$$

As a result, Eq. 2.28 may be rewritten as

$$p_u \frac{\partial v_1}{\partial t} + p_u^2\, v_j \frac{\partial v_1}{\partial x_j} = -\frac{\partial p}{\partial x_1} - (\mu + |v_1|)\, \frac{\beta_o (1-n_p)}{n_p} \cdot \frac{T'\sqrt{gH'}}{d_p'}\, p_u^2\, v_1 \tag{2.31}$$

As long as p_u and μ are on the order of unity or less, the term $\frac{\partial p}{\partial x_1}$ may be assumed to be on the same order as the term containing $(|v_1|\, v_1)$ in Eq. 2.31. Under this assumption, the parameter p_u may be taken as

$$p_u = \sqrt{\frac{n_p}{\beta_o\,(1-n_p)} \cdot \frac{d_p'}{T'\sqrt{gH'}}} \tag{2.32}$$

The normalized horizontal momentum equation, Eq. 2.31, may then be expressed as

$$p_u\,\frac{\partial v_1}{\partial t} + p_u^2\, v_j\,\frac{\partial v_1}{\partial x_j} = -\frac{\partial p}{\partial x_1} - (\mu + |v_1|)\, v_1 \tag{2.33}$$

Substituting Eq. 2.26 together with Eqs. 2.3, 2.4, 2.29, and 2.32 into the vertical component of Eq. 2.23 yields

$$\frac{1}{\sigma^2}\left(p_u\,\frac{\partial v_2}{\partial t} + p_u^2\, v_j\,\frac{\partial v_2}{\partial x_j}\right) = -\frac{\partial}{\partial x_2}(p + x_2) - \frac{1}{\sigma^2}\left(\mu + \sqrt{v_1^2 + \frac{1}{\sigma^2}v_2^2}\right) v_2 \tag{2.34}$$

For the case of $\sigma^2 \gg 1$, Eq. 2.34 may be simplified by neglecting the terms on the order of $\frac{1}{\sigma^2}$

$$\frac{\partial}{\partial x_2}(p + x_2) = 0 \tag{2.35}$$

Eq. 2.35 is integrated with respect to x_2 to get an explicit expression for the pressure p under two distinct conditions. First, for the region inside the permeable underlayer where the water table is exposed to air, the dynamic boundary condition at the water table located at $x_2 = \eta$ may be taken as

$$p = 0 \qquad \text{at} \quad x_2 = \eta \tag{2.36}$$

Integrating Eq. 2.35 with respect to x_2 and employing Eq. 2.36 yields the hydrostatic pressure distribution

$$p = \eta - x_2 \tag{2.37}$$

Second, for the region inside the permeable underlayer situated under the flow over the rough slope, the pressure at the interface located at $x_2 = z_b$ between the flow fields over the rough slope and inside the permeable underlayer needs to be matched. The pressure from the flow over the rough slope is given by Eq. 2.21, which at the interface $x_2 = z_b$ gives

$$p = \eta - z_b + \frac{\tau_{22}}{\sigma} \qquad \text{at} \quad x_2 = z_b \tag{2.38}$$

where η is the normalized free surface elevation above SWL. Assuming that the value of $\frac{\tau_{22}}{\sigma}$ at $x_2 = z_b$ is negligible, the pressure governed by Eq. 2.35 inside the permeable underlayer situated under the flow over the rough slope may also be expressed by Eq. 2.37. Thus, Eq. 2.37 may be applied to the flow inside the permeable underlayer whether η is the normalized water table or free surface elevation.

Finally, the significance of the parameter μ defined by Eq. 2.29 can be seen by evaluating the ratio of the term expressing the laminar flow resistance to the term expressing the turbulence flow resistance in Eq. 2.23 as shown below:

$$\begin{aligned}
\frac{\alpha' v_i'}{\beta' v_i' \sqrt{v_j' v_j'}} &= \frac{\alpha'}{\beta'} \left(\sqrt{v_j' v_j'}\right)^{-1} \\
&= \frac{\alpha_o \, (1 - n_p)^3 \, \nu}{\left(n_p \, d_p'\right)^2} \cdot \frac{n_p^3 \, d_p'}{\beta_o \, (1 - n_p)} \cdot \left(\sqrt{(v_1')^2 + (v_2')^2}\right)^{-1} \\
&= \frac{\alpha_o \, (1 - n_p)^2}{\beta_o} \cdot \frac{n_p}{p_q} \cdot \frac{\nu}{d_p' \, \sqrt{g H'}} \left(\sqrt{v_1^2 + \frac{1}{\sigma^2} v_2^2}\right)^{-1} \\
&= \mu \cdot \left(\sqrt{v_1^2 + \frac{1}{\sigma^2} v_2^2}\right)^{-1} \\
&\Downarrow \ \text{Use Eq. 2.30} \\
\frac{\alpha' v_i'}{\beta' v_i' \sqrt{v_j' v_j'}} &\simeq \mu \cdot (|v_1|)^{-1}
\end{aligned} \tag{2.39}$$

Since v_1 is assumed to be on the order of unity, the parameter μ expresses the order of magnitude of the laminar flow resistance as compared to the turbulent flow resistance.

Chapter 3

APPROXIMATE ONE-DIMENSIONAL EQUATIONS

3.1 Introduction

Approximate one-dimensional governing equations will be derived for the analysis domain depicted in Figure 3.1, which shows normalized structure geometry and variables in contrast to the physical definition sketch in Figure 2.1. The normalized variables shown in Figure 3.1 are explained in the following. The normalized coordinate system used hereafter is denoted by (x, z) with $x = x_1$ and $z = x_2$. The toe of the slope is located at $x = 0$ where d_t is the normalized water depth below SWL at the toe. The upper and lower boundaries of the permeable underlayer are located at $z = z_b$ and $z = z_p$, respectively, where z_b and z_p are given functions of x. The impermeable slope constitutes the lower boundary at $z = z_p$. The primary cover layer on top of the permeable underlayer may be treated separately as surface roughness (Madsen and White 1976). The free surface and the water table inside the permeable underlayer, denoted by η in Figure 3.1, are assumed to be continuous at the moving waterline situated at $x = x_s$ where the instantaneous water depth, $h = (\eta - z_b)$, above the rough slope is zero. The thickness of the permeable underlayer in the region $0 \leq x \leq x_s$ is given by $h_p = (z_b - z_p)$, while the depth below the water table in the region $x_s \leq x \leq x_w$ is expressed as $h_p = (\eta - z_p)$ where $h_p = 0$ at $x = x_w$. Since η varies with t and x, x_s and x_w are unknown functions of t.

3.2 Flow over Rough Slope

Approximate one-dimensional governing equations for the flow over the rough slope are derived from the two-dimensional continuity equation given by Eq. 2.9, the approximate horizontal momentum equation given by Eq. 2.13, and the approximate vertical momentum equation given by Eq. 2.21.

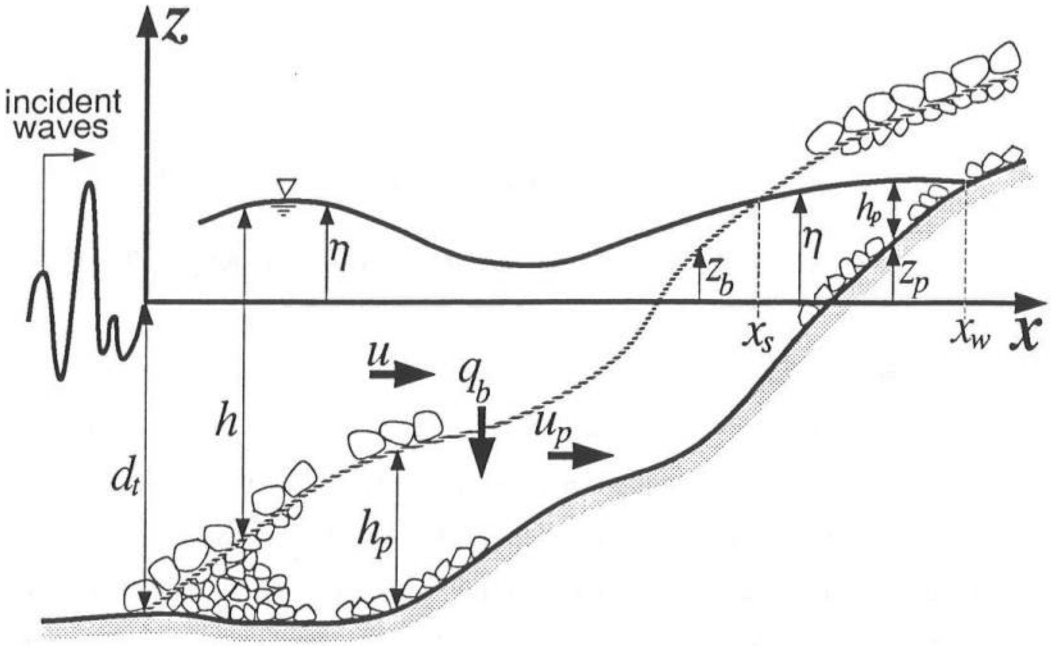

Figure 3.1: One-dimensional model for flow over rough slope and inside permeable underlayer.

Substitution of Eq. 2.21 into Eq. 2.13 yields

$$\frac{\partial u_1}{\partial t} + u_1 \frac{\partial u_1}{\partial x} + u_2 \frac{\partial u_1}{\partial z} = -\frac{\partial \eta}{\partial x} + \frac{\partial \tau_{zx}}{\partial z} \tag{3.1}$$

The term $\left(u_1 \frac{\partial u_1}{\partial x} + u_2 \frac{\partial u_1}{\partial z}\right)$ in Eq. 3.1 can be manipulated as follows:

$$\begin{aligned} u_1 \frac{\partial u_1}{\partial x} + u_2 \frac{\partial u_1}{\partial z} &= \frac{\partial u_1^2}{\partial x} - u_1 \frac{\partial u_1}{\partial x} + \frac{\partial (u_1 u_2)}{\partial z} - u_1 \frac{\partial u_2}{\partial z} \\ &= \frac{\partial u_1^2}{\partial x} + \frac{\partial (u_1 u_2)}{\partial z} - u_1 \underbrace{\left(\frac{\partial u_1}{\partial x} + \frac{\partial u_2}{\partial z}\right)}_{=0 \text{ by Eq. 2.9}} \\ &= \frac{\partial u_1^2}{\partial x} + \frac{\partial (u_1 u_2)}{\partial z} \end{aligned}$$

Eq. 3.1 then becomes

$$\frac{\partial u_1}{\partial t} + \frac{\partial u_1^2}{\partial x} + \frac{\partial (u_1 u_2)}{\partial z} = -\frac{\partial \eta}{\partial x} + \frac{\partial \tau_{zx}}{\partial z} \tag{3.2}$$

The physical free surface of the flow over the rough slope may be expressed as

$$S'(x', z', t') = z' - \eta'(x', t') = 0 \tag{3.3}$$

The kinematic boundary condition at the free surface requiring that the fluid particle at the free surface stays at the free surface is written as

$$\begin{aligned} \frac{DS'(x',z',t')}{Dt'} &= 0 \qquad \text{at} \quad z' = \eta' \\ &\Downarrow \\ -\frac{\partial \eta'}{\partial t'} - u'_1 \frac{\partial \eta'}{\partial x'} + u'_2 &= 0 \qquad \text{at} \quad z' = \eta' \\ \text{Normalized using Eq. 2.3} \quad &\Downarrow \\ -\frac{\partial \eta}{\partial t} - u_1 \frac{\partial \eta}{\partial x} + u_2 &= 0 \qquad \text{at} \quad z = \eta \end{aligned} \tag{3.4}$$

At the interface located at $z' = z'_b$ between the flow over the rough slope and the flow inside the permeable underlayer, the volume flux is expressed as

$$u'_1 \frac{dz'_b}{dx'} - u'_2 = q'_b \qquad \text{at} \quad z' = z'_b \tag{3.5}$$

where q'_b is the volume influx per unit horizontal area into the permeable underlayer which is taken to be positive downward as shown in its normalized form, q_b, in Figure 3.1. In this analysis, q'_b is normalized as

$$q_b = \frac{T' \, q'_b}{p_q \, H'} \tag{3.6}$$

Eq. 3.5 can then be expressed in the following normalized form:

$$u_1 \frac{dz_b}{dx} - u_2 = p_q q_b \qquad \text{at} \quad z = z_b \tag{3.7}$$

where use is made of Eq. 2.3 to normalize the left hand side of Eq. 3.5. The normalized volume influx q_b in Eq. 3.7 is unknown and needs to be obtained by analyzing the flow inside the permeable underlayer.

The one-dimensional continuity equation for the flow over the rough slope is obtained by integrating Eq. 2.9 with respect to z from $z=z_b$ to $z=\eta$ and applying Leibniz rule [*e.g.*, Greenberg (1988)] and the boundary conditions expressed by Eqs. 3.4 and 3.7.

$$\begin{aligned}
\int_{z_b}^{\eta} \frac{\partial u_1}{\partial x} dz + \int_{z_b}^{\eta} \frac{\partial u_2}{\partial z} dz &= 0 \\
\text{Leibniz rule is used} &\Downarrow \\
\frac{\partial}{\partial x} \int_{z_b}^{\eta} u_1 dz - [u_1]_{z=\eta} \frac{\partial \eta}{\partial x} + [u_1]_{z=z_b} \frac{dz_b}{dx} &+ [u_2]_{z=\eta} - [u_2]_{z=z_b} = 0 \\
&\Downarrow \\
\left[-u_1 \frac{\partial \eta}{\partial x} + u_2\right]_{z=\eta} + \frac{\partial}{\partial x} \int_{z_b}^{\eta} u_1 dz &+ \left[u_1 \frac{dz_b}{dx} - u_2\right]_{z=z_b} = 0 \\
\text{Eqs. 3.4 and 3.7 are used} &\Downarrow \\
\frac{\partial \eta}{\partial t} + \frac{\partial m}{\partial x} + p_q q_b &= 0 \qquad (3.8)
\end{aligned}$$

where m is the normalized volume flux per unit width and defined as

$$m = \int_{z_b}^{\eta} u_1 dz \qquad (3.9)$$

Closely related to the normalized volume flux m is the normalized depth-averaged horizontal velocity u defined as

$$u = \frac{m}{h} \qquad (3.10)$$

where h is the instantaneous water depth as shown in Figure 3.1.

The one-dimensional horizontal momentum equation for the flow over the rough slope is obtained by integrating Eq. 3.2 with respect to z from $z = z_b$ to $z = \eta$, applying the appropriate boundary conditions, and imposing assumptions to be discussed as the derivation proceeds in the following.

$$\underbrace{\int_{z_b}^{\eta} \frac{\partial u_1}{\partial t} dz}_{\mathbf{A}} + \underbrace{\int_{z_b}^{\eta} \frac{\partial u_1^2}{\partial x} dz}_{\mathbf{B}} + \underbrace{\int_{z_b}^{\eta} \frac{\partial (u_1 u_2)}{\partial z} dz}_{\mathbf{C}} = \underbrace{-\int_{z_b}^{\eta} \frac{\partial \eta}{\partial x} dz}_{\mathbf{D}} + \underbrace{\int_{z_b}^{\eta} \frac{\partial \tau_{zx}}{\partial z} dz}_{\mathbf{E}} \qquad (3.11)$$

The five integrals in Eq. 3.11 are evaluated one at a time for clarity. The term **A** in Eq. 3.11 is evaluated using Leibniz rule

$$\int_{z_b}^{\eta} \frac{\partial u_1}{\partial t} dz = \frac{\partial}{\partial t} \int_{z_b}^{\eta} u_1 dz - [u_1]_{z=\eta} \frac{\partial \eta}{\partial t} + [u_1]_{z=z_b} \underbrace{\frac{\partial z_b}{\partial t}}_{=0} = \frac{\partial m}{\partial t} - [u_1]_{z=\eta} \frac{\partial \eta}{\partial t} \qquad (3.12)$$

where use is made of Eq. 3.9.

The term **B** in Eq. 3.11 is evaluated using Leibniz rule

$$\begin{aligned}
\int_{z_b}^{\eta} \frac{\partial u_1^2}{\partial x} dz &= \frac{\partial}{\partial x} \int_{z_b}^{\eta} u_1^2 dz - \left[u_1^2\right]_{z=\eta} \frac{\partial \eta}{\partial x} + \left[u_1^2\right]_{z=z_b} \frac{dz_b}{dx} \\
&= \frac{\partial}{\partial x} \left[u^2 \int_{z_b}^{\eta} \left(\frac{u_1}{u}\right)^2 dz\right] - \left[u_1^2\right]_{z=\eta} \frac{\partial \eta}{\partial x} + \left[u_1^2\right]_{z=z_b} \frac{dz_b}{dx} \\
&\Downarrow \\
\int_{z_b}^{\eta} \frac{\partial u_1^2}{\partial x} dz &= \frac{\partial}{\partial x} (C_m \; m \; u) - \left[u_1^2\right]_{z=\eta} \frac{\partial \eta}{\partial x} + \left[u_1^2\right]_{z=z_b} \frac{dz_b}{dx} \qquad (3.13)
\end{aligned}$$

where use is made of Eq. 3.10 and C_m is the momentum correction coefficient defined as

$$C_m = \frac{1}{h} \int_{z_b}^{\eta} \left(\frac{u_1}{u}\right)^2 dz \qquad (3.14)$$

The term **C** in Eq. 3.11 reduces to

$$\int_{z_b}^{\eta} \frac{\partial (u_1 u_2)}{\partial z} dz = \left[u_1 u_2\right]_{z=\eta} - \left[u_1 u_2\right]_{z=z_b} \qquad (3.15)$$

The term **D** in Eq. 3.11 is rewritten using $h = (\eta - z_b)$

$$\begin{aligned}
- \int_{z_b}^{\eta} \frac{\partial \eta}{\partial x} dz &= - \, h \, \frac{\partial \eta}{\partial x} = - \, h \, \left(\frac{\partial h}{\partial x} + \frac{dz_b}{dx}\right) \\
&\Downarrow \\
- \int_{z_b}^{\eta} \frac{\partial \eta}{\partial x} dz &= - \frac{\partial}{\partial x} \left(\frac{h^2}{2}\right) - \theta \, h \qquad (3.16)
\end{aligned}$$

where θ is the normalized gradient of the interface located at $z = z_b$ between the flow over the rough slope and the flow inside the permeable underlayer, and is given by

$$\begin{aligned}
\theta = \frac{dz_b}{dx} &= \frac{T' \sqrt{g H'}}{H'} \; \overbrace{\frac{dz_b'}{dx'}}^{\text{physical}} = \overbrace{T' \sqrt{\frac{g}{H'}}}^{=\sigma} \; \frac{dz_b'}{dx'} \\
&\Downarrow \\
\theta &= \frac{dz_b}{dx} = \sigma \, \frac{dz_b'}{dx'} \qquad (3.17)
\end{aligned}$$

For a uniform slope, θ given by Eq. 3.17 is proportional to the surf similarity parameter, $\xi = \frac{\theta}{\sqrt{2\pi}}$.

The term **E** in Eq. 3.11 is evaluated as follows:

$$\begin{aligned} \int_{z_b}^{\eta} \frac{\partial \tau_{zx}}{\partial z} dz &= [\tau_{zx}]_{z=\eta} - [\tau_{zx}]_{z=z_b} \\ &\Downarrow \\ \int_{z_b}^{\eta} \frac{\partial \tau_{zx}}{\partial z} dz &= -\tau_b \end{aligned} \qquad (3.18)$$

where the dynamic boundary condition $\tau_{zx}=0$ at the free surface $z=\eta$ given in Eq. 2.16 is used, and τ_b is the normalized bottom friction, τ_{zx} at $z=z_b$, which has been expressed as

$$\tau_b = \frac{1}{2}\, \sigma\, f'\, |u|u \qquad (3.19)$$

where the constant bottom friction factor f' has been calibrated for rough impermeable slopes (Kobayashi, Otta, and Roy 1987; Kobayashi and Greenwald 1988). This friction factor f' represents the roughness effect of the primary cover layer on the flow.

Substitution of Eqs. 3.12, 3.13, 3.15, 3.16, and 3.18 into Eq. 3.11 yields the one-dimensional x-momentum equation which can be simplified as follows:

$$\begin{aligned} \frac{\partial m}{\partial t} + \frac{\partial}{\partial x}(C_m\, m\, u) \quad &+ \\ \overbrace{\left[u_1\left(-\frac{\partial \eta}{\partial t} - u_1\frac{\partial \eta}{\partial x} + u_2\right)\right]_{z=\eta}}^{\text{Apply Eq. 3.4 here}} \quad &+ \\ [u_1]_{z=z_b}\ \overbrace{\left[u_1\frac{dz_b}{dx} - u_2\right]_{z=z_b}}^{\text{Apply Eq. 3.7 here}} \quad &= \quad -\frac{\partial}{\partial x}\left(\frac{h^2}{2}\right) - \theta\, h - \tau_b \\ &\Downarrow \\ \frac{\partial m}{\partial t} + \frac{\partial}{\partial x}\left(C_m\, \frac{m^2}{h} + \frac{h^2}{2}\right) \quad &+ \quad \theta\, h + \frac{1}{2}\sigma f'|u|u + p_q\ [u_1]_{z=z_b}\ q_b = 0 \end{aligned} \qquad (3.20)$$

The normalized horizontal fluid velocity u_1 at $z = z_b$ in Eq. 3.20 needs a special treatment, although the physical horizontal fluid velocity should be continuous at $z=z_b$. Both flow fields over the rough slope and inside the permeable underlayer exert influence at their interface located at $z = z_b$. An impartial symbol u_b is used hereafter to denote the normalized horizontal fluid velocity at $z = z_b$. For the one-dimensional model with the two flow fields which will eventually be derived in this chapter, u_b may need to be expressed as (Kobayashi and Wurjanto 1990)

$$u_b = \begin{cases} u & \text{for } q_b \geq 0 \\ p_u u_p & \text{for } q_b < 0 \end{cases} \tag{3.21}$$

which implies that u_b is determined by the vertically-averaged velocity of the flow above the rough slope for the case of influx ($q_b \geq 0$) and the flow inside the permeable underlayer for the case of outflux ($q_b < 0$). The normalized velocity u_b in Eq. 3.21 is related to its physical counterpart by

$$u_b = \frac{u_b'}{\sqrt{gH'}} \tag{3.22}$$

The velocity u_p in Eq. 3.21 will be explained in Section 3.3. Replacing $[u_1]_{z=z_b}$ by u_b in Eq. 3.20 gives

$$\frac{\partial m}{\partial t} + \frac{\partial}{\partial x}\left(C_m \frac{m^2}{h} + \frac{h^2}{2}\right) + \theta\, h + \frac{1}{2}\sigma f'|u|u + p_q\, u_b\, q_b = 0 \tag{3.23}$$

The coefficient C_m defined by Eq. 3.14 was discussed in Kobayashi and Wurjanto (1992) where the following approximation was made:

$$C_m \simeq 1 \tag{3.24}$$

which may result in errors on the order of 10%. This 10% estimate is explained again for clarity. Figure 3.2 depicts the vertical distribution of the horizontal fluid velocity u_1 assumed by Svendsen and Madsen (1984) for which $u_1 = u_s$ at $z = \eta$ and u_1 varies in the turbulent region $(\eta - b) \leq z \leq \eta$ with b being its thickness, while $u_1 = u_o$ in the region $z_b \leq z \leq (\eta - b)$ below the turbulent region. Figure 3.3 shows the computed values of the momentum correction coefficient C_m as a function of b/h and u_s/u_o. These values may be compared with the typical range of $1 < C_m < 1.06$ for turbulent flow in regular open channels (Henderson 1966). Since h, b, u_s, and u_o vary with time and location, it is difficult to estimate the typical range of C_m for the present problem even for the assumed vertical velocity distribution. Kobayashi and Wurjanto (1992) tentatively suggested that the assumption $C_m \simeq 1$ as stated in Eq. 3.24 might result in errors on the order of 10%.

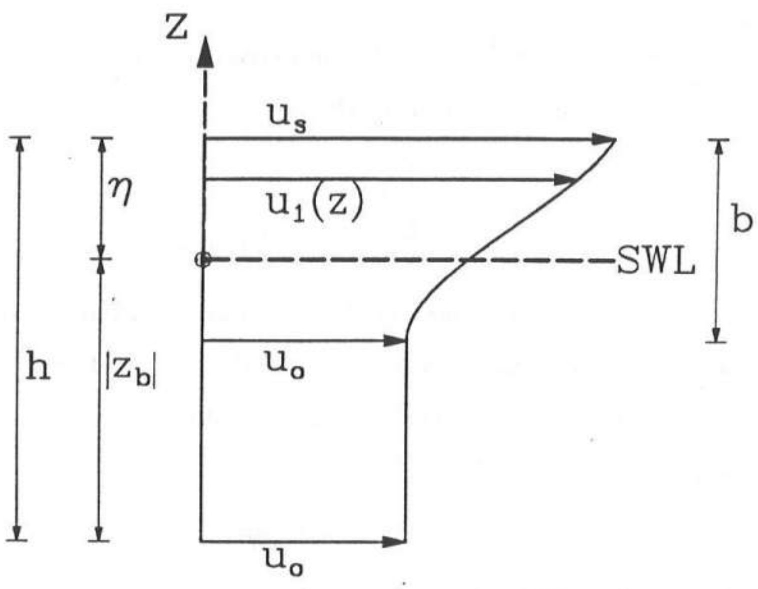

Figure 3.2: Vertical distribution of horizontal fluid velocity u_1 assumed by Svendsen and Madsen (1984).

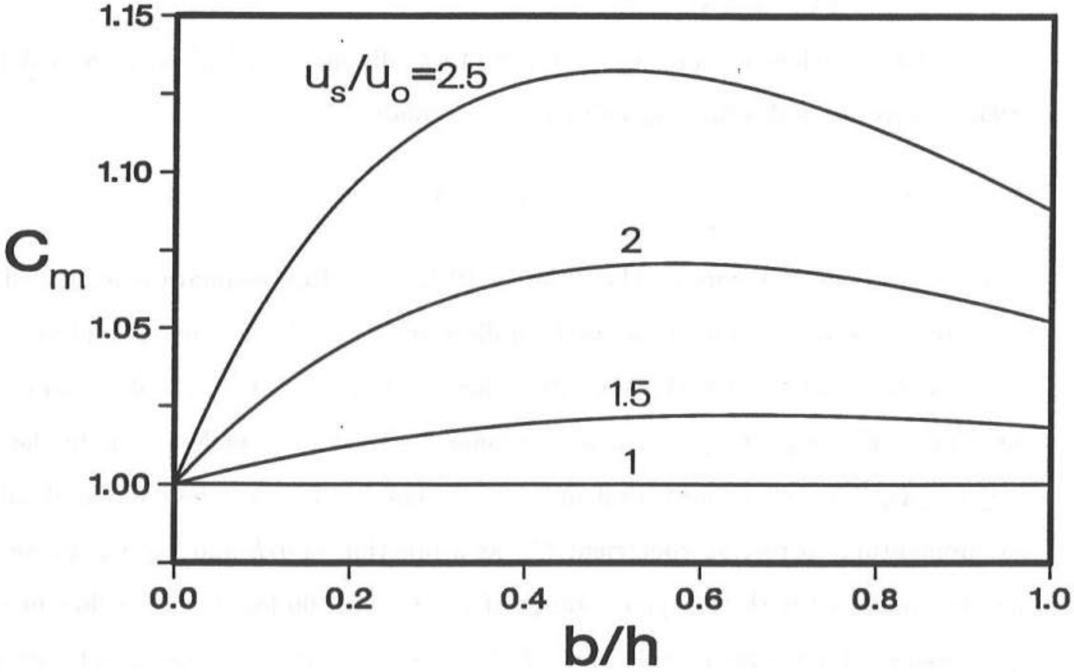

Figure 3.3: Momentum correction coefficient C_m computed as a function of b/h and u_s/u_o for vertical distribution of horizontal fluid velocity u_1 assumed by Svendsen and Madsen (1984).

The approximation expressed by Eq. 3.24 is adopted here since the vertical velocity variation is not computed in the one-dimensional model. Hence, Eq. 3.23 is approximated by

$$\frac{\partial m}{\partial t} + \frac{\partial}{\partial x}\left(\frac{m^2}{h} + \frac{h^2}{2}\right) + \theta\, h + \frac{1}{2}\sigma f'|u|u + p_q\, u_b\, q_b = 0 \tag{3.25}$$

3.3 Flow inside Permeable Underlayer without Free Surface

Approximate one-dimensional governing equations for the flow inside the permeable underlayer in the region $0 \le x \le x_s$ are derived from the two-dimensional continuity equation given by Eq. 2.27, the approximate horizontal momentum equation given by Eq. 2.33, and the approximate vertical momentum equation given by Eq. 2.37.

Substitution of Eq. 2.37 into Eq. 2.33 yields

$$p_u\, \frac{\partial v_1}{\partial t} + p_u^2\, v_1\, \frac{\partial v_1}{\partial x} + p_u^2\, v_2\, \frac{\partial v_1}{\partial z} = -\frac{\partial \eta}{\partial x} - (\mu + |v_1|)\, v_1 \tag{3.26}$$

Similar to the rearrangement from Eq. 3.1 to Eq. 3.2 to facilitate the use of Leibniz rule, Eq. 3.26 is rewritten as follows:

$$p_u\, \frac{\partial v_1}{\partial t} + p_u^2\, \frac{\partial v_1^2}{\partial x} + p_u^2\, \frac{\partial (v_1 v_2)}{\partial z} = -\frac{\partial \eta}{\partial x} - (\mu + |v_1|)\, v_1 \tag{3.27}$$

where use is made of Eq. 2.27 in the process.

Since the volume influx into the permeable underlayer, q_b', must be continuous at the interface located at $z' = z_b'$ between the flow over the rough slope and the flow inside the permeable underlayer, the flux equation for the permeable underlayer in the region $0 \le x' \le x_s'$ corresponding to Eq. 3.7 is given as

$$v_1'\, \frac{dz_b'}{dx'} - v_2' \;=\; q_b' \qquad \text{at} \quad z' = z_b'$$

$$\text{Normalized using} \quad \Downarrow \quad \text{Eqs. 2.3, 2.26, and 3.6}$$

$$v_1\, \frac{dz_b}{dx} - v_2 \;=\; q_b \qquad \text{at} \quad z = z_b \tag{3.28}$$

The kinematic boundary condition at the lower boundary of the permeable underlayer located at $z' = z_p'$ states that the fluid particle at the assumed impermeable boundary stays there. Introducing the function defined as

$$B'(x', z') = z' - z_p'(x') = 0 \tag{3.29}$$

which describes the physical impermeable boundary, the kinematic boundary condition at the impermeable boundary requires

$$\begin{aligned}
\frac{DB'(x',z')}{Dt'} &= 0 \qquad \text{at} \quad z = z_p \\
&\Downarrow \\
\frac{\partial B'}{\partial t'} + \frac{v_1'}{n_p}\frac{\partial B'}{\partial x'} + \frac{v_2'}{n_p}\frac{\partial B'}{\partial z'} &= 0 \qquad \text{at} \quad z' = z_p' \\
&\Downarrow \\
-v_1'\frac{dz_p'}{dx'} + v_2' &= 0 \qquad \text{at} \quad z' = z_p' \\
\text{Normalized using} \;\; &\Downarrow \;\; \text{Eqs. 2.3 and 2.26} \\
-v_1\frac{dz_p}{dx} + v_2 &= 0 \qquad \text{at} \quad z = z_p
\end{aligned} \tag{3.30}$$

The one-dimensional continuity equation for the flow inside the permeable underlayer in the region $0 \leq x \leq x_s$ is obtained by integrating Eq. 2.27 with respect to z from $z = z_p$ to $z = z_b$ and applying the boundary conditions expressed by Eqs. 3.28 and 3.30.

$$\begin{aligned}
\int_{z_p}^{z_b} \frac{\partial v_1}{\partial x} dz + \int_{z_p}^{z_b} \frac{\partial v_2}{\partial z} dz &= 0 \\
\text{Leibniz rule is used} \;\; &\Downarrow \\
\frac{\partial}{\partial x}\int_{z_p}^{z_b} v_1 dz - [v_1]_{z=z_b}\frac{dz_b}{dx} + [v_1]_{z=z_p}\frac{dz_p}{dx} + [v_2]_{z=z_b} &- [v_2]_{z=z_p} = 0 \\
&\Downarrow \\
\frac{\partial}{\partial x}\int_{z_p}^{z_b} v_1 dz - \left[v_1\frac{dz_b}{dx} - v_2\right]_{z=z_b} + \left[v_1\frac{dz_p}{dx} - v_2\right]_{z=z_p} &= 0 \\
\text{Eqs. 3.28 and 3.30 are used} \;\; &\Downarrow \\
\frac{1}{p_u}\frac{\partial m_p}{\partial x} - q_b &= 0 \\
&\Downarrow \\
\frac{\partial m_p}{\partial x} - p_u\, q_b &= 0
\end{aligned} \tag{3.31}$$

where m_p is the normalized discharge per unit width in the permeable underlayer defined as

$$m_p = \begin{cases} p_u \displaystyle\int_{z_p}^{z_b} v_1 dz & \text{for} \quad 0 \leq x \leq x_s \\ p_u \displaystyle\int_{z_p}^{\eta} v_1 dz & \text{for} \quad x_s \leq x \leq x_w \end{cases} \tag{3.32}$$

where the flow inside the permeable underlayer in the region $x_s \leq x \leq x_w$ will be described in Section 3.4. The relation between the normalized discharge m_p and its physical counterpart m_p' is given by

$$m_p = \frac{m_p'}{n_p H' \sqrt{gH'}} \tag{3.33}$$

with the physical discharge m_p' expressed as

$$m_p' = \begin{cases} \displaystyle\int_{z_p'}^{z_b'} v_1' dz' & \text{for} \quad 0 \leq x' \leq x_s' \\ \displaystyle\int_{z_p'}^{\eta'} v_1' dz' & \text{for} \quad x_s' \leq x' \leq x_w' \end{cases} \tag{3.34}$$

Similar to the normalized depth-averaged horizontal velocity u given by Eq. 3.10 for the flow over the rough slope, the normalized vertically-averaged horizontal discharge velocity u_p for the flow inside the permeable underlayer is defined as

$$u_p = \frac{m_p}{p_u \, h_p} \tag{3.35}$$

where $h_p = (z_b - z_p)$ for $0 \leq x \leq x_s$ and $h_p = (\eta - z_p)$ for $x_s \leq x \leq x_w$ as shown in Figure 3.1.

The one-dimensional horizontal momentum equation for the flow inside the permeable underlayer in the region $0 \leq x \leq x_s$ is obtained by integrating Eq. 3.27 with respect to z from $z = z_p$ to $z = z_b$, employing the appropriate boundary conditions, and adopting additional assumptions along the way.

$$\begin{aligned} p_u \int_{z_p}^{z_b} \frac{\partial v_1}{\partial t} dz + p_u^2 \int_{z_p}^{z_b} \frac{\partial v_1^2}{\partial x} dz \quad &+ \quad p_u^2 \int_{z_p}^{z_b} \frac{\partial (v_1 v_2)}{\partial z} dz \\ &= \quad -\int_{z_p}^{z_b} \frac{\partial \eta}{\partial x} dz - \int_{z_p}^{z_b} (\mu + |v_1|)\, v_1 dz \\ &\Downarrow \end{aligned}$$

$$\begin{aligned} p_u \frac{\partial}{\partial t} \overbrace{\int_{z_p}^{z_b} v_1 dz}^{\substack{\text{Use} \\ \text{Eq. 3.32}}} - p_u \, [v_1]_{z=z_b} \overbrace{\frac{\partial z_b}{\partial t}}^{=0} \quad &+ \quad p_u \, [v_1]_{z=z_p} \overbrace{\frac{\partial z_p}{\partial t}}^{=0} \\ + p_u^2 \frac{\partial}{\partial x} \int_{z_p}^{z_b} v_1^2 dz - p_u^2 \left[v_1^2\right]_{z=z_b} \frac{dz_b}{dx} \quad &+ \quad p_u^2 \left[v_1^2\right]_{z=z_p} \frac{dz_p}{dx} \\ + p_u^2 \, [v_1 v_2]_{z=z_b} - p_u^2 \, [v_1 v_2]_{z=z_p} \quad &= \quad -h_p \frac{\partial \eta}{\partial x} - \mu \overbrace{\int_{z_p}^{z_b} v_1 dz}^{\substack{\text{Use} \\ \text{Eq. 3.32}}} - \int_{z_p}^{z_b} |v_1|\, v_1 dz \\ &\Downarrow \end{aligned}$$

$$\begin{aligned} \frac{\partial m_p}{\partial t} + p_u^2 \frac{\partial}{\partial x} \int_{z_p}^{z_b} v_1^2 dz \quad &+ \quad p_u \overbrace{[p_u v_1]_{z=zb}}^{\substack{\text{Replace} \\ \text{by } u_b}} \overbrace{\left[-v_1 \frac{dz_b}{dx} + v_2\right]_{z=zb}}^{\text{Apply Eq. 3.28 here}} \\ + p_u^2 \overbrace{\left[v_1 \left(v_1 \frac{dz_p}{dx} - v_2\right)\right]_{z=zp}}^{\text{Apply Eq. 3.30 here}} \quad &= \quad -h_p \frac{\partial h}{\partial x} - h_p \overbrace{\frac{dz_b}{dx}}^{\substack{\text{Use} \\ \text{Eq. 3.17}}} \\ &\quad\; -\mu \frac{m_p}{p_u} - \int_{z_p}^{z_b} |v_1|\, v_1 dz \\ &\Downarrow \end{aligned}$$

$$\begin{aligned} \frac{\partial m_p}{\partial t} + p_u^2 \frac{\partial}{\partial x} \int_{z_p}^{z_b} v_1^2 dz - p_u \, u_b \, q_b \quad &+ \quad h_p \frac{\partial h}{\partial x} + \theta \, h_p \\ &+ \quad \mu \frac{m_p}{p_u} + \int_{z_p}^{z_b} |v_1|\, v_1 dz = 0 \end{aligned} \tag{3.36}$$

It is noted that the replacement of $[p_u v_1]_{z=zb}$ by u_b in the process of deriving Eq. 3.36 is in concordance with the matching of the physical horizontal fluid velocity at $z=z_b$ as explained in relation to Eq. 3.21.

To simplify Eq. 3.36, the following assumptions are made:

$$\left.\begin{array}{ll} \dfrac{1}{h_p}\displaystyle\int_{z_p}^{z_b}\left(\frac{v_1}{u_p}\right)^2 dz \simeq 1 & \text{for} \quad 0 \leq x \leq x_s \\ \dfrac{1}{h_p}\displaystyle\int_{z_p}^{\eta}\left(\frac{v_1}{u_p}\right)^2 dz \simeq 1 & \text{for} \quad x_s \leq x \leq x_w \end{array}\right\} \tag{3.37}$$

$$\left.\begin{array}{ll} \dfrac{1}{h_p}\displaystyle\int_{z_p}^{z_b}\left(\frac{|v_1|}{|u_p|}\frac{v_1}{u_p}\right) dz \simeq 1 & \text{for} \quad 0 \leq x \leq x_s \\ \dfrac{1}{h_p}\displaystyle\int_{z_p}^{\eta}\left(\frac{|v_1|}{|u_p|}\frac{v_1}{u_p}\right) dz \simeq 1 & \text{for} \quad x_s \leq x \leq x_w \end{array}\right\} \tag{3.38}$$

where the approximations for $x_s \leq x \leq x_w$ will be used in Section 3.4. The above assumptions for the flow inside the permeable underlayer are similar to the assumption $C_m \simeq 1$ expressed by Eq. 3.24 for the flow over the rough slope. Applying Eqs. 3.37 and 3.38 to Eq. 3.36 produces

$$\frac{\partial m_p}{\partial t} + \frac{\partial}{\partial x}\overbrace{\left(p_u^2 h_p u_p^2\right)}^{\substack{\text{Use} \\ \text{Eq. 3.35}}} - p_u\, u_b\, q_b + h_p\,\frac{\partial h}{\partial x} \;+\; \theta\, h_p + \mu\,\frac{m_p}{p_u} + \overbrace{h_p\,|u_p|\,u_p}^{\substack{\text{Use} \\ \text{Eq. 3.35}}} = 0$$

$$\Downarrow$$

$$\frac{\partial m_p}{\partial t} + \frac{\partial}{\partial x}\left(\frac{m_p^2}{h_p}\right) - p_u\, u_b\, q_b + h_p\,\frac{\partial h}{\partial x} \;+\; \theta\, h_p + \frac{m_p}{p_u}\left(\mu + \frac{|m_p|}{p_u h_p}\right) = 0 \tag{3.39}$$

3.4 Flow inside Permeable Underlayer with Free Surface

Approximate one-dimensional governing equations for the flow inside the permeable underlayer in the region $x_s \leq x \leq x_w$ are derived from the two-dimensional continuity equation given by Eq. 2.27 and the approximate horizontal momentum equation given by Eq. 3.27.

The kinematic boundary condition at the water table is derived in a manner similar to Eq. 3.4 at the free surface of the flow over the rough slope.

$$-\frac{\partial \eta'}{\partial t'} - \frac{v_1'}{n_p}\frac{\partial \eta'}{\partial x'} + \frac{v_2'}{n_p} \;=\; 0 \qquad \text{at} \quad z' = \eta'$$

$$\text{Normalized using} \quad \Downarrow \quad \text{Eqs. 2.3 and 2.26}$$

$$-\frac{\partial \eta}{\partial t} - p_u v_1 \frac{\partial \eta}{\partial x} + p_u v_2 \;=\; 0 \qquad \text{at} \quad z = \eta \tag{3.40}$$

The one-dimensional continuity equation for the flow inside the permeable underlayer in the region $x_s \leq x \leq x_w$ is obtained by integrating Eq. 2.27 with respect to z from $z = z_p$ to $z = \eta$ and applying the boundary conditions expressed by Eqs. 3.30 and 3.40.

$$\int_{z_p}^{\eta} \frac{\partial v_1}{\partial x} dz + \int_{z_p}^{\eta} \frac{\partial v_2}{\partial z} dz = 0$$

$$\text{Leibniz rule is used} \quad \Downarrow$$

$$\frac{\partial}{\partial x} \int_{z_b}^{\eta} v_1 dz - [v_1]_{z=\eta} \frac{\partial \eta}{\partial x} + [v_1]_{z=z_p} \frac{dz_p}{dx} + [v_2]_{z=\eta} - [v_2]_{z=z_p} = 0$$

$$\Downarrow$$

$$\frac{\partial}{\partial x} \overbrace{\int_{z_p}^{\eta} v_1 dz}^{\substack{\text{Use} \\ \text{Eq. 3.32}}} - \left[v_1 \frac{\partial \eta}{\partial x} - v_2 \right]_{z=\eta} + \left[v_1 \frac{dz_p}{dx} - v_2 \right]_{z=z_p} = 0$$

$$\text{Eqs. 3.30 and 3.40 are used} \quad \Downarrow$$

$$\frac{\partial \eta}{\partial t} + \frac{\partial m_p}{\partial x} = 0 \tag{3.41}$$

The one-dimensional horizontal momentum equation for the flow inside the permeable underlayer in the region $x_s \leq x \leq x_w$ is obtained by integrating Eq. 3.27 with respect to z from $z = z_p$ to $z = \eta$ and applying the boundary conditions and assumptions in a manner similar to the derivation of Eq. 3.39.

$$\begin{aligned} p_u \int_{z_p}^{\eta} \frac{\partial v_1}{\partial t} dz + p_u^2 \int_{z_p}^{\eta} \frac{\partial v_1^2}{\partial x} dz &+ p_u^2 \int_{z_p}^{\eta} \frac{\partial (v_1 v_2)}{\partial z} dz \\ &= -\int_{z_p}^{\eta} \frac{\partial \eta}{\partial x} dz - \int_{z_p}^{\eta} (\mu + |v_1|)\, v_1 dz \\ &\Downarrow \end{aligned}$$

$$\Downarrow$$

$$p_u \frac{\partial}{\partial t} \overbrace{\int_{z_p}^{\eta} v_1 dz}^{\substack{\text{Use} \\ \text{Eq. 3.32}}} - p_u \left[v_1\right]_{z=\eta} \frac{\partial \eta}{\partial t} \;+\; p_u \left[v_1\right]_{z=z_p} \overbrace{\frac{\partial z_p}{\partial t}}^{=0}$$

$$+ p_u^2 \frac{\partial}{\partial x} \overbrace{\int_{z_p}^{\eta} v_1^2 dz}^{\substack{\text{Use} \\ \text{Eq. 3.37}}} - p_u^2 \left[v_1^2\right]_{z=\eta} \frac{\partial \eta}{\partial x} \;+\; p_u^2 \left[v_1^2\right]_{z=z_p} \frac{dz_p}{dx}$$

$$+ p_u^2 \left[v_1 v_2\right]_{z=\eta} - p_u^2 \left[v_1 v_2\right]_{z=z_p} \;=\; -h_p \frac{\partial \eta}{\partial x} - \mu \overbrace{\int_{z_p}^{\eta} v_1 dz}^{\substack{\text{Use} \\ \text{Eq. 3.32}}} - \overbrace{\int_{z_p}^{\eta} \left|v_1\right| v_1 dz}^{\substack{\text{Use} \\ \text{Eq. 3.38}}}$$

$$\Downarrow$$

$$\frac{\partial m_p}{\partial t} + \frac{\partial}{\partial x} \overbrace{\left(p_u^2 h_p u_p^2\right)}^{\substack{\text{Use} \\ \text{Eq. 3.35}}} \;+\; p_u^2 \overbrace{\left[v_1 \left(-\frac{\partial \eta}{\partial t} - v_1 \frac{\partial \eta}{\partial x} + v_2\right)\right]_{z=\eta}}^{\text{Apply Eq. 3.40 here}}$$

$$+ p_u^2 \overbrace{\left[v_1 \left(v_1 \frac{dz_p}{dx} - v_2\right)\right]_{z=zp}}^{\text{Apply Eq. 3.30 here}} \;=\; -h_p \frac{\partial h_p}{\partial x} - h_p \quad \overbrace{\frac{dz_p}{dx}}^{\substack{\text{See} \\ \text{Eq. 3.43}}}$$

$$-\mu \frac{m_p}{p_u} - \overbrace{h_p \left|u_p\right| u_p}^{\substack{\text{Use} \\ \text{Eq. 3.35}}} = 0$$

$$\Downarrow$$

$$\frac{\partial m_p}{\partial t} + \frac{\partial}{\partial x} \left(\frac{m_p^2}{h_p} + \frac{h_p^2}{2}\right) \;+\; \theta_p \, h_p + \frac{m_p}{p_u} \left(\mu + \frac{\left|m_p\right|}{p_u h_p}\right) = 0 \tag{3.42}$$

where θ_p is the normalized gradient of the impermeable slope $z{=}z_p$ given by

$$\theta_p = \frac{dz_p}{dx} = \sigma \frac{dz_p'}{dx'} \tag{3.43}$$

which is similar to the definition of θ in Eq. 3.17. The physical inclination θ_p' of the impermeable slope located at $z'{=}z_p'$ is depicted in Figure 2.1.

Chapter 4

NUMERICAL METHODS

4.1 Introduction

For easy reference, the analysis domains of the three flow fields discussed in Chapter 3 are referred to as

- *Region 1* for the flow over the rough slope,
- *Region 2* for the flow inside the permeable underlayer with $0 \le x \le x_s$, and
- *Region 3* for the flow inside the permeable underlayer with $x_s \le x \le x_w$.

The three regions are visualized in Figure 4.1 for clarity.

The three one-dimensional continuity equations, Eqs. 3.8, 3.31, and 3.41, and the three one-dimensional horizontal momentum equations, Eqs. 3.25, 3.39, and 3.42, are rewritten in the following as a recapitulation.

REGION 1:

$$\frac{\partial h}{\partial t} + \frac{\partial m}{\partial x} + p_q q_b = 0 \tag{4.1}$$

$$\frac{\partial m}{\partial t} + \frac{\partial}{\partial x}\left(\frac{m^2}{h} + \frac{h^2}{2}\right) + \theta h + f|u|u + p_q u_b q_b = 0 \tag{4.2}$$

REGION 2:

$$\frac{\partial m_p}{\partial x} - p_u q_b = 0 \tag{4.3}$$

$$\frac{\partial m_p}{\partial t} + \frac{\partial}{\partial x}\left(\frac{m_p^2}{h_p}\right) - p_u u_b q_b + h_p \frac{\partial h}{\partial x} + \theta h_p + \frac{m_p}{p_u}\left(\mu + \frac{|m_p|}{p_u h_p}\right) = 0 \tag{4.4}$$

REGION 3:

$$\frac{\partial h_p}{\partial t} + \frac{\partial m_p}{\partial x} = 0 \tag{4.5}$$

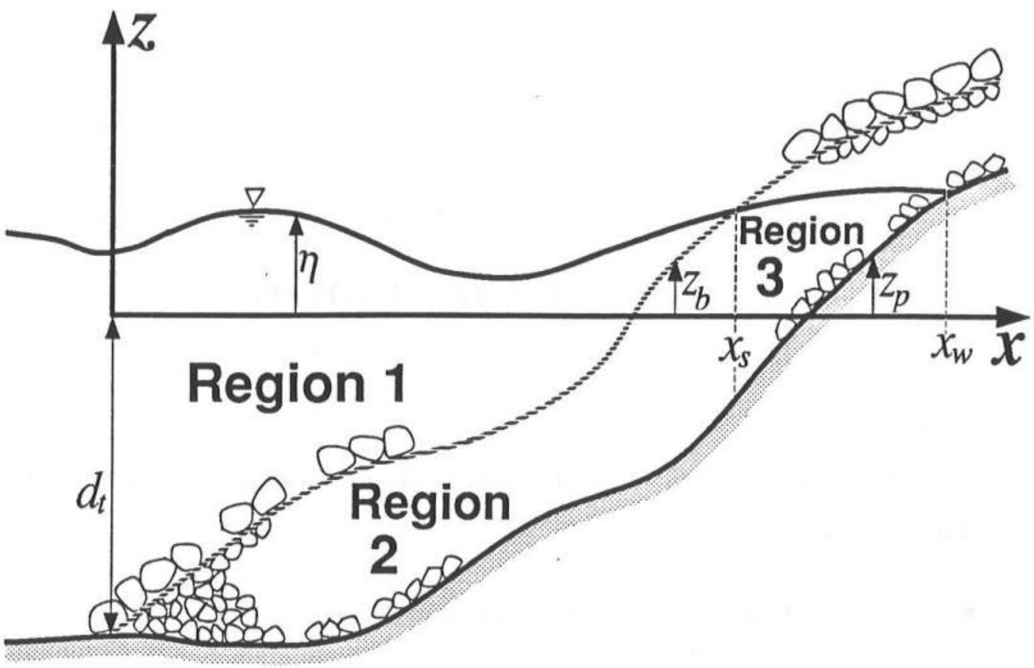

Figure 4.1: Three regions for computation of flow fields.

$$\frac{\partial m_p}{\partial t} + \frac{\partial}{\partial x}\left(\frac{m_p^2}{h_p} + \frac{h_p^2}{2}\right) + \theta_p h_p + \frac{m_p}{p_u}\left(\mu + \frac{|m_p|}{p_u h_p}\right) = 0 \tag{4.6}$$

with the normalized bottom friction factor f given by

$$f = \frac{1}{2}\,\sigma\, f' \tag{4.7}$$

The present numerical model, which is time-dependent and one-dimensional with two layers, is developed on the basis of the three one-dimensional continuity equations, Eqs. 4.1, 4.3, and 4.5, and the three one-dimensional horizontal momentum equations, Eqs. 4.2, 4.4, and 4.6, derived in Chapter 3. In addition, the assumption expressed by Eq. 3.21 is used to estimate the horizontal fluid velocity at the interface between Regions 1 and 2. The numerical procedures used in the present model are given in WK 92 without the derivation of the adopted finite difference methods. A summary of the procedures is given in the following.

Use is made of a finite difference grid of constant space size Δx and varying time step Δt in which Δt is reduced in a semi-automated manner whenever numerical difficulties occur at the waterlines situated at $x = x_s$ and $x = x_w$. The initial time $t = 0$ for the computation marching forward in time is taken to be the time when the specified incident wave train arrives at the seaward boundary $x = 0$ and there is no wave action in the region $x \geq 0$. At the seaward boundary $x = 0$, the normalized incident wave train, $\eta_i = \eta_i'/H'$, is prescribed as a function of time t and the normalized reflected wave train, $\eta_r = \eta_r'/H'$, is computed as a function of t from the characteristics advancing seaward where Eqs. 4.1 and 4.2 are expressed in characteristic forms (Kobayashi and Wurjanto 1990). It is assumed that $z_b = z_p$ at $x = 0$ as shown in Figure 4.1 so that $h_p = 0$ and $m_p = 0$ at $x = 0$. At the moving waterline $x = x_s$ on the rough slope, h_p and m_p inside the permeable underlayer are assumed to be continuous. Simplified versions of the predictor-corrector-smoothing procedure described by Kobayashi and Wurjanto (1990) are used to track the locations x_s and x_w of the moving waterlines on the permeable and impermeable slopes, respectively.

For the known values at all the spatial nodes of $h = (\eta - z_b)$, $m = uh$, q_b, $m_p = p_u h_p u_p$, $h_p = (z_b - z_p)$ or $(\eta - z_p)$, x_s and x_w at the time level t, the values of these variables at all the spatial nodes at the next time level $t^* = (t + \Delta t)$, which are denoted by the asterisk, are computed in three stages as follows:

1. First, for Region 1, h^* and m^* together with x_s^* are computed from Eqs. 4.1 and 4.2 with Eq. 3.21 using the explicit dissipative Lax-Wendroff method employed by Kobayashi and Wurjanto (1990) where the treatment of q_b and $u_b q_b$ in Eqs. 4.1 and 4.2 is improved herein.

2. Second, for Region 2 where $h_p^* = (z_b - z_p)$, m_p^* is computed from Eq. 4.4 which is solved using the MacCormack method (MacCormack 1969), which is similar but simpler than the Lax-Wendroff method. Then q_b^* is computed using Eq. 4.3 in which $\frac{\partial m_p^*}{\partial x}$ is approximated by the central finite difference.

3. Third, for Region 3, m_p^* and h_p^* together with x_w^* are computed from Eqs. 4.5 and 4.6 which are also solved using the MacCormack method.

The finite difference equations used in the numerical model PBREAK are derived herein in the following sequence:

- Lax-Wendroff method without dissipation for Region 1 (Section 4.2), and
- Lax-Wendroff method with dissipation for Region 1 (Section 4.3).

In addition, the MacCormack method used to solve the flow fields in Regions 2 and 3 is discussed in Section 4.4 to clarify the similarity and difference between the Lax-Wendroff and MacCormack methods.

4.2 Lax-Wendroff Method without Dissipation

First, the terms *without dissipation* and *with dissipation* used for the Lax-Wendroff method (Lax and Wendroff 1960) need to be clarified to avoid confusion.

In the present problem, large jumps of values may occur at the steep fronts of breaking and broken waves. This phenomenon resembles a *shock wave*, which is a discontinuity in the solution (*e.g.*, Roache 1982), which could create numerical problems. Numerical treatments of shock waves are aimed at smearing the shock over a wider but limited space, thus, reducing potential numerical problems. This is normally done by the introduction of an explicit or implicit artificial dissipation. The notions *explicit* and *implicit* refer to whether an artificial viscosity appears explicitly (hence, *explicit*) or not (hence, *implicit*) in the finite difference equations (Roache 1982).

The numerical method proposed by Lax and Wendroff (1960) has an option to include an explicit artificial dissipation. This section derives the Lax-Wendroff method for the flow field in Region 1 *without* the explicit artificial dissipation. The next section, Section 4.3, will derive the explicit artificial dissipation term which is added to the scheme derived in this section to produce the dissipative Lax-Wendroff scheme used for the flow field in Region 1.

The following vectors are introduced to express the governing equations 4.1 through 4.6 in a vector form.

$$\mathbf{U}^{[1]} = \begin{pmatrix} U_1^{[1]} \\ \\ U_2^{[1]} \end{pmatrix} = \begin{pmatrix} m \\ \\ h \end{pmatrix} \tag{4.8}$$

$$\mathbf{F}^{[1]} = \begin{pmatrix} F_1^{[1]} \\ \\ F_2^{[1]} \end{pmatrix} = \begin{pmatrix} \frac{m^2}{h} + \frac{h^2}{2} \\ \\ m \end{pmatrix} \tag{4.9}$$

$$\mathbf{G}^{[1]} = \begin{pmatrix} G_1^{[1]} \\ \\ G_2^{[1]} \end{pmatrix} = \begin{pmatrix} \theta h + f|u|u + p_q u_b q_b \\ \\ p_q q_b \end{pmatrix} \tag{4.10}$$

$$\mathbf{U}^{[2]} = (m_p) \tag{4.11}$$

$$\mathbf{F}^{[2]} = \left(\frac{m_p^2}{h_p}\right) \tag{4.12}$$

$$\mathbf{G}^{[2]} = \left(- p_u u_b q_b + h_p \frac{\partial h}{\partial x} + \theta h_p + \frac{m_p}{p_u}\left[\mu + \frac{|m_p|}{p_u h_p}\right]\right) \tag{4.13}$$

$$\mathbf{U}^{[3]} = \begin{pmatrix} U_1^{[3]} \\ \\ U_2^{[3]} \end{pmatrix} = \begin{pmatrix} m_p \\ \\ h_p \end{pmatrix} \tag{4.14}$$

$$\mathbf{F}^{[3]} = \begin{pmatrix} F_1^{[3]} \\ \\ F_2^{[3]} \end{pmatrix} = \begin{pmatrix} \frac{m_p^2}{h_p} + \frac{h_p^2}{2} \\ \\ m_p \end{pmatrix} \tag{4.15}$$

$$\mathbf{G}^{[3]} = \begin{pmatrix} G_1^{[3]} \\ \\ G_2^{[3]} \end{pmatrix} = \begin{pmatrix} \theta_p h_p + \frac{m_p}{p_u}\left[\mu + \frac{|m_p|}{p_u h_p}\right] \\ \\ 0 \end{pmatrix} \tag{4.16}$$

The normalized governing equations 4.1, 4.2, and 4.4 through 4.6 can now be written in the following vector form:

$$\frac{\partial \mathbf{U}^{[k]}}{\partial t} + \frac{\partial \mathbf{F}^{[k]}}{\partial x} + \mathbf{G}^{[k]} = 0 \tag{4.17}$$

where the bracketed superscript $[k]$ with $k = 1$, 2, and 3 denotes the region k to which Eq. 4.17 applies. It is noted that each of the vectors $\mathbf{U}^{[2]}$, $\mathbf{F}^{[2]}$, and $\mathbf{G}^{[2]}$ has only one element. Eq. 4.3, which is not included in Eq. 4.17, is used to express the normalized volume influx q_b in terms of one of the dependent variables involved in Eq. 4.17.

$$q_b = \frac{1}{p_u}\frac{\partial m_p}{\partial x} = \frac{1}{p_u}\frac{\partial \mathbf{U}^{[2]}}{\partial x} \quad \text{for Regions 1 and 2} \tag{4.18}$$

The Lax-Wendroff method based on the component k=1 (Region 1) of Eq. 4.17 will be derived in the following since the original method did not include the term $\mathbf{G}^{[1]}$. The Lax-Wendroff method originates from a Taylor expansion in time of the vector $\mathbf{U}^{[1]}$. To prepare for the use of the Taylor expansion, the first and second derivatives with respect to time t of the vector $\mathbf{U}^{[1]}$ are sought. The first derivative is found simply by rearranging the component k=1 of Eq. 4.17 as follows:

$$\frac{\partial \mathbf{U}^{[1]}}{\partial t} = -\left(\frac{\partial \mathbf{F}^{[1]}}{\partial x} + \mathbf{G}^{[1]}\right) \tag{4.19}$$

Since the derivation in the rest of this section is limited to Region 1, the bracketed superscript [1] is omitted for brevity, except in the parts of the derivation that involve quantities from Region 2. The second derivative of the vector $\mathbf{U}$ with respect to time t is evaluated in the following:

$$\begin{aligned}
\frac{\partial^2 \mathbf{U}}{\partial t^2} &= \frac{\partial}{\partial t}\frac{\partial \mathbf{U}}{\partial t} = -\frac{\partial}{\partial t}\left(\frac{\partial \mathbf{F}}{\partial x} + \mathbf{G}\right) = -\frac{\partial}{\partial x}\frac{\partial \mathbf{F}}{\partial t} - \frac{\partial \mathbf{G}}{\partial t} = -\frac{\partial}{\partial x}\left(\frac{\partial \mathbf{F}}{\partial \mathbf{U}}\frac{\partial \mathbf{U}}{\partial t}\right) - \frac{\partial \mathbf{G}}{\partial t} \\
&\Downarrow \\
\frac{\partial^2 \mathbf{U}}{\partial t^2} &= \frac{\partial}{\partial x}\left[\mathbf{A}\left(\frac{\partial \mathbf{F}}{\partial x} + \mathbf{G}\right)\right] - \frac{\partial \mathbf{G}}{\partial t} \qquad (4.20)
\end{aligned}$$

where use is made of Eq. 4.19 and the matrix $\mathbf{A}$ is the Jacobian given as

$$\mathbf{A} = \frac{\partial \mathbf{F}}{\partial \mathbf{U}} = \begin{pmatrix} \dfrac{\partial F_1}{\partial U_1} & \dfrac{\partial F_1}{\partial U_2} \\ \dfrac{\partial F_2}{\partial U_1} & \dfrac{\partial F_2}{\partial U_2} \end{pmatrix} \tag{4.21}$$

The four elements of the matrix **A** in Eq. 4.21 are evaluated in the following:

$$\begin{aligned} \frac{\partial F_1}{\partial U_1} &= \frac{\partial}{\partial m}\left(\frac{m^2}{h} + \frac{h^2}{2}\right) = 2\frac{m}{h} \\ \frac{\partial F_1}{\partial U_2} &= \frac{\partial}{\partial h}\left(\frac{m^2}{h} + \frac{h^2}{2}\right) = h - \frac{m^2}{h^2} \\ \frac{\partial F_2}{\partial U_1} &= \frac{\partial m}{\partial m} = 1 \\ \frac{\partial F_2}{\partial U_2} &= \frac{\partial m}{\partial h} = 0 \end{aligned}$$

so that the matrix **A** can now be expressed as

$$\mathbf{A} = \begin{pmatrix} 2\frac{m}{h} & \left(h - \frac{m^2}{h^2}\right) \\ & \\ 1 & 0 \end{pmatrix} \tag{4.22}$$

First, the simpler second element of the term $\frac{\partial \mathbf{G}}{\partial t}$ in Eq. 4.20 is evaluated as follows:

$$\begin{aligned} \frac{\partial G_2}{\partial t} &= \frac{\partial}{\partial t}(p_q q_b) = p_q \frac{\partial}{\partial t} \overset{\text{Use}}{\overset{\text{Eq. 4.18}}{\overbrace{(q_b)}}} = \frac{p_q}{p_u}\frac{\partial}{\partial x} \overbrace{\left(\frac{\partial \mathbf{U}^{[2]}}{\partial t}\right)}^{\text{Use Eq. 4.17}} \\ &\Downarrow \\ \frac{\partial G_2}{\partial t} &= -n_p \left[\frac{\partial}{\partial x}\left(\frac{\partial \mathbf{F}^{[2]}}{\partial x} + \mathbf{G}^{[2]}\right)\right] \end{aligned} \tag{4.23}$$

In addition,

$$\frac{\partial q_b}{\partial t} = \frac{1}{p_q}\frac{\partial G_2}{\partial t} = -\frac{1}{p_u}\left[\frac{\partial}{\partial x}\left(\frac{\partial \mathbf{F}^{[2]}}{\partial x} + \mathbf{G}^{[2]}\right)\right] \tag{4.24}$$

Second, the more complicated first element of the term $\frac{\partial \mathbf{G}}{\partial t}$ in Eq. 4.20 is worked out in the following:

$$\begin{aligned}
\frac{\partial G_1}{\partial t} &= \frac{\partial}{\partial t}\left(\theta h + f|u|u + p_q u_b q_b\right) = \theta \overbrace{\frac{\partial h}{\partial t}}^{\substack{\text{Use}\\ \text{Eq. 4.1}}} + f\frac{\partial}{\partial t}\left(|u|u\right) + p_q \frac{\partial}{\partial t}\left(u_b q_b\right) \\
&\Downarrow \\
\frac{\partial G_1}{\partial t} &= -\,\theta\,\frac{\partial m}{\partial x} - \theta\, p_q\, q_b + f\frac{\partial}{\partial t}\left(|u|u\right) + p_q \frac{\partial}{\partial t}\left(u_b q_b\right) \qquad (4.25)
\end{aligned}$$

The term $\frac{\partial}{\partial t}\left(|u|u\right)$ in Eq. 4.25 is evaluated as follows:

$$\begin{aligned}
\frac{\partial}{\partial t}\left(|u|u\right) &= \frac{\partial}{\partial t}\left(\frac{|m|\,m}{h^2}\right) \\
&= \begin{cases} \frac{\partial}{\partial t}\left(\frac{m^2}{h^2}\right) & \text{for } m \geq 0 \\ -\frac{\partial}{\partial t}\left(\frac{m^2}{h^2}\right) & \text{for } m < 0 \end{cases} \\
&= \begin{cases} 2\frac{m}{h^2}\frac{\partial m}{\partial t} - 2\frac{m^2}{h^3}\frac{\partial h}{\partial t} & \text{for } m \geq 0 \\ -2\frac{m}{h^2}\frac{\partial m}{\partial t} + 2\frac{m^2}{h^3}\frac{\partial h}{\partial t} & \text{for } m < 0 \end{cases} \\
&= \frac{2}{h^2}\left(|m|\,\frac{\partial m}{\partial t} - |m|\,\frac{m}{h}\,\frac{\partial h}{\partial t}\right) = 2\frac{|m|}{h^2}\left(\overbrace{\frac{\partial m}{\partial t}}^{\substack{\text{Use}\\ \text{Eq. 4.2}}} - u \overbrace{\frac{\partial h}{\partial t}}^{\substack{\text{Use}\\ \text{Eq. 4.1}}}\right) \\
&= 2\frac{|u|}{h}\left[-\frac{\partial}{\partial x}\left(\frac{m^2}{h} + \frac{h^2}{2}\right) - \theta h - f|u|u - p_q u_b q_b + u\frac{\partial m}{\partial x} + p_q u q_b\right] \\
&= 2\frac{|u|}{h}\Bigg[-2\frac{m}{h}\frac{\partial m}{\partial x} + \frac{m^2}{h^2}\frac{\partial h}{\partial x} - h\frac{\partial h}{\partial x} + u\frac{\partial m}{\partial x} \\
&\qquad\qquad -\theta h - f|u|u + p_q\left(u - u_b\right) q_b \Bigg] \\
&\Downarrow \\
\frac{\partial}{\partial t}\left(|u|u\right) &= 2\frac{|u|}{h}\left[\left(u^2 - h\right)\frac{\partial h}{\partial x} - u\frac{\partial m}{\partial x} - \theta h - f|u|u + p_q\left(u - u_b\right) q_b\right] \qquad (4.26)
\end{aligned}$$

The term $\frac{\partial}{\partial t}\left(u_b q_b\right)$ in Eq. 4.25 is worked out using Eq. 3.21 as follows:

$$\begin{aligned}
\frac{\partial}{\partial t}\left(u_b q_b\right) &= u_b\frac{\partial q_b}{\partial t} + q_b\frac{\partial u_b}{\partial t} \\
&\Downarrow
\end{aligned}$$

$$\begin{aligned}
&\Downarrow \\
\frac{\partial}{\partial t}\left(u_b q_b\right) &= \begin{cases} u\dfrac{\partial q_b}{\partial t} + q_b\dfrac{\partial u}{\partial t} & \text{for } q_b \geq 0 \\ p_u u_p\dfrac{\partial q_b}{\partial t} + p_u q_b\dfrac{\partial u_p}{\partial t} & \text{for } q_b < 0 \end{cases} \\
&= \begin{cases} u\dfrac{\partial q_b}{\partial t} + q_b\dfrac{\partial}{\partial t}\left(\dfrac{m}{h}\right) & \text{for } q_b \geq 0 \\ p_u u_p\dfrac{\partial q_b}{\partial t} + \dfrac{q_b}{h_p}\dfrac{\partial m_p}{\partial t} & \text{for } q_b < 0 \end{cases} \\
&= \begin{cases} \dfrac{m}{h}\dfrac{\partial q_b}{\partial t} + q_b\left(\dfrac{1}{h}\dfrac{\partial m}{\partial t} - \dfrac{m}{h^2}\dfrac{\partial h}{\partial t}\right) & \text{for } q_b \geq 0 \\ \dfrac{m_p}{h_p}\dfrac{\partial q_b}{\partial t} + \dfrac{q_b}{h_p}\dfrac{\partial \mathbf{U}^{[2]}}{\partial t} & \text{for } q_b < 0 \end{cases} \\
&= \begin{cases} \dfrac{m}{h}\dfrac{\partial q_b}{\partial t} + q_b\left(\dfrac{1}{h}\dfrac{\partial U_1^{[1]}}{\partial t} - \dfrac{m}{h^2}\dfrac{\partial U_2^{[1]}}{\partial t}\right) & \text{for } q_b \geq 0 \\ \dfrac{m_p}{h_p}\dfrac{\partial q_b}{\partial t} + \dfrac{q_b}{h_p}\dfrac{\partial \mathbf{U}^{[2]}}{\partial t} & \text{for } q_b < 0 \end{cases} \\
&\Downarrow \quad \text{Use Eq. 4.17} \\
\frac{\partial}{\partial t}\left(u_b q_b\right) &= \begin{cases} \dfrac{m}{h}\dfrac{\partial q_b}{\partial t} - \dfrac{q_b}{h}\left(\dfrac{\partial F_1^{[1]}}{\partial x} + G_1^{[1]} - u\dfrac{\partial F_2^{[1]}}{\partial x} - uG_2^{[1]}\right) & \text{for } q_b \geq 0 \\ \dfrac{m_p}{h_p}\dfrac{\partial q_b}{\partial t} - \dfrac{q_b}{h_p}\left(\dfrac{\partial \mathbf{F}^{[2]}}{\partial x} + \mathbf{G}^{[2]}\right) & \text{for } q_b < 0 \end{cases} \qquad (4.27)
\end{aligned}$$

The term $\frac{\partial q_b}{\partial t}$ in Eq. 4.27 is given by Eq. 4.24. Using the relations given in Eqs. 4.26 and 4.27, Eq. 4.25 can now be written as

$$\begin{aligned}
\frac{\partial G_1}{\partial t} = &- \theta\,\frac{\partial m}{\partial x} - \theta\, p_q\, q_b \\
&+ 2f\,\frac{|u|}{h}\left[\left(u^2 - h\right)\frac{\partial h}{\partial x} - u\frac{\partial m}{\partial x} - \theta h - f|u|u + p_q\left(u - u_b\right)q_b\right] \\
&+ \begin{cases} p_q\dfrac{m}{h}\dfrac{\partial q_b}{\partial t} - p_q\dfrac{q_b}{h}\left(\dfrac{\partial F_1^{[1]}}{\partial x} + G_1^{[1]} - u\dfrac{\partial F_2^{[1]}}{\partial x} - uG_2^{[1]}\right) & \text{for } q_b \geq 0 \\ p_q\dfrac{m_p}{h_p}\dfrac{\partial q_b}{\partial t} - p_q\dfrac{q_b}{h_p}\left(\dfrac{\partial \mathbf{F}^{[2]}}{\partial x} + \mathbf{G}^{[2]}\right) & \text{for } q_b < 0 \end{cases} \qquad (4.28)
\end{aligned}$$

with the term $\frac{\partial q_b}{\partial t}$ given by Eq. 4.24.

The vector $\mathbf{U}$ is expanded in time to the second order using the Taylor series:

$$\mathbf{U}(x, t + \Delta t) = \mathbf{U} + \Delta t\frac{\partial \mathbf{U}}{\partial t} + \frac{(\Delta t)^2}{2}\frac{\partial^2 \mathbf{U}}{\partial t^2} + \bigcirc\left[(\Delta t)^3\right] \qquad (4.29)$$

in which all the terms on the right hand side are evaluated at the location x and the time t, and the notation $\bigcirc\left[(\Delta t)^3\right]$ refers to additional terms of order $(\Delta t)^3$ and higher.

The accuracy of the difference $|\mathbf{U}(x,t+\Delta t)-\mathbf{U}|$, which is the second order in time, determines the order of accuracy in time of the numerical method (Richtmyer and Morton 1967). The essence of the Lax-Wendroff method is to eliminate the time derivatives involved in Eq. 4.29 and replace them with the corresponding spatial derivatives. Denoting $\mathbf{U}^* = \mathbf{U}(x,t+\Delta t)$ and substituting Eqs. 4.19 and 4.20 into Eq. 4.29 yield

$$\begin{aligned}\mathbf{U}^* &= \mathbf{U} - \Delta t\,\frac{\partial \mathbf{F}}{\partial x} - \Delta t\,\mathbf{G} \\ &\quad + \frac{(\Delta t)^2}{2}\,\frac{\partial}{\partial x}\left[\mathbf{A}\left(\frac{\partial \mathbf{F}}{\partial x}+\mathbf{G}\right)\right] - \frac{(\Delta t)^2}{2}\cdot\begin{pmatrix}\frac{\partial G_1}{\partial t}\\ \frac{\partial G_2}{\partial t}\end{pmatrix}\end{aligned} \tag{4.30}$$

where the terms $\frac{\partial G_1}{\partial t}$ and $\frac{\partial G_2}{\partial t}$ are given by Eqs. 4.28 and 4.23, respectively. Eq. 4.30 no longer includes time derivatives. Thus, the elimination of the time derivatives has been accomplished. The next step is to discretize Eq. 4.30. For this purpose let the indices j, $(j-1)$, and $(j+1)$ indicate the nodal locations x, $(x-\Delta x)$, and $(x+\Delta x)$, respectively, where Δx is constant throughout the time-marching computation. The asterisk indicates the next time level $(t+\Delta t)$ as in Eq. 4.30. Quantities written without an asterisk in the following are of the present time level and known.

To discretize the spatial derivatives involved in Eq. 4.30, the central finite difference is used so that a second-order accuracy in space is obtained. The discretized form of Eq. 4.30 is as follows:

$$\begin{aligned}\mathbf{U}_j^* &= \mathbf{U}_j - \Delta t\left(\frac{\partial \mathbf{F}}{\partial x}\right)_j - \Delta t\,\mathbf{G}_j \\ &\quad + \frac{(\Delta t)^2}{2}\left\{\frac{\partial}{\partial x}\left[\mathbf{A}\left(\frac{\partial \mathbf{F}}{\partial x}+\mathbf{G}\right)\right]\right\}_j - \frac{(\Delta t)^2}{2}\cdot\begin{pmatrix}\left[\frac{\partial G_1}{\partial t}\right]_j\\ \left[\frac{\partial G_2}{\partial t}\right]_j\end{pmatrix}\end{aligned} \tag{4.31}$$

The term $\left(\frac{\partial \mathbf{F}}{\partial x}\right)_j$ in Eq. 4.31 is expressed as

$$\left(\frac{\partial \mathbf{F}}{\partial x}\right)_j = \frac{1}{2\Delta x}\left(\mathbf{F}_{j+1}-\mathbf{F}_{j-1}\right) \tag{4.32}$$

The term $\left\{\frac{\partial}{\partial x}\left[\mathbf{A}\left(\frac{\partial \mathbf{F}}{\partial x}+\mathbf{G}\right)\right]\right\}_j$ in Eq. 4.31 is given by

$$\left\{\frac{\partial}{\partial x}\left[\mathbf{A}\left(\frac{\partial \mathbf{F}}{\partial x}+\mathbf{G}\right)\right]\right\}_j = \frac{1}{(\Delta x)^2}\left(\mathbf{H}_j-\mathbf{H}_{j-1}\right) \tag{4.33}$$

with

$$\mathbf{H}_j = \frac{1}{2}\left[\mathbf{A}_{j+1} + \mathbf{A}_j\right]\left[(\mathbf{F}_{j+1} - \mathbf{F}_j) + \frac{\Delta x}{2}(\mathbf{G}_{j+1} + \mathbf{G}_j)\right] \tag{4.34}$$

where the matrix **A** is given by Eq. 4.22.

Define the difference $\Delta\mathbf{U}$ as

$$\Delta\mathbf{U}_j = \mathbf{U}_{j+1} - \mathbf{U}_{j-1} \tag{4.35}$$

and a new vector **B** as

$$\mathbf{B}_j = \frac{1}{\Delta x}\left(\mathbf{F}_{j+1}^{[2]} - \mathbf{F}_j^{[2]}\right) + \frac{1}{2}\left(\mathbf{G}_{j+1}^{[2]} + \mathbf{G}_j^{[2]}\right) \tag{4.36}$$

Using the definition of the difference $\Delta\mathbf{U}$ in Eq. 4.35, Eq. 4.18 can be discretized as

$$(q_b)_j = \frac{1}{2\,\Delta x\; p_u}\Delta\mathbf{U}_j^{[2]} \tag{4.37}$$

Using the definition of the vector **B** in Eq. 4.36, Eq. 4.24 can be discretized as

$$\left(\frac{\partial q_b}{\partial t}\right)_j = -\frac{1}{\Delta x\; p_u}\;(\mathbf{B}_j - \mathbf{B}_{j-1}) \tag{4.38}$$

The two elements of the term $\left(\frac{\partial \mathbf{G}}{\partial t}\right)_j$ in Eq. 4.31 are discretized in the following:

$$\left(\frac{\partial \mathbf{G}}{\partial t}\right)_j = \begin{pmatrix} \left[\frac{\partial G_1}{\partial t}\right]_j \\ \left[\frac{\partial G_2}{\partial t}\right]_j \end{pmatrix} = \frac{1}{\Delta x}\,\mathbf{S}_j + \frac{n_p}{\Delta x}\,\mathbf{P}_j \tag{4.39}$$

where the vector **S** is chosen to be the same as the vector **S** used for the impermeable slope (Wurjanto and Kobayashi 1991), whereas the vector **P** includes the remaining terms related to the permeability of the slope.

The vector **S** in Eq. 4.39 is given by

$$\mathbf{S}_j = \begin{pmatrix} (S_1)_j \\ 0 \end{pmatrix} \tag{4.40}$$

where the element $(S_1)_j$ is defined in the following:

$$(S_1)_j \;=\; -\,\Delta x\,\theta_j\left(\frac{\partial m}{\partial x}\right)_j +\; \Delta x\;2f\,\frac{|u_j|}{h_j}\left[\left(u^2 - h\right)\frac{\partial h}{\partial x} - u\frac{\partial m}{\partial x} - \theta h - f|u|u\right]_j$$

$$\Downarrow$$

$$\Downarrow$$

$$\begin{aligned}(S_1)_j &= \Delta x\, 2f\,\frac{|u_j|}{h_j}\left[\left(u_j^2 - h_j\right)\frac{h_{j+1}-h_{j-1}}{2\Delta x} - u_j\frac{m_{j+1}-m_{j-1}}{2\Delta x} - \theta_j h_j - f|u_j|u_j\right] \\ &\quad - \frac{1}{2}\theta_j\,(m_{j+1}-m_{j-1}) \end{aligned} \tag{4.41}$$

Substituting Eq. 4.41 into Eq. 4.40 would result in a cumbersome expression for the vector **S**. To avoid this, define

$$e_j = 2f\frac{|u_j|}{h_j}\left[\left(u_j^2 - h_j\right)\frac{h_{j+1}-h_{j-1}}{2\Delta x} - u_j\frac{m_{j+1}-m_{j-1}}{2\Delta x} - \theta_j h_j - f|u_j|u_j\right] \tag{4.42}$$

so that the vector **S** can be expressed concisely as

$$\mathbf{S}_j = \begin{pmatrix} \Delta x\; e_j - \frac{1}{2}\theta_j\,(m_{j+1}-m_{j-1}) \\ 0 \end{pmatrix} \tag{4.43}$$

The vector **P** in Eq. 4.39 is expressed as

$$\mathbf{P}_j = \begin{pmatrix} (P_1)_j \\ (P_2)_j \end{pmatrix} \tag{4.44}$$

The element P_1 in Eq. 4.44 is worked out as follows:

$$\begin{aligned}(P_1)_j &= -\frac{\Delta x}{n_p}\,\theta_j\,p_q\,(q_b)_j + \frac{\Delta x}{n_p}\,2f\,\frac{|u_j|}{h_j}\left[u_j - (u_b)_j\right]\,p_q\,(q_b)_j \\ &\quad + \begin{cases} \dfrac{\Delta x}{n_p}\,p_q\,\dfrac{m_j}{h_j}\left(\dfrac{\partial q_b}{\partial t}\right)_j \\ \qquad - \dfrac{\Delta x}{n_p}\,p_q\,\dfrac{1}{h_j}\,(q_b)_j\left(\dfrac{\partial F_1^{[1]}}{\partial x} + G_1^{[1]} - u\dfrac{\partial F_2^{[1]}}{\partial x} - uG_2^{[1]}\right)_j & \text{for } q_b \ge 0 \\ \\ \dfrac{\Delta x}{n_p}\,p_q\,\dfrac{(m_p)_j}{(h_p)_j}\left(\dfrac{\partial q_b}{\partial t}\right)_j \\ \qquad - \dfrac{\Delta x}{n_p}\,p_q\,\dfrac{1}{(h_p)_j}\,(q_b)_j\left(\dfrac{\partial \mathbf{F}^{[2]}}{\partial x} + \mathbf{G}^{[2]}\right)_j & \text{for } q_b < 0 \end{cases}\end{aligned}$$

$$\Downarrow$$

$$\Downarrow$$

$$
\begin{aligned}
(P_1)_j \;&=\; f\,\frac{|u_j|}{h_j}\,\Big[u_j-(u_b)_j\Big]\,\overbrace{(2\,\Delta x\;p_u)\;(q_b)_j}^{\text{Use Eq. 4.37}}-\theta_j\,\overbrace{(\Delta x\;p_u)\;(q_b)_j}^{\text{Use Eq. 4.37}} \\
&\quad + \begin{cases}
\dfrac{m_j}{h_j}\,\overbrace{(\Delta x\;p_u)\left(\dfrac{\partial q_b}{\partial t}\right)_j}^{\text{Use Eq. 4.38}} & \\
\qquad -\dfrac{1}{h_j}\,\overbrace{(\Delta x\;p_u)\,(q_b)_j}^{\text{Use Eq. 4.37}}\cdot & \\
\qquad\qquad \cdot\left(\dfrac{\partial F_1^{[1]}}{\partial x}+G_1^{[1]}-u\dfrac{\partial F_2^{[1]}}{\partial x}-uG_2^{[1]}\right)_j & \text{for } q_b\geq 0 \\[2ex]
\dfrac{(m_p)_j}{(h_p)_j}\,\overbrace{(\Delta x\;p_u)\left(\dfrac{\partial q_b}{\partial t}\right)_j}^{\text{Use Eq. 4.38}} & \\
\qquad -\dfrac{1}{(h_p)_j}\,\underbrace{(\Delta x\;p_u)\,(q_b)_j}_{\text{Use Eq. 4.37}}\left(\dfrac{\partial \mathbf{F}^{[2]}}{\partial x}+\mathbf{G}^{[2]}\right)_j & \text{for } q_b<0
\end{cases} \\
&=\; f\,\frac{|u_j|}{h_j}\Big[u_j-(u_b)_j\Big]\,\Delta\mathbf{U}_j^{[2]}-\frac{1}{2}\theta_j\Delta\mathbf{U}_j^{[2]} \\
&\quad - \begin{cases}
\dfrac{m_j}{h_j}\,(\mathbf{B}_j-\mathbf{B}_{j-1}) & \\
\qquad +\dfrac{1}{2h_j}\,\Delta\mathbf{U}_j^{[2]}\left(\dfrac{\partial F_1^{[1]}}{\partial x}+G_1^{[1]}-u\dfrac{\partial F_2^{[1]}}{\partial x}-uG_2^{[1]}\right)_j & \text{for } q_b\geq 0 \\[2ex]
\dfrac{(m_p)_j}{(h_p)_j}\,(\mathbf{B}_j-\mathbf{B}_{j-1}) & \\
\qquad +\dfrac{1}{2(h_p)_j}\,\Delta\mathbf{U}_j^{[2]}\left(\dfrac{\partial \mathbf{F}^{[2]}}{\partial x}+\mathbf{G}^{[2]}\right)_j & \text{for } q_b<0
\end{cases}
\end{aligned}
$$

$$\Downarrow$$

$$
(P_1)_j \;=\; f\,\frac{|u_j|}{h_j}\Big[u_j-(u_b)_j\Big]\,\Delta\mathbf{U}_j^{[2]}-\frac{1}{2}\theta_j\Delta\mathbf{U}_j^{[2]}-\tilde{P}_j \qquad (4.45)
$$

with $\tilde{P}$ given by

$$\tilde{P}_j = \begin{cases} \begin{aligned} & \frac{m_j}{h_j}\left(\mathbf{B}_j - \mathbf{B}_{j-1}\right) \\ & \qquad + \frac{1}{2h_j}\Delta\mathbf{U}_j^{[2]} \left[\frac{\left(F_1^{[1]}\right)_{j+1} - \left(F_1^{[1]}\right)_{j-1}}{2\Delta x} + \left(G_1^{[1]}\right)_j \right. \\ & \qquad \qquad \left. - u_j \frac{\left(F_2^{[1]}\right)_{j+1} - \left(F_2^{[1]}\right)_{j-1}}{2\Delta x} - u_j \left(G_2^{[1]}\right)_j \right] \end{aligned} & \text{for } q_b \geq 0 \\ \\ \begin{aligned} & \frac{\left(m_p\right)_j}{\left(h_p\right)_j}\left(\mathbf{B}_j - \mathbf{B}_{j-1}\right) \\ & \qquad + \frac{1}{2\left(h_p\right)_j}\Delta\mathbf{U}_j^{[2]} \left(\frac{\mathbf{F}_{j+1}^{[2]} - \mathbf{F}_{j-1}^{[2]}}{2\Delta x} + \mathbf{G}_j^{[2]} \right) \end{aligned} & \text{for } q_b < 0 \end{cases} \tag{4.46}$$

The element P_2 in Eq. 4.44 is worked out as follows:

$$\begin{aligned} \left(P_2\right)_j &= \frac{\Delta x}{n_p} \overbrace{\left(\frac{\partial G_2}{\partial t}\right)_j}^{\text{Use Eq. 4.24}} = \frac{\Delta x}{n_p}\, p_q \left(\frac{\partial q_b}{\partial t}\right)_j = \overbrace{\left(\Delta x\ p_u\right)\left(\frac{\partial q_b}{\partial t}\right)_j}^{\text{Use Eq. 4.38}} \\ & \Downarrow \\ \left(P_2\right)_j &= -\left(\mathbf{B}_j - \mathbf{B}_{j-1}\right) \end{aligned} \tag{4.47}$$

Substituting Eqs. 4.45 and 4.47 into Eq. 4.44 yields the following expression for the vector $\mathbf{P}$:

$$\mathbf{P}_j = \begin{pmatrix} \frac{f\left|u_j\right|}{h_j}\left[u_j - \left(u_b\right)_j\right]\Delta\mathbf{U}_j^{[2]} - \frac{1}{2}\theta_j\ \Delta\mathbf{U}_j^{[2]} - \tilde{P}_j \\ -\left(\mathbf{B}_j - \mathbf{B}_{j-1}\right) \end{pmatrix} \tag{4.48}$$

where $\Delta\mathbf{U}_j$, $\tilde{P}_j$, and $\mathbf{B}_j$ are given by Eqs. 4.35, 4.46, and 4.36, respectively.

Substituting Eqs. 4.32, 4.33, and 4.39 into Eq. 4.31 yields the finite difference equation for Region 1 based on the Lax-Wendroff method without dissipation.

$$\begin{aligned} \mathbf{U}_j^{[1]*} &= \mathbf{U}_j^{[1]} - \frac{\Delta t}{\Delta x}\left[\frac{1}{2}\left(\mathbf{F}_{j+1}^{[1]} - \mathbf{F}_{j-1}^{[1]}\right) + \Delta x\ \mathbf{G}_j^{[1]}\right] \\ & \quad + \frac{1}{2}\left(\frac{\Delta t}{\Delta x}\right)^2\Big[\left(\mathbf{H}_j - \mathbf{H}_{j-1}\right) - \Delta x\ \mathbf{S}_j\Big] - \frac{n_p}{2}\frac{\left(\Delta t\right)^2}{\Delta x}\mathbf{P}_j \end{aligned} \tag{4.49}$$

where the vectors $\mathbf{H}_j$, $\mathbf{S}_j$, and $\mathbf{P}_j$ are given by Eqs. 4.34, 4.43, and 4.48, respectively.

It is now clear that the addition of the terms $p_q q_b$ and $p_q u_b q_b$ in Eqs. 4.1 and 4.2 due to the presence of the permeable underlayer increases the algebraic manipulations required for the Lax-Wendroff method considerably, as compared to the case for impermeable slopes (Wurjanto and Kobayashi 1991).

4.3 Lax-Wendroff Method with Dissipation

One might erroneously regard the Lax-Wendroff method used in Section 4.2 as *dissipative* since the formulation may be considered as an approximation of a parabolic type diffusion equation (Richtmyer and Morton 1967, Hibberd 1977). Hibberd (1977) argued that without the explicit artificial dissipation, energy would be merely shifted into higher-frequency components resulting in the formation of parasitic waves near a jump. The artificial dissipation is intended to reduce these unwanted parasitic waves. This artificial dissipation is used in the present numerical model following the experience of Hibberd and Peregrine (1979) who utilized the Lax-Wendroff method for studying the behavior of bores over sloping beaches. Hibberd and Peregrine (1979, p. 330) stated as follows:

> With a single bore incident on the beach these [parasitic] oscillations do not unduly affect the solution away from the bore or the stability of the scheme. However, in further work to be reported on periodic solutions where bores advance into thin, fast-moving back-wash from previous waves such oscillations prove unacceptable.

Incident irregular wave trains specified in the present work include much more individual waves than the periodic waves computed by Hibberd and Peregrine (1979) and Packwood (1980). As a result, the inclusion of the artificial dissipation in the Lax-Wendroff method herein is judged to be necessary.

The Lax-Wendroff method with dissipation for the flow field in Region 1 originates from a modification of the component k=1 of Eq. 4.17 where an artificial viscosity term is added as follows:

$$\frac{\partial \mathbf{U}^{[1]}}{\partial t} + \frac{\partial \mathbf{F}^{[1]}}{\partial x} + \mathbf{G}^{[1]} = \frac{\Delta x}{2} \frac{\partial}{\partial x} \left(\mathbf{Q} \frac{\partial \mathbf{U}^{[1]}}{\partial x} \right) \tag{4.50}$$

The method to derive the matrix $\mathbf{Q}$ in Eq. 4.50 is the same as that used by Hibberd (1977) for a system of governing equations similar to Eq. 4.17 where the vector $\mathbf{G}^{[1]}$ has no effect on the outcome.

The added term in Eq. 4.50 affects the first derivative $\frac{\partial \mathbf{U}}{\partial t}$ in Eq. 4.19, which becomes

$$\frac{\partial \mathbf{U}^{[1]}}{\partial t} = -\left(\frac{\partial \mathbf{F}^{[1]}}{\partial x} + \mathbf{G}^{[1]}\right) + \frac{\Delta x}{2}\,\frac{\partial}{\partial x}\left(\mathbf{Q}\frac{\partial \mathbf{U}^{[1]}}{\partial x}\right) \tag{4.51}$$

However, the second derivative $\frac{\partial^2 \mathbf{U}}{\partial t^2}$ in Eq. 4.20 is assumed to be unaffected by the added term in Eq. 4.50.

Define a new vector $\mathbf{D}$ as

$$\mathbf{D} = \Delta t\,\frac{\Delta x}{2}\,\frac{\partial}{\partial x}\left(\mathbf{Q}\frac{\partial \mathbf{U}^{[1]}}{\partial x}\right) \tag{4.52}$$

which is introduced to carry the effects of the added artificial dissipation in the numerical scheme. The finite difference equation for the flow field in Region 1 using the dissipative Lax-Wendroff method based on Eq. 4.29 together with Eqs. 4.51 and 4.20 becomes the same as Eq. 4.49 with the vector $\mathbf{D}_j$ added on its right hand side.

$$\begin{aligned}\mathbf{U}_j^{[1]*} &= \mathbf{U}_j^{[1]} - \frac{\Delta t}{\Delta x}\left[\frac{1}{2}\left(\mathbf{F}_{j+1}^{[1]} - \mathbf{F}_{j-1}^{[1]}\right) + \Delta x\;\mathbf{G}_j^{[1]}\right] \\ &\quad + \frac{1}{2}\left(\frac{\Delta t}{\Delta x}\right)^2\left[\left(\mathbf{H}_j - \mathbf{H}_{j-1}\right) - \Delta x\;\mathbf{S}_j\right] - \frac{n_p}{2}\frac{(\Delta t)^2}{\Delta x}\mathbf{P}_j + \mathbf{D}_j\end{aligned} \tag{4.53}$$

The bracketed superscript [1] is omitted for the rest of this section since the discussion in this section involves only the flow in Region 1.

The introduction of the artificial dissipation in the numerical scheme is intended to smear the large jump of values over a wider but limited space. The matrix $\mathbf{Q}$ in Eq. 4.50 needs to be selected to satisfy this requirement. The matrix $\mathbf{Q}$ at the location $(x + \frac{\Delta x}{2})$ is denoted by $\mathbf{Q}_j$ with the index j instead of $(j + \frac{1}{2})$ for simplicity, and is regarded to be a function of the vector $\mathbf{U}_j$ at the location x and the vector $\mathbf{U}_{j+1}$ at $(x + \Delta x)$ as expressed in the following:

$$\mathbf{Q}_j = \mathbf{Q}_j\left(\mathbf{U}_j, \mathbf{U}_{j+1}\right) \tag{4.54}$$

The matrix $\mathbf{Q}_j$ is so chosen as to produce the desired dissipation when the two values of $\mathbf{U}$ are widely different but negligible dissipation when the two values are nearly equal (Richtmyer and Morton 1967). Accordingly, the matrix $\mathbf{Q}$ takes the following form of a polynomial in $\mathbf{A}$ (Lax and Wendroff 1960):

$$\mathbf{Q} = q_1\,\mathbf{I} + q_2\,\mathbf{A} + \ldots + q_n\,\mathbf{A}^{n-1} \quad \text{for } n \text{ dependent variables} \tag{4.55}$$

where $\mathbf{I}$ is a unit matrix and n=2 for the matrix $\mathbf{A}$ given by Eq. 4.22. The coefficients q_1 and q_2 are determined using an eigenvalue analysis as will be performed for the matrix $\mathbf{A}$ given by Eq. 4.22, following Lax and Wendroff (1960), as explained more clearly by Richtmyer and Morton (1967) and Hibberd (1977).

Let λ be the eigenvalue of the matrix $\mathbf{A}$ given by Eq. 4.22 and κ the eigenvalue of the matrix $\mathbf{Q}$ given by Eq. 4.55 with n=2.

The eigenvalue λ of the matrix $\mathbf{A}$ is evaluated by equating to zero the determinant of the matrix $(\mathbf{A} - \lambda\,\mathbf{I})$.

$$\begin{aligned}
\det(\mathbf{A} - \lambda\,\mathbf{I}) &= 0 \\
&\Downarrow \\
\begin{vmatrix} \left(2\frac{m}{h} - \lambda\right) & \left(h - \frac{m^2}{h^2}\right) \\ 1 & -\lambda \end{vmatrix} &= 0 \\
&\Downarrow \\
\lambda^2 - 2\lambda u + \left(u^2 - h\right) &= 0 \\
&\Downarrow \\
\left[\lambda - \left(u + \sqrt{h}\right)\right]\left[\lambda - \left(u - \sqrt{h}\right)\right] &= 0 \\
&\Downarrow \\
\lambda_1 = \varphi \quad \text{and} \quad \lambda_2 = \psi &
\end{aligned} \tag{4.56}$$

with

$$\varphi = u + c \quad ; \quad \psi = u - c \quad ; \quad c = \sqrt{h} \tag{4.57}$$

Similarly, the eigenvalue κ of the matrix $\mathbf{Q}$ is evaluated by equating to zero the determinant of the matrix $(\mathbf{Q} - \kappa\,\mathbf{I})$.

$$\begin{aligned}
\det(\mathbf{Q} - \kappa\,\mathbf{I}) &= 0 \\
&\Downarrow \\
\det(q_1\,\mathbf{I} + q_2\,\mathbf{A} - \kappa\,\mathbf{I}) &= 0 \\
&\Downarrow \\
\begin{vmatrix} (q_1 + 2q_2 u - \kappa) & [q_2\,(h - u^2)] \\ q_2 & q_1 - \kappa \end{vmatrix} &= 0 \\
&\Downarrow
\end{aligned}$$

$$(\kappa_1 - q_1) - q_2\ \overbrace{(u + \sqrt{h})}^{\text{Use Eq. 4.57}}\ = 0 \quad \text{and} \quad (\kappa_2 - q_1) - q_2\ \overbrace{(u - \sqrt{h})}^{\text{Use Eq. 4.57}}\ = 0$$

$$\Downarrow$$

$$\kappa_1 = q_1 + q_2\varphi \quad \text{and} \quad \kappa_2 = q_1 + q_2\psi \tag{4.58}$$

The coefficients $(q_1)_j$ and $(q_2)_j$ at the location $(x + \frac{\Delta x}{2})$ indicated by the index j instead of $(j + \frac{1}{2})$ for simplicity are obtained by relating the eigenvalues of the matrix $\mathbf{Q}_j$ at the location $(x + \frac{\Delta x}{2})$ to those of the matrix $\mathbf{A}$ at the locations x and $(x + \Delta x)$ indicated by the indices j and $(j + 1)$, respectively.

$$(\kappa_i)_j = \epsilon_i\ |(\lambda_i)_{j+1} - (\lambda_i)_j| \quad \text{with} \quad i = 1, 2$$

$$\Downarrow$$

$$(q_1)_j + \frac{1}{2}(q_2)_j\,(\varphi_{j+1} + \varphi_j) \quad = \quad \epsilon_1\ |\varphi_{j+1} - \varphi_j| \tag{4.59}$$

$$(q_1)_j + \frac{1}{2}(q_2)_j\,(\psi_{j+1} + \psi_j) \quad = \quad \epsilon_2\ |\psi_{j+1} - \psi_j| \tag{4.60}$$

where ϵ_1 and ϵ_2 are positive constants of the order unity determining the amount of artificial dissipation. The artificial dissipation is supposed to increase with the increase of ϵ_1 and ϵ_2. In the numerical model PBREAK, ϵ_1 and ϵ_2 are specified by the user.

Solving Eqs. 4.59 and 4.60 yields the following expressions for the coefficients q_1 and q_2:

$$\begin{aligned}(q_1)_j &= -\frac{1}{2\,(c_{j+1}+c_j)}\Big[\epsilon_1|\varphi_{j+1}-\varphi_j|\,(\psi_{j+1}+\psi_j) \\ &\qquad\qquad -\epsilon_2|\psi_{j+1}-\psi_j|\,(\varphi_{j+1}+\varphi_j)\Big] \qquad (4.61)\\ (q_2)_j &= \frac{1}{(c_{j+1}+c_j)}\Big[\epsilon_1|\varphi_{j+1}-\varphi_j| - \epsilon_2|\psi_{j+1}-\psi_j|\Big] \qquad (4.62)\end{aligned}$$

The discretized form of Eq. 4.55 with n=2 gives the value of $\mathbf{Q}_j$ at $(x+\frac{\Delta x}{2})$.

$$\mathbf{Q}_j = (q_1)_j\,\mathbf{I} + \frac{1}{2}(q_2)_j\,(\mathbf{A}_j+\mathbf{A}_{j+1}) \qquad (4.63)$$

where q_1, q_2, and $\mathbf{A}$ are given by Eqs. 4.61, 4.62, and 4.22, respectively.

Finally, the term $\mathbf{D}_j$ at the location x in Eq. 4.53 is given by discretizing Eq. 4.52 as

$$\mathbf{D}_j = \frac{1}{2}\frac{\Delta t}{\Delta x}\left[\mathbf{Q}_j\left(\mathbf{U}^{[1]}_{j+1}-\mathbf{U}^{[1]}_j\right) - \mathbf{Q}_{j-1}\left(\mathbf{U}^{[1]}_j-\mathbf{U}^{[1]}_{j-1}\right)\right] \qquad (4.64)$$

where the matrix $\mathbf{Q}_j$ at the location $(x+\frac{\Delta x}{2})$ is given by Eq. 4.63 and the matrix $\mathbf{Q}_{j-1}$ corresponds to the location $(x-\frac{\Delta x}{2})$.

It should be mentioned that the final expression given by Eq. 4.53 has been given in WK 92 without proof since the above derivations are very lengthy. The dissipative Lax-Wendroff method presented herein for the permeable slope reduces to that used for the corresponding impermeable slope if q_b=0 and u_b=0 in Eqs. 4.1 and 4.2.

Even though the computation of the flow field in Region 1 is by default dissipative in the present numerical model, the explicit numerical dissipation can be turned off simply by specifying the numerical damping coefficients ϵ_1=ϵ_2=0. All the computations in the present work are made with non-zero ϵ_1 and ϵ_2, except for one case in Chapter 6 where ϵ_1 and ϵ_2 are specified to be zero. This particular computation is intended to find out whether the explicit numerical dissipation will modify the computed flow field noticeably or not. The experiences with RBREAK for impermeable slopes have indicated that the explicit numerical dissipation modifies the computed flow field very little but tends to improve the numerical stability.

4.4 A Discussion on the MacCormack Method

While the flow field in Region 1 is computed using the dissipative Lax-Wendroff method derived in Sections 4.2 and 4.3, the flow fields in Regions 2 and 3 are computed using the MacCormack method (MacCormack 1969). This is because the MacCormack method without explicit numerical dissipation is much easier to apply in Regions 2 and 3 where the physical dissipation due to the flow resistance inside the permeable underlayer is expected to improve the numerical stability. Even though the MacCormack method is generally regarded to be in the class of *two-step Lax-Wendroff methods*, it is not clear whether the MacCormack method could be derived from the Lax-Wendroff method in an analytical manner, as Roache (1982, p. 253) put it

> It is not at all obvious that the [MacCormack] method is a Lax-Wendroff type, nor even that it is consistent with the partial differential equation, but the excellent results obtained bolster confidence.

On the other hand, for systems of equations in the form of Eq. 4.17 *without* the term **G**, Peyret and Taylor (1983) cited Lerat and Peyret (1973, 1974, 1975) who proposed a generalized two-step scheme that could yield the Lax-Wendroff or MacCormack method by adopting certain assumptions and choosing specific coefficients. The purpose of the discussion in this section is to show that the MacCormack method closely resembles the non-dissipative Lax-Wendroff method derived in Section 4.2 for a special case. Consequently, the derivation of the non-dissipative Lax-Wendroff method in Section 4.2 should be sufficient as a basis for the use of the MacCormack method in the numerical model PBREAK. Furthermore, the numerical stability criterion imposed on the numerical method for Region 1 should be appropriate for Regions 2 and 3. It is noted that the numerical stability criterion imposed in the numerical model PBREAK is adopted from Packwood (1980) for the case of impermeable slopes.

Consider a system of equations in the form of Eq. 4.17

$$\frac{\partial \mathbf{U}}{\partial t} + \frac{\partial \mathbf{F}}{\partial x} + \mathbf{G} = 0 \tag{4.65}$$

in which the vectors **U**, **F**, and **G** are regarded to be general where the vectors given in Eqs. 4.8 through 4.16 may be considered as an example.

The discussion in this section is given in the following manner. First, the non-dissipative Lax-Wendroff method will be derived using Eq. 4.65 in a slightly different manner from that in Section 4.2. Second, the MacCormack method is developed from Eq. 4.65 under an assumed special condition. The resulting finite difference equations from both methods are then compared to examine the similarity between the two methods under the assumed special condition.

Non-dissipative Lax-Wendroff Method

The initial procedure in the present derivation is identical to that in Section 4.2. Eq. 4.31 is rewritten as

$$\begin{aligned}\mathbf{U}_j^* &= \mathbf{U}_j - \Delta t\left(\frac{\partial \mathbf{F}}{\partial x}\right)_j - \Delta t\,\mathbf{G}_j \\ &\quad + \frac{(\Delta t)^2}{2}\left\{\frac{\partial}{\partial x}\left[\mathbf{A}\left(\frac{\partial \mathbf{F}}{\partial x} + \mathbf{G}\right)\right]\right\}_j - \frac{(\Delta t)^2}{2}\left(\frac{\partial \mathbf{G}}{\partial t}\right)_j \qquad (4.66)\end{aligned}$$

where the matrix $\mathbf{A}$ is the Jacobian $\mathbf{A} = \frac{\partial \mathbf{F}}{\partial \mathbf{U}}$.

The term $\frac{\partial \mathbf{G}}{\partial t}$ in Eq. 4.66 is rearranged for the special case where $\mathbf{G}$ depends on $\mathbf{U}$ only.

$$\frac{\partial \mathbf{G}}{\partial t} = \frac{\partial \mathbf{G}}{\partial \mathbf{U}} \quad \overset{\text{Use Eq. 4.65}}{\overbrace{\frac{\partial \mathbf{U}}{\partial t}}} \quad = -\mathbf{Y}\left(\frac{\partial \mathbf{F}}{\partial x} + \mathbf{G}\right) \qquad (4.67)$$

where the matrix $\mathbf{Y}$ is the Jacobian $\mathbf{Y} = \frac{\partial \mathbf{G}}{\partial \mathbf{U}}$. It is noted that the Jacobian $\mathbf{Y}$ does not exist for $\mathbf{G}^{[1]}$ defined by Eq. 4.10.

Eq. 4.67 is substituted into Eq. 4.66 and the resulting equation is then discretized further.

$$\begin{aligned}\mathbf{U}_j^* &= \mathbf{U}_j - \Delta t\left(\frac{\partial \mathbf{F}}{\partial x}\right)_j - \Delta t\,\mathbf{G}_j \\ &\quad + \frac{(\Delta t)^2}{2}\left\{\frac{\partial}{\partial x}\left[\mathbf{A}\left(\frac{\partial \mathbf{F}}{\partial x} + \mathbf{G}\right)\right]\right\}_j + \frac{(\Delta t)^2}{2}\left[\mathbf{Y}\left(\frac{\partial \mathbf{F}}{\partial x} + \mathbf{G}\right)\right]_j \\ &\Downarrow \\ \mathbf{U}_j^* &= \mathbf{U}_j - \frac{1}{2}\frac{\Delta t}{\Delta x}\left(\mathbf{F}_{j+1} - \mathbf{F}_{j-1}\right)\end{aligned}$$

$$+\frac{1}{4}\left(\frac{\Delta t}{\Delta x}\right)^2\left[\ (\mathbf{A}_{j+1}+\mathbf{A}_j)(\mathbf{F}_{j+1}-\mathbf{F}_j)-(\mathbf{A}_j+\mathbf{A}_{j-1})(\mathbf{F}_j-\mathbf{F}_{j-1})\ \right]$$
$$-\Delta t\ \mathbf{G}_j+\frac{(\Delta t)^2}{2}\mathbf{Y}_j\mathbf{G}_j$$
$$+\frac{1}{4}\frac{(\Delta t)^2}{\Delta x}\mathbf{Y}_j(\mathbf{F}_{j+1}-\mathbf{F}_{j-1})+\frac{1}{4}\frac{(\Delta t)^2}{\Delta x}(\mathbf{A}_{j+1}\mathbf{G}_{j+1}-\mathbf{A}_{j-1}\mathbf{G}_{j-1}) \qquad (4.68)$$

Eq. 4.68 corresponds to the full form of Eq. 4.65. The first two lines on the right hand side of Eq. 4.68 corresponds to Eq. 4.65 with **G**=0 and hence **Y**=0.

MacCormack Method

The MacCormack method consists of two steps, one of a forward space difference and another of a backward space difference, which are interchangeable (Roache 1982, Anderson *et al.* 1984). The *backward-forward* setting used by Fennema and Chaudhry (1986) is adopted for convenience dealing with the landward boundary conditions as explained in WK 92. Their use of the term *predictor* step referring to the *first* step and the term *corrector* step for the *second* step is also adopted here.

PREDICTOR STEP:

$$\dot{\mathbf{U}}_j=\mathbf{U}_j-\frac{\Delta t}{\Delta x}\Big(\mathbf{F}_j-\mathbf{F}_{j-1}\Big)-\Delta t\ \mathbf{G}_j \qquad (4.69)$$

CORRECTOR STEP:

$$\ddot{\mathbf{U}}_j=\dot{\mathbf{U}}_j-\frac{\Delta t}{\Delta x}\Big(\dot{\mathbf{F}}_{j+1}-\dot{\mathbf{F}}_j\Big)-\Delta t\ \dot{\mathbf{G}}_j \qquad (4.70)$$

The value of the vector **U** at the next time level $t^*=(t+\Delta t)$ is given by

$$\mathbf{U}_j^*=\frac{1}{2}\Big(\mathbf{U}_j+\ddot{\mathbf{U}}_j\Big) \qquad (4.71)$$

The quantities written with an overhead dot ($\dot{}$) in Eq. 4.70 are evaluated after the predictor step but before the corrector step.

It is assumed in the following that the Jacobians **A** and **Y** are constant, and **F** and **G** can be expressed in the following forms:

$$\mathbf{F}=\mathbf{A}\ \mathbf{U}\quad ;\quad \mathbf{G}=\mathbf{Y}\ \mathbf{U} \qquad (4.72)$$

It then follows that

$$\dot{\mathbf{F}}=\mathbf{A}\ \dot{\mathbf{U}}\quad ;\quad \dot{\mathbf{G}}=\mathbf{Y}\ \dot{\mathbf{U}} \qquad (4.73)$$

Utilizing the relations expressed in Eqs. 4.69, 4.70, and 4.73, Eq. 4.71 is manipulated as follows:

$$
\begin{aligned}
\mathbf{U}_j^* &= \frac{1}{2}\left(\mathbf{U}_j + \overbrace{\ddot{\mathbf{U}}_j}^{\text{Use Eq. 4.70}} \right) \\
&= \frac{1}{2}\left[\mathbf{U}_j + \overbrace{\dot{\mathbf{U}}_j}^{\text{Use Eq. 4.69}} - \frac{\Delta t}{\Delta x}\left(\overbrace{\dot{\mathbf{F}}_{j+1} - \dot{\mathbf{F}}_j}^{\text{Use Eq. 4.73}} \right) - \Delta t \overbrace{\dot{\mathbf{G}}_j}^{\text{Use Eq. 4.73}} \right] \\
&= \frac{1}{2}\mathbf{U}_j + \frac{1}{2}\left[\mathbf{U}_j - \frac{\Delta t}{\Delta x}\left(\mathbf{F}_j - \mathbf{F}_{j-1} \right) - \Delta t\, \mathbf{G}_j \right] \\
&\quad - \frac{1}{2}\frac{\Delta t}{\Delta x}\,\mathbf{A}\left(\overbrace{\dot{\mathbf{U}}_{j+1} - \dot{\mathbf{U}}_j}^{\text{Use Eq. 4.69}} \right) - \frac{1}{2}\Delta t\, \mathbf{Y} \overbrace{\dot{\mathbf{U}}_j}^{\text{Use Eq. 4.69}} \\
&= \mathbf{U}_j - \frac{1}{2}\frac{\Delta t}{\Delta x}\left(\mathbf{F}_j - \mathbf{F}_{j-1} \right) - \frac{1}{2}\Delta t\, \mathbf{G}_j \\
&\quad - \frac{1}{2}\frac{\Delta t}{\Delta x}\,\mathbf{A}\left[\mathbf{U}_{j+1} - \frac{\Delta t}{\Delta x}\left(\mathbf{F}_{j+1} - \mathbf{F}_j \right) - \Delta t\, \mathbf{G}_{j+1} \right. \\
&\qquad\qquad \left. - \mathbf{U}_j + \frac{\Delta t}{\Delta x}\left(\mathbf{F}_j - \mathbf{F}_{j-1} \right) + \Delta t\, \mathbf{G}_j \right] \\
&\quad - \frac{1}{2}\Delta t\, \mathbf{Y}\left[\mathbf{U}_j - \frac{\Delta t}{\Delta x}\left(\mathbf{F}_j - \mathbf{F}_{j-1} \right) - \Delta t\, \mathbf{G}_j \right] \\
&= \mathbf{U}_j - \frac{1}{2}\frac{\Delta t}{\Delta x}\left(\mathbf{F}_j - \mathbf{F}_{j-1} \right) - \frac{1}{2}\Delta t\, \mathbf{G}_j - \frac{1}{2}\frac{\Delta t}{\Delta x}\left[\overbrace{\mathbf{A}\mathbf{U}_{j+1}}^{\text{Use Eq. 4.72}} - \overbrace{\mathbf{A}\mathbf{U}_j}^{\text{Use Eq. 4.72}} \right] \\
&\quad + \frac{1}{2}\left(\frac{\Delta t}{\Delta x} \right)^2 \left[\mathbf{A}\left(\mathbf{F}_{j+1} - \mathbf{F}_j \right) - \mathbf{A}\left(\mathbf{F}_j - \mathbf{F}_{j-1} \right) \right] - \frac{1}{2}\Delta t \overbrace{\mathbf{Y}\mathbf{U}_j}^{\text{Use Eq. 4.72}} \\
&\quad + \frac{(\Delta t)^2}{2}\,\mathbf{Y}\,\mathbf{G}_j + \frac{1}{2}\frac{(\Delta t)^2}{\Delta x}\,\mathbf{Y}\left(\mathbf{F}_j - \mathbf{F}_{j-1} \right) + \frac{1}{2}\frac{(\Delta t)^2}{\Delta x}\,\mathbf{A}\left(\mathbf{G}_{j+1} - \mathbf{G}_j \right) \\
&\Downarrow \\
\mathbf{U}_j^* &= \mathbf{U}_j - \frac{1}{2}\frac{\Delta t}{\Delta x}\left(\mathbf{F}_{j+1} - \mathbf{F}_{j-1} \right) \\
&\quad + \frac{1}{2}\left(\frac{\Delta t}{\Delta x} \right)^2 \left[\mathbf{A}\left(\mathbf{F}_{j+1} - \mathbf{F}_j \right) - \mathbf{A}\left(\mathbf{F}_j - \mathbf{F}_{j-1} \right) \right] \\
&\quad - \Delta t\, \mathbf{G}_j + \frac{(\Delta t)^2}{2}\mathbf{Y}\mathbf{G}_j \\
&\quad + \frac{1}{2}\frac{(\Delta t)^2}{\Delta x}\,\mathbf{Y}\left(\mathbf{F}_j - \mathbf{F}_{j-1} \right) + \frac{1}{2}\frac{(\Delta t)^2}{\Delta x}\,\mathbf{A}\left(\mathbf{G}_{j+1} - \mathbf{G}_j \right) \qquad (4.74)
\end{aligned}
$$

Eq. 4.74 corresponds to the full form of Eq. 4.65. The first two lines on the right hand side of Eq. 4.74 corresponds to Eq. 4.65 with **G**=0. Comparing Eq. 4.68 and 4.74 for the case where the Jacobians **A** and **Y** are constant and Eq. 4.72 is satisfied, it may be concluded that

- the Lax-Wendroff and MacCormack methods based on the full form of Eq. 4.65 are almost identical, and
- the Lax-Wendroff and MacCormack methods based on Eq. 4.65 with **G**=0 are identical.

The MacCormack method is simple to implement since it does not involve complicated terms like the Jacobian **A** in the Lax-Wendroff method. The implementation of the MacCormack method to solve the flow fields in Regions 2 and 3 is sufficiently described in WK 92 and is not repeated here. The artificial dissipation in the form of Eq. 4.64 or in the form used by Fennema and Chaudhry (1986) could have been added to the MacCormack method but is not included in WK 92 since the turbulent and laminar flow resistance inside the permeable underlayer is normally significant and expected to cause sufficient physical dissipation.

Chapter 5

ONE-DIMENSIONAL ENERGY EQUATIONS

In the line of work from the first numerical model IBREAK (Kobayashi and Wurjanto 1989a) to the present numerical model PBREAK, the energy equation was first introduced by Kobayashi and Wurjanto (1989c) who invoked the analogy between wave breaking and hydraulic jump so that the rate of energy dissipation due to wave breaking could be estimated without analyzing the dissipation processes explicitly. The idea is extended in the present work. In addition to computing the flow fields in the three regions using the one-dimensional continuity and momentum equations, the numerical model PBREAK also estimates energy fluxes and dissipation rates in the flow fields using the one-dimensional energy equations derived in this chapter.

5.1 Energy Equation for Region 1

The one-dimensional energy equation for the flow in Region 1 is obtained by multiplying Eq. 3.1 by the normalized horizontal velocity u_1 and then integrating the resulting equation with respect to z from the interface $z = z_b$ between Regions 1 and 2 to the free surface $z = \eta$.

First, multiply Eq. 3.1 by u_1

$$\begin{aligned}
u_1 \frac{\partial u_1}{\partial t} + u_1\, u_1 \frac{\partial u_1}{\partial x} + u_2\, u_1 \frac{\partial u_1}{\partial z} &= -u_1 \frac{\partial \eta}{\partial x} + u_1 \frac{\partial \tau_{zx}}{\partial z} \\
&\Downarrow \\
\frac{\partial}{\partial t}\left(\frac{u_1^2}{2}\right) + u_1 \frac{\partial}{\partial x}\left(\frac{u_1^2}{2}\right) + u_2 \frac{\partial}{\partial z}\left(\frac{u_1^2}{2}\right) &= -u_1 \frac{\partial \eta}{\partial x} + u_1 \frac{\partial \tau_{zx}}{\partial z} \\
&\Downarrow
\end{aligned}$$

$$\Downarrow$$

$$\begin{aligned}\frac{\partial}{\partial t}\left(\frac{u_1^2}{2}\right)+\frac{\partial}{\partial x}\left(\frac{u_1^3}{2}\right)-\frac{u_1^2}{2}\frac{\partial u_1}{\partial x} & + \\ \frac{\partial}{\partial z}\left(\frac{u_1^2u_2}{2}\right)-\frac{u_1^2}{2}\frac{\partial u_2}{\partial z} & = -u_1\,\frac{\partial \eta}{\partial x}+u_1\,\frac{\partial \tau_{zx}}{\partial z}\end{aligned}$$

$$\Downarrow$$

$$\begin{aligned}\frac{\partial}{\partial t}\left(\frac{u_1^2}{2}\right)+\frac{\partial}{\partial x}\left(\frac{u_1^3}{2}\right)+\frac{\partial}{\partial z}\left(\frac{u_1^2u_2}{2}\right) & - \\ \frac{u_1^2}{2}\overbrace{\left(\frac{\partial u_1}{\partial x}+\frac{\partial u_2}{\partial z}\right)}^{=0 \text{ by Eq. 2.9}} & = -u_1\,\frac{\partial \eta}{\partial x}+u_1\,\frac{\partial \tau_{zx}}{\partial z}\end{aligned}$$

$$\Downarrow$$

$$\frac{\partial}{\partial t}\left(\frac{u_1^2}{2}\right)+\frac{\partial}{\partial x}\left(\frac{u_1^3}{2}\right)+\frac{\partial}{\partial z}\left(\frac{u_1^2u_2}{2}\right) = -u_1\,\frac{\partial \eta}{\partial x}+u_1\,\frac{\partial \tau_{zx}}{\partial z} \tag{5.1}$$

Next, integrate Eq. 5.1 with respect to z from $z = z_b$ to$z = \eta$.

$$\begin{aligned}\int_{z_b}^{\eta}\frac{\partial}{\partial t}\left(\frac{u_1^2}{2}\right)dz+\int_{z_b}^{\eta}\frac{\partial}{\partial x}\left(\frac{u_1^3}{2}\right)dz & + \\ \int_{z_b}^{\eta}\frac{\partial}{\partial z}\left(\frac{u_1^2u_2}{2}\right)dz & = -\int_{z_b}^{\eta}\left(u_1\,\frac{\partial \eta}{\partial x}\right)dz+\int_{z_b}^{\eta}\left(u_1\,\frac{\partial \tau_{zx}}{\partial z}\right)dz\end{aligned}$$

Leibniz rule is used $\Downarrow$

$$\begin{aligned}\frac{\partial}{\partial t}\overbrace{\int_{z_b}^{\eta}\frac{u_1^2}{2}dz}^{\text{Use Eq. 3.14}}\;-\frac{1}{2}\left[u_1^2\right]_{z=\eta}\frac{\partial \eta}{\partial t} & + \frac{1}{2}\left[u_1^2\right]_{z=z_b}\overbrace{\frac{\partial z_b}{\partial t}}^{=0} \\ +\frac{\partial}{\partial x}\int_{z_b}^{\eta}\frac{u_1^3}{2}dz-\frac{1}{2}\left[u_1^3\right]_{z=\eta}\frac{\partial \eta}{\partial x} & + \frac{1}{2}\left[u_1^3\right]_{z=z_b}\frac{dz_b}{dx} \\ +\frac{1}{2}\left[u_1^2u_2\right]_{z=\eta}-\frac{1}{2}\left[u_1^2u_2\right]_{z=z_b} & = -\frac{\partial \eta}{\partial x}\overbrace{\int_{z_b}^{\eta}u_1dz}^{\text{Use Eq. 3.9}}+\int_{z_b}^{\eta}\left(u_1\,\frac{\partial \tau_{zx}}{\partial z}\right)dz\end{aligned}$$

$$\Downarrow$$

$$\Downarrow$$

$$\begin{aligned}
\frac{\partial}{\partial t}\left(\frac{1}{2}C_m h u^2\right) + \frac{\partial}{\partial x}\int_{z_b}^{\eta}\frac{u_1^3}{2}dz \quad &+ \quad \frac{1}{2}\overbrace{\left[u_1^2\left(-\frac{\partial \eta}{\partial t} - u_1\frac{\partial \eta}{\partial x} + u_2\right)\right]_{z=\eta}}^{\text{Apply Eq. 3.4 here}} \\
+\frac{1}{2}\overbrace{\left[u_1^2\right]_{z=z_b}}^{\substack{\text{Replace}\\ \text{by } u_b^2}}\overbrace{\left[u_1\frac{dz_b}{dx} - u_2\right]_{z=z_b}}^{\text{Apply Eq. 3.7 here}} \quad &= \quad -m\frac{\partial \eta}{\partial x} + \int_{z_b}^{\eta}\left(u_1\,\frac{\partial \tau_{zx}}{\partial z}\right)dz \\
&\Downarrow \\
\frac{\partial}{\partial t}\left(\frac{1}{2}C_m h u^2\right) + \frac{\partial}{\partial x}\int_{z_b}^{\eta}\frac{u_1^3}{2}dz + \frac{1}{2}p_q q_b u_b^2 \quad &= \quad -m\frac{\partial \eta}{\partial x} + \int_{z_b}^{\eta}\left(u_1\,\frac{\partial \tau_{zx}}{\partial z}\right)dz \qquad (5.2)
\end{aligned}$$

To simplify Eq. 5.2, (**1**) define the energy correction coefficient C_e as

$$C_e = \frac{1}{h}\int_{z_b}^{\eta}\left(\frac{u_1}{u}\right)^3 dz \qquad (5.3)$$

(**2**) denote the last term in Eq. 5.2 by $(-D)$ where D represents the normalized rate of energy dissipation per unit horizontal area for the flow in Region 1

$$D = -\int_{z_b}^{\eta}\left(u_1\,\frac{\partial \tau_{zx}}{\partial z}\right)dz \qquad (5.4)$$

and (**3**) manipulate the term $\left(m\frac{\partial \eta}{\partial x}\right)$ as follows:

$$\begin{aligned}
m\frac{\partial \eta}{\partial x} \quad &= \quad \frac{\partial}{\partial x}(m\eta) - \eta\overbrace{\frac{\partial m}{\partial x}}^{\text{Use Eq. 4.1}} \\
&= \quad \frac{\partial}{\partial x}(hu\eta) + \eta\frac{\partial h}{\partial t} + p_q q_b \eta = \frac{\partial}{\partial x}(hu\eta) + \eta\left(\frac{\partial \eta}{\partial t} - \overbrace{\frac{\partial z_b}{\partial t}}^{=0}\right) + p_q q_b \eta \\
&\Downarrow \\
m\frac{\partial \eta}{\partial x} \quad &= \quad \frac{1}{2}\frac{\partial \eta^2}{\partial t} + \frac{\partial}{\partial x}(hu\eta) + p_q q_b \eta \qquad (5.5)
\end{aligned}$$

Substituting Eqs. 5.3, 5.4, and 5.5 into Eq. 5.2 yields

$$\frac{\partial}{\partial t}\left(\frac{1}{2}C_m h u^2 + \frac{1}{2}\eta^2\right) + \frac{\partial}{\partial x}\left(\frac{1}{2}C_e h u^3 + hu\eta\right) = -D - p_q q_b\left(\frac{1}{2}u_b^2 + \eta\right) \qquad (5.6)$$

In addition to the rate of dissipation, D, given by Eq. 5.4, the following energy quantities for the flow in Region 1 are introduced:

$$E = \begin{cases} \frac{1}{2}\left(C_m h u^2 + \eta^2\right) & \text{for } z_b \leq 0 \\ \frac{1}{2}\left(C_m h u^2 + \eta^2 - z_b^2\right) & \text{for } z_b > 0 \end{cases} \tag{5.7}$$

$$F = hu\left(\frac{1}{2}C_e u^2 + \eta\right) \tag{5.8}$$

$$D_p^{[2]} = p_q q_b\left(\frac{1}{2}u_b^2 + \eta\right) \qquad 0 \leq x \leq x_s \tag{5.9}$$

where

E = normalized specific energy, defined as the sum of kinetic and potential energy per unit horizontal area, of the flow in Region 1

F = normalized horizontal energy flux per unit width of the flow in Region 1

$D_p^{[2]}$ = normalized vertical energy flux per unit horizontal area from Region 1 to Region 2

It is noted that in the definition of the normalized specific energy E in Eq. 5.7, the datum for the potential energy is taken to be SWL except for the region above SWL where the water exists only in the range $z_b \leq z \leq \eta$.

Utilizing the definition of the energy quantities in Eqs. 5.7 through 5.9, Eq. 5.6 can concisely be rewritten as

$$\frac{\partial E}{\partial t} + \frac{\partial F}{\partial x} = -D - D_p^{[2]} \tag{5.10}$$

Eq. 5.10 expresses the instantaneous wave energy balance in Region 1. The assumption of $C_m \simeq 1$ has already been made in Eq. 3.24. The following assumption is now made:

$$C_e \simeq 1 \tag{5.11}$$

Kobayashi and Wurjanto (1992) indicated that the assumption $C_e \simeq 1$ might cause errors on the order of 30%. This 30% estimate was made in line with the approximation of the momentum correction coefficient $C_m \simeq 1$ in Section 3.2 where the vertical distribution of the horizontal fluid velocity proposed by Svendsen and Madsen (1984) was used to

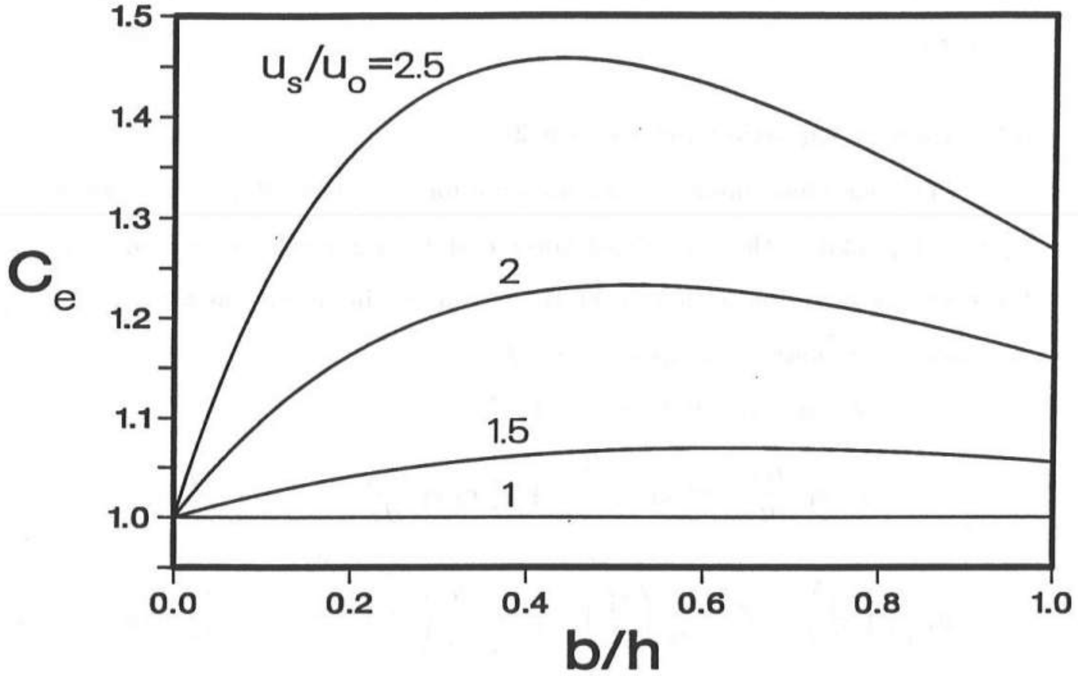

Figure 5.1: Energy correction coefficient C_e computed as a function of b/h and u_s/u_o for vertical distribution of horizontal fluid velocity u_1 assumed by Svendsen and Madsen (1984).

compute C_m as a function of b/h and u_s/u_o (see Figure 3.2 and the related explanation in Section 3.2). Using the same velocity profile, the energy correction coefficient C_e was also computed as a function of b/h and u_s/u_o as plotted in Figure 5.1. The tentative estimate of ○ (10%) errors resulted from the assumption $C_m \simeq 1$ roughly corresponded to ○ (30%) errors as a result of the assumption $C_e \simeq 1$. The assumption $C_e \simeq 1$ is made herein despite of the associated large errors so as to estimate the energy balance in the flow field at least qualitatively. It should be stated that the computed flow fields using the continuity and momentum equations are not affected by this approximation $C_e \simeq 1$.

With the assumptions $C_m \simeq 1$ and $C_e \simeq 1$ now in place, the specific energy E, the horizontal energy flux F, and the vertical energy flux $D_p^{[2]}$ can be computed for the flow field determined by the one-dimensional continuity and momentum equations. The rate of energy dissipation, D, may then be estimated approximately using Eq. 5.10. Eq. 5.10

will be time-averaged at the end of this chapter along with the energy balance equations for Regions 2 and 3.

5.2 Energy Equation for Region 2

The one-dimensional energy equation for the flow in Region 2 is obtained by multiplying Eq. 3.26 by the normalized horizontal discharge velocity v_1 and then integrating the resulting equation with respect to z from the impermeable bottom $z = z_p$ to the interface $z = z_b$ between Regions 1 and 2.

Multiplying Eq. 3.26 by v_1 yields

$$
\begin{aligned}
p_u\, v_1 \frac{\partial v_1}{\partial t} + p_u^2\, v_1\, v_1 \frac{\partial v_1}{\partial x} + p_u^2\, v_2\, v_1 \frac{\partial v_1}{\partial z} &= -v_1 \frac{\partial \eta}{\partial x} - (\mu + |v_1|)\, v_1^2 \\
&\Downarrow \\
p_u \frac{\partial}{\partial t}\left(\frac{v_1^2}{2}\right) + p_u^2\, v_1 \frac{\partial}{\partial x}\left(\frac{v_1^2}{2}\right) + p_u^2\, v_2 \frac{\partial}{\partial z}\left(\frac{v_1^2}{2}\right) &= -v_1 \frac{\partial \eta}{\partial x} - (\mu + |v_1|)\, v_1^2 \\
&\Downarrow \\
p_u \frac{\partial}{\partial t}\left(\frac{v_1^2}{2}\right) + p_u^2 \frac{\partial}{\partial x}\left(\frac{v_1^3}{2}\right) - p_u^2 \frac{v_1^2}{2} \frac{\partial v_1}{\partial x} &+ \\
p_u^2 \frac{\partial}{\partial z}\left(\frac{v_1^2 v_2}{2}\right) - p_u^2 \frac{v_1^2}{2} \frac{\partial v_2}{\partial z} &= -v_1 \frac{\partial \eta}{\partial x} - (\mu + |v_1|)\, v_1^2 \\
&\Downarrow \\
p_u \frac{\partial}{\partial t}\left(\frac{v_1^2}{2}\right) + p_u^2 \frac{\partial}{\partial x}\left(\frac{v_1^3}{2}\right) + p_u^2 \frac{\partial}{\partial z}\left(\frac{v_1^2 v_2}{2}\right) &- \\
p_u^2 \frac{v_1^2}{2} \overbrace{\left(\frac{\partial v_1}{\partial x} + \frac{\partial v_2}{\partial z}\right)}^{=0 \text{ by Eq. 2.27}} &= -v_1 \frac{\partial \eta}{\partial x} - (\mu + |v_1|)\, v_1^2 \\
&\Downarrow \\
p_u \frac{\partial}{\partial t}\left(\frac{v_1^2}{2}\right) + p_u^2 \frac{\partial}{\partial x}\left(\frac{v_1^3}{2}\right) + p_u^2 \frac{\partial}{\partial z}\left(\frac{v_1^2 v_2}{2}\right) &= -v_1 \frac{\partial \eta}{\partial x} - (\mu + |v_1|)\, v_1^2 \qquad (5.12)
\end{aligned}
$$

As a preparation for integration of Eq. 5.12 with respect to z from $z = z_p$ to $z = z_b$, the following approximations are made to be consistent with the approximation $C_e \simeq 1$ in Eq. 5.11:

$$\left.\begin{aligned} &\frac{1}{h_p}\int_{z_p}^{z_b}\left(\frac{v_1}{u_p}\right)^3 dz \simeq 1 \qquad \text{for} \quad 0 \le x \le x_s \\ &\frac{1}{h_p}\int_{z_p}^{\eta}\left(\frac{v_1}{u_p}\right)^3 dz \simeq 1 \qquad \text{for} \quad x_s \le x \le x_w \end{aligned}\right\} \tag{5.13}$$

$$\left.\begin{aligned} &\frac{1}{h_p}\int_{z_p}^{z_b}\left(\frac{|v_1|\, v_1^2}{|u_p|\, u_p^2}\right) dz \simeq 1 \qquad \text{for} \quad 0 \le x \le x_s \\ &\frac{1}{h_p}\int_{z_p}^{\eta}\left(\frac{|v_1|\, v_1^2}{|u_p|\, u_p^2}\right) dz \simeq 1 \qquad \text{for} \quad x_s \le x \le x_w \end{aligned}\right\} \tag{5.14}$$

where the approximations for $x_s \le x \le x_w$ will later be used for Region 3. In addition, the following algebraic manipulation will be utilized:

$$\begin{aligned} \frac{m_p}{p_u}\frac{\partial \eta}{\partial x} &= \frac{1}{p_u}\frac{\partial}{\partial x}(m_p \eta) - \frac{1}{p_u}\eta \overbrace{\frac{\partial m_p}{\partial x}}^{\text{Use Eq. 4.3}} = \frac{1}{p_u}\frac{\partial}{\partial x}(p_u u_p h_p \eta) - \frac{1}{p_u}\eta p_u q_b \\ &\Downarrow \\ \frac{m_p}{p_u}\frac{\partial \eta}{\partial x} &= \frac{\partial}{\partial x}(u_p h_p \eta) - q_b \eta \end{aligned} \tag{5.15}$$

The approximations expressed in Eqs. 5.13 and 5.14, and the relation given by Eq. 5.15 are utilized in the following integration of Eq. 5.12 with respect to z from $z = z_p$ to $z = z_b$:

$$\begin{aligned} p_u \int_{z_p}^{z_b} \frac{\partial}{\partial t}\left(\frac{v_1^2}{2}\right) dz + p_u^2 \int_{z_p}^{z_b} \frac{\partial}{\partial x}\left(\frac{v_1^3}{2}\right) dz \; &+ \; p_u^2 \int_{z_p}^{z_b} \frac{\partial}{\partial z}\left(\frac{v_1^2 v_2}{2}\right) dz \\ = -\int_{z_p}^{z_b}\left(v_1 \frac{\partial \eta}{\partial x}\right) dz \; &- \; \mu \overbrace{\int_{z_p}^{z_b} v_1^2 dz}^{\text{Use Eq. 3.37}} - \overbrace{\int_{z_p}^{z_b} |v_1|\, v_1^2 dz}^{\text{Use Eq. 5.14}} \\ \text{Leibniz rule is used} \; \Downarrow \end{aligned}$$

$$\Downarrow$$

$$\begin{aligned}
p_u \frac{\partial}{\partial t} \overbrace{\int_{z_p}^{z_b} \frac{v_1^2}{2} dz}^{\text{Use Eq. 3.37}} -\frac{1}{2} p_u \left[v_1^2\right]_{z=z_b} \overbrace{\frac{\partial z_b}{\partial t}}^{=0} &+ \frac{1}{2} p_u \left[v_1^2\right]_{z=z_p} \overbrace{\frac{\partial z_p}{\partial t}}^{=0} \\
+p_u^2 \frac{\partial}{\partial x} \overbrace{\int_{z_p}^{z_b} \frac{v_1^3}{2} dz}^{\text{Use Eq. 5.13}} -\frac{1}{2} p_u^2 \left[v_1^3\right]_{z=z_b} \frac{dz_b}{dx} &+ \frac{1}{2} p_u^2 \left[v_1^3\right]_{z=z_p} \frac{dz_p}{dx} \\
+\frac{1}{2} p_u^2 \left[v_1^2 v_2\right]_{z=z_b} - \frac{1}{2} p_u^2 \left[v_1^2 v_2\right]_{z=z_p} &= -\frac{\partial \eta}{\partial x} \overbrace{\int_{z_p}^{z_b} v_1 dz}^{\text{Use Eq. 3.32}} \\
&\quad -\mu u_p^2 h_p - \left|u_p\right| u_p^2 h_p
\end{aligned}$$

$$\Downarrow$$

$$\begin{aligned}
\frac{\partial}{\partial t}\left(\frac{1}{2} p_u u_p^2 h_p\right) + \frac{\partial}{\partial x}\left(\frac{1}{2} p_u^2 u_p^3 h_p\right) &- \frac{1}{2} \overbrace{\left[p_u^2 v_1^2\right]_{z=z_b}}^{\substack{\text{Replace} \\ \text{by } u_b^2}} \overbrace{\left[v_1 \frac{dz_b}{dx} - v_2\right]_{z=z_b}}^{\text{Apply Eq. 3.28 here}} \\
+\frac{1}{2} p_u^2 \overbrace{\left[v_1^2 \left(v_1 \frac{dz_p}{dx} - v_2\right)\right]_{z=z_p}}^{\text{Apply Eq. 3.30 here}} &= - \overbrace{\frac{m_p}{p_u} \frac{\partial \eta}{\partial x}}^{\text{Use Eq. 5.15}} - \left(\mu + \left|u_p\right|\right) u_p^2 h_p
\end{aligned}$$

$$\text{Multiply by } p_q = n_p p_u \quad \Downarrow$$

$$\begin{aligned}
\frac{\partial}{\partial t}\left(\frac{1}{2} n_p p_u^2 u_p^2 h_p\right) + \frac{\partial}{\partial x}\left(\frac{1}{2} p_q p_u^2 u_p^3 h_p\right) &= \frac{1}{2} p_q q_b u_b^2 - p_q \frac{\partial}{\partial x}\left(u_p h_p \eta\right) \\
&+ p_q q_b \eta - p_q \left(\mu + \left|u_p\right|\right) u_p^2 h_p
\end{aligned}$$

$$\Downarrow$$

$$\begin{aligned}
\frac{\partial}{\partial t}\left(\frac{1}{2} n_p p_u^2 u_p^2 h_p\right) + \frac{\partial}{\partial x}\left[p_q u_p h_p \left(\frac{1}{2} p_u^2 u_p^2 + \eta\right)\right] &= p_q q_b \left(\frac{1}{2} u_b^2 + \eta\right) \\
&- p_q \left(\mu + \left|u_p\right|\right) u_p^2 h_p \qquad (5.16)
\end{aligned}$$

The following energy quantities for the flow in Region 2 are introduced:

$$E_p^{[2]} = \begin{cases} \frac{1}{2} n_p p_u^2 u_p^2 h_p & \text{for } z_b \leq 0, \ 0 \leq x \leq x_s \\ \frac{1}{2} n_p \left(p_u^2 u_p^2 h_p + z_b^2\right) & \text{for } z_b > 0, \ 0 \leq x \leq x_s \end{cases} \qquad (5.17)$$

$$F_p = p_q u_p h_p \left(\frac{1}{2} p_u^2 u_p^2 + \eta \right) \tag{5.18}$$

$$D_r = p_q \left(|u_p| + \mu \right) u_p^2 h_p \tag{5.19}$$

where

$E_p^{[2]}$ = normalized specific energy of the flow inside the permeable underlayer in Region 2 where the potential energy is taken relative to SWL

F_p = normalized horizontal energy flux per unit width of the flow inside the permeable underlayer

D_r = normalized rate of energy dissipation per unit horizontal area due to the laminar and turbulent flow resistance

It is noted that the definition of the normalized specific energy $E_p^{[2]}$ given by Eq. 5.17 is valid only for Region 2, whereas the definitions of the normalized energy flux F_p and the normalized energy dissipation rate D_r given by Eqs. 5.18 and 5.19 will be shown to be valid for Region 3 as well as Region 2. Utilizing the definitions of the energy quantities in Eqs. 5.9, 5.17, 5.18, and 5.19, Eq. 5.16 can now be rewritten as

$$\frac{\partial E_p^{[2]}}{\partial t} + \frac{\partial F_p}{\partial x} = D_p^{[2]} - D_r \quad \text{for Region 2} \tag{5.20}$$

All the four terms in Eq. 5.20 can be computed for the flow fields determined by the continuity and momentum equations. Hence, Eq. 5.20 may be used to check the energy balance computed by the numerical model PBREAK. The time-averaged form of Eq. 5.20 will be derived at the end of this chapter.

5.3 Energy Equation for Region 3

The procedure in deriving the one-dimensional energy equation for the flow in Region 3 is identical to that for the flow in Region 2 except that

1. the upper limit of the integration is the water table at $z = \eta$, and
2. the boundary condition at the water table $z = \eta$ is given by Eq. 3.40.

The following relation will be needed in the derivation of the energy equation for the flow in Region 3:

$$\begin{aligned}
\frac{m_p}{p_u}\frac{\partial \eta}{\partial x} &= \frac{1}{p_u}\frac{\partial}{\partial x}(m_p\eta) - \frac{1}{p_u}\eta \overbrace{\frac{\partial m_p}{\partial x}}^{\text{Use Eq. 4.5}} = \frac{1}{p_u}\frac{\partial}{\partial x}(p_u u_p h_p \eta) + \frac{1}{p_u}\eta\frac{\partial \eta}{\partial t} \\
&\Downarrow \\
\frac{m_p}{p_u}\frac{\partial \eta}{\partial x} &= \frac{\partial}{\partial x}(u_p h_p \eta) + \frac{1}{2p_u}\frac{\partial \eta^2}{\partial t} \qquad (5.21)
\end{aligned}$$

The energy equation for the flow in Region 3 is derived by integrating Eq. 5.12 from $z = z_p$ to $z = \eta$.

$$\begin{aligned}
p_u \int_{z_p}^{\eta} \frac{\partial}{\partial t}\left(\frac{v_1^2}{2}\right) dz + p_u^2 \int_{z_p}^{\eta} \frac{\partial}{\partial x}\left(\frac{v_1^3}{2}\right) dz \;&+\; p_u^2 \int_{z_p}^{\eta} \frac{\partial}{\partial z}\left(\frac{v_1^2 v_2}{2}\right) dz \\
= -\int_{z_p}^{\eta}\left(v_1 \frac{\partial \eta}{\partial x}\right) dz \;&-\; \mu \overbrace{\int_{z_p}^{\eta} v_1^2 dz}^{\text{Use Eq. 3.37}} - \overbrace{\int_{z_p}^{\eta} |v_1|\, v_1^2 dz}^{\text{Use Eq. 5.14}}
\end{aligned}$$

$$\text{Leibniz rule is used} \quad \Downarrow$$

$$\begin{aligned}
& p_u \frac{\partial}{\partial t} \overbrace{\int_{z_p}^{\eta} \frac{v_1^2}{2} dz}^{\text{Use Eq. 3.37}} - \frac{1}{2} p_u \left[v_1^2\right]_{z=\eta} \frac{\partial \eta}{\partial t} + \frac{1}{2} p_u \left[v_1^2\right]_{z=z_p} \overbrace{\frac{\partial z_p}{\partial t}}^{=0} \\
& + p_u^2 \frac{\partial}{\partial x} \overbrace{\int_{z_p}^{\eta} \frac{v_1^3}{2} dz}^{\text{Use Eq. 5.13}} - \frac{1}{2} p_u^2 \left[v_1^3\right]_{z=\eta} \frac{\partial \eta}{\partial x} + \frac{1}{2} p_u^2 \left[v_1^3\right]_{z=z_p} \frac{d z_p}{dx} \\
& + \frac{1}{2} p_u^2 \left[v_1^2 v_2\right]_{z=\eta} - \frac{1}{2} p_u^2 \left[v_1^2 v_2\right]_{z=z_p} = -\frac{\partial \eta}{\partial x} \overbrace{\int_{z_p}^{\eta} v_1 dz}^{\text{Use Eq. 3.32}} - \mu u_p^2 h_p - |u_p|\, u_p^2 h_p
\end{aligned}$$

$$\Downarrow$$

$$\Downarrow$$

$$\begin{aligned}\frac{\partial}{\partial t}\left(\frac{1}{2}p_u u_p^2 h_p\right)+\frac{\partial}{\partial x}\left(\frac{1}{2}p_u^2 u_p^3 h_p\right) &- \frac{1}{2}p_u \overbrace{\left[v_1^2\left(\frac{\partial \eta}{\partial t}+p_u v_1\frac{\partial \eta}{\partial x}-p_u v_2\right)\right]_{z=\eta}}^{\text{Apply Eq. 3.40 here}} \\ +\frac{1}{2}p_u^2 \overbrace{\left[v_1^2\left(v_1\frac{dz_p}{dx}-v_2\right)\right]_{z=z_p}}^{\text{Apply Eq. 3.30 here}} &= - \overbrace{\frac{m_p}{p_u}\frac{\partial \eta}{\partial x}}^{\text{Use Eq. 5.21}} - (\mu+|u_p|)\, u_p^2 h_p\end{aligned}$$

$$\text{Multiply by } p_q = n_p p_u \quad \Downarrow$$

$$\begin{aligned}\frac{\partial}{\partial t}\left(\frac{1}{2}n_p p_u^2 u_p^2 h_p\right)+\frac{\partial}{\partial x}\left(\frac{1}{2}p_q p_u^2 u_p^3 h_p\right) &= - p_q\frac{\partial}{\partial x}(u_p h_p \eta)-\frac{1}{2}\frac{p_q}{p_u}\frac{\partial \eta^2}{\partial t} \\ &\quad - p_q(\mu+|u_p|)\, u_p^2 h_p\end{aligned}$$

$$\Downarrow$$

$$\frac{\partial}{\partial t}\left[\frac{1}{2}n_p\left(p_u^2 u_p^2 h_p+\eta^2\right)\right]+\frac{\partial}{\partial x}\left[p_q u_p h_p\left(\frac{1}{2}p_u^2 u_p^2+\eta\right)\right] = - p_q(\mu+|u_p|)\, u_p^2 h_p \tag{5.22}$$

The normalized specific energy $E_p^{[3]}$ for Region 3 is defined as follows:

$$E_p^{[3]} = \begin{cases} \frac{1}{2}n_p\left(p_u^2 u_p^2 h_p+\eta^2\right) & \text{for } z_p \le 0,\ x_s \le x \le x_w \\ \frac{1}{2}n_p\left(p_u^2 u_p^2 h_p+\eta^2-z_p^2\right) & \text{for } z_p > 0,\ x_s \le x \le x_w \end{cases} \tag{5.23}$$

where the datum for the potential energy is taken to be SWL except for the region above SWL where the water exists only in the range $z_p \le z \le \eta$.

Utilizing the definitions of the energy quantities in Eqs. 5.18, 5.19, and 5.23, Eq. 5.22 can now be rewritten as

$$\frac{\partial E_p^{[3]}}{\partial t}+\frac{\partial F_p}{\partial x} = -D_r \quad \text{for Region 3} \tag{5.24}$$

5.4 Time-Averaged Energy Equations

The numerical model PBREAK computes many time-averaged quantities for various purposes. It is hence imperative to clarify the definition of time average used in the model. The time average denoted by an overbar is defined as follows:

$$\overline{V} = \frac{1}{t_{max} - t_{min}} \int_{t_{min}}^{t_{max}} V(t)dt \tag{5.25}$$

where

V = computed time-varying quantity at given location x

t_{min} = normalized time when the time averaging begins

t_{max} = normalized time when the time averaging ends

It is noted that t_{max} also denotes the computation duration starting from $t = 0$.

Since the waterlines x_s and x_w are moving, Regions 2 and 3 are not fixed domains, and the time averaging of the energy equations for Regions 2 and 3 is hard to perform separately. As a result, the energy equations for Regions 2 and 3, Eqs. 5.20 and 5.24, are unified as follows:

$$\frac{\partial E_p}{\partial t} + \frac{\partial F_p}{\partial x} = D_p - D_r \quad \text{for Regions 2 and 3} \tag{5.26}$$

where F_p and D_r are given by Eqs. 5.18 and Eq. 5.19, and

$$E_p = \begin{cases} E_p^{[2]} & \text{for Region 2 } (0 \le x \le x_s) \\ E_p^{[3]} & \text{for Region 3 } (x_s \le x \le x_w) \end{cases} \tag{5.27}$$

$$D_p = \begin{cases} D_p^{[2]} & \text{for Region 2 } (0 \le x \le x_s) \\ 0 & \text{for Region 3 } (x_s \le x \le x_w) \end{cases} \tag{5.28}$$

where $E_p^{[2]}$, $E_p^{[3]}$, and $D_p^{[2]}$ are given by Eqs. 5.17, 5.23, and 5.9, respectively.

The new definition of the normalized vertical energy flux given by Eq. 5.28 is also adopted for the energy equation for Region 1, and Eq. 5.10 is rewritten as

$$\frac{\partial E}{\partial t} + \frac{\partial F}{\partial x} = -D - D_p \qquad \text{for Region 1} \tag{5.29}$$

where E, F, and D_p are given by Eqs. 5.7, 5.8, and 5.28, respectively.

Integrating the finalized energy equations, Eqs. 5.26 and 5.29, from t=t_{min} to t=t_{max} yields the following time-averaged energy equations:

REGION 1:

$$\overline{D} = -\frac{d\overline{F}}{dx} - \overline{D_p} - \frac{E(t_{max}) - E(t_{min})}{t_{max} - t_{min}} \tag{5.30}$$

REGIONS 2 AND 3:

$$\frac{d\overline{F_p}}{dx} + \overline{D_r} - \overline{D_p} + \frac{E_p(t_{max}) - E_p(t_{min})}{t_{max} - t_{min}} = 0 \tag{5.31}$$

In the numerical model PBREAK, Eq. 5.30 is used to estimate the normalized time-averaged rate $\overline{D}$ of energy dissipation per unit horizontal area for the flow in Region 1.

For random waves, the computation duration is typically long and $(t_{max} - t_{min})$ is much greater than unity. The last term on the left hand side of Eq. 5.31 is then negligible. For such cases, Eqs. 5.31 may be reduced to

$$\frac{d\overline{F_p}}{dx} + \overline{D_r} - \overline{D_p} = 0 \qquad \text{for Regions 2 and 3 when } (t_{max} - t_{min}) \gg 1 \tag{5.32}$$

which is used herein to check the energy balance for the flow in Regions 2 and 3.

Chapter 6

COMPARISON BETWEEN NUMERICAL MODEL AND EXPERIMENT

6.1 Experiment on Irregular Wave Run-up and Reflection

Six test runs for irregular wave reflection and run-up on rough impermeable and permeable slopes were conducted by Cox (1989). The tests were performed in a wave tank whose dimension was 30m long, 2.5m wide, and 1.5m high. The water depth in the tank was d_t'=0.40m. The rough impermeable slope consisted of a 1:3 plywood slope with a single layer of glued gravel installed at a distance of 25m from the wave paddle. The rough permeable slope was constructed by placing a thick layer of loose gravel on top of the 1:3 glued gravel slope. The median diameter of the gravel was d_p'=0.021m. The thickness of the entire gravel layer perpendicular to the impermeable base was 0.2m. The impermeable and permeable slopes were exposed to three different incident irregular waves. For each of the six runs, measurements were made of the incident and reflected waves in front of the slope and the waterline oscillations on the slope. The three test runs for the rough impermeable slope were used by Kobayashi, Cox, and Wurjanto (1990) to evaluate the numerical model RBREAK for impermeable slopes developed by Wurjanto and Kobayashi (1991). The six test runs for the impermeable and permeable slopes were compared by Kobayashi, Cox, and Wurjanto (1991) to examine the permeability effect on irregular wave run-up and reflection. The experimental procedures were already explained in these papers.

This chapter presents and discusses comparison between the numerical model PBREAK with the three test runs for the permeable slope, which are denoted by Runs P1, P2, and P3. In addition, attempts are made to interpret the computed results and gain an insight into the physical processes associated with irregular wave interactions with permeable slopes. Both time series and spectral analyses are employed using the standard subroutines provided by Cox, Kobayashi, and Wurjanto (1991).

The experiment conducted by Cox (1989) may contain errors on the order of 5% on the basis of instrument calibrations and repeated test runs. The experiment is definitely more accurate than the present numerical model with expected errors of 10% or greater because of the assumptions of $C_m \simeq 1$ as well as $(\cot\theta')^2 \gg 1$ made in Eqs. 3.24 and 2.8, respectively.

6.2 Summary of Input to Numerical Model

The 0.2m thick loose gravel layer is separated into the primary cover layer and the permeable underlayer. The top single layer whose thickness equals to d_p'=0.021m is assumed to be the primary cover layer determining the bottom friction factor f' used in Eq. 3.19 since the value of f' has been calibrated for the 1:3 slope with the single layer of glued gravel by Kobayashi and Greenwald (1988). The remaining 0.179m thick gravel layer is considered to be the permeable underlayer. The seaward boundary x'=0 for the numerical model is taken to be located at the intersection between the upper boundary of the permeable underlayer and the horizontal bottom of the wave tank. The upper and lower boundaries of the permeable underlayer, denoted by $z_b'(x')$ and $z_p'(x')$, respectively, are then given by

$$z_b' = -d_t' + x'\tan\theta' \qquad \text{for } x' \geq 0 \tag{6.1}$$

$$z_p' = \begin{cases} -d_t' & \text{for } 0 \leq x' \leq 0.566\text{m} \\ -d_t' + (x' - 0.566\text{m})\tan\theta' & \text{for } x' \geq 0.566\text{m} \end{cases} \tag{6.2}$$

with $d_t' = 0.40$m and $\cot\theta' = 3$. Figure 6.1 shows the permeable slope geometry specified as input to the numerical model. The other input data related to the permeable underlayer are:

- Porosity of the permeable underlayer, n_p=0.48.

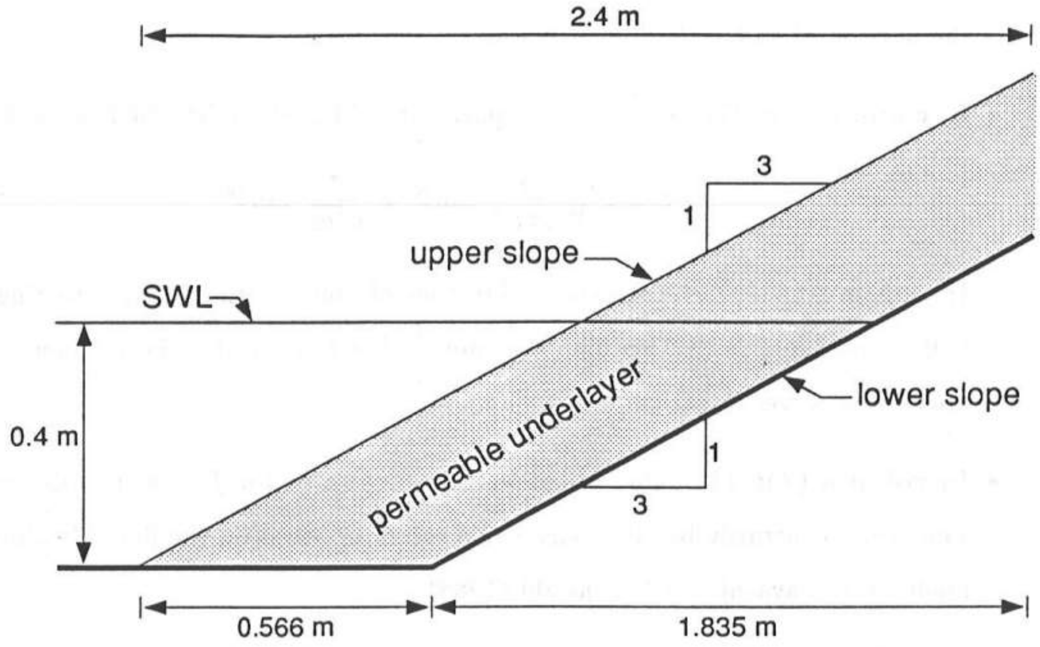

Figure 6.1: Permeable slope geometry specified as input to numerical model.

- Characteristic diameter d'_p used in Eqs. 2.24 and 2.25, which is represented by the median gravel diameter 0.021m.
- Temperature of water, 20°C, which results in kinematic viscosity ν = 1.004x10^{-6} m^2/s for the fresh water used in the experiment.
- Empirical constants α_o and β_o in Eqs. 2.24 and 2.25, which could be calibrated but are simply taken as α_o=1140 and β_o=2.7. These are the median values of the ranges suggested by Madsen and White (1976).

The characteristic wave height H' and period T' used for the normalization of the governing equations are taken to be the significant wave height H'_s and the mean period T'_m of the measured incident wave train for each run. The zero-upcrossing method is used to separate the wave train into individual waves. The values of $H' = H'_s$ and $T' = T'_m$ for each of the three runs are listed in Table 6.1 along with the following:

- **In column (4):** The parameter σ defined in Eq. 2.4 expressing the ratio between the horizontal and vertical length scales.

- **In column (5):** The surf similarity parameter ξ based on H' and T' and given by

$$\xi = T'\sqrt{\frac{g}{2\pi H'}}\ \tan\theta' = \frac{\sigma}{\sqrt{2\pi}}\ \tan\theta' \tag{6.3}$$

- **In column (6):** The normalized duration of computation, t_{max}, starting from t=0 as discussed in Section 5.4. It is noted that t_{max} is also the number of zero-upcrossing waves in each run.

- **In column (7):** The value of the bottom friction factor f', which is determined somewhat arbitrarily but is a reasonable estimate based on the limited calibration made by Kobayashi and Greenwald (1988).

- **In column (8):** The spectral estimate of the normalized significant wave height H_{mo} defined as

$$H_{mo} = 4\sqrt{m_o} \tag{6.4}$$

  where m_o is the zero moment of the normalized incident wave spectrum $S_i(f_*)$ computed from the normalized incident wave train $\eta_i(t)$ with $0 < t \leq t_{max}$ where f_* is the normalized frequency defined as

$$f_* = f'_* T' \tag{6.5}$$

- **In column (9):** The normalized peak period T_p of the incident wave spectrum defined as $T_p = T'_p/T'$

- **In column (10):** The surf similarity parameter ξ_p based on the spectral parameters $H_{mo} = H'_{mo}/H'$ and T_p, and given by

$$\xi_p = T'_p\sqrt{\frac{g}{2\pi H'_{mo}}}\ \tan\theta' = \frac{T_p}{\sqrt{H_{mo}}}\ \xi \tag{6.6}$$

- **In column (11):** The parameter p_u defined by Eq. 2.32 as explained later.

Table 6.1: Three test runs compared with numerical model.

RUN No.	H' [m]	T' [sec]	σ	ξ	t_{max}	f'	H_{mo}	T_p	ξ_p	p_u	μ
(1)	(2)	(3)	(4)	(5)	(6)	(7)	(8)	(9)	(10)	(11)	(12)
P1	.0685	1.082	12.9	1.72	170.98	.05	1.01	1.09	1.88	.090	.074
P2	.0535	1.357	18.4	2.44	268.98	.05	1.03	1.56	3.75	.085	.088
P3	.0457	1.738	25.5	3.39	210.01	.10	1.06	1.58	5.22	.079	.104

- **In column (12):** The parameter μ defined by Eq. 2.29 as explained later.

The value of the parameter σ for the three runs ranges from 12.9 to 25.5. Thus, the required condition of $\sigma^2 \gg 1$ stated in Eq. 2.8 is well satisfied. The other required condition in Eq. 2.8, $(\cot\theta')^2 \gg 1$, is less satisfied for the relatively steep slope $\cot\theta' = 3$. This may cause errors on the order of 10%.

Both parameters p_u and μ are small for these tests. The parameter p_u ranges from 0.079 to 0.090, whereas the parameter μ from 0.074 to 0.104. The small values of the parameter p_u imply that the order of magnitude of the fluid velocity inside the permeable underlayer is small relative to that over the rough slope. The small values of the parameters μ indicate that the laminar flow resistance is small as compared to the turbulent flow resistance inside the permeable underlayer. As a result, scale effects in these small-scale tests should be small.

For the purpose of the computation of the hydraulic stability of armor units to be discussed in Chapter 7, the *armor stability* parameters listed below need to be specified as input to the numerical model. The following values are based on the related work by Kobayashi and Greenwald (1988) and Kobayashi, Cox, and Wurjanto (1991):

- Specific density of the gravel, s_g=2.7.

- Frictional angle of armor units, ϕ=50°.

- Area coefficient, C_2=0.9.

- Volume coefficient, C_3=0.6.
- Drag coefficient, C_D=0.5.
- Lift coefficient, C_L=0.3.
- Inertia coefficient, C_M=1.5.
- Upper limit of the normalized fluid acceleration, a_{max}=1.0.
- Lower limit of the normalized fluid acceleration, a_{min}=−0.8.

Lastly, the numerical model also requires the following *computation* and *experimental* parameters specified as input:

1. Space interval $\Delta x'$ of the finite difference grid where the normalized space interval $\Delta x = \dfrac{\Delta x'}{T'\sqrt{gH'}}$.
2. Largest normalized time step Δt of the finite difference grid based on the numerical stability of the adopted explicit finite difference method as well as the convenience of storing computed time series as discussed in WK 92.
3. Numerical damping coefficients ϵ_1 and ϵ_2 in Eqs. 4.61 and 4.62 for the dissipative Lax-Wendroff scheme discussed in Section 4.3.
4. Largest normalized water depth δ_s used to determine the location x_s of the *upper* computational waterline in the numerical model PBREAK.
5. Largest normalized water depth δ_w used to determine the location x_w of the *lower* computational waterline in the numerical model PBREAK.
6. Normalized time t_{min} in Eq. 5.25 marking the beginning of the time averaging process as discussed in Section 5.4 where use is made of t_{min}=0 corresponding to the beginning of the measurements and computation.
7. Physical water depth δ_r' corresponding to the vertical distance of the waterline meter placed above the upper boundary of the permeable underlayer to measure the waterline oscillations.

Table 6.2: Computation parameters specified as input to numerical model.

RUN No.	$\Delta x'$ [m]	Δx	Largest Δt	ϵ_1	ϵ_2	Largest δ_s	Largest δ_w
(1)	(2)	(3)	(4)	(5)	(6)	(7)	(8)
P1	0.006	0.00676	0.00118	1	1	0.001	0.001–0.002
P2	0.006	0.00610	0.00100	1	1	0.001	0.001–0.002
P3	0.006	0.00516	0.00080	1	1	0.001	0.001

RUN No.	t_{min}	δ'_r [m]	δ'_a [m]
(1)	(9)	(10)	(11)
P1	0	0.0275	0.021
P2	0	0.0275	0.021
P3	0	0.0275	0.021

8. Physical water depth δ'_a marking the landward limit of the armor stability computation where the choice of $\delta'_a = d'_p$ is reasonable since the armor units are assumed to be fully submerged in the numerical model.

The computation for each run may consist of a number of *sequences* as summarized in the following. Whenever a non-remediable numerical problem is encountered, the present sequence is terminated and the user is called to manually specify different computation parameters for the next sequence. This sequential computation along with examples is explained in detail in WK 92. The computation parameters Δt, ϵ_1, ϵ_2, δ_s, and δ_w are adjustable by the user from one sequence to another to overcome various numerical problems. The space interval Δx is fixed during the computation for each run. The experimental parameters t_{min}, δ'_r, and δ'_a are related to the specific experiment conducted by Cox (1989) and have nothing to do with numerical problems. The specified values of the parameters listed above are given in Table 6.2. The number of sequences of the computation was two for Run P1, three for Run P2, and one for Run P3.

6.3 Comparison Between Measured and Computed Reflected Waves

The measured time series of the reflected wave train and waterline oscillation for each of Runs P1, P2, and P3 are available for comparison with the numerical model. Since the performance of a numerical model is judged primarily by the agreement between the measured and computed results, it is imperative to show all the figures depicting the comparison between the numerical model and the measurements for all the three runs. The comparison between the measured and computed reflected waves is presented first in the following.

The free surface elevations at the toe and at two locations seaward of the toe were measured for each test run. The measured free surface elevations were used to separate the incident wave train $\eta_i'(t')$ and the reflected wave train $\eta_r'(t')$ at the toe of the slope. The separated incident and reflected wave trains were termed the measured incident and reflected waves (Kobayashi, Cox, and Wurjanto 1990). The separation procedure based on linear wave theory was judged to be sufficiently accurate since the water depth at the toe of the slope was deep enough to apply the linear theory with some confidence. The normalized incident and reflected wave trains are denoted by $\eta_i(t)$ and $\eta_r(t)$ where the significant wave height, $H' = H_s'$, and the mean period, $T' = T_m'$, are used for the normalization. The normalized incident wave trains for Runs P1, P2, and P3 were plotted in WK 92. The measured and computed reflected wave trains for the three runs are shown in Figures 6.2, 6.3, and 6.4. The numerical model predicts the overall trend of the reflected waves but tends to underestimate the crest heights and trough depths. It is also noted that the reflection from the permeable slope increases with the increase of the surf similarity parameters ξ and ξ_p listed in Table 6.1 for each of the three runs.

Figure 6.5 presents the normalized measured and computed reflected wave spectra $S_r(f_*)$ for the three runs. The normalized incident wave spectra $S_i(f_*)$ are also plotted to show the incident wave energy at given frequency. Since Figure 6.5 is the first spectral plot presented herein, it is appropriate to clarify the present spectral analysis procedures which are outlined as follows:

1. The normalized time duration is $0 < t \leq t_{max}$ where the value of t_{max} for each test

Table 6.3: Effective range of normalized frequency domain.

RUN No.	$(f_*)_{min}$	$(f_*)_{max}$
(1)	(2)	(3)
P1	0.12	1.6
P2	0.15	2.0
P3	0.19	2.6

run is given in Table 6.1.

2. In performing the Fourier transform, the mean of the time series has been removed.
3. The spectral quantities are presented in a smoothed form where a band-averaging method is used with 16 degrees of freedom.
4. The effective range of the frequency resolution as dictated by the spacings of the three wave gages was $0.11\text{Hz} < f'_* < 1.5\text{Hz}$ (Kobayashi, Cox, and Wurjanto 1991), where the measured wave components outside the effective range were negligible. The corresponding normalized range is $(f_*)_{min} < f_* < (f_*)_{max}$ where the values of $(f_*)_{min}$ and $(f_*)_{max}$ are listed in Table 6.3.
5. To be consistent with the frequency resolution limitation, the integration of a spectrum to find its zero moment is performed over the effective frequency range $(f_*)_{min} < f_* < (f_*)_{max}$ only.

Furthermore, to examine the wave reflection by the frequency component, the reflection coefficient $r(f_*)$ may be defined as the square root of the ratio between the reflected and incident wave spectral densities at the normalized frequency f_*:

$$r(f_*) = \sqrt{\frac{S_r(f_*)}{S_i(f_*)}} \tag{6.7}$$

Figures 6.6, 6.7, and 6.8 depict the variations of the measured and computed reflection coefficient r in the frequency domain for Runs P1, P2, and P3, respectively.

Also plotted in these figures are the measured and computed coherence squared γ_{ir}^2 and phase difference θ_{ir} [*e.g.*, Bendat and Piersol (1986)] between the incident and reflected waves. The average reflection coefficient $\overline{r}$ may be defined as

$$\overline{r} = \sqrt{\frac{(m_o)_r}{m_o}} \tag{6.8}$$

where m_o is the zero moment of the normalized incident wave spectrum $S_i(f_*)$ as introduced in relation with Eq. 6.4, and $(m_o)_r$ is the zero moment of the normalized reflected wave spectrum $S_r(f_*)$. The measured and computed values of the average reflection coefficient $\overline{r}$ are listed in columns (2) and (7) in Table 6.4.

The numerical model tends to overestimate the reflection of wave components with longer periods and the dissipation of wave components with shorter periods. The overall characteristics of the waves reflected from the permeable slope are predicted well by the numerical model. The crests and troughs of the time series shown in Figures 6.2–6.4 as well as the reflection coefficient in the high frequency range shown in Figures 6.6–6.8 are not predicted very well probably because of the assumption of long waves made in the numerical model which may not be appropriate for the high frequency wave components at $x = 0$.

The coherence squared between any two time series indicates how the two time series are related. The coherence squared of unity indicates that the two time series are fully correlated. Zero coherence means no correlation whatsoever. Therefore, the coherence squared is a measure of degree of correlation between two processes. On the other hand, the phase difference $\theta_{ir}(f_*)$ may be related to the normalized travel time given by $\left(\frac{-\theta_{ir}}{2\pi f_*}\right)$ for the wave component f_* propagating up-slope from x=0 and then down-slope to x=0 (Kobayashi, Cox, and Wurjanto 1990). The coherence squared and phase difference are used herein, in addition to the time series and power spectral densities, to examine the agreement between the measured and computed results. These quantities turn out to be harder to predict accurately.

The numerical model generally predicts the coherence squared γ_{ir}^2 and the phase

Table 6.4: Measured and computed values of average reflection coefficient $\overline{r}$, wave set-up $\overline{Z_r^U}$, significant swash height h_s^U, significant run-up R_s^U, and maximum run-up R_{max}^U on the upper slope.

RUN No.	MEASURED					COMPUTED				
	$\overline{r}$	$\overline{Z_r^U}$	h_s^U	R_s^U	R_{max}^U	$\overline{r}$	$\overline{Z_r^U}$	h_s^U	R_s^U	R_{max}^U
(1)	(2)	(3)	(4)	(5)	(6)	(7)	(8)	(9)	(10)	(11)
P1	0.120	0.047	1.047	0.668	1.324	0.093	0.061	1.067	0.573	1.006
P2	0.211	0.055	1.578	0.963	1.458	0.154	0.047	1.413	0.781	1.112
P3	0.282	0.051	2.092	1.192	2.280	0.258	0.045	1.746	0.940	1.851

difference θ_{ir} reasonably well for the low and peak frequency components, but unsatisfactorily for the higher frequency components. This may be due to the long wave assumption underlying the numerical model which may not be appropriate for the high frequency wave components at $x = 0$. The examination of Figures 6.5–6.8 indicates that the coherence squared tends to become small in the frequency range where the measured incident and reflected wave components are small and may not be very accurate. It is noted that the measured and computed phase differences θ_{ir} are plotted herein in the range of $-180° \leq \theta_{ir} \leq 180°$. As Kobayashi, Cox, and Wurjanto (1990) pointed out, the agreement would appear better if the normalized travel time $\left(\frac{-\theta_{ir}}{2\pi f_*}\right)$ were plotted, instead of θ_{ir}, as a function of f_* without the restriction of $-180° \leq \theta_{ir} \leq 180°$. It can be seen in Figures 6.6–6.8 that the phase difference θ_{ir} would decrease monotonically with increasing normalized frequency f_* if the restriction of $-180° \leq \theta_{ir} \leq 180°$ were not imposed for the plotting purpose.

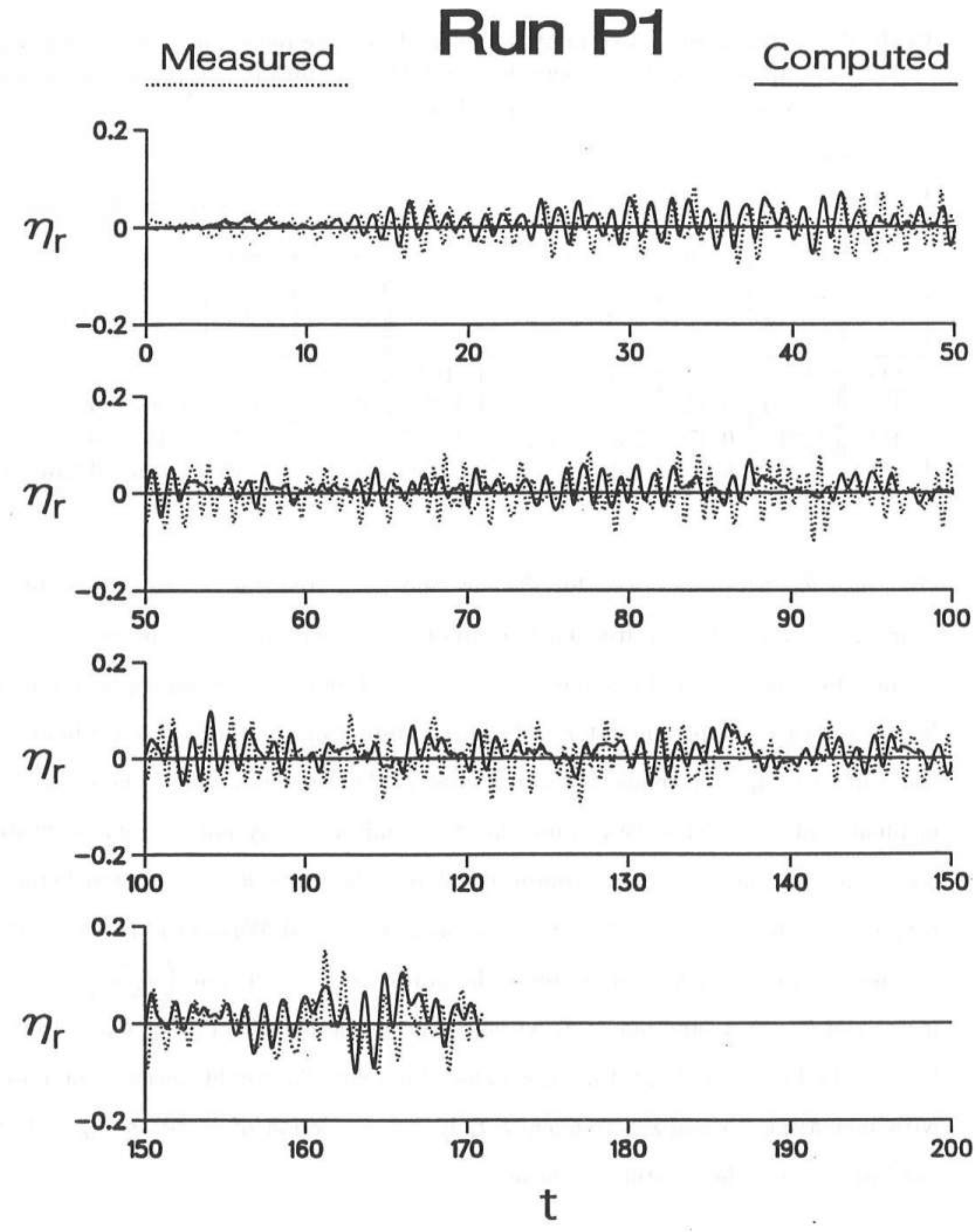

Figure 6.2: Measured and computed reflected wave trains at x=0 for Run P1.

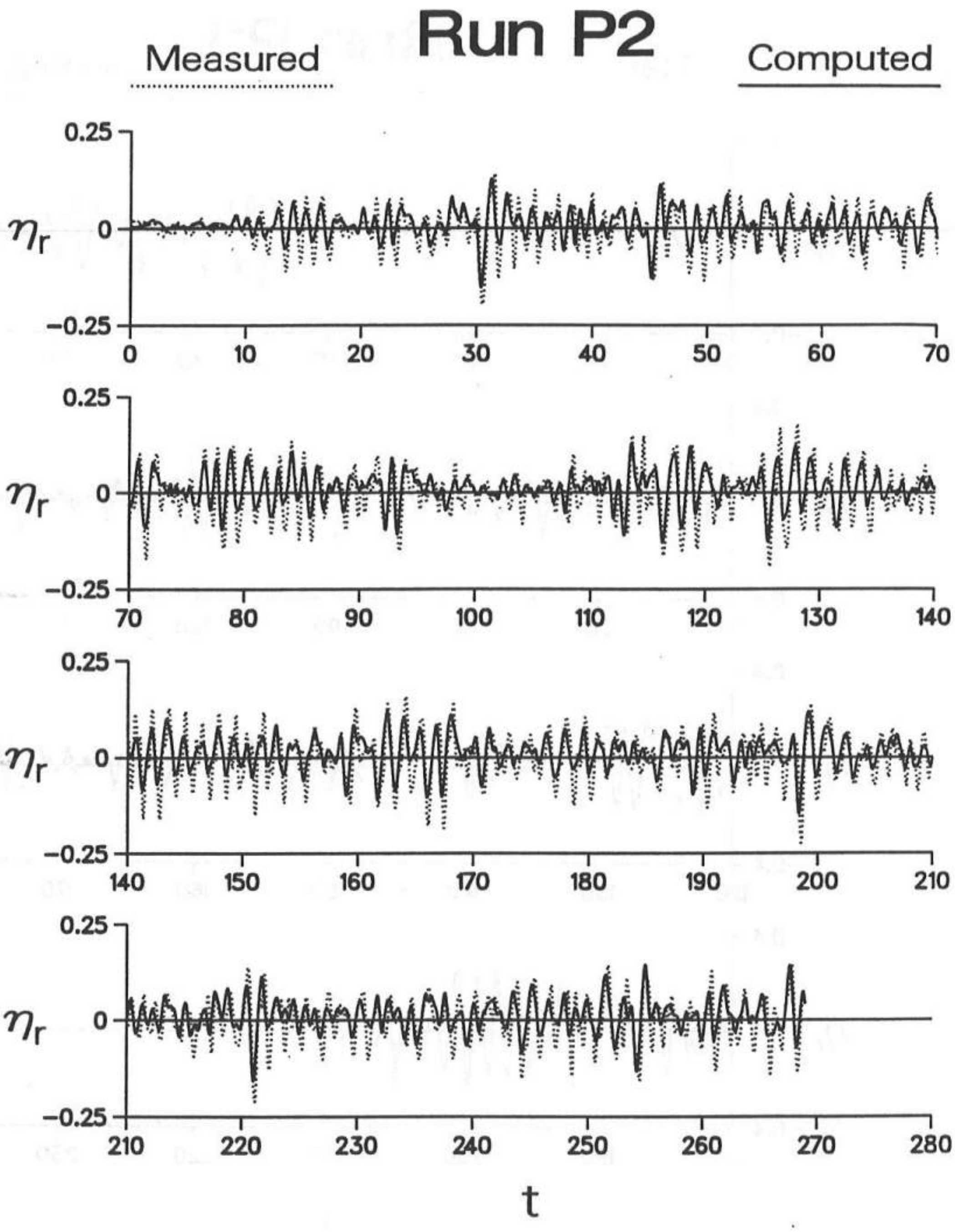

Figure 6.3: Measured and computed reflected wave trains at x=0 for Run P2.

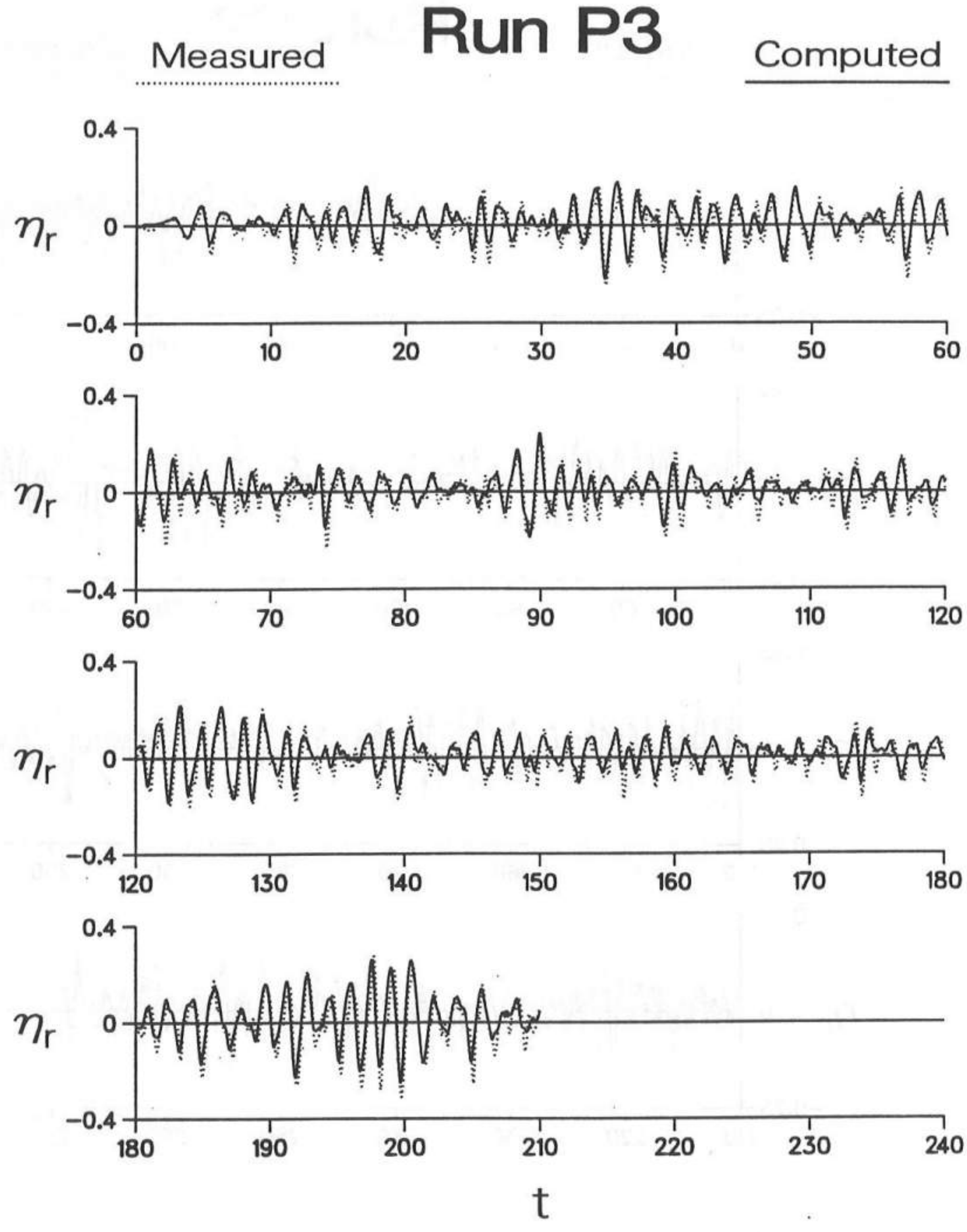

Figure 6.4: Measured and computed reflected wave trains at x=0 for Run P3.

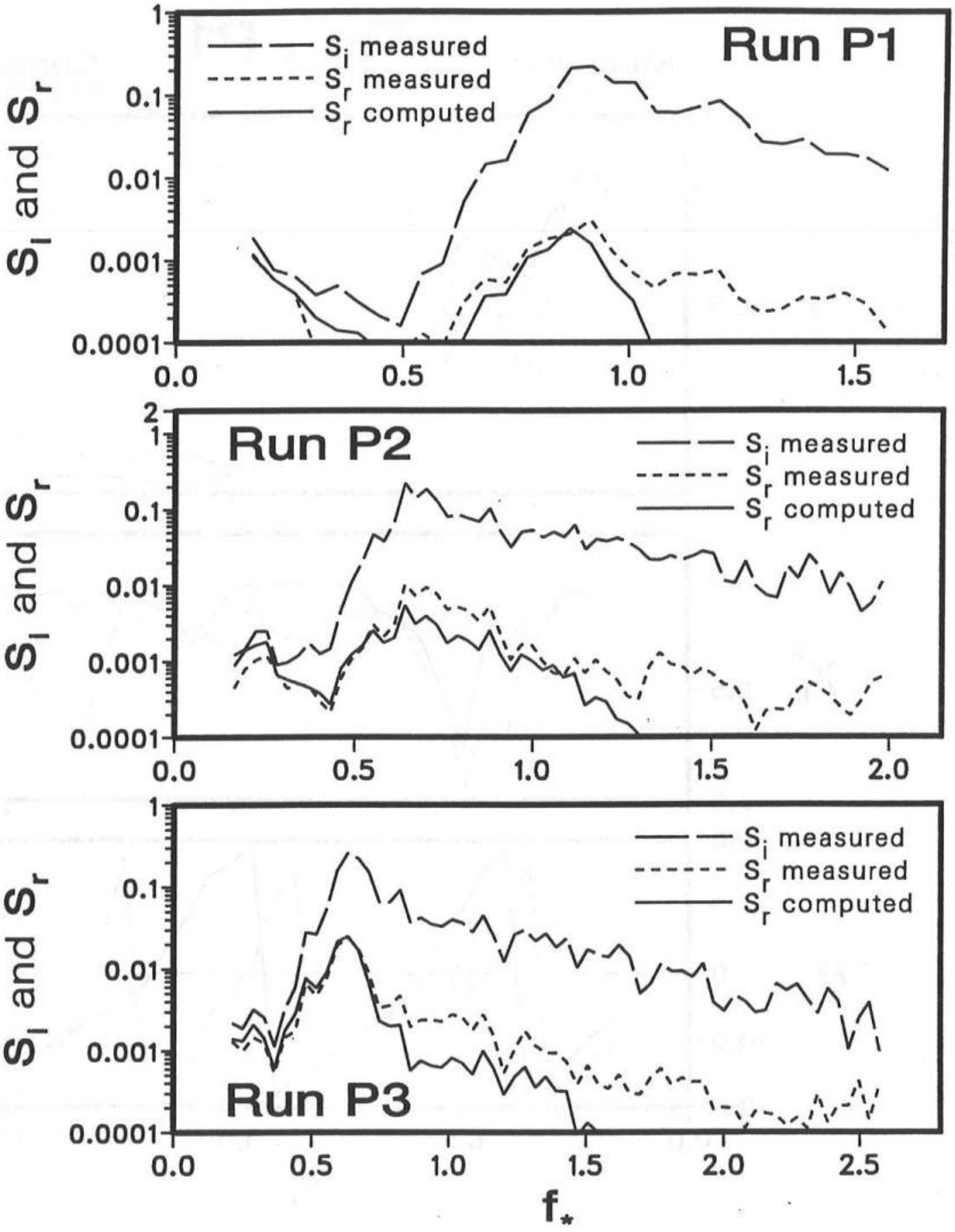

Figure 6.5: Measured and computed reflected wave spectra shown relative to incident wave spectrum at $x=0$ for three runs.

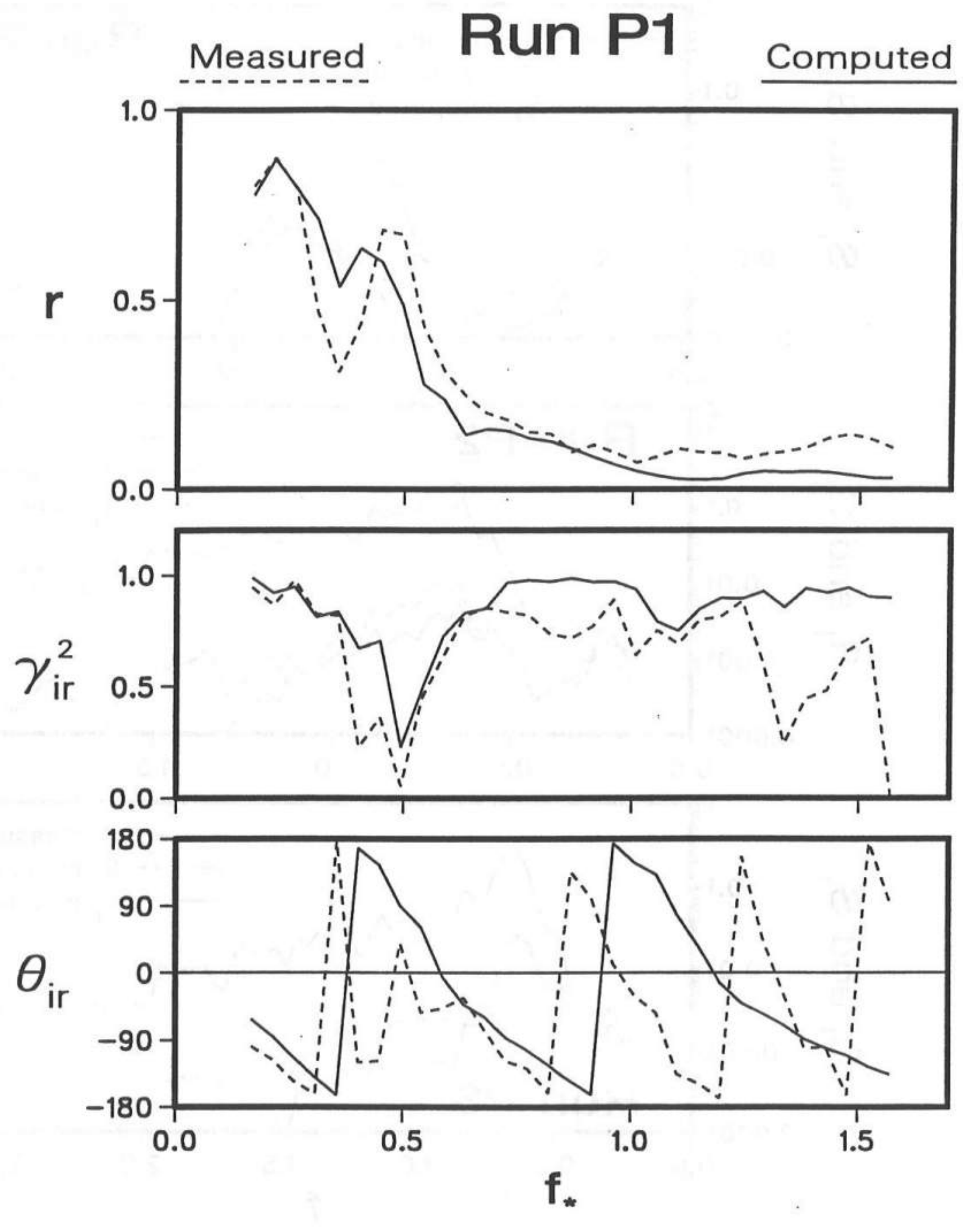

Figure 6.6: Measured and computed reflection coefficient, coherence and phase between incident and reflected waves at x=0 for Run P1.

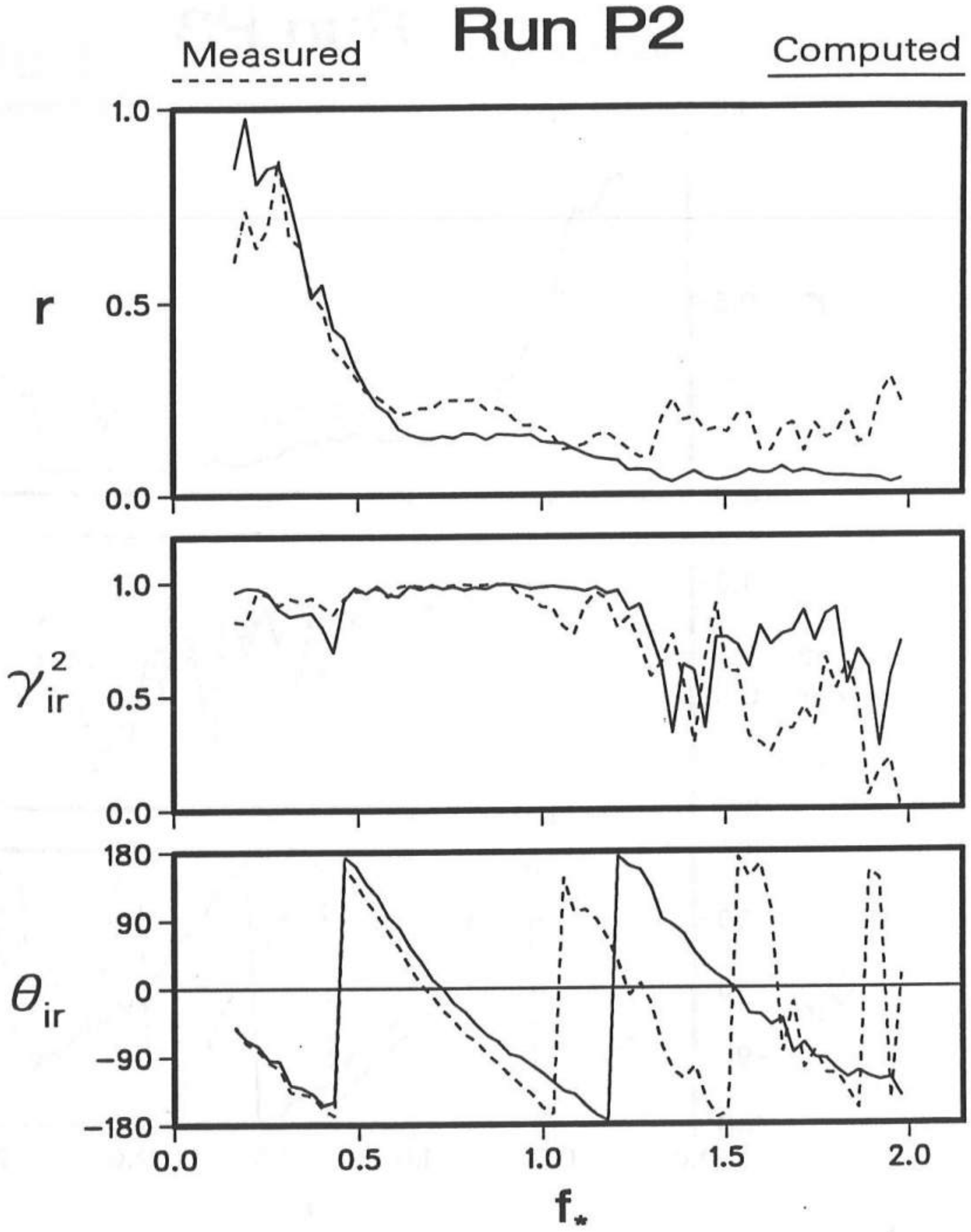

Figure 6.7: Measured and computed reflection coefficient, coherence and phase between incident and reflected waves at x=0 for Run P2.

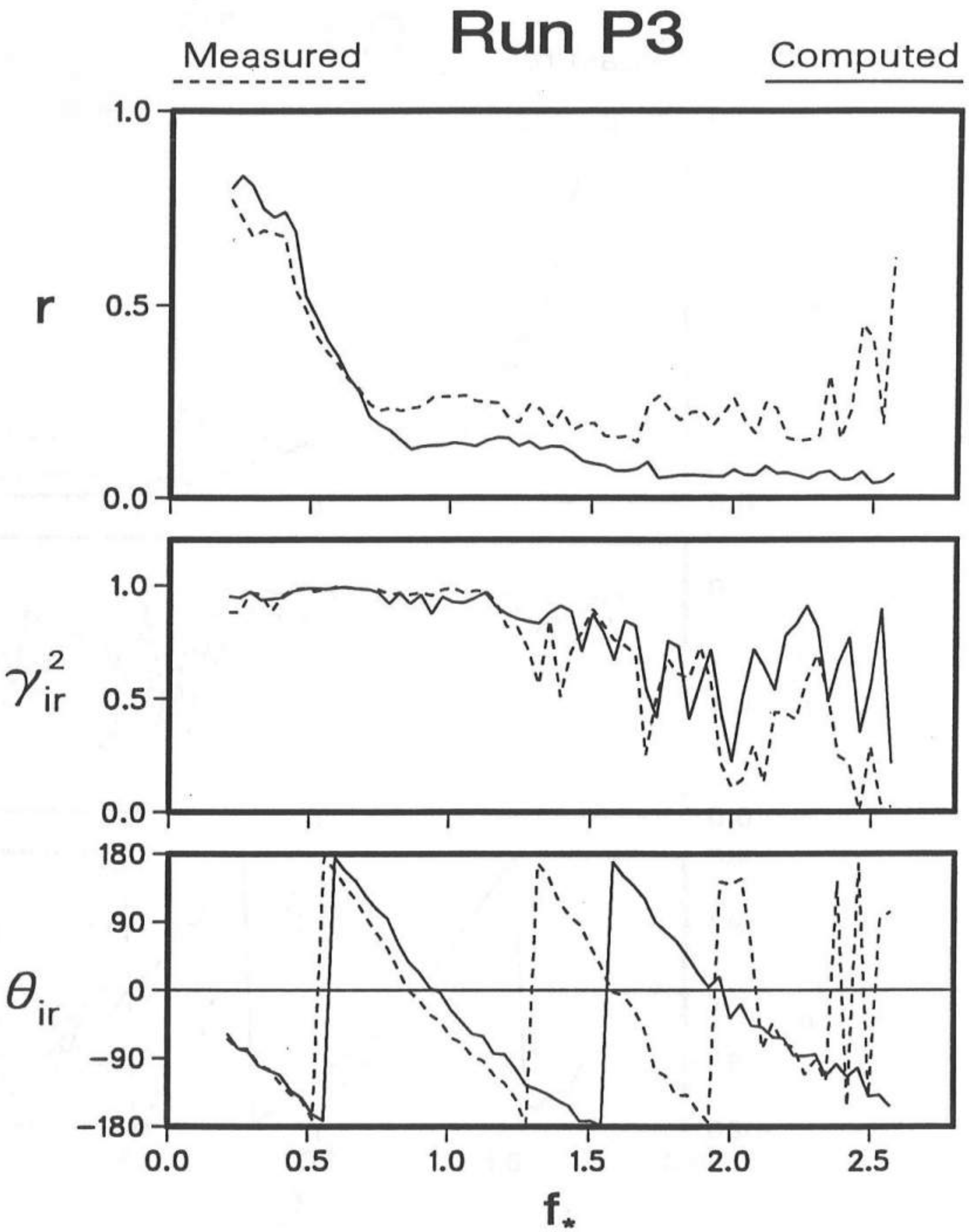

Figure 6.8: Measured and computed reflection coefficient, coherence and phase between incident and reflected waves at x=0 for Run P3.

6.4 Comparison Between Measured and Computed Waterline Oscillations

Cox (1989) used a waterline meter of wire-resistance type to measure the waterline oscillation on the rough permeable slope which is called the *upper* slope hereafter for brevity. The meter measured the elevation $(Z_r^U)'$ above SWL of the intersection between the instantaneous free surface situated at $z' = \eta'$ and the platinum wire placed at $z' = (z_b' + \delta_r')$ where $\delta_r' \simeq 0.0275$m as indicated in Table 6.2.

Figures 6.9, 6.10, and 6.11 present the measured and computed time series of the normalized waterline elevation $Z_r^U(t)$ for Runs P1, P2, and P3 where the significant wave height $H' = H_s'$ and the mean period $T' = T_m'$ are used to normalize the physical elevation $(Z_r^U)'$ and the time t', respectively. The numerical model predicts the waterline oscillation better than the reflected wave train at $x = 0$ perhaps because the assumption of long waves is more appropriate near the waterline.

The normalized spectra $S_U(f_*)$ corresponding to the normalized waterline elevation $Z_r^U(t)$ for Runs P1, P2, and P3 are shown in Figures 6.12, 6.13, and 6.14 together with the coherence squared γ_{iU}^2 and the phase θ_{iU} between the incident waves and the waterline oscillations on the upper slope. The agreement between the measured and computed spectra $S_U(f_*)$ is good in both low and high frequency ranges. The numerical model predicts the coherence squared γ_{iU}^2 well near the peak frequency but marginally for the low and high frequency ranges probably because of the long wave assumption used in the model and noise in the measurement. The phase difference $\theta_{iU}(f_*)$ is related to the normalized travel time given by $\left(\frac{-\theta_{iU}}{2\pi f_*}\right)$ for the wave component f_* propagating from x=0 to the moving waterline on the upper slope (Kobayashi, Cox, and Wurjanto 1991). The model performs reasonably well in predicting the phase difference θ_{iU} except for the high frequency components, even though there is a lag between the measured and computed θ_{iU} for Runs P2 and P3. For the high frequency range, however, the numerical model predicts the phase difference poorly. This may be related to the underestimation of the crest (run-up) elevations of $Z_r(t)$ by the present numerical model as shown in Figures 6.9–6.11.

Furthermore, to examine the statistics of the run-up and swash on the upper slope, the time series $Z_r^U(t)$ with $0 < t \leq t_{max}$ is separated into individual swash events using a zero-upcrossing method. Several definitions related to the waterline oscillation are first introduced. The *set-up* used herein refers to the time-averaged value of the waterline elevation above SWL over the specified duration. The set-up on the upper slope denoted by $\overline{Z_r^U}$ is the time-averaged value of the time series $Z_r^U(t)$ according to Eq. 5.25. *Run-up* is defined as the highest elevation above SWL reached by the waterline of the physical depth δ_r' during an individual swash event. *Swash height* is the vertical distance between the highest and lowest points reached by the waterline corresponding to the depth δ_r' during an individual swash event. Listed in the following are the run-up and swash statistics calculated from this time series analysis, where the superscript ^{U} denotes the *upper* slope:

- h_s^U = normalized significant swash height, defined as the average of the highest one-third swash heights, on the upper slope.
- R_s^U = normalized significant run-up, defined as the average of the highest one-third run-up elevations above SWL, on the upper slope.
- R_{max}^U = normalized maximum run-up, defined as the highest elevation above SWL reached by the waterline during $0 < t \leq t_{max}$, on the upper slope.
- R_P^U = normalized run-up corresponding to the specific value of P where P is the exceedance probability estimated by

  $$P = \frac{n}{N_o + 1} \tag{6.9}$$

  where n is the rank of the individual run-up elevations and N_o the number of the swash events during $0 < t \leq t_{max}$.

The measured and computed values of the set-up $\overline{Z_r^U}$, the significant swash height h_s^U, the significant run-up R_s^U, and the maximum run-up R_{max}^U on the upper slope are given in Table 6.4. The present numerical model generally underestimates the run-up and swash height as is also apparent in Figures 6.9–6.11. The agreement could be improved by reducing the friction factor f' listed in Table 6.1 and based on the limited calibration for the rough impermeable slope since the values of f' for the rough impermeable and permeable slopes may not be the same.

Finally, the measured and computed exceedance probabilities P as a function of (R_p^U/R_s^U) for the three runs are presented in Figure 6.15 along with the exceedance probability P_R according to the Rayleigh distribution given by

$$P_R = \exp\left[-2\left(R_p^U/R_s^U\right)^2\right] \qquad . \tag{6.10}$$

The numerical model predicts the measured run-up distribution well partly because the measured and computed values of R_p in Figure 6.15 are normalized by the measured and computed values of R_s, respectively, to offset the underestimation of R_s and R_p for small P by the numerical model. The numerical model predicts the data points for small P much better than the Rayleigh distribution.

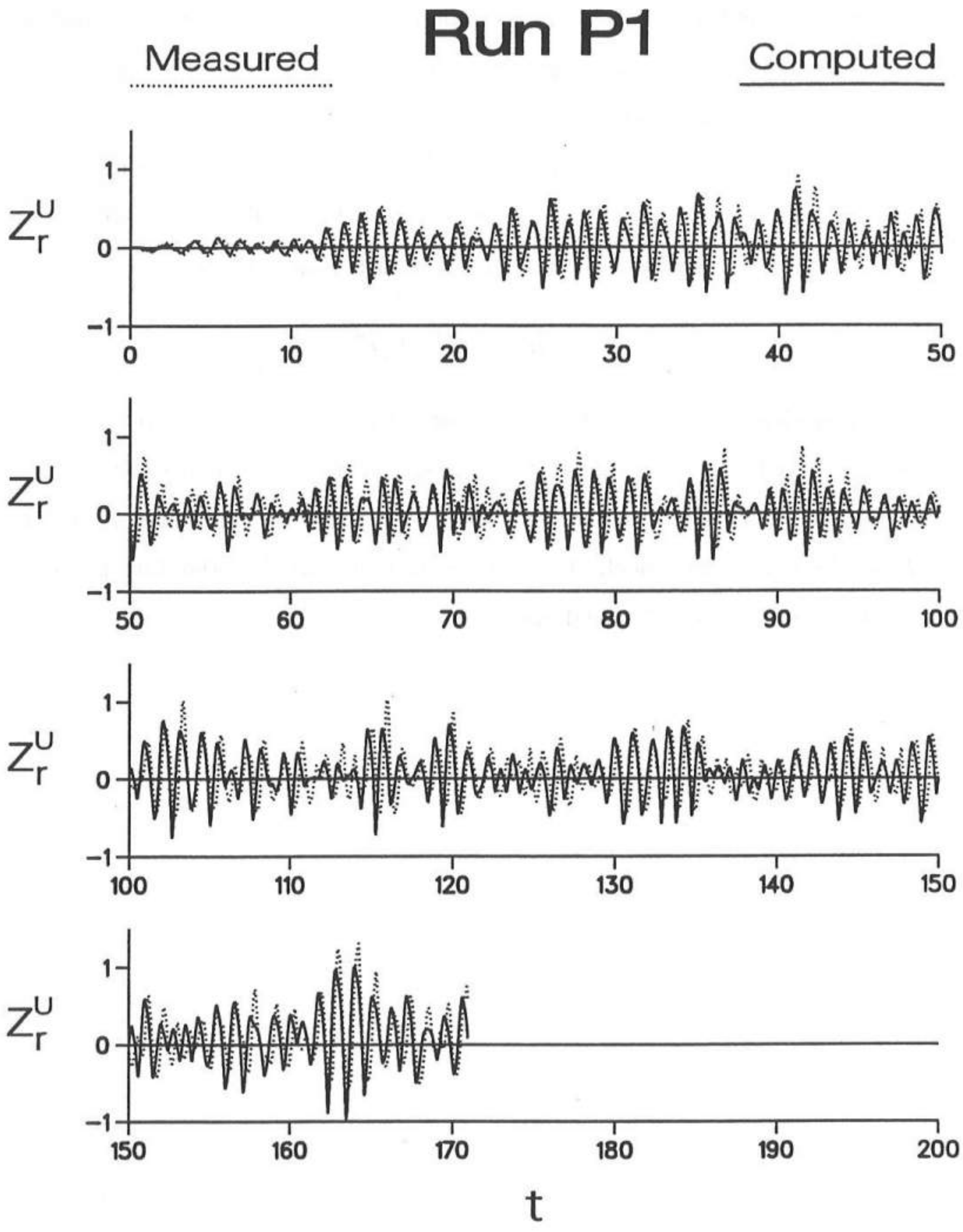

Figure 6.9: Measured and computed waterline oscillations on upper slope for Run P1.

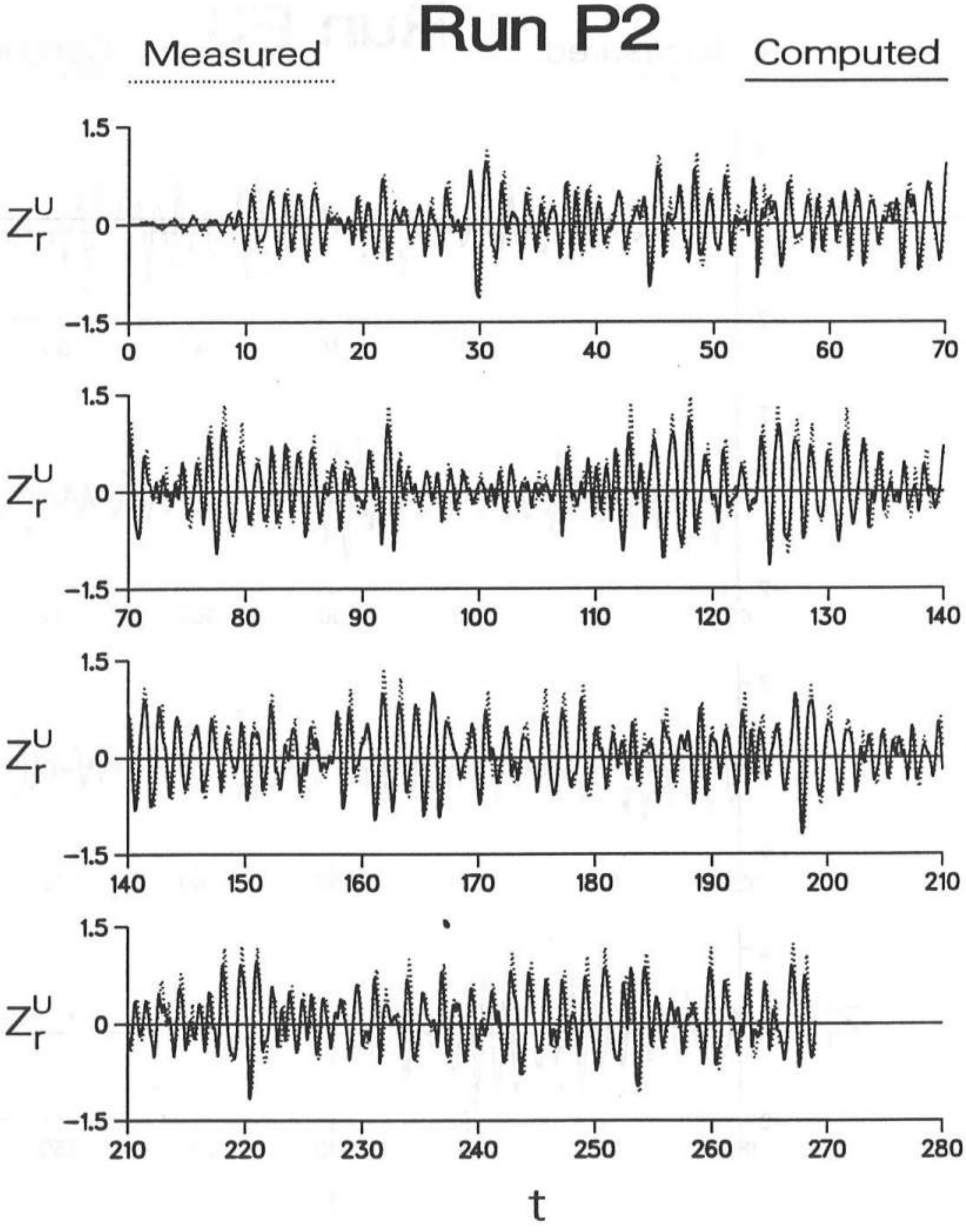

Figure 6.10: Measured and computed waterline oscillations on upper slope for Run P2.

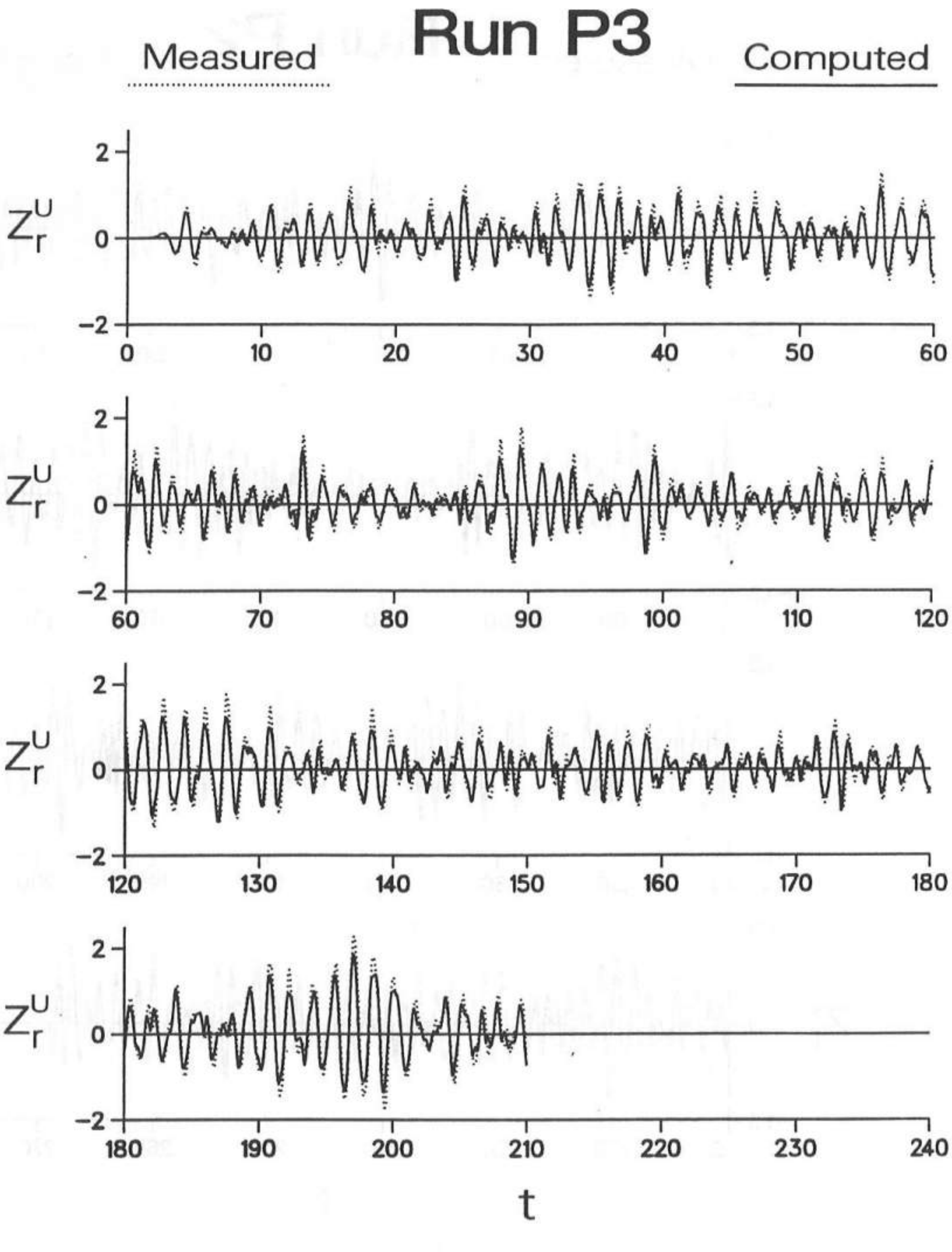

Figure 6.11: Measured and computed waterline oscillations on upper slope for Run P3.

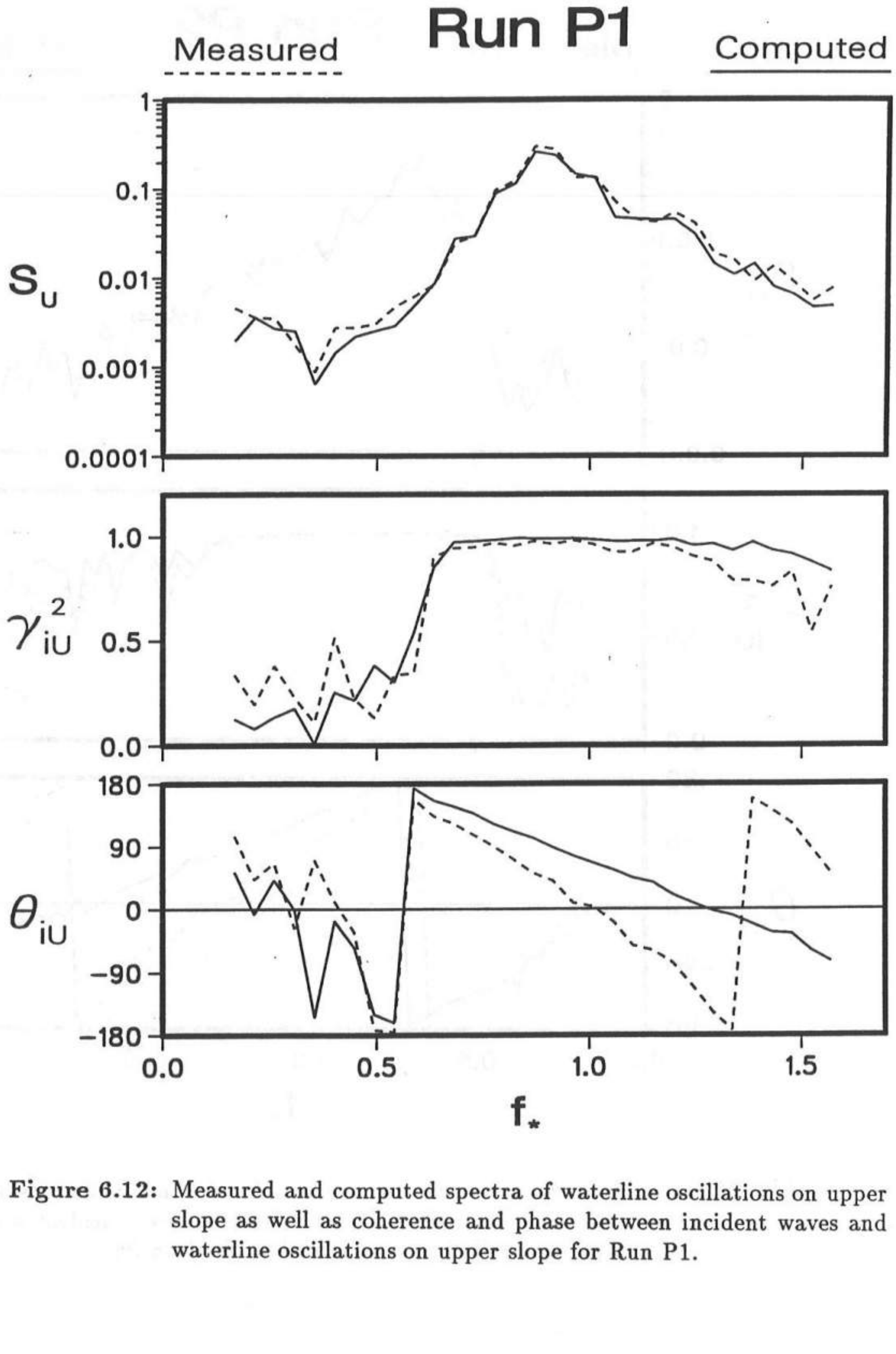

Figure 6.12: Measured and computed spectra of waterline oscillations on upper slope as well as coherence and phase between incident waves and waterline oscillations on upper slope for Run P1.

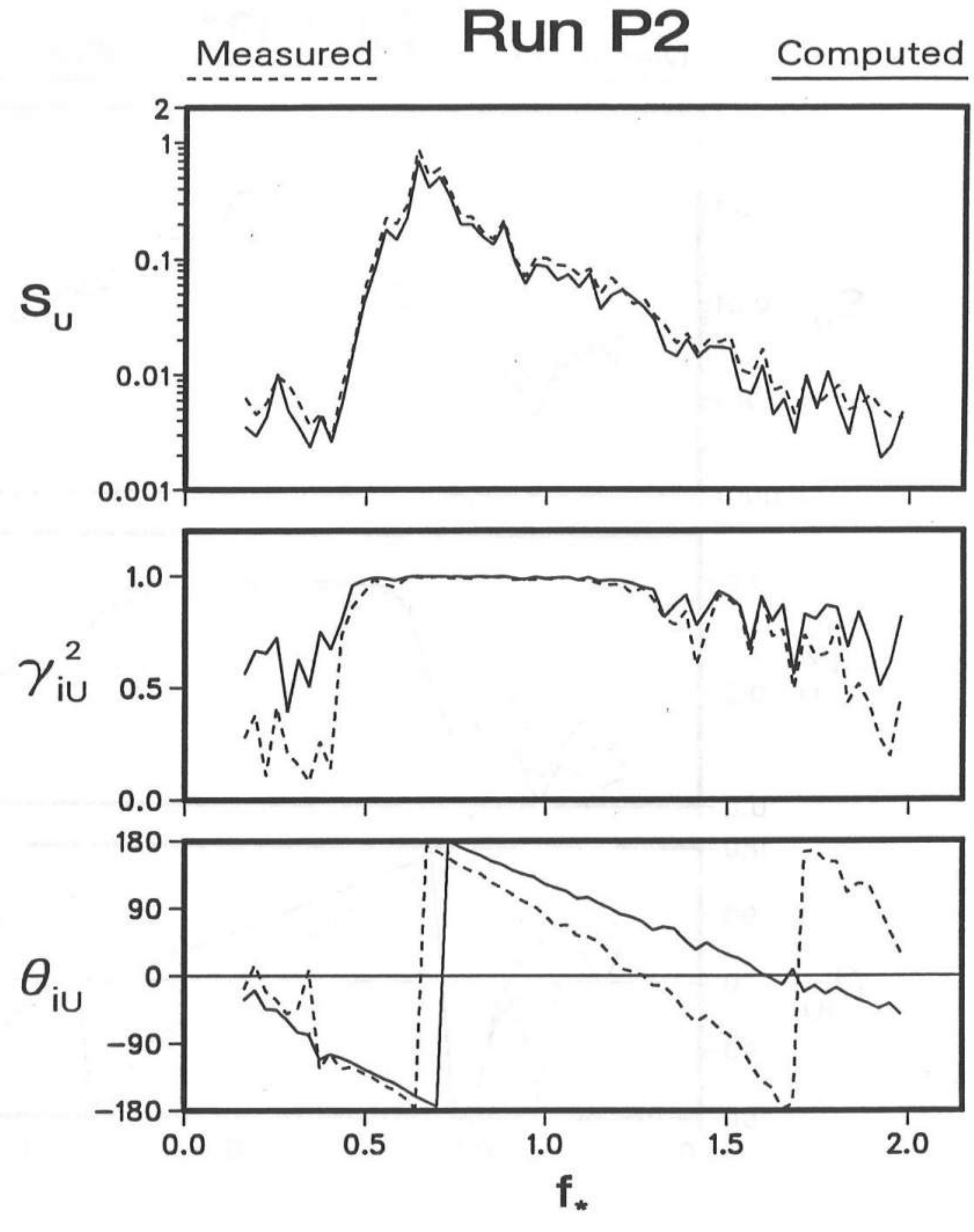

Figure 6.13: Measured and computed spectra of waterline oscillations on upper slope as well as coherence and phase between incident waves and waterline oscillations on upper slope for Run P2.

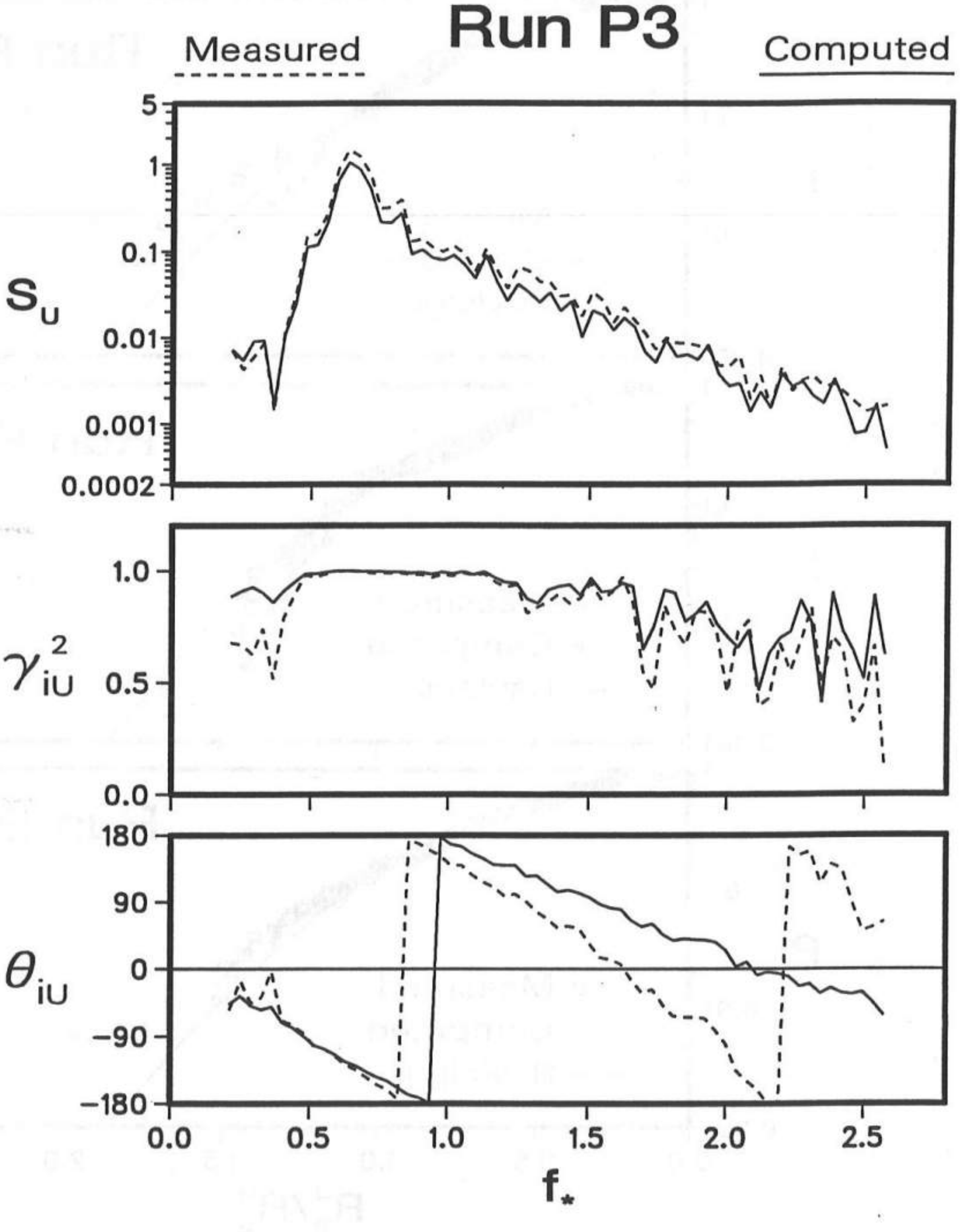

Figure 6.14: Measured and computed spectra of waterline oscillations on upper slope as well as coherence and phase between incident waves and waterline oscillations on upper slope for Run P3.

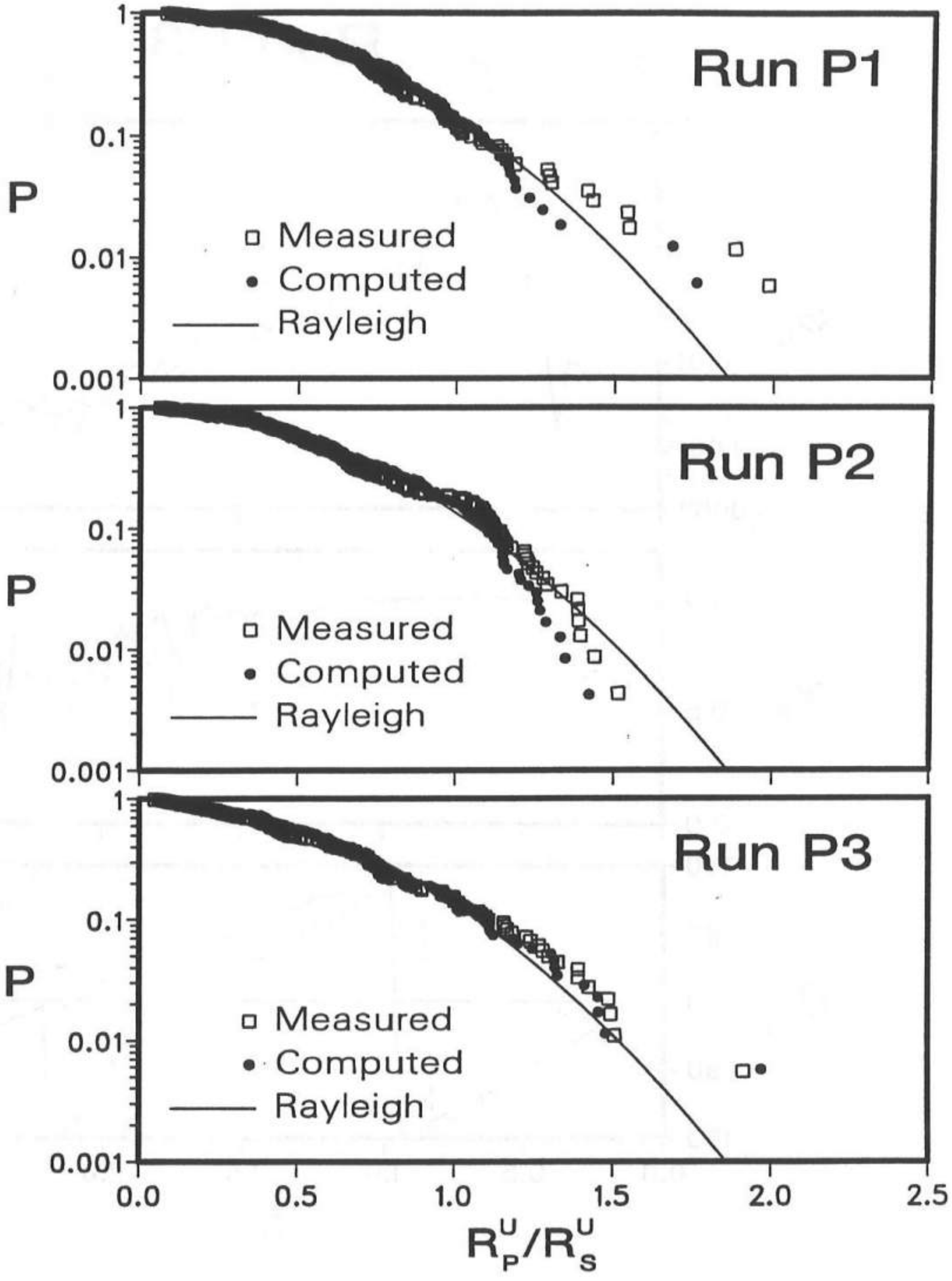

Figure 6.15: Measured and computed exceedance probability of run-up as compared with Rayleigh distribution for three runs.

6.5 Computed Time-Dependent Flow Fields

The agreement between the numerical model and the measurements discussed in the preceding two sections may be good enough to allow one to examine, at least qualitatively, the quantities which were not measured in the tests conducted by Cox (1989).

The computed results for Runs P1, P2, and P3 that can be obtained directly from the numerical model without additional analyses have already been presented in WK 92 in the normalized form. The presented results include:

1. Reflected wave train $\eta_r(t)$ at the seaward boundary $x=0$ (Figures 6.2–6.4).
2. Time series of the waterline elevation on the upper slope, $Z_r^U(t)$ (Figures 6.9–6.11).
3. Time series of the waterline elevation on the lower slope, $Z_r^L(t)$, where the lower slope corresponds to the impermeable lower boundary of the permeable underlayer (Figure 6.16 for Run P2).
4. Portions of time series of the free surface elevation $\eta(t)$ at three different locations (Figure 6.17 for Run P2).
5. Instantaneous spatial variations of the free surface and water table elevation η (Figure 6.18 for Run P2).
6. Instantaneous spatial variations of the depth-averaged horizontal velocity u over the upper slope, defined by Eq. 3.10 (Figure 6.18 for Run P2).
7. Instantaneous spatial variations of the volume influx q_b into the permeable underlayer, introduced in Eq. 3.7 (Figure 6.19 for Run P2).

8. Instantaneous spatial variations of the horizontal fluid velocity u_b at the upper boundary of the permeable underlayer, defined by Eq. 3.21
(Figure 6.19 for Run P2).

9. Instantaneous spatial variations of the vertically-averaged discharge velocity u_p inside the permeable underlayer, defined by Eq. 3.35
(Figure 6.20 for Run P2).

10. Instantaneous spatial variations of the discharge m_p inside the permeable underlayer, defined by Eq. 3.32
(Figure 6.20 for Run P2).

11. Spatial variations of the mean, maximum, and minimum values of η where the maximum and minimum values indicated by the subscripts $_{max}$ and $_{min}$ are with respect to t during $0 < t \leq t_{max}$ at given location x
(Figure 6.21 for Run P2).

12. Spatial variations of the mean, maximum, and minimum values of u
(Figure 6.22 for Run P2).

13. Spatial variations of the mean, maximum, and minimum values of the horizontal volume flux m over the upper slope, defined by Eq. 3.9
(Figure 6.23 for Run P2).

14. Spatial variations of the mean, maximum, and minimum values of q_b
(Figure 6.24 for Run P2).

15. Spatial variations of the mean, maximum, and minimum values of u_p
(Figure 6.25 for Run P2).

16. Spatial variations of the mean, maximum, and minimum values of m_p
(Figure 6.26 for Run P2).

17. Time-averaged mass balance for the flow over the upper slope in Region 1
(Figure 6.32 for Run P2).

18. Time-averaged mass balance for the flow inside the permeable underlayer in Regions 2 and 3
    (Figure 6.33 for Run P2).
19. Time-averaged energy quantities for the flow over the upper slope in Region 1
    (Figure 6.35 for Run P2).
20. Time-averaged energy quantities for the flow inside the permeable underlayer in Regions 2 and 3
    (Figure 6.36 for Run P2).
21. Time-averaged energy balance for the flow inside the permeable underlayer in Regions 2 and 3
    (Figure 6.37 for Runs P2 and P3).

The reflected waves and waterline oscillations on the upper slope have been examined in detail in Sections 6.3 and 6.4 to evaluate the numerical model using the measurements. The rest of the items in the above list will be presented to the degree necessary to explain the hydrodynamics involved with the irregular wave interaction with the rough permeable slope. The computed results for Run P2 presented in Figures 6.16 through 6.31 are representative unless stated otherwise. The time-averaged mass and energy balances will be presented separately in the next two sections. Figures 6.16 through 6.31 are explained in somewhat arbitrary order in the following.

Figure 6.22 needs a special attention regarding the spike appearing in the spatial variation of the maximum depth-averaged horizontal velocity u_{max}. To eliminate spikes like this, which tend to occur at the moving waterline, WK 92 suggested a measure that in effect would reduce the largest time step Δt allowed in the computation. To demonstrate this remedy, another computation for Run P2 is performed using the largest allowable time step Δt of 0.5x10^{-3}, which is one half of the value used in the first computation as listed in Table 6.2. The spatial variations in Figure 6.22 from the first computation with $(\Delta t)_{max}$=1.0x10^{-3} are replotted in Figure 6.27 along with the results from the second computation with $(\Delta t)_{max}$=0.5x10^{-3}. The second computation does not exhibit any spike, indicating that the spike is numerical by origin. The computation for Run P3 with the input parameters as listed in Table 6.2 also exhibited similar spikes. The appearance of spikes in the spatial variations of u_{max} and u_{min} is an unwanted nuisance but *can* be remedied. To provide a stronger basis for this claim, the second computation for Run P3 is performed using $(\Delta t)_{max}$=0.267x10^{-3}, which is one third of the value used in the first computation as listed in Table 6.2. The spatial variations of u_{max}, $\overline{u}$, and u_{min} from the two computations for Run P3 are shown in Figure 6.28. It can be seen in this figure that no spike appears in the second computation.

It should be pointed out that in the numerical model, the depth-averaged horizontal velocity u is obtained by dividing the horizontal volume flux m by the water depth h as given by Eq. 3.10. The dependent variables computed directly by the numerical model for Region 1 are m and h, the two elements of the vector $\mathbf{U}$ in Eq. 4.8. The spatial variations of the maximum and minimum values of m and h themselves do not exhibit any spike even if spikes exist in u_{max} and u_{min}, as can be seen in Figures 6.21, 6.22, and 6.23 for Run P2. Moreover, the spikes always occur near the waterline x_s on the upper slope. These facts indicate that this spike problem is related to the landward boundary condition at the moving waterline x_s. The present Lax-Wendroff scheme does not show any numerical problem as long as the adopted numerical stability criterion given in WK 92 is satisfied. As a matter of fact, the adopted numerical stability criterion is *always* imposed in selecting the largest time step Δt as explained in relation to Table 6.2. It is also noted that even when spikes do appear in the spatial variations of u_{max} and u_{min}, the mean value $\overline{u}$ is hardly affected. This is because the values of u_{max} and u_{min} occur only once during the computation duration, which is generally long for random waves, and can easily be affected by local numerical problems.

While the waterline oscillations on the lower slope shown in Figure 6.16 can not be measured using a waterline meter unlike the waterline oscillations on the upper slope shown in Figure 6.10, some realistic features can be observed. First, the waves are significantly damped as they enter the permeable underlayer, which is realistic in the light of the measured water table elevations presented by Bruun and Johannesson (1976) and Hall (1991). The vertical range of the waterline oscillations on the lower slope is about one-third of that on the upper slope for the three runs. Second, the high-frequency wave components are damped more than the low-frequency wave components as shown in Figure 6.29 where the computed spectra $S_U(f_*)$ and $S_L(f_*)$ of the waterline oscillations on the upper and lower slopes for Runs P2 and P3 are plotted.

Figures 6.30 and 6.31 are intended to show how the waterline oscillations on the lower slope, Z_r^L, are related to the incident wave train, η_i, and the waterline oscillations on the upper slope, Z_r^U, for Run P2. Figure 6.30 depicts the coherence squared γ_{iL}^2 and the phase difference θ_{iL} between η_i and Z_r^L where the corresponding spectra are also plotted to make it easier to interpret the figure. As compared to Figure 6.13 depicting the coherence squared γ_{iU}^2 between η_i and Z_r^U, Figure 6.30 indicates that the degree of coherence between η_i and Z_r^L is less than that between η_i and Z_r^U. Figure 6.31 shows the coherence squared γ_{UL}^2 and the phase difference θ_{UL} between Z_r^U and Z_r^L. It can be seen in Figures 6.30 and 6.31 that the degree of coherence between η_i and Z_r^L is about the same as that between Z_r^U and Z_r^L.

In Figure 6.18, the shaded areas correspond to the permeable underlayer and the permeable underlayer is relatively thick compared to the wave height H' used for the normalization. The presence of the thick permeable underlayer modifies the wave patterns. In the case of an impermeable slope, waves can only up-rush and down-rush on the slope. The permeable underlayer, on the contrary, absorbs waves as can be seen from the spatial variations of η at different time levels shown in Figure 6.18 for Run P2. As a result, the type of wave breaking in the presence of a thick permeable underlayer will be different from wave breaking on impermeable slopes. The dominant breaker types for the three impermeable slope test runs conducted by Cox (1989) were plunging, collapsing and surging. The spatial variations of the free surface elevation η shown in Figure 6.18 do not show very steep fronts computed in the case of impermeable slopes [*e.g.*, Wurjanto and Kobayashi (1991), Kobayashi and Wurjanto (1992)]. The lack of very steep fronts is also reflected in Figure 6.17 where asymmetry of wave profiles are not very apparent even in very shallow water where the locations of x=0.31, 0.61, and 0.92 on the rough permeable slope can be found in Figure 6.18. Comparison of the variations of η and u in in Figure 6.18 reveals the sequence of water up-rushing and down-rushing on the permeable slope from t=124.75 to t=126.

The spatial variations of the normalized volume influx q_b shown in Figure 6.19 indicate water flowing into the permeable underlayer during wave up-rush and water outflow in the region below the trough of the free surface η shown in Figure 6.18. The corresponding variations of the normalized horizontal velocity u_b is also shown in Figure 6.19. The sudden jumps in the variations of u_b are the consequence of the assumption made to estimate u_b using Eq. 3.21 for the present one-dimensional model.

Comparing Figures 6.20 and 6.18, the flux inside the permeable underlayer appears to be driven mainly by the hydrostatic pressure gradient related to the term $(-\frac{\partial\eta}{\partial x})$ in Eq. 3.27 as is the case with the thin permeable underlayer (Kobayashi and Wurjanto 1990). Since $m_p = p_u h_p u_p$ from Eq. 3.35 and h_p approaches zero at the waterline on the lower slope, m_p approaches zero at this waterline even though u_p does not approach zero.

Figures 6.21 through 6.26 show the maximum, mean, and minimum values of η, u, m, q_b, u_p, and m_p for Run P2. These values are readily available from the numerical model but can not be verified using available experimental data. The variations of η_{max}, $\overline{\eta}$, and η_{min}, however, look realistic in the light of the work of Bruun and Johannesson (1976) who observed wave set-up inside a porous breakwater. A spike in the variation of u_{max} in Figure 6.22 has been discussed. The variations of $(u_p)_{max}$ and $(u_p)_{min}$ in Figure 6.25 also show spikes near the landward end. However, the variations of $(m_p)_{max}$ and $(m_p)_{min}$ in Figure 6.25 do not exhibit any spike. This is similar to the spike problem in the variations of u_{max} and u_{min} already discussed. It is noted that the dependent variables obtained directly by the numerical model for Region 2 and 3 are m_p and h_p, whereas u_p is obtained using Eq. 3.35. The small mean fluxes and velocities in Figures 6.22 through 6.26 will be discussed in detail in Section 6.6. Finally, these figures show that the order of magnitude of η, u, m, u_p, and m_p is indeed unity but the order of magnitude of q_b can be much greater than unity. The normalization of q_b' given by Eq. 3.6 could be modified since $p_q q_b$ with $p_q = (n_p p_u) = 0.041$ for Run P2 is much less than q_b.

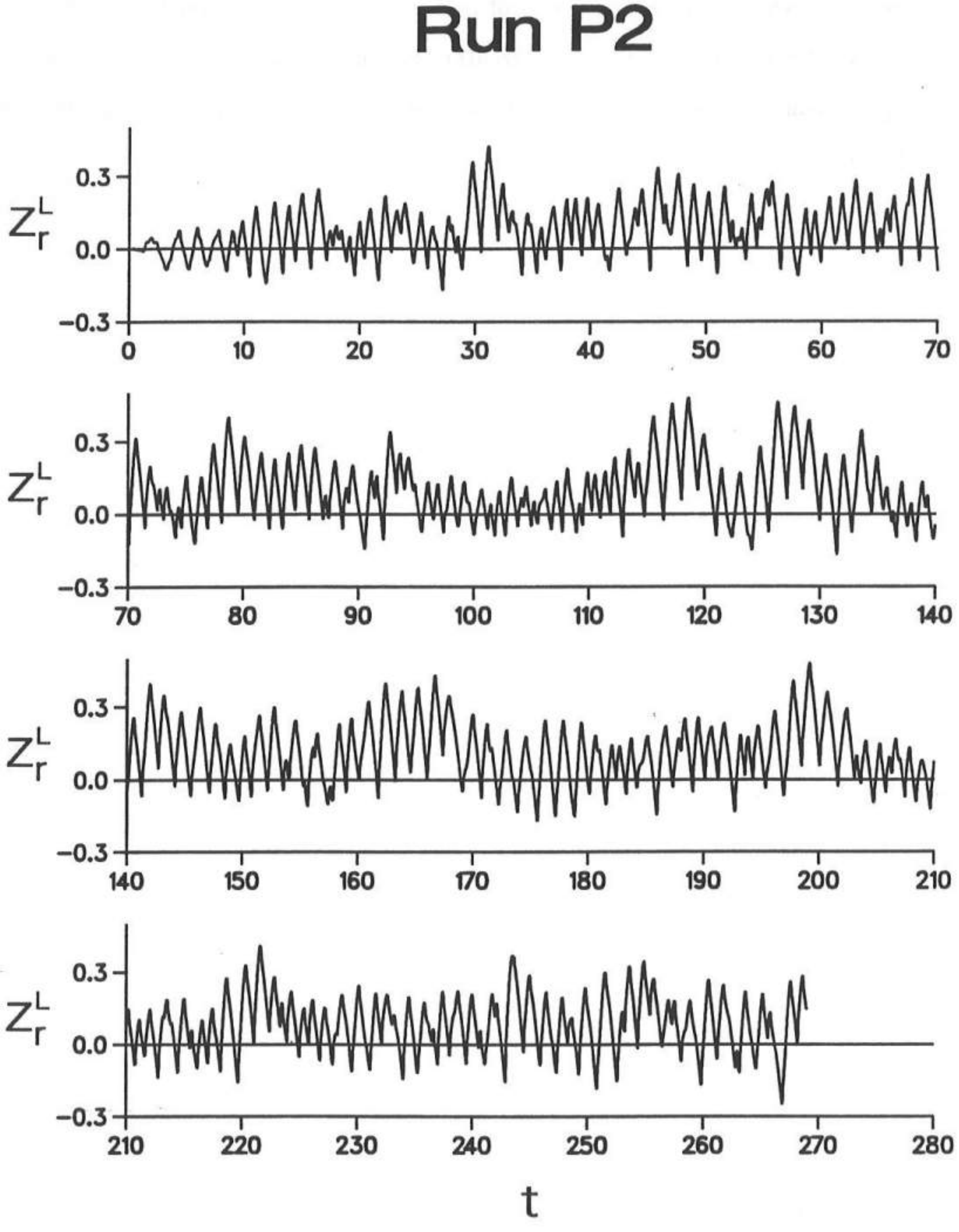

Figure 6.16: Computed waterline oscillations on lower slope for Run P2.

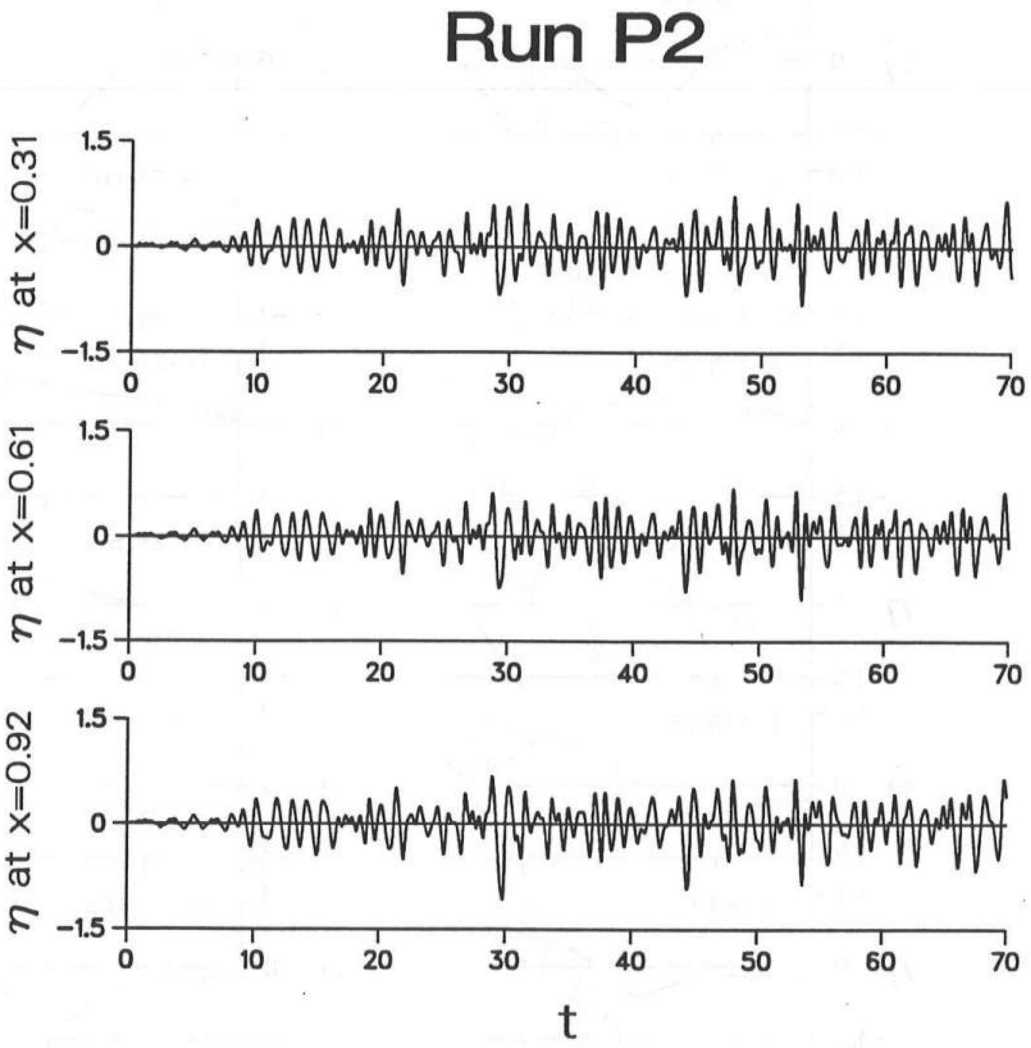

Figure 6.17: Portions of time series of surface elevation $\eta(x,t)$ at $x = 0.31, 0.61$, and 0.92 for Run P2.

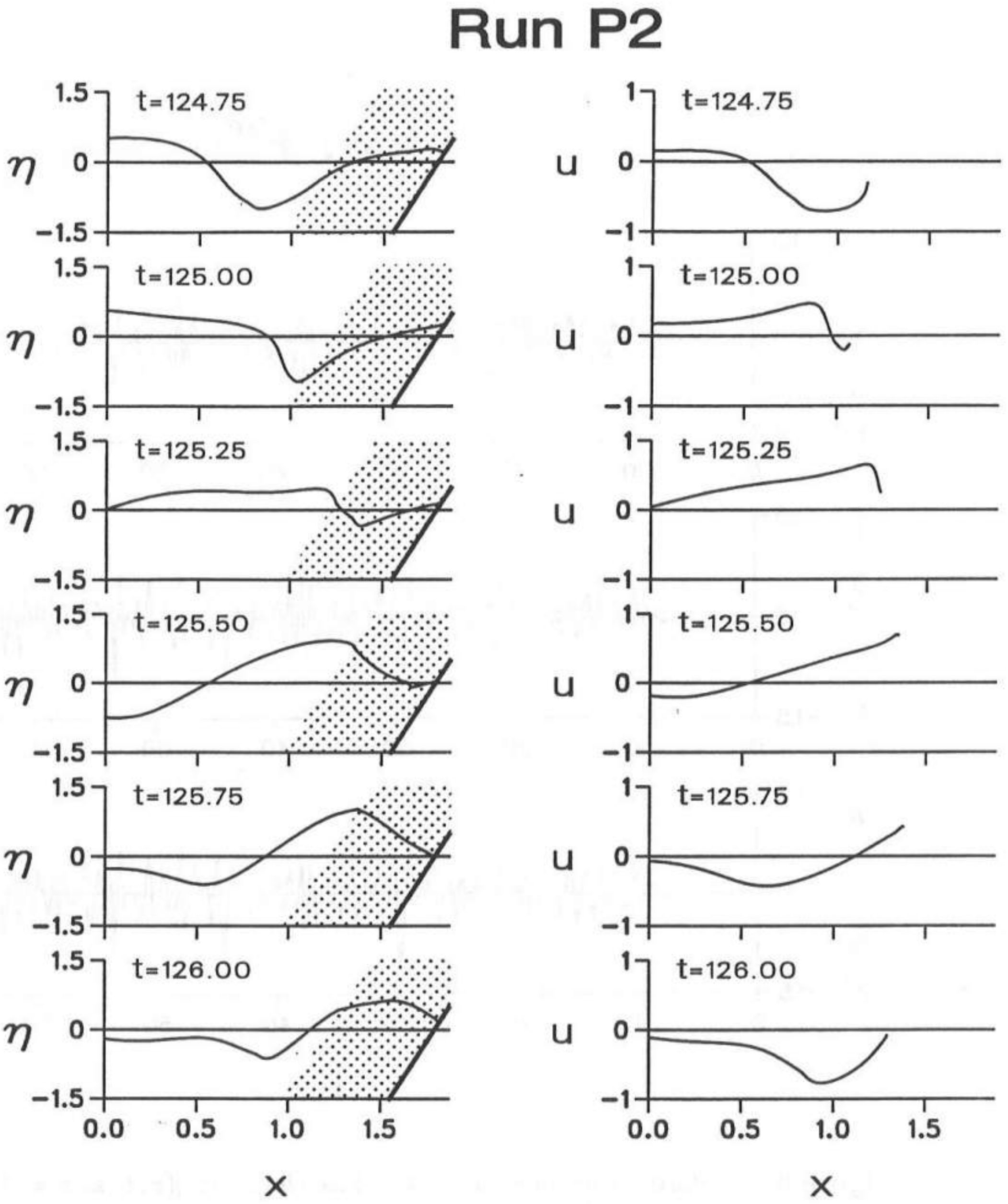

Figure 6.18: Instantaneous spatial variations of free surface elevation η and depth-averaged horizontal velocity u for Run P2.

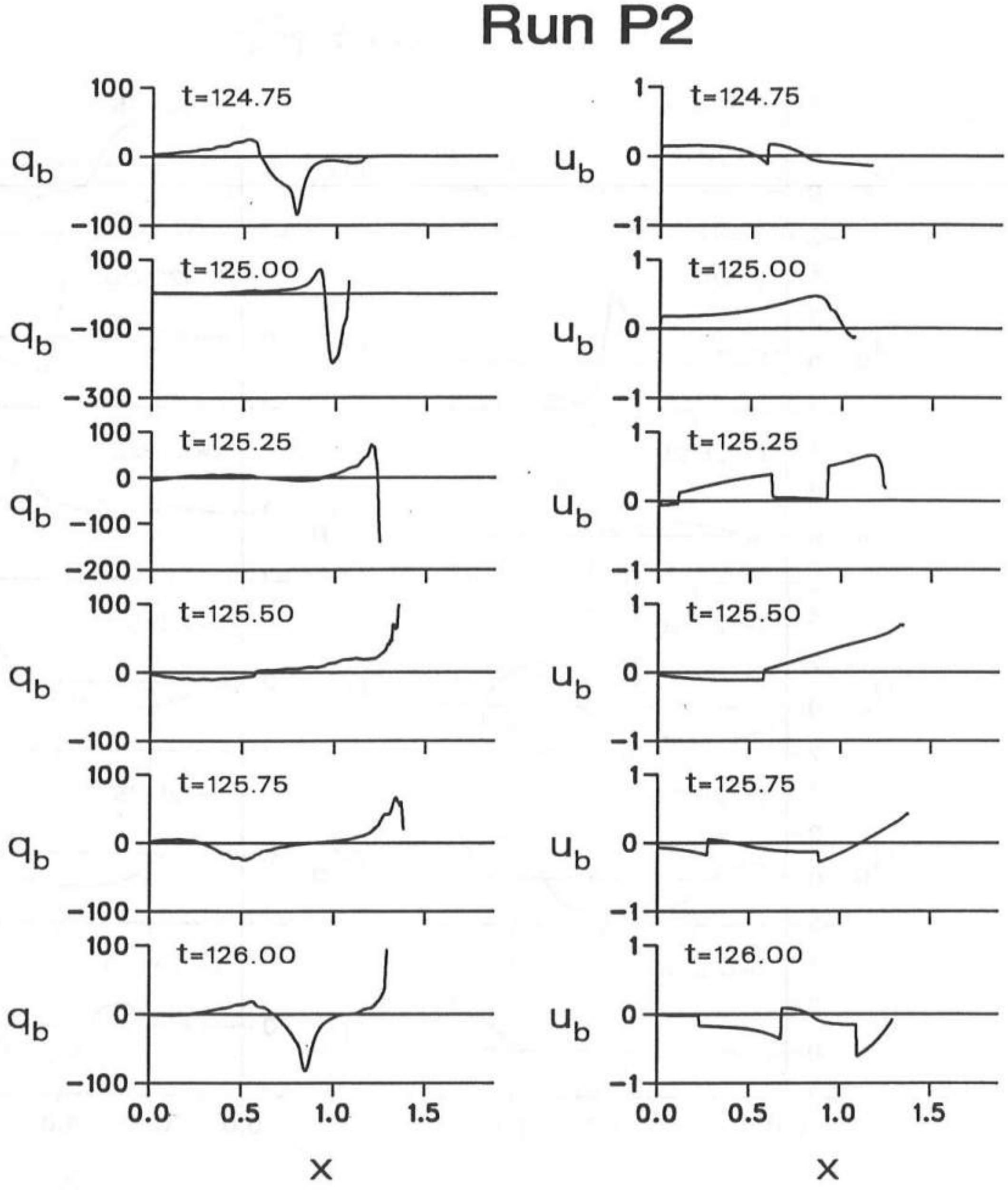

Figure 6.19: Instantaneous spatial variations of volume influx q_b and horizontal velocity u_b for Run P2.

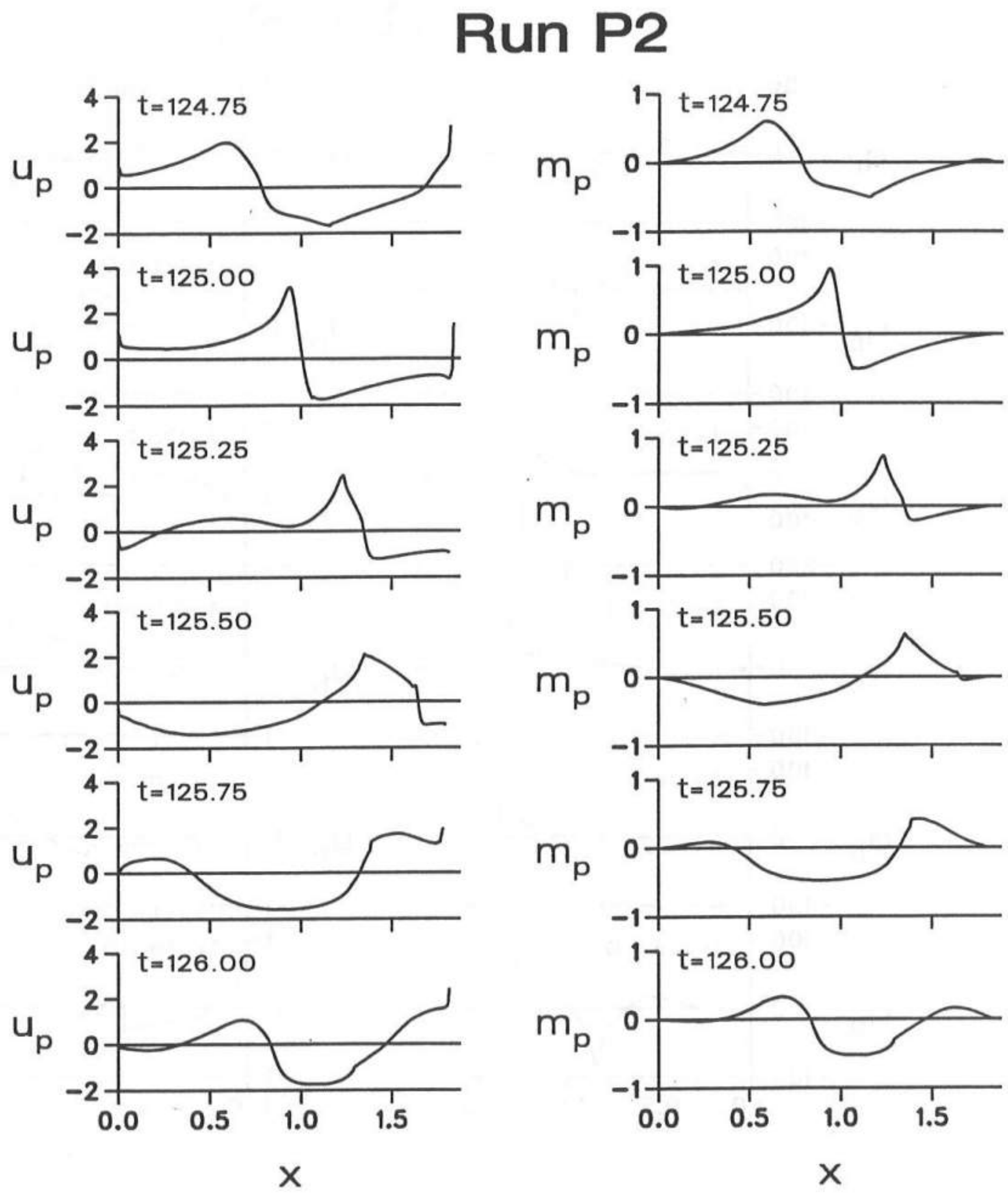

Figure 6.20: Instantaneous spatial variations of vertically-averaged discharge velocity u_p and discharge m_p for Run P2.

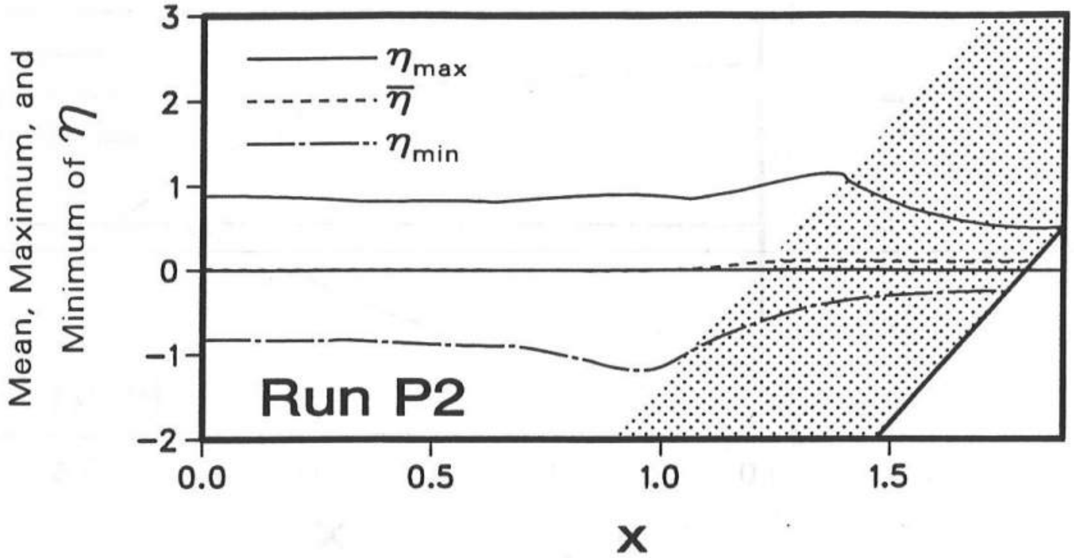

Figure 6.21: Mean, maximum, and minimum values of free surface and water table elevation η for Run P2.

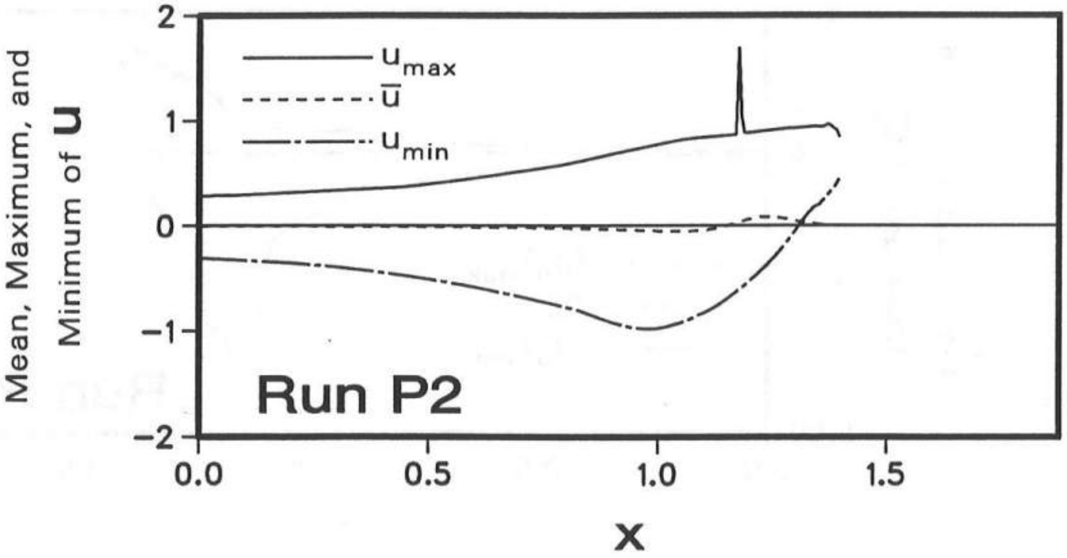

Figure 6.22: Mean, maximum, and minimum values of depth-averaged horizontal velocity u for Run P2.

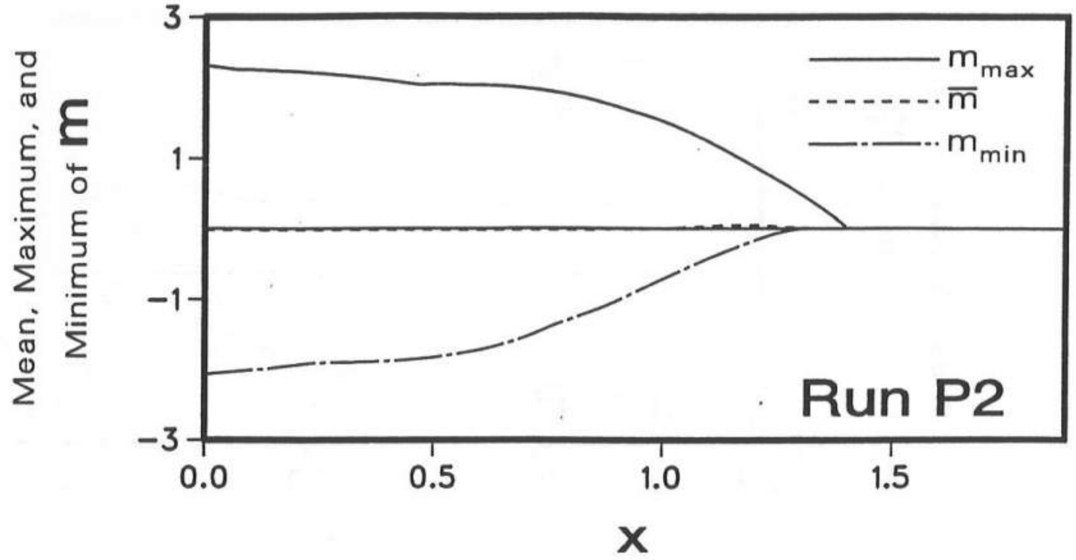

Figure 6.23: Mean, maximum, and minimum values of horizontal volume flux m for Run P2.

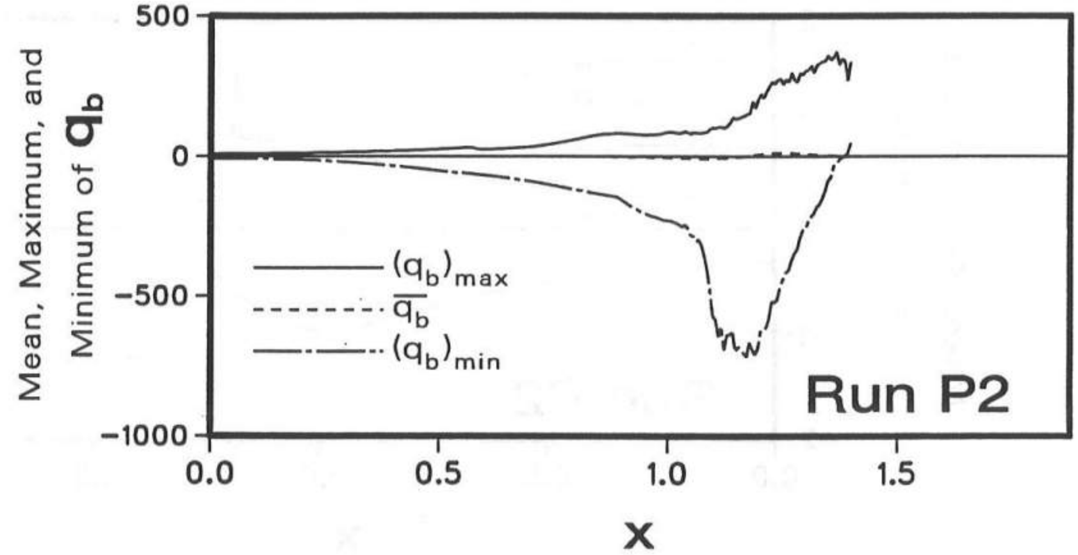

Figure 6.24: Mean, maximum, and minimum values of volume influx q_b for Run P2.

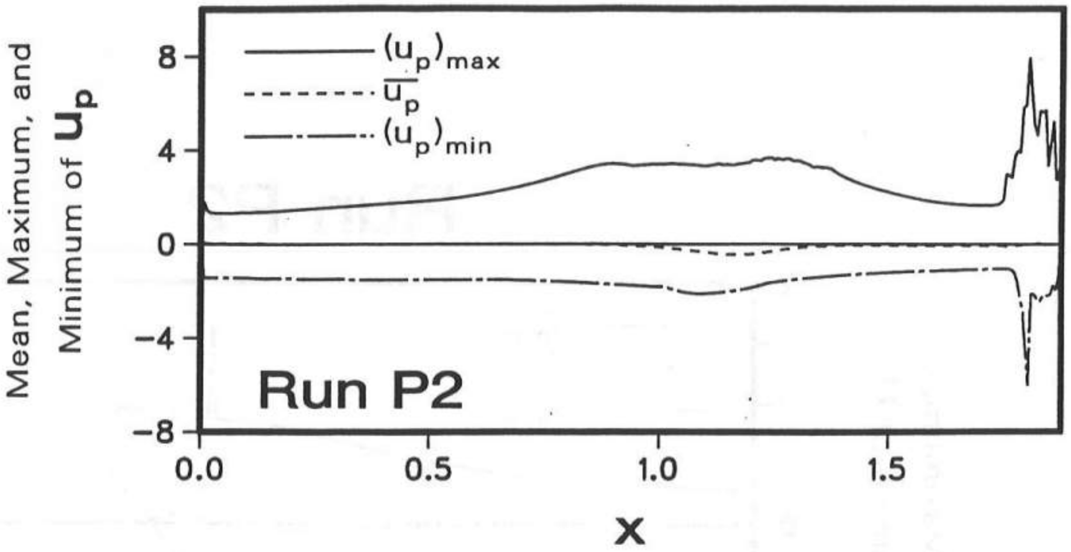

Figure 6.25: Mean, maximum, and minimum values of vertically-averaged discharge velocity u_p for Run P2.

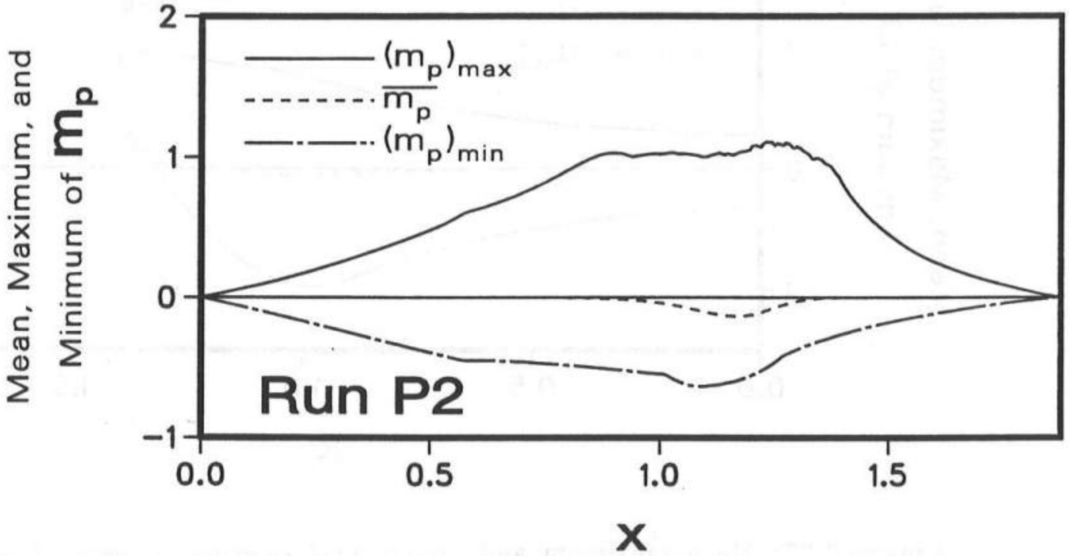

Figure 6.26: Mean, maximum, and minimum values of discharge m_p for Run P2.

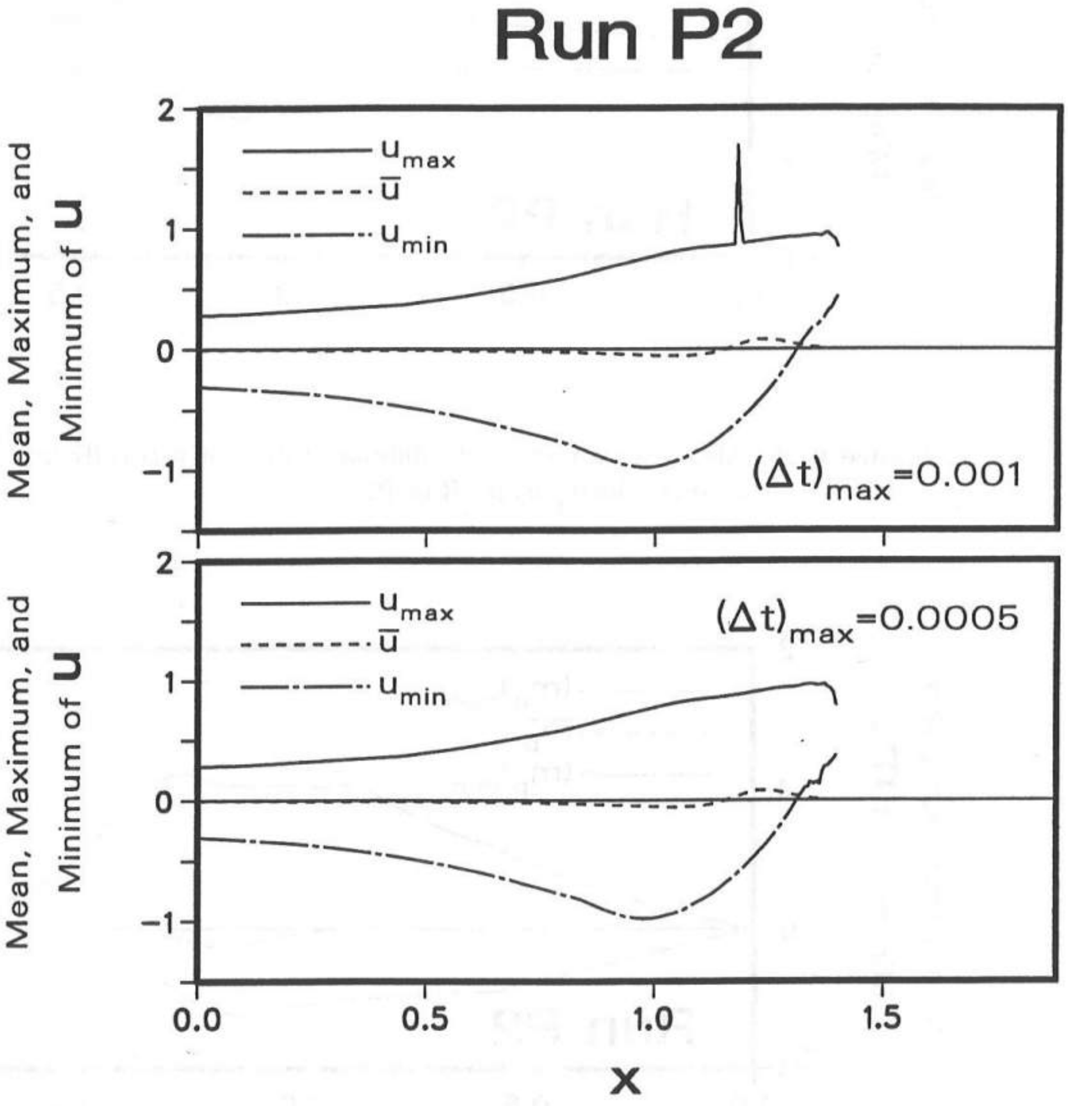

Figure 6.27: Mean, maximum, and minimum values of depth-averaged horizontal velocity u for Run P2 from two computations with different values of maximum allowable time step Δt.

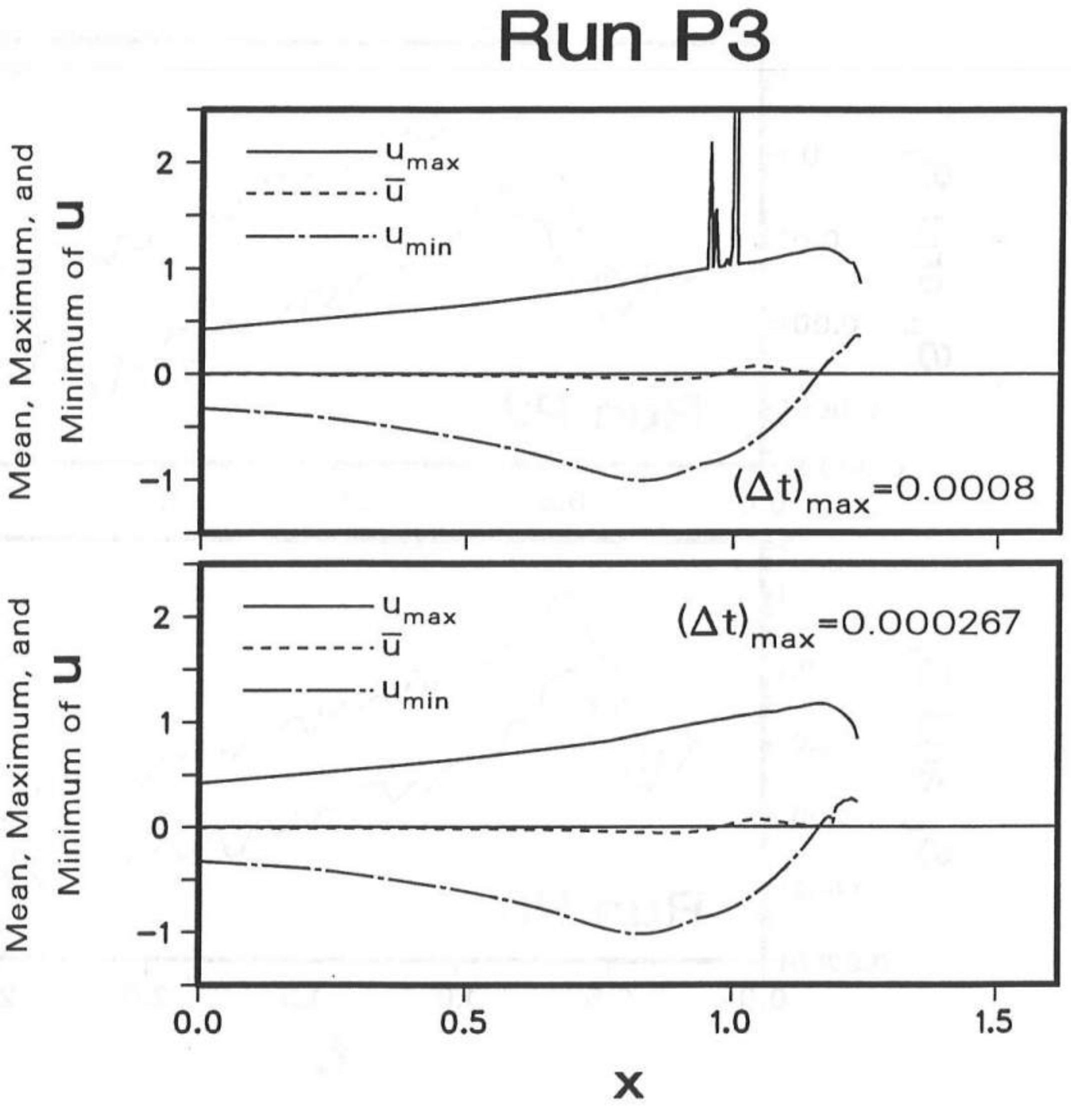

Figure 6.28: Mean, maximum, and minimum values of depth-averaged horizontal velocity u for Run P3 from two computations with different values of maximum allowable time step Δt.

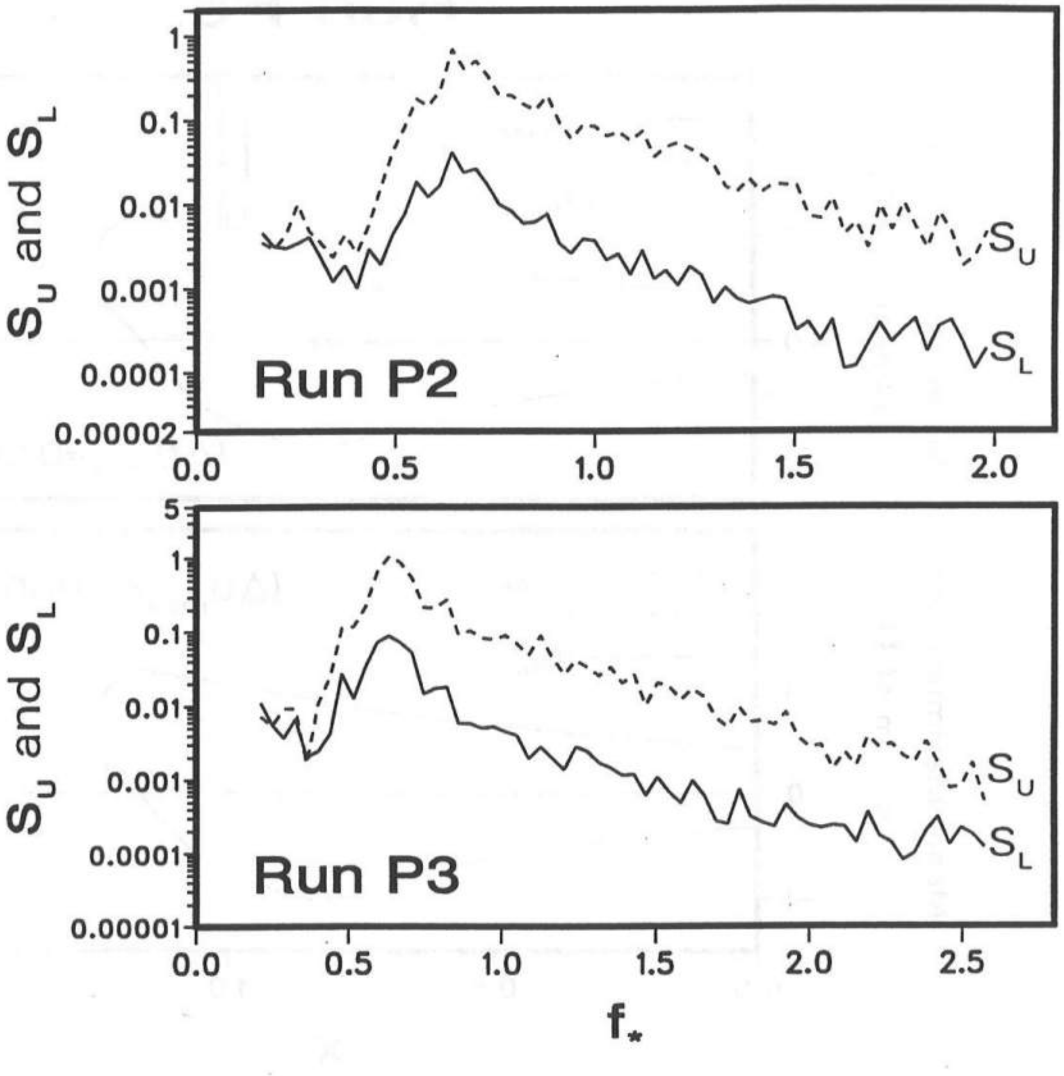

Figure 6.29: Computed spectra of upper and lower waterline oscillations for Runs P2 and P3.

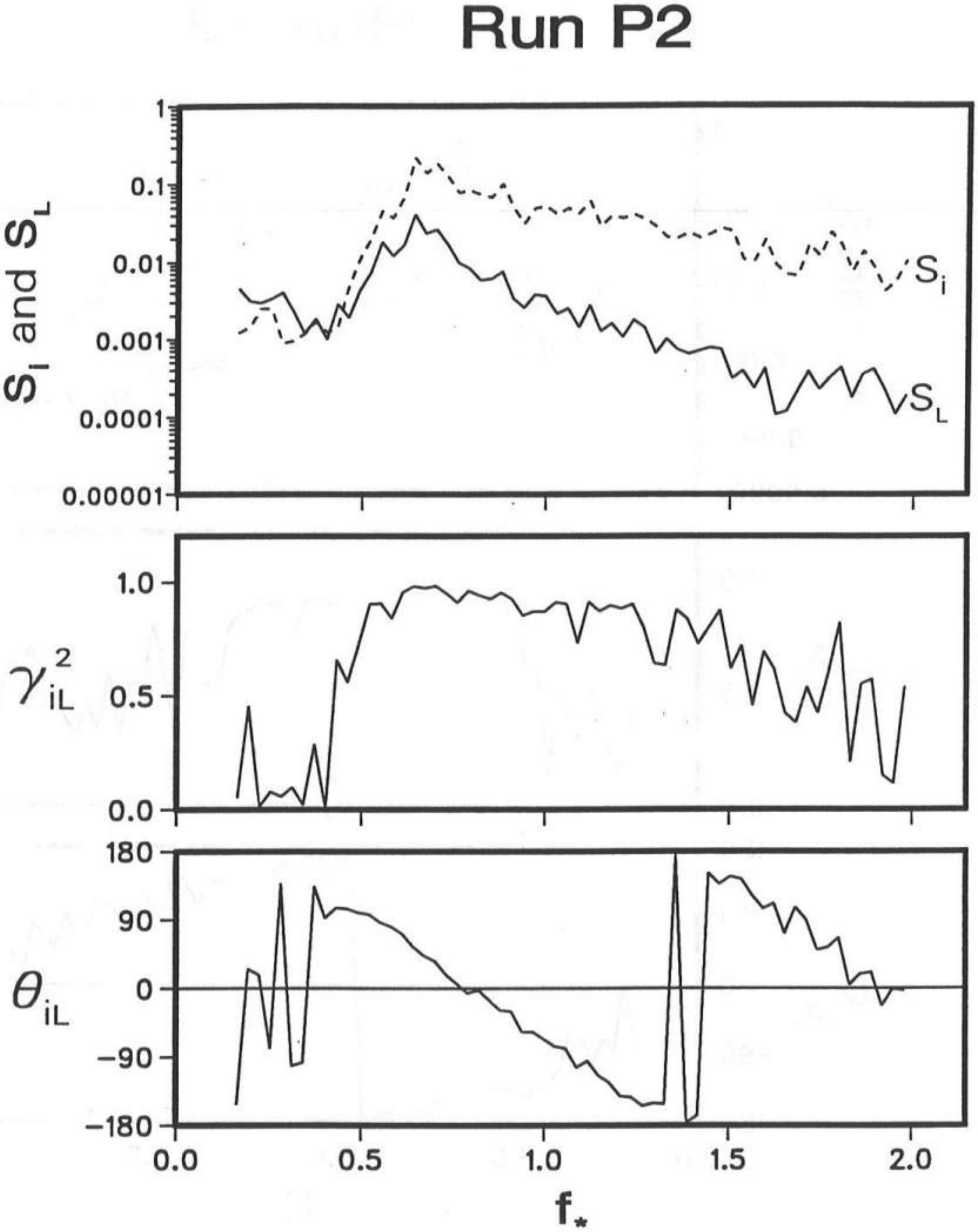

Figure 6.30: Spectra, coherence, and phase of incident waves and computed waterline oscillations on lower slope for Run P2.

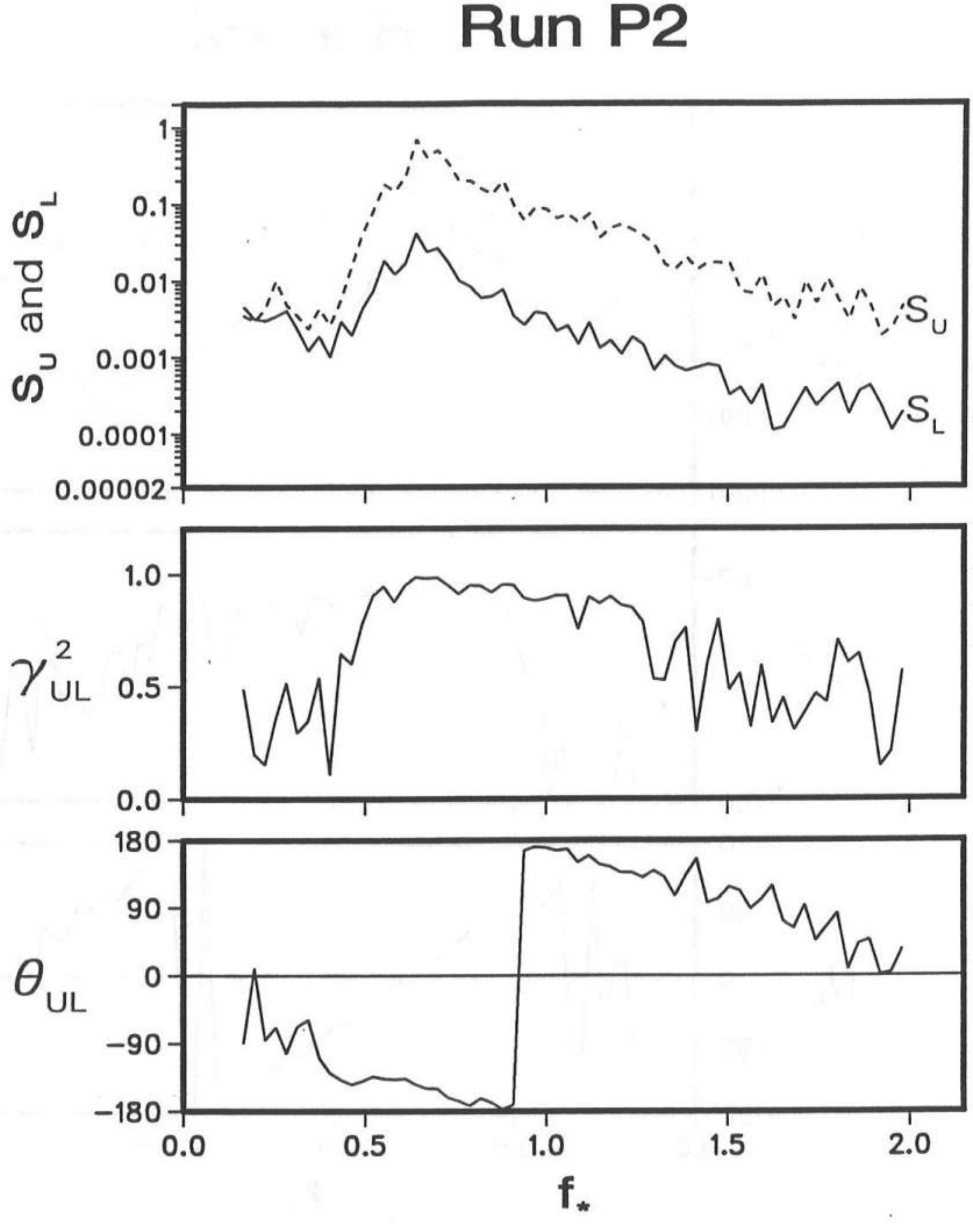

Figure 6.31: Computed spectra, coherence, and phase of waterline oscillations on upper and lower slopes for Run P2.

6.6 Time-Averaged Mass Balance

Being based on the continuity equations, the computed flow fields need to satisfy the time-averaged mass balance. This is one way to check the accuracy of the numerical model. The three one-dimensional continuity equations, Eqs. 3.8, 3.31, and 3.41, are time-averaged in a manner similar to the time-averaging of the energy equations in Section 5.4.

Integrating Eq. 3.8 with the definition of the time average given by Eq. 5.25 yields the time-averaged equation of mass for Region 1.

$$\frac{d\overline{m}}{dx} + p_q\overline{q_b} + \frac{h(t_{max}) - h(t_{min})}{t_{max} - t_{min}} = 0 \tag{6.11}$$

The time averaging of the continuity equations for Regions 2 and 3 separated by the moving waterline x_s on the upper slope becomes easier by combining the two continuity equations into one equation. The volume influx q_b given by Eq. 4.18 is rewritten as

$$q_b = \begin{cases} \dfrac{1}{p_u}\dfrac{\partial m_p}{\partial x} & \text{for Regions 1 and 2 } (0 \leq x \leq x_s) \\ 0 & \text{for Region 3 } (x_s \leq x \leq x_w) \end{cases} \tag{6.12}$$

where q_b is set equal to zero in the region $x \geq x_s$ during the time-marching computation. Introducing a new parameter I defined as

$$I = \begin{cases} 0 & \text{for Region 2 } (0 \leq x \leq x_s) \\ 1 & \text{for Region 3 } (x_s \leq x \leq x_w) \end{cases} \tag{6.13}$$

the continuity equations for Regions 2 and 3, Eqs. 3.31 and 3.41, can be unified as follows:

$$p_u q_b - \frac{\partial m_p}{\partial x} - I\,\frac{\partial \eta}{\partial t} = 0 \tag{6.14}$$

Integrating Eq. 6.14 with the definition of the time average given by Eq. 5.25 yields the time-averaged equation of mass for Regions 2 and 3.

$$p_u\overline{q_b} - \frac{d\overline{m_p}}{dx} - \int_{t_{min}}^{t_{max}} I\frac{\partial \eta}{\partial t}dt = 0 \tag{6.15}$$

For random waves, the computation duration is typically long and $(t_{max} - t_{min})$ is much greater than unity. The terms associated with water storage effects and involving the integral limits t_{min} and t_{max} in Eqs. 6.11 and 6.15 should then be negligible, and Eqs. 6.11 and 6.15 may be approximated by

$$\frac{d\overline{m}}{dx} + p_q\overline{q_b} = 0 \tag{6.16}$$

$$p_q\overline{q_b} - n_p\,\frac{d\overline{m_p}}{dx} = 0 \tag{6.17}$$

The computed spatial variations of $\frac{d\overline{m}}{dx}$, $p_q\overline{q_b}$, and $-n_p\frac{d\overline{m_p}}{dx}$ are plotted in Figures 6.32 and 6.33 for Run P2 to check whether the computed results satisfy Eqs. 6.16 and 6.17.

To show that the last terms in Eqs. 6.11 and 6.15 are indeed negligible, the last term of Eq. 6.11 is expressed as

$$R_h(x) = \frac{h(x, t_{max}) - h(x, t_{min})}{t_{max} - t_{min}} \tag{6.18}$$

For I=1, the last term of Eq. 6.15 is identical to R_h given by Eq. 6.18 since $\eta(x,t) = h(x,t) + z_b(x)$. The largest absolute value of R_h for the three runs are listed in Table 6.5. Compared to the values of $\frac{d\overline{m}}{dx}$, $p_q\overline{q_b}$, and $n_p\frac{d\overline{m_p}}{dx}$ as plotted in Figures 6.32 and 6.33 for Run P2, the value of R_h is indeed negligible. This is also true for Runs P1 and P3. Thus, the water storage effects in Eqs. 6.11 and 6.15 are negligible for the three runs.

Figure 6.32 also shows the sum of the two terms in Eq. 6.16 as a function of x for Run P2. Eq. 6.16 requires that the sum be zero. Similarly, Figure 6.33 also shows the sum of the two terms $p_q\overline{q_b}$ and $-n_p\frac{d\overline{m_p}}{dx}$ in Eq. 6.17 as a function of x for Run P2 where Eq. 6.17 requires that the sum be zero. These requirements are not satisfied in the vicinity of the still waterline on the upper slope where z_b=0 (located at x=1.22 for Run P2). The computed results for Runs P1 and P3 are similar to those shown in Figures 6.32 and 6.33 for Run P2. This problem may be attributed to the landward boundary condition, which is somewhat intuitive, used in the numerical model of WK 92. It should be noted that the time-averaged quantities are harder to predict accurately since they are small relative to the corresponding time-varying quantities as shown in Figures 6.23, 6.24, and 6.26.

Figure 6.34 shows the spatial variations of three normalized time-averaged volume fluxes: the horizontal volume flux $\overline{m}$ in Region 1, the volume influx $\overline{q_b}$ (shown as

Table 6.5: Largest absolute values of R_h, R_E, and R_{E_P}.

RUN	$\|R_h\|_{max}$	$\|R_E\|_{max}$	$\|R_{E_P}\|_{max}$
P1	.003956	.002515	.000178
P2	.000976	.000454	.000057
P3	.003544	.001723	.000398

$p_q\overline{q_b}$) between Regions 1 and 2, and the horizontal discharge $\overline{m_p}$ (shown as $n_p\overline{m_p}$) in Regions 2 and 3 for Runs P2 and P3. The time-averaged volume flux $\overline{q_b}$ is into the permeable underlayer above SWL and out of the permeable underlayer below SWL where q_b has been taken to be positive downward. Correspondingly, the time-averaged volume fluxes $\overline{m}$ and $\overline{m_p}$ are landward and seaward, respectively, in the vicinity of SWL. The mean depth-averaged horizontal velocity u in Region 1 and the mean vertically-averaged discharge velocity u_p in Regions 2 and 3 have been plotted in Figures 6.22 and 6.25, respectively. The computed values of $\overline{u_p}$ are negative and consistent with the computed seaward volume flux inside the permeable underlayer. On the other hand, the computed values of $\overline{u}$ are negative below SWL and positive above SWL. Since $\overline{u}$ is negative and related to undertow for impermeable slopes as shown by Kobayashi, DeSilva, and Watson (1989), the permeability effect produces the time-averaged landward volume flux and fluid velocity above SWL. The overall mass balance requires that the three time-averaged volume fluxes approach zero at x=0. Figure 6.34 indicates that $\overline{m}$ approaches a very small negative value at x=0. The computed results for Run P1 show similar patterns. This implies that the seaward boundary condition used in the numerical model may need to be adjusted to predict $\overline{m}$=0 at x=0.

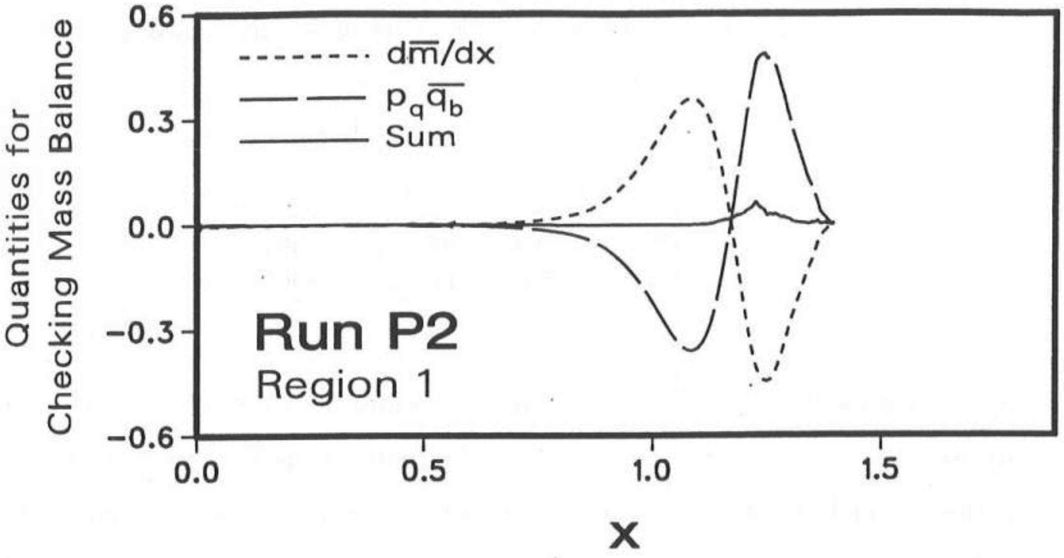

Figure 6.32: Mass balance for Region 1 for Run P2.

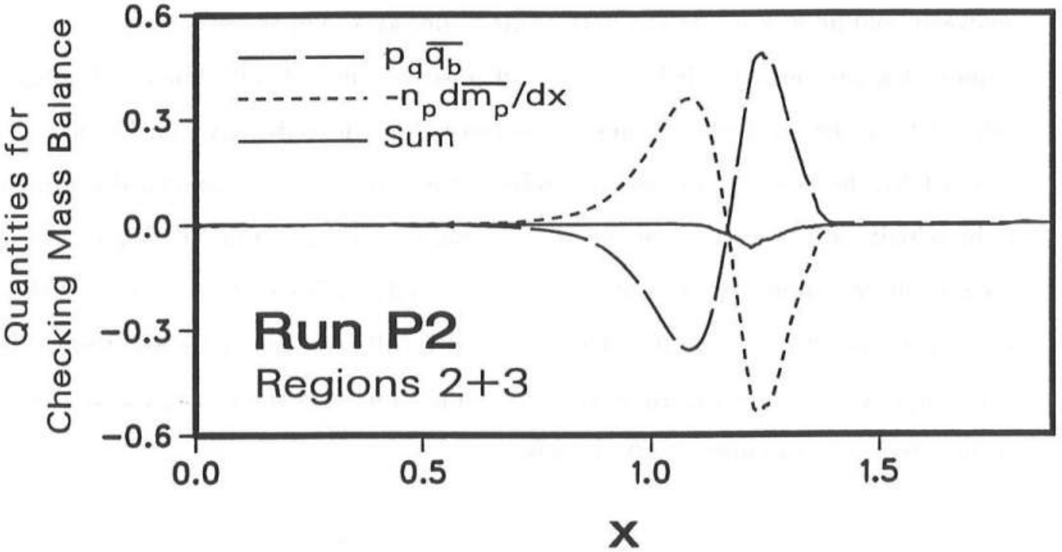

Figure 6.33: Mass balance for Regions 2 and 3 for Run P2.

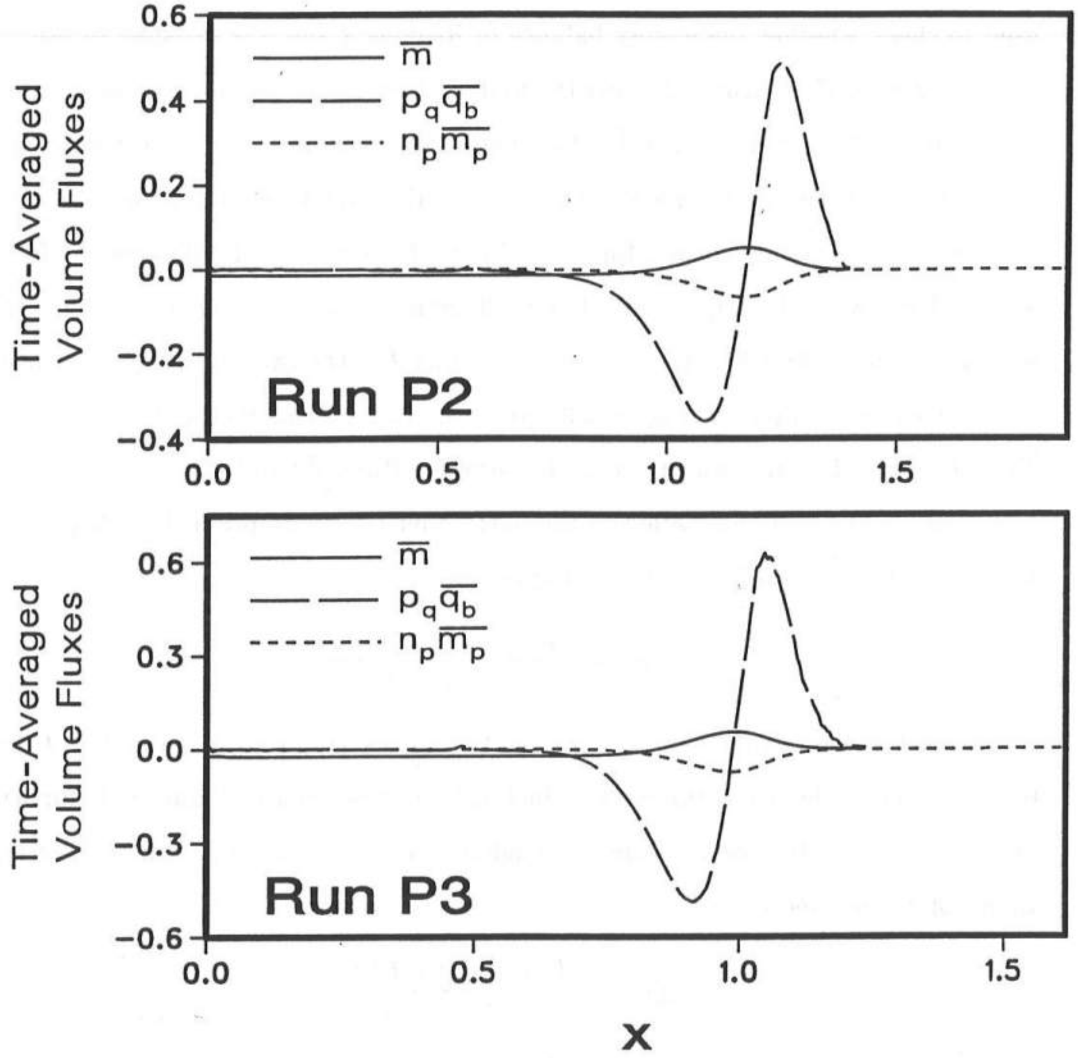

Figure 6.34: Time-averaged volume fluxes for Runs P2 and P3.

6.7 Time-Averaged Energy Balance

The time-averaged energy equations derived in Section 5.4 serve the following purposes in this study: (**1**) Eq. 5.30 is used to estimate the normalized time-averaged rate of energy dissipation per unit horizontal area in Region 1, $\overline{D}$, and (**2**) Eq. 5.32 is used to check whether the energy balance in Regions 2 and 3 is satisfied or not.

Figure 6.35 for Run P2 shows the four time-averaged normalized energy quantities in Region 1: the specific energy $\overline{E}$, the horizontal energy flux $\overline{F}$, the vertical energy flux $\overline{D_p}$, the rate of energy dissipation $\overline{D}$, of which the first three quantities are computed and the last is estimated using Eq. 5.30. Figure 6.36 for Run P2 depicts the four time-averaged normalized energy quantities in Region 2 and 3: the specific energy $\overline{E_p}$, the horizontal energy flux $\overline{F_p}$, the vertical energy flux $\overline{D_p}$, the rate of energy dissipation $\overline{D_r}$, all of which are computed. Figure 6.37 plots the three terms involved in Eq. 5.32: $\frac{d\overline{F_p}}{dx}$, $\overline{D_r}$, $-\overline{D_p}$, and the sum, which should be zero, for Runs P2 and P3.

Eq. 5.32 is a simplification of Eq. 5.31 under the assumption that $(t_{max} - t_{min}) \gg 1$. The neglected term in Eq. 5.31 is expressed as R_{E_P}:

$$R_{E_P}(x) = \frac{E_P(x, t_{max}) - E_P(x, t_{min})}{t_{max} - t_{min}} \tag{6.19}$$

The largest absolute values of R_{E_P} for the three runs are listed in Table 6.5. Compared to the values of the other three terms in Eq. 5.31 as plotted in Figure 6.37 for Runs P2 and P3, the neglected term is indeed negligible. Table 6.5 also shows the largest absolute values of R_E defined as

$$R_E(x) = \frac{E(x, t_{max}) - E(x, t_{min})}{t_{max} - t_{min}} \tag{6.20}$$

which is the last term in Eq. 5.30, to show that this term is also small. In the numerical model, however, Eq. 5.30 used to estimate the normalized rate of energy dissipation, $\overline{D}$, is *not* simplified by neglecting the term defined by Eq. 6.20.

The specific energy $\overline{E}$ shown in Figure 6.35 increases somewhat and then decreases landward, whereas the energy flux $\overline{F}$ decreases landward. This decrease of $\overline{F}$ in Eq. 5.30 is mostly caused by the energy flux $\overline{D_p}$ into the permeable underlayer. The double peaks of $\overline{D_p}$ in the vicinity of the still waterline where $z_b = 0$ may be related to the spatial variation of $\overline{q_b}$ shown in Figure 6.34 where D_p is defined by Eqs. 5.9 and 5.28. The rate of energy dissipation $\overline{D}$ due to the shear stress in the flow over the rough slope is small for Run P2 as shown in Figure 6.35. This is also true even for Run P1 with the surf similarity parameters ξ=1.72 and ξ_p=1.88, as listed in Table 6.1, which would correspond to plunging waves if the slope were impermeable. The small dissipation rate in the flow over the rough slope is in qualitative agreement with the visual observations of Kobayashi, Cox, and Wurjanto (1991) who noticed more intense wave breaking and chaotic flow on the impermeable slope than on the permeable slope.

The rate of energy dissipation $\overline{D_r}$ inside the permeable underlayer depicted in Figure 6.36 is roughly the same as $\overline{D_p}$ except in the region of $\overline{D_p}$=0 which is situated landward of the intersection between the envelope of η_{max} and the upper slope in Figure 6.21. This implies that $\overline{D_p}$ and $\overline{D_r}$ are dominant in Eq. 5.32 except that $\frac{d\overline{F_p}}{dx}=-\overline{D_r}$ when $\overline{D_p}$=0.

Eq. 5.32 requires that the sum of the three terms $\frac{d\overline{F_p}}{dx}$, $\overline{D_r}$, and $-\overline{D_p}$ be zero. This requirement is not satisfied in the vicinity of the still waterline on the upper slope where z_b=0, as shown in Figure 6.37 for Runs P2 and P3. This problem is similar to the time-averaged mass balance problem discussed in the preceding section, indicating some numerical difficulties at the moving waterline. It can be seen in Figure 6.37 that the results for Runs P2 and P3 look similar. The corresponding results for Run P1 is also similar. The permeability effects appear to reduce the differences associated with the surf similarity parameters ξ and ξ_p listed in Table 6.1.

The numerical damping coefficients ϵ_1 and ϵ_2 are listed as input to the numerical model in Table 6.2. These coefficients are associated with the artificial dissipation of the Lax-Wendroff scheme used to solve the flow field in Region 1. One may legitimately question how these user-specified coefficients influence the outcome of the numerical model. To answer this question, a second computation for Run P1 is executed using $\epsilon_1=\epsilon_2=3$ as compared to $\epsilon_1=\epsilon_2=1$ in the first computation. This difference in the value of the damping coefficients should appear in the time-averaged energy quantities for Region 1 such as those plotted in Figure 6.35. Figure 6.38 presents the time-averaged energy quantities for Region 1 from the two computations for Run P1. The increase of the numerical damping coefficients ϵ_1 and ϵ_2 has not caused any noticeable difference, indicating that the computed results are not sensitive to the values of ϵ_1 and ϵ_2 of the order unity.

Further, one may ask whether the artificial numerical dissipation described in Section 4.3 is needed at all in this numerical model. To answer this question, a third computation for Run P1 is executed using $\epsilon_1=\epsilon_2=0$ which means that the artificial numerical dissipation is deactivated. Figure 6.39 presents the time-averaged energy quantities for Region 1 from the first computation for Run P1 using $\epsilon_1=\epsilon_2=1$ and the third computation using $\epsilon_1=\epsilon_2=0$. There is no noticeable difference between the two results. This implies that the dissipation of energy in Region 1 is numerical but implicit since the physical dissipation mechanism in Region 1 is not modeled in the present one-dimensional model. In this case, the artificial explicit damping of the Lax-Wendroff method has turned out to be secondary perhaps because the energy dissipation in Region 1 is small relative to that in Regions 2 and 3 as shown in Figures 6.35 and 6.36. However, the artificial damping has been effective in reducing numerical problems. The computation using $\epsilon_1=\epsilon_2=0$ has undergone considerably more [remediable] numerical problems than those using non-zero ϵ_1 and ϵ_2. It is therefore recommended that the numerical damping coefficients ϵ_1 and ϵ_2 be specified to be on the order of unity to reduce possible numerical problems.

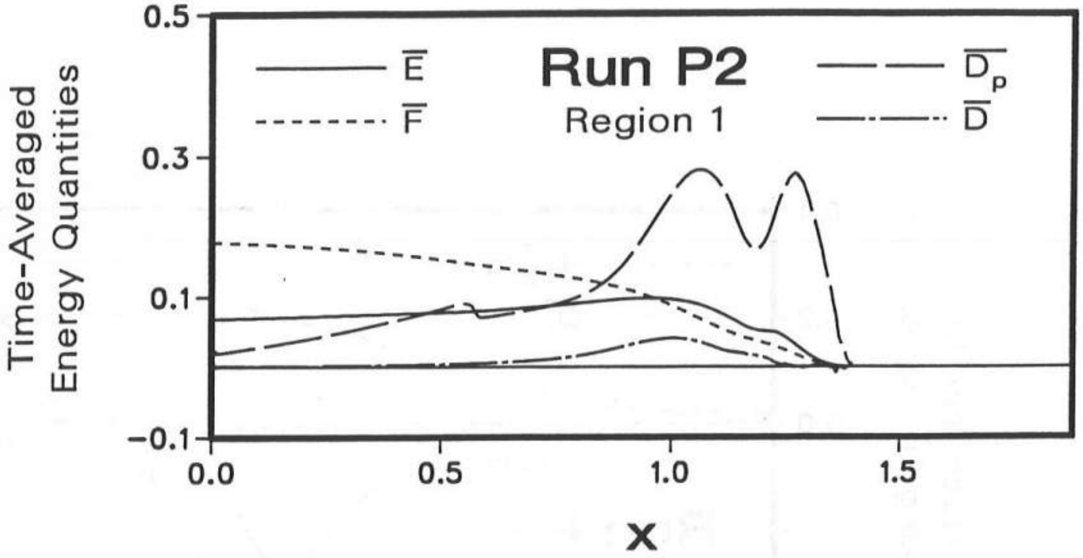

Figure 6.35: Time-averaged energy quantities for Region 1 for Run P2.

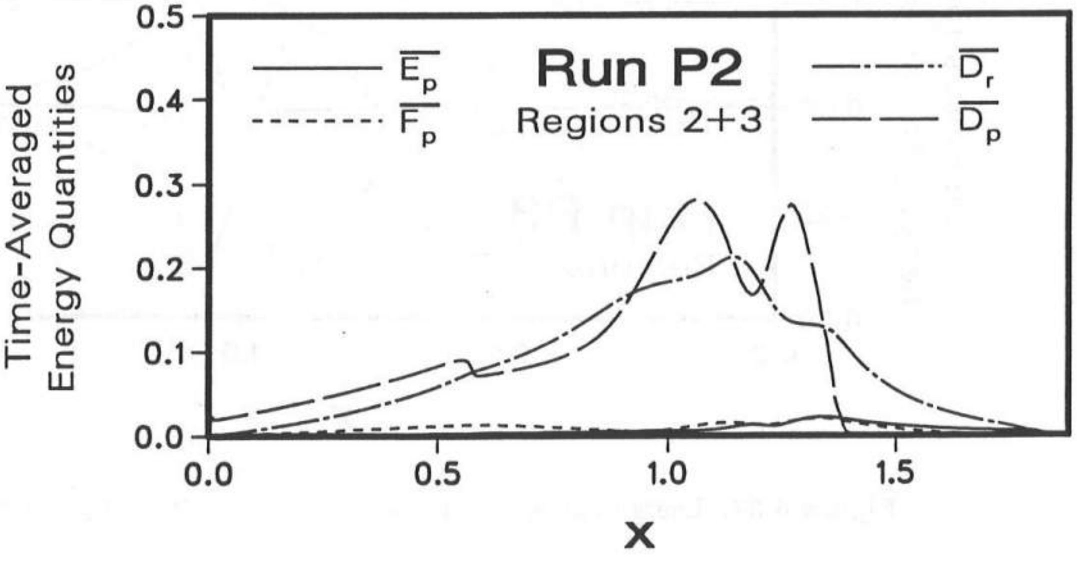

Figure 6.36: Time-averaged energy quantities for Regions 2 and 3 for Run P2.

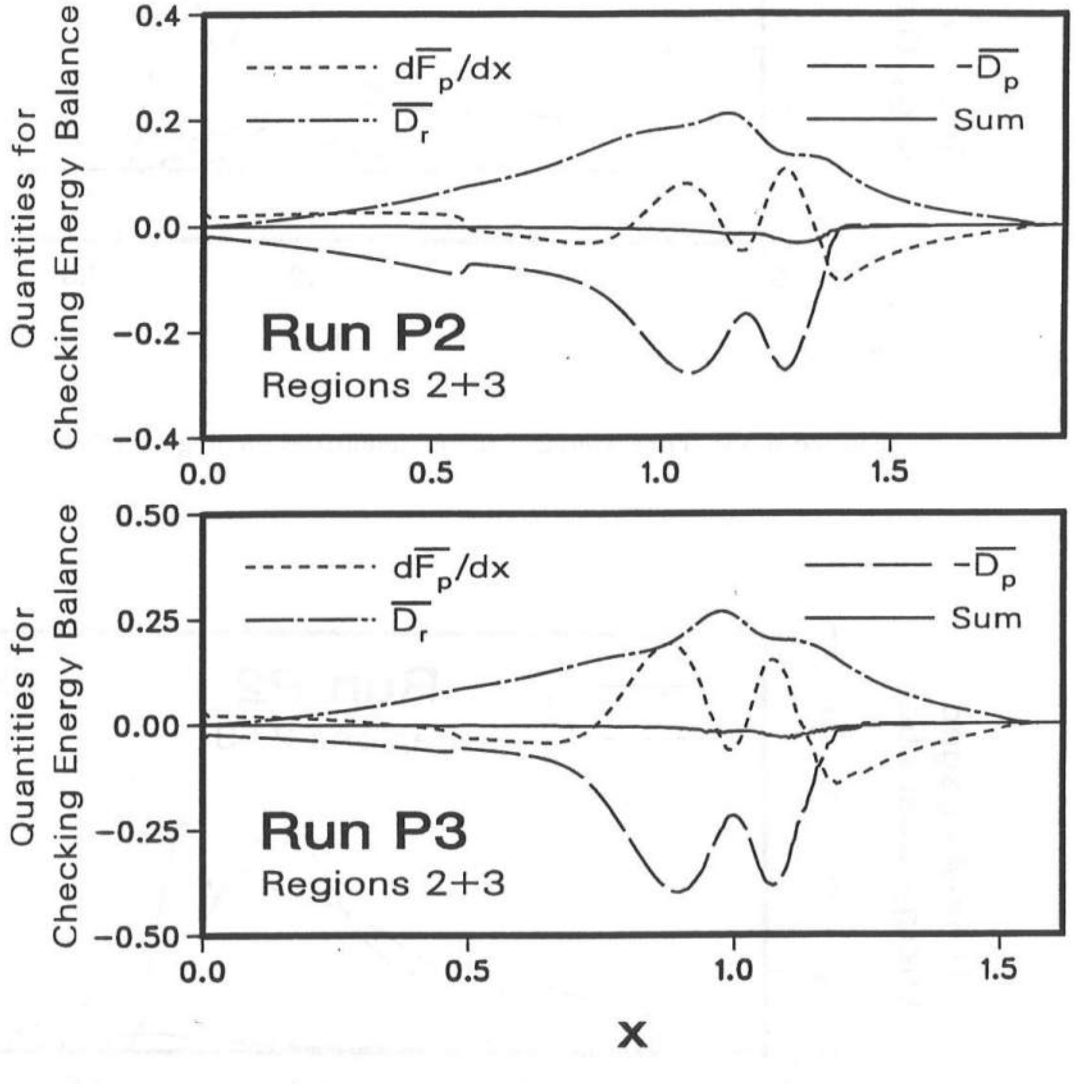

Figure 6.37: Energy balance for Regions 2 and 3 for Runs P2 and P3.

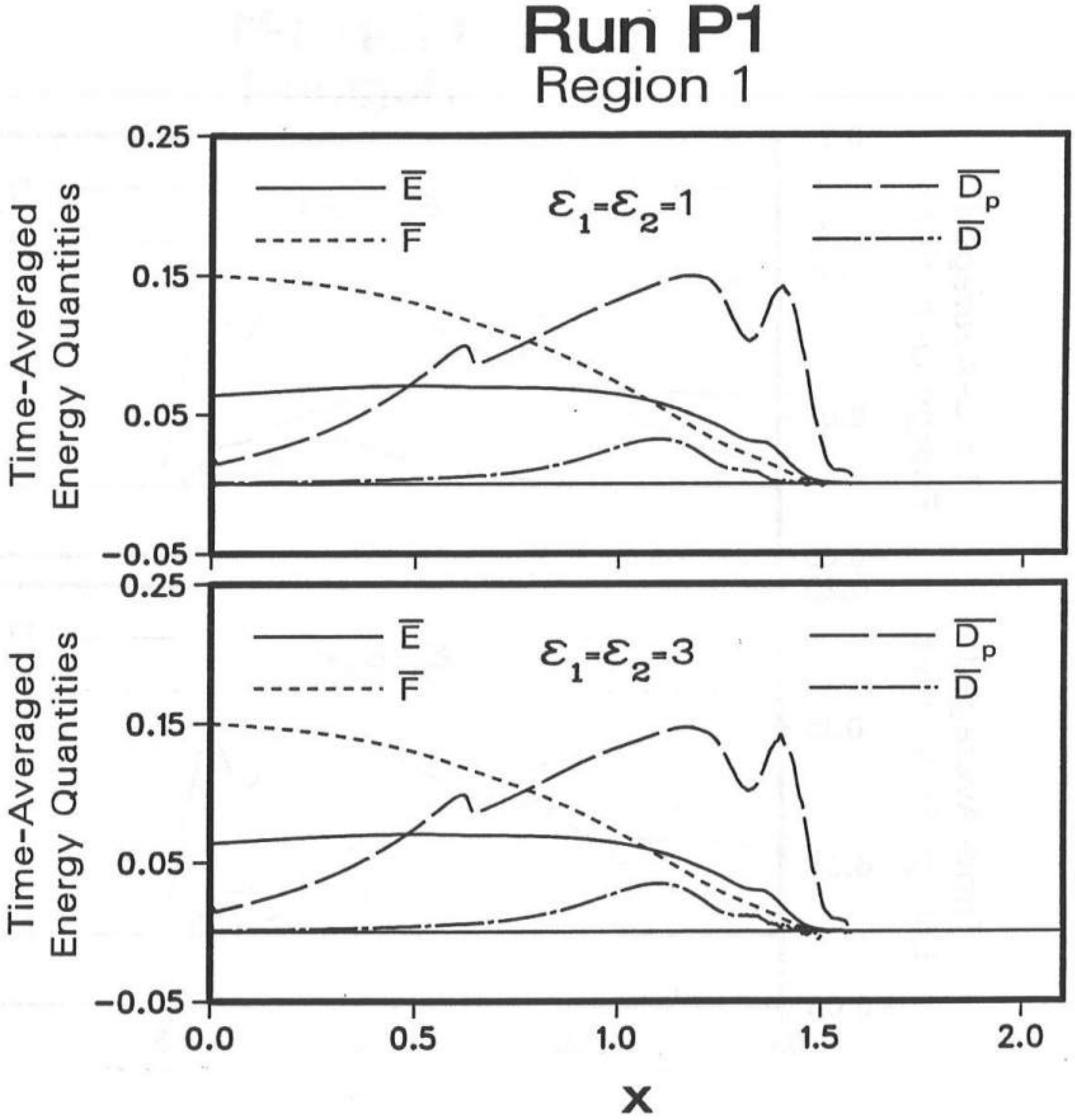

Figure 6.38: Time-averaged energy quantities for Region 1 for Run P1 from two computations with $\epsilon_1=\epsilon_2=1$ and $\epsilon_1=\epsilon_2=3$.

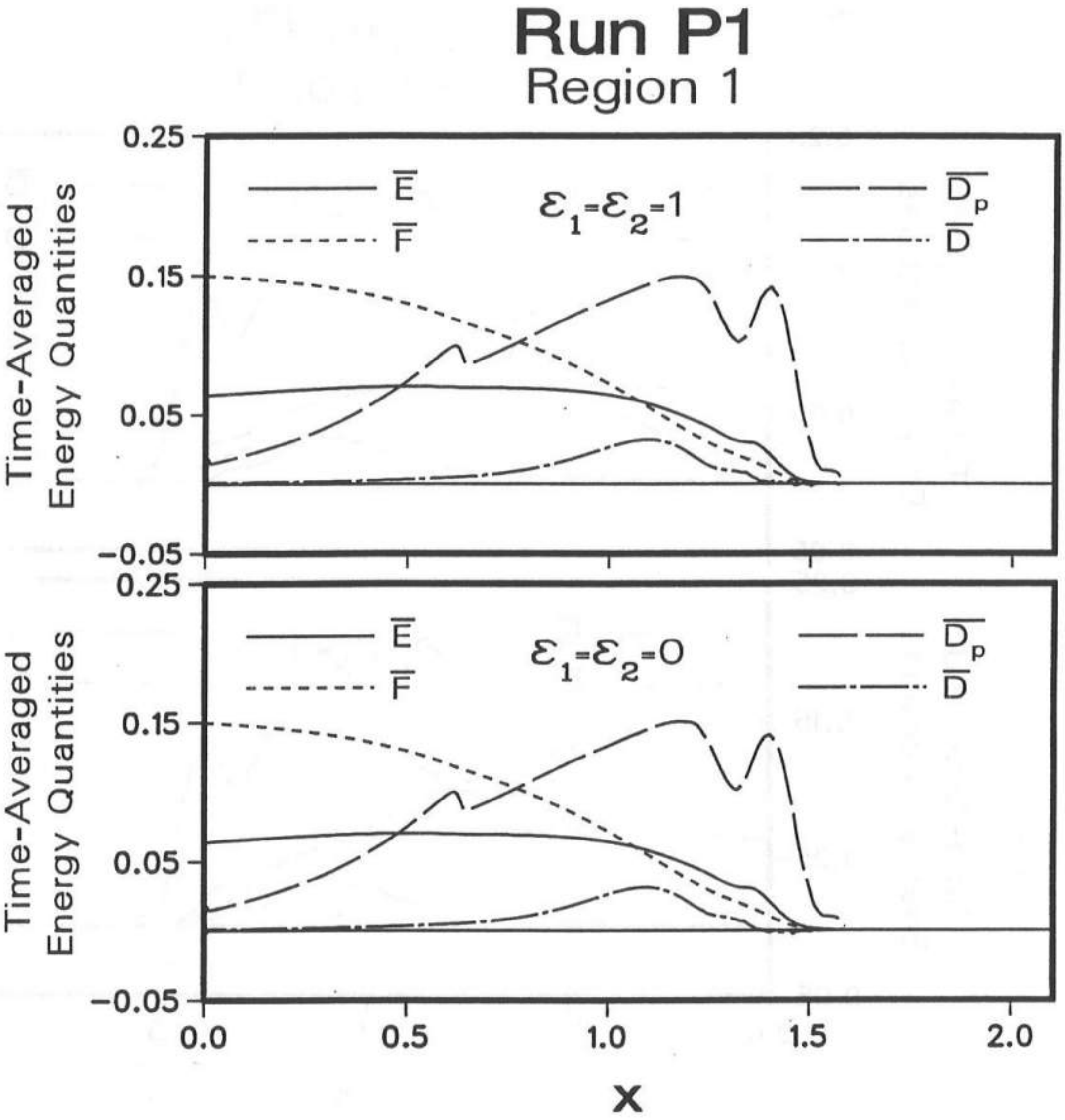

Figure 6.39: Time-averaged energy quantities for Region 1 for Run P1 from two computations with $\epsilon_1=\epsilon_2=1$ and $\epsilon_1=\epsilon_2=0$.

6.8 Sensitivity of Computed Results to Finite Difference Grid

The finite difference grid in the numerical model PBREAK consists of the space interval Δx and the time step Δt. The space interval Δx is fixed during a computation, whereas the time step Δt may vary.

Section 6.5 has shown two computations for each of Runs P2 and P3 using different values of Δt but the same value of Δx. The computed results have been presented in term of the spatial variations of the mean $\overline{u}$, maximum u_{max}, and minimum u_{min} of the depth-averaged horizontal velocity u in Figures 6.27 and 6.28. On the other hand, Section 6.7 has shown three computations for Run P1 using the same value of Δx but different values of the damping coefficients ϵ_1 and ϵ_2, which result in different values of Δt since the increase of ϵ_1 and ϵ_2 causes the reduction of Δt to satisfy the numerical stability criterion given in WK 92. The results have been presented in Figures 6.38 and 6.39 in terms of the time-averaged energy quantities in Region 1. It may be concluded from these figures that the computed results are not sensitive to the time step Δt as long as the numerical stability criterion is satisfied for the specified space interval Δx which needs to be small enough to yield an adequate spatial resolution.

To examine the effect of different values of the space interval Δx, two more computations for Run P1 are performed using $\Delta x'$=0.0075m and $\Delta x'$=0.004m, in contrast to the previous three computations with $\Delta x'$=0.006m where the normalized space interval is given by $\Delta x = \dfrac{\Delta x'}{T'\sqrt{gH'}}$ with T'=1.082s and H'=0.0685m for Run P1. These space intervals are small relative to the computation domain shown in Figure 6.1. Figure 6.40 shows the spatial variations of the the mean $\overline{\eta}$, maximum η_{max}, and minimum η_{min} of the free surface and water table elevation η from the three computations for Run P1 with the same damping coefficients ϵ_1=ϵ_2=1 but the different values of Δx. It may be concluded from this figure that the computed results are not sensitive to the space interval Δx as long as Δx is sufficiently small. It is noted that the different values of Δx result in the different values of Δt because of the imposed numerical stability criterion.

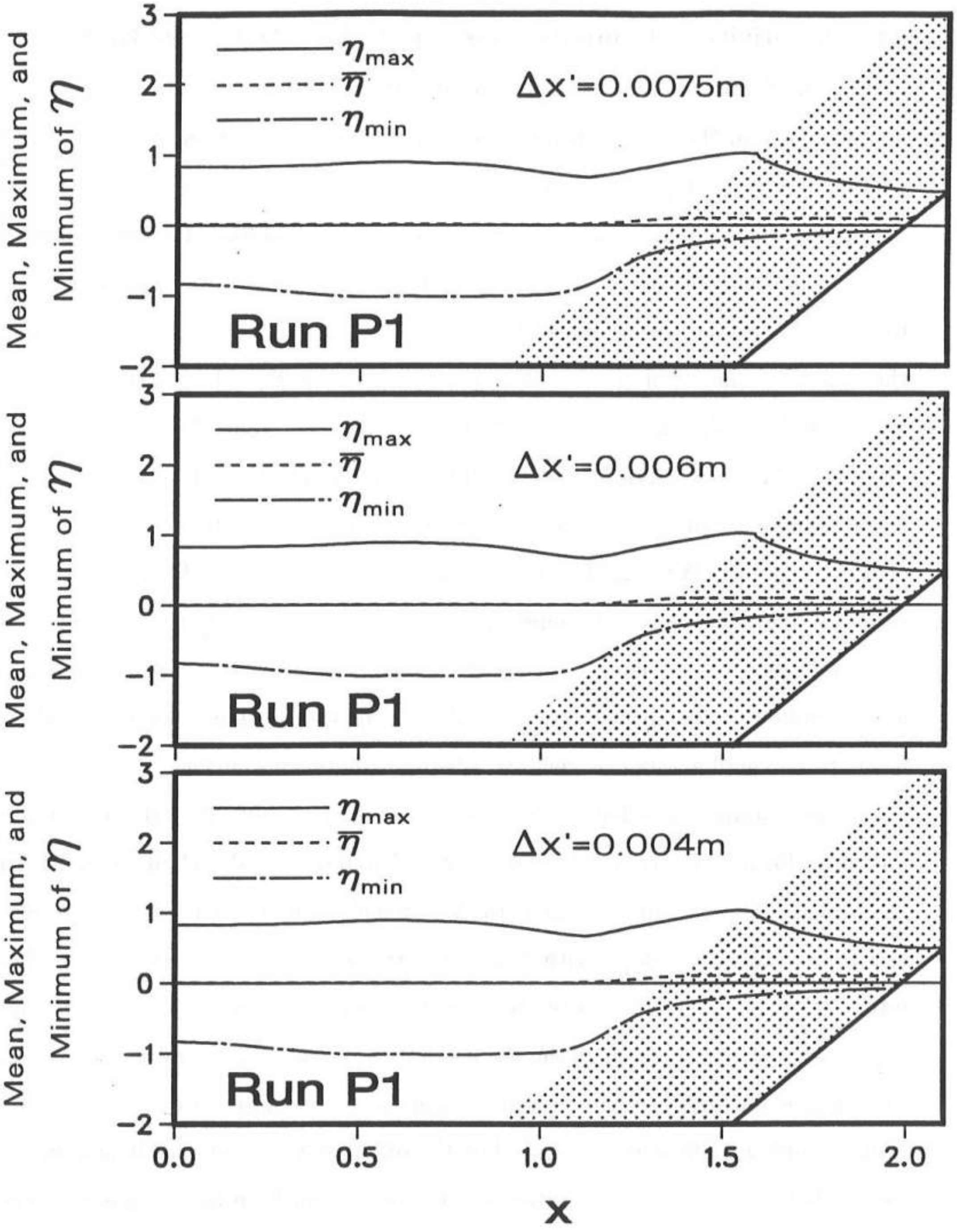

Figure 6.40: Mean, maximum, and minimum values of free surface and water table elevation η for Run P1 from three computations with different values of Δx.

Chapter 7

COMPARISON BETWEEN PERMEABLE AND IMPERMEABLE SLOPES

7.1 Introduction

Kobayashi, Cox, and Wurjanto (1991) examined the permeability effects on irregular wave run-up and reflection by comparing the six test runs for the permeable and impermeable slopes conducted by Cox (1989). It was found very difficult to generate the identical incident wave trains for the permeable and impermeable slope tests in a wave tank.

In the present work, use is made of the numerical model for impermeable slopes developed by Wurjanto and Kobayashi (1991) to compute the *hypothetical* Run IJ with J=1,2,3 in which the impermeable slope without the permeable underlayer is subjected to the same incident irregular wave train of Run PJ explained in Chapter 6. This chapter examines how the permeable and impermeable slopes affect the flow fields induced by the identical incident irregular wave train.

The input data related to the incident wave trains have already been explained in Chapter 6. The impermeable structure geometry is given by Figure 6.1 with the upper slope being impermeable. The following input parameters for Run IJ with J=1,2,3 are identical to those for Run PJ summarized in Section 6.2:

- Bottom friction factor f'.
- Space interval Δx of the finite difference grid.
- Physical water depth δ'_r associated with the waterline meter used to measure the waterline oscillations on the rough permeable slope.

- Physical water depth δ'_a marking the landward limit of the armor stability computation, which is taken as the median gravel diameter.
- All the armor stability parameters required as input to the numerical model.

The numerical model RBREAK of Wurjanto and Kobayashi (1991) used to compute Runs I1, I2, and I3 uses a finite-difference scheme similar to the dissipative Lax-Wendroff method discussed in Section 4.3. The damping coefficients ϵ_1 and ϵ_2 are required as input. The landward boundary algorithm of RBREAK at the moving waterline on the impermeable slope is similar but more involved than the simplified treatment at the moving waterline x_w on the impermeable slope of the present numerical model PBREAK. The largest normalized water depth δ_s defining its computational waterline is also required as input to RBREAK. Table 7.1 lists the values of ϵ_1, ϵ_2, and δ_s specified for Runs I1, I2, and I3. Also listed is the largest allowable value of the time step Δt used in each run.

It is relevant to mention here that Kobayashi and Wurjanto (1992), who applied the numerical model RBREAK to beaches, found that their computations using $\epsilon_1=\epsilon_2=1$ and $\epsilon_1=\epsilon_2=2$ produced essentially the same results. The discussion in Section 6.7 related to Figure 6.38, where $\epsilon_1=\epsilon_2=1$ and $\epsilon_1=\epsilon_2=3$ are used, has come to the same conclusion for the numerical model PBREAK. The damping coefficients ϵ_1 and ϵ_2 of the order unity may influence the numerical stability of the dissipative Lax-Wendroff scheme where the increase of the damping coefficients tends to improve the numerical stability of the computation. However, these coefficients do not make any noticeable difference in the computed results as long as the computation is successful.

The subsequent sections compare and discuss the computed results for the flow fields over the rough permeable and impermeable slopes for Runs PJ and IJ with J=1, 2, and 3.

7.2 Irregular Wave Reflection

Figure 7.1 shows the computed reflected wave spectra $S_r(f_*)$ for the six runs. This figure indicates that the permeable underlayer dissipates the incident high-frequency

Table 7.1: Computation parameters specified as input to computations for Runs I1, I2, and I3.

Run No.	Largest Δt	ϵ_1	ϵ_2	δ_s
(1)	(2)	(3)	(4)	(5)
I1	0.001176	1	1	0.003
I2	0.000667	2	2	0.003
I3	0.000526	2	2	0.003

wave components but damps low-frequency wave components little. This is consistent with the conclusion drawn from the discussion comparing the waterline oscillations on the upper and lower slopes in Section 6.5.

The computed values of the average reflection coefficient $\overline{r}$ defined by Eq. 6.8 for the six runs are listed in columns (2) and (7) of Table 7.2. The zero moment $(m_o)_r$ in Eq. 6.8 is computed from the spectra shown in Figure 7.1. Comparison of the values of $\overline{r}$ for the permeable and impermeable slopes exposed to the same incident irregular wave train indicates that the thick permeable underlayer reduces $\overline{r}$ by a factor of more than two.

Figures 7.2 and 7.3 depict the computed reflection coefficient $r(f_*)$ defined by Eq. 6.7 together with the coherence squared γ_{ir}^2 and the phase difference θ_{ir} between the incident and reflected waves for Runs P1 and I1 as well as P3 and I3. The computed values of the reflection coefficient r exceeding unity for Run I1 in Figure 7.2 may not be correct since r should not exceed unity unless additional waves propagating seaward are generated in the region $x > 0$. It is also noted that the coherence squared for Run I1 shown in Figure 7.2 is well below unity.

The plots of the coherence squared γ_{ir}^2 and the phase difference θ_{ir} for Run I3 shown in Figure 7.3 may be more reliable than those for Run I1. The permeability effects on the coherence and phase difference may thus be discussed using Figure 7.3. The results for Runs P2 and I2, which are not presented here, show trends similar to

Table 7.2: Computed values of average reflection coefficient $\overline{r}$, wave set-up $\overline{Z_r^U}$, significant swash height h_s^U, significant run-up R_s^U, and maximum run-up R_{max} for permeable (P) and impermeable (I) slopes.

RUN No.	PERMEABLE (P)					IMPERMEABLE (I)				
	$\overline{r}$	$\overline{Z_r^U}$	h_s^U	R_s^U	R_{max}^U	$\overline{r}$	$\overline{Z_r^U}$	h_s^U	R_s^U	R_{max}^U
(1)	(2)	(3)	(4)	(5)	(6)	(7)	(8)	(9)	(10)	(11)
1	0.093	0.061	1.067	0.573	1.006	0.195	0.123	1.648	0.914	1.482
2	0.154	0.047	1.413	0.781	1.112	0.549	0.138	2.741	1.521	2.199
3	0.282	0.051	2.092	1.192	2.280	0.658	0.113	3.201	1.718	3.239

those shown in Figure 7.3 for Runs P3 and I3. Figure 7.3 indicates that the permeability effects on the coherence is limited to the high-frequency range, for which both numerical models do not perform very well anyway. The phase differences shown in Figure 7.3 indicate that the travel time up-slope from x=0 and then back down-slope to x=0, as explained in Section 6.3, on the impermeable slope is slightly greater than that on the corresponding permeable slope. These findings based on the computed results are in accordance with those based on the corresponding measured results presented and explained by Kobayashi, Cox, and Wurjanto (1991).

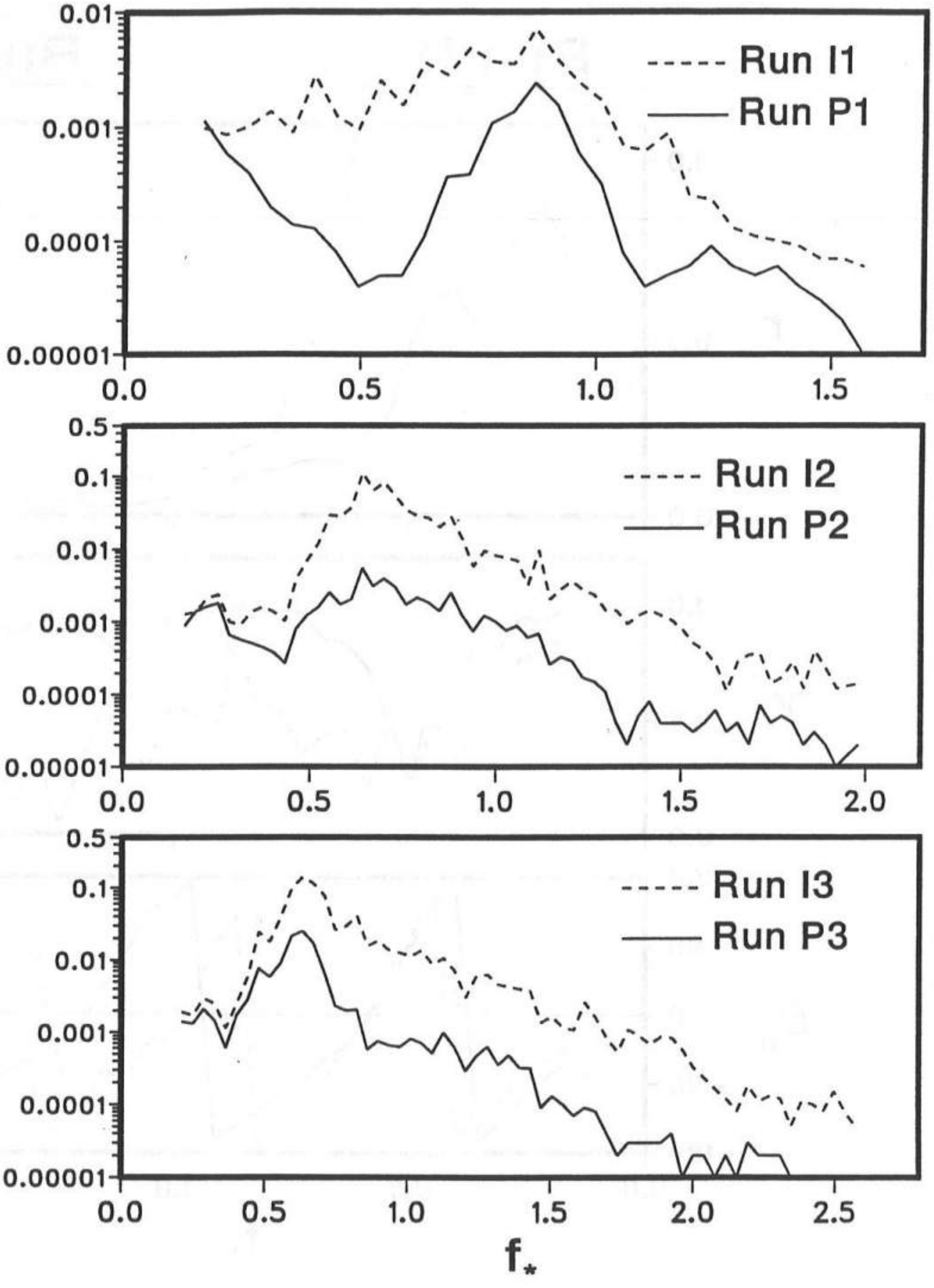

Figure 7.1: Computed reflected wave spectra at x=0 for six runs.

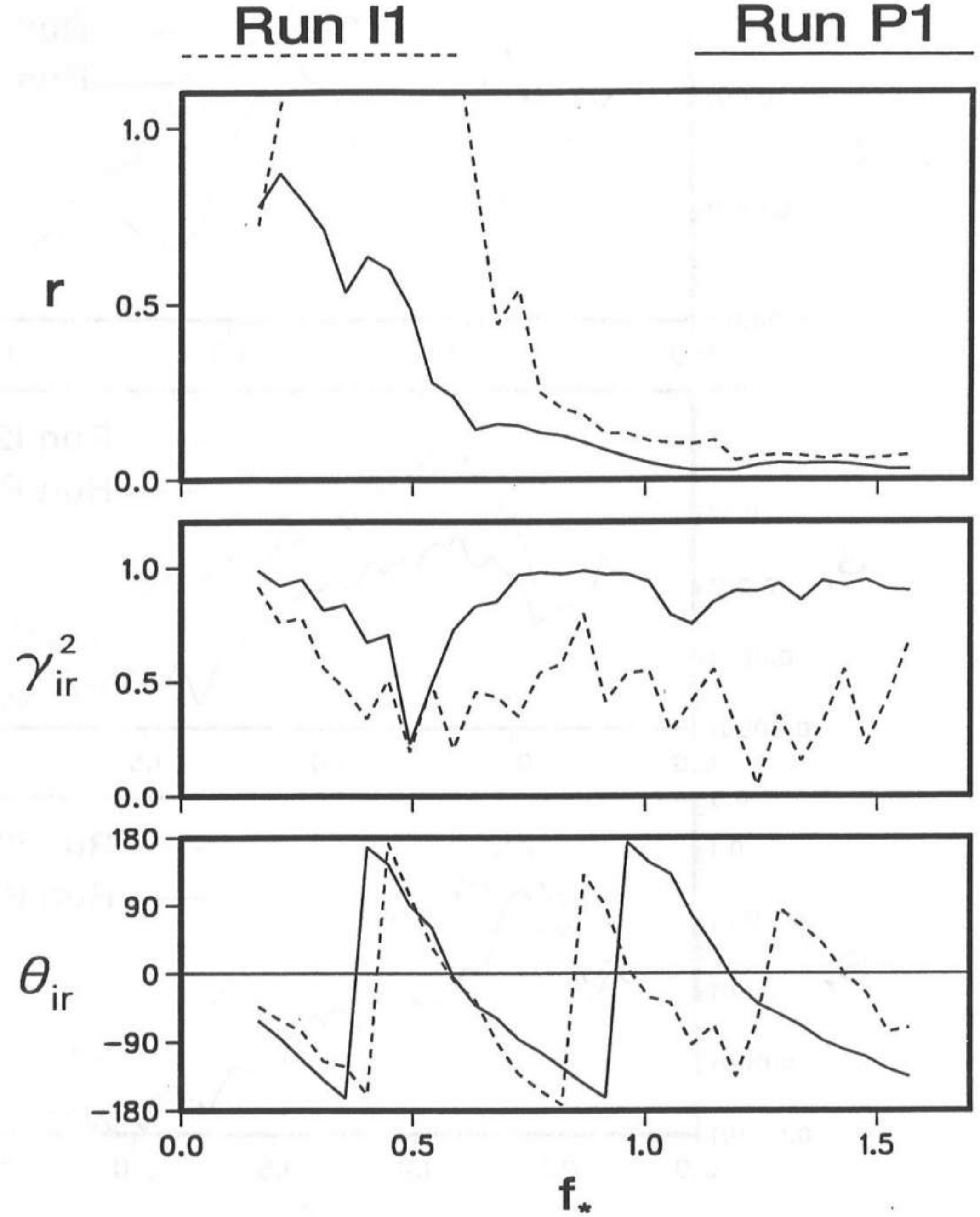

Figure 7.2: Computed reflection coefficient, coherence and phase between incident and reflected waves at $x=0$ for Runs P1 and I1.

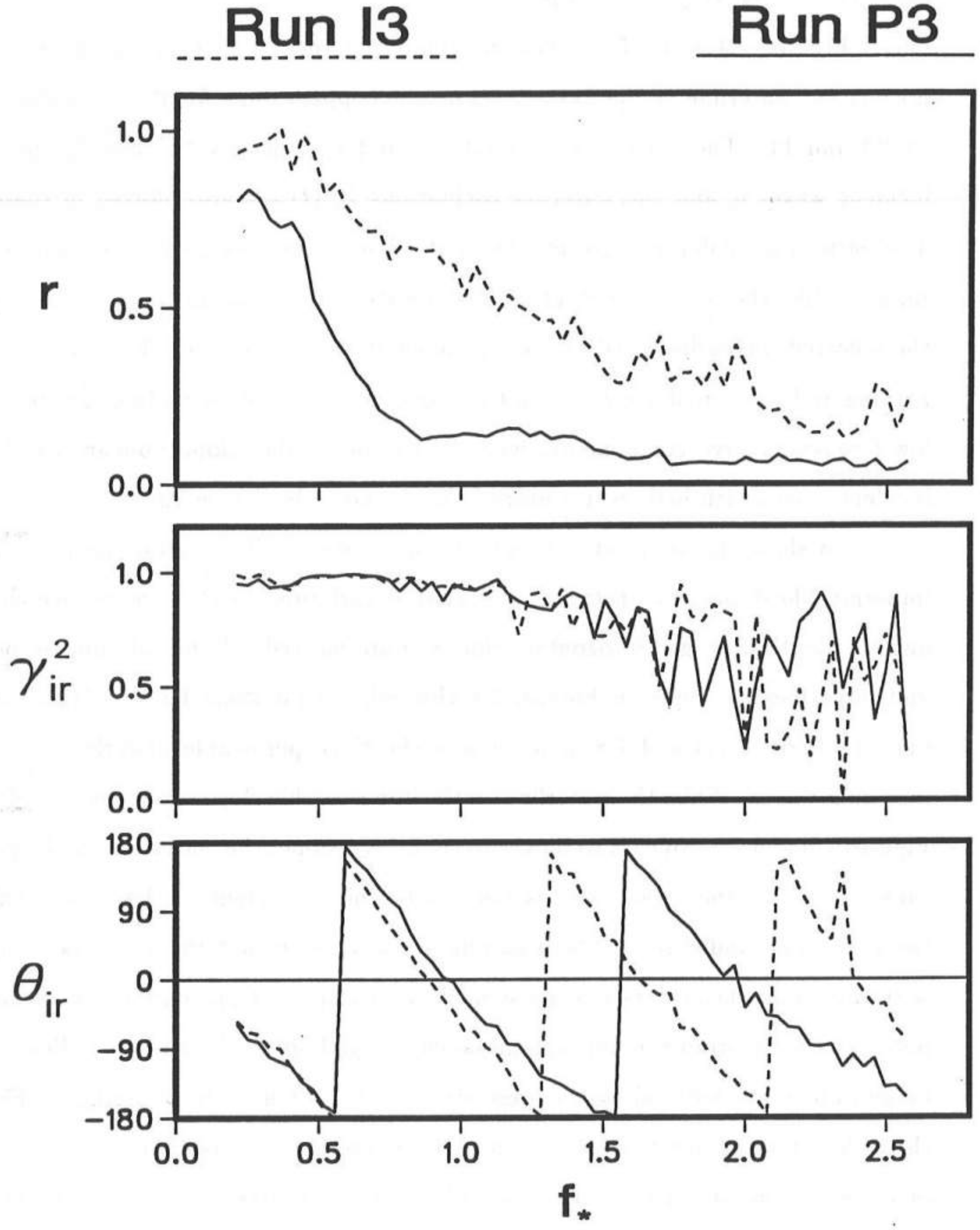

Figure 7.3: Computed reflection coefficient, coherence and phase between incident and reflected waves at x=0 for Runs P3 and I3.

7.3 Irregular Wave Run-up

Figures 7.4 and 7.5 present the computed spectra $S_U(f_*)$ corresponding to the normalized waterline oscillations $Z_r^U(t)$ on the (upper) slope for Runs P1 and I1 as well as P3 and I3. The coherence squared γ_{iU}^2 and the phase difference θ_{iU} between the incident waves η_i and the waterline oscillations $Z_r^U(t)$ are also plotted in these figures. The permeable underlayer reduces the waterline oscillations across the entire frequency range, unlike the selective reduction of the waterline oscillations on the lower slope and the reflected waves discussed in Sections 6.5 and 7.2, respectively. The interaction of up-rushing and down-rushing water on the impermeable slope seems to generate additional low-frequency wave components, whereas the permeable slope appears to absorb the incident waves with little water up-rushing as shown in Figure 7.6.

To show the contrast between the waterline oscillations on the permeable and impermeable slopes, the instantaneous spatial variations of the free surface elevation η and the depth-averaged horizontal velocity u are plotted side by side for the permeable and impermeable slopes in Figures 7.6 through 7.9 for Runs P1 and I1 as well as P3 and I3. Figures 7.6 and 7.8 indicate how the thick permeable underlayer absorbs the incoming waves. While the waterline on the impermeable slope shown on the left panel of Figures 7.6 and 7.8 appears to moves freely on the slope, the waterline on the permeable slope shown on the right panel is tied up to the movement of the water table inside the permeable underlayer. These two figures also show that the water table inside the permeable underlayer does not move much, which in effect prevents the waterline on the permeable slope from running up and down freely. Figures 7.7 and 7.9 indicate that the magnitude of u is reduced by the presence of the thick permeable underlayer. Figures 7.6 through 7.9 also show that the permeable underlayer does not allow very steep fronts of waves to develop in the surf zone. The very steep fronts on the impermeable slope are associated with the local phenomena of wave breaking, which can not be predicted accurately by the two numerical models used herein.

The permeable underlayer effects on η and u are summed up in Figures 7.10 and 7.11 which show the spatial variations of the mean, maximum, and minimum values of η and u with respect to t over $0 < t \leq t_{max}$ for the permeable and impermeable slopes for Runs P1 and I1 as well as P3 and I3. As has also been shown in the preceding four figures, the thick permeable underlayer reduces the vertical range of η and the magnitude of u in the vicinity of the still waterline. It is noted that the still waterline intersects the (upper) slope at x=1.353 for Runs P1 and I1 and x=1.031 for Runs P3 and I3. The mean water level $\overline{\eta}$ on the impermeable slope is shown to approach η_{max} asymptotically since $h = (\eta - z_b) > 0$ in the region reached by up-rushing water during $0 < t \leq t_{max}$, whereas $\overline{\eta}$ on the permeable slope is connected to that inside the permeable underlayer. The negative value of $\overline{u}$ is related to the undertow on a beach (Kobayashi, DeSilva, and Watson 1989), whereas the time-averaged fluxes for the permeable slope shown in Figure 6.34 result in the positive value of of $\overline{u}$ above SWL. This suggests that the permeability may affect the net cross-shore transport of gravel and sand.

A comment should be given regarding the presentation of Figures 7.10 and 7.11. The spikes which originally appeared in the spatial variations of u_{max} and u_{min} in these two figures have been removed manually. This manual smoothing may be justified in the light of the discussion in Section 6.5 in relation to Figure 6.22 where it is argued that the spikes are localized numerical problems that are remediable and do not affect the overall computation results. Instead of using the manual smoothing, the spikes could have been removed using the remedial measures suggested and demonstrated in that discussion, and the remedied results without any spike could have been presented here. In any case, the computed results presented herein are those obtained by using the computation parameters listed in Table 6.2.

A time series analysis is performed for the waterline oscillations on the impermeable slope to obtain the run-up and swash statistics corresponding to those presented in columns (8)–(11) of Table 6.4 and in Figure 6.15 for the permeable slope. The statistics are presented in Table 7.2 and in Figure 7.12 where the corresponding results for the permeable slope are also presented for comparison. For both permeable and impermeable slopes, the significant swash height h_s^U, the significant run-up R_s^U, and the maximum run-up R_{max}^U increase with the increase of ξ and ξ_p where the values of ξ and ξ_p are listed in Table 6.1. The computed values presented in Table 7.2 also indicate that the thick permeable underlayer reduces h_s^U, R_s^U, R_{max}^U, and the set-up $\overline{Z_r^U}$ by a factor of slightly less than two. The probability distributions of the normalized run-up (R_p^U / R_s^U) for the permeable and impermeable slopes shown in Figure 7.12 are very close to each other, which indicates that the normalized run-up distribution is affected little by the permeable underlayer. The permeability effect on run-up may be accounted for by R_s^U only as a first approximation.

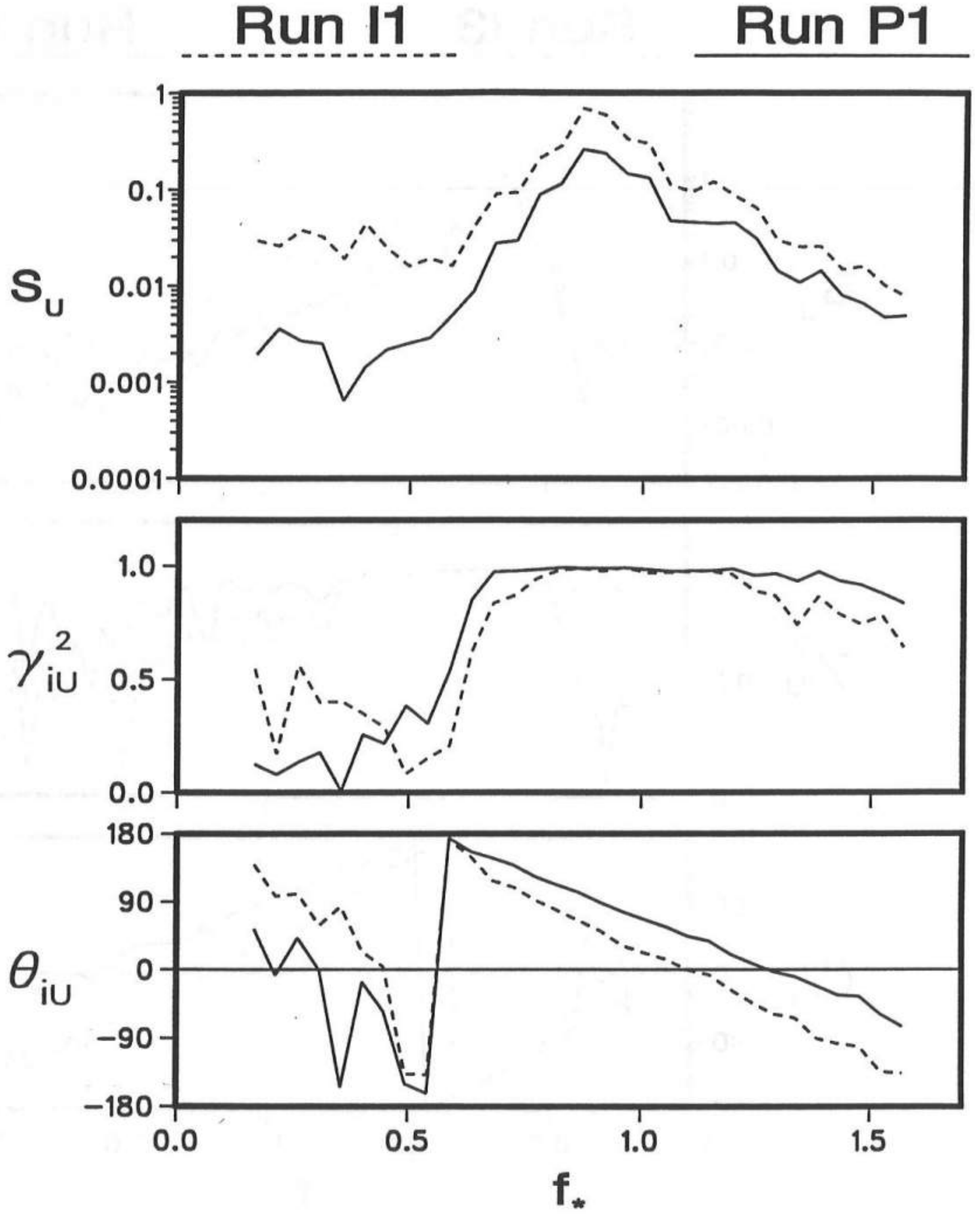

Figure 7.4: Computed spectra of waterline oscillations on 1:3 slope as well as coherence and phase between incident waves and waterline oscillations for Runs P1 and I1.

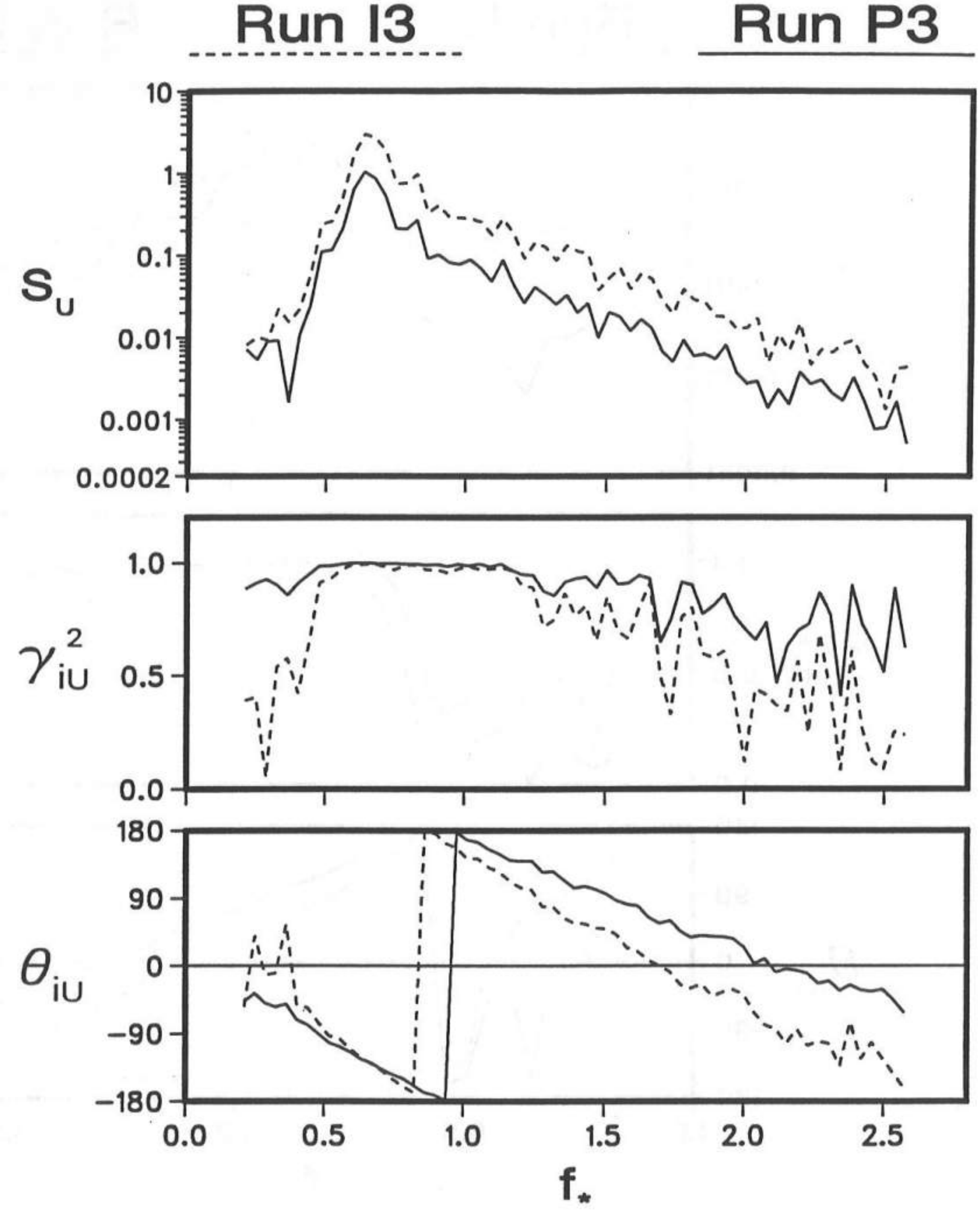

Figure 7.5: Computed spectra of waterline oscillations on 1:3 slope as well as coherence and phase between incident waves and waterline oscillations for Runs P3 and I3.

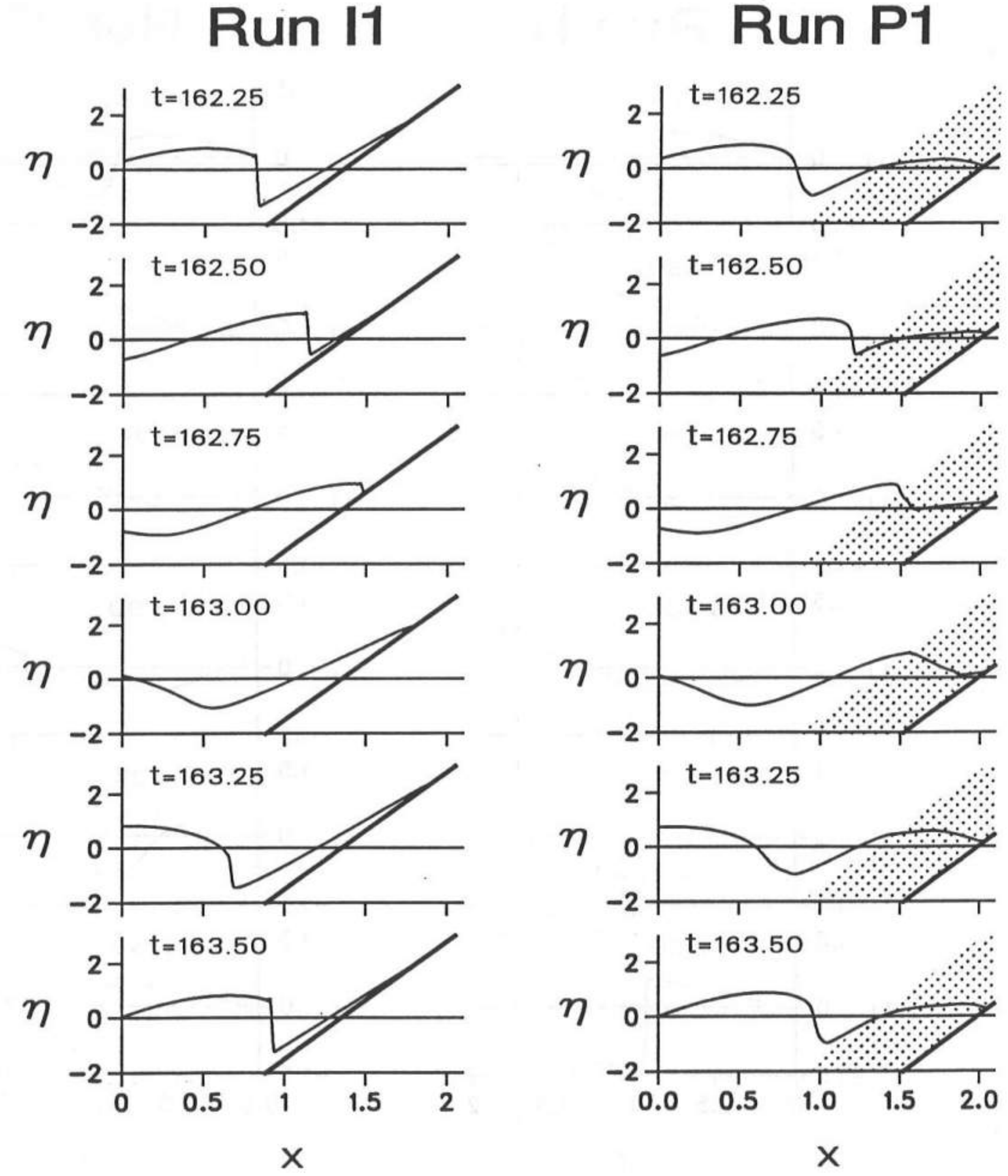

Figure 7.6: Instantaneous spatial variations of free surface elevation η for Runs P1 and I1.

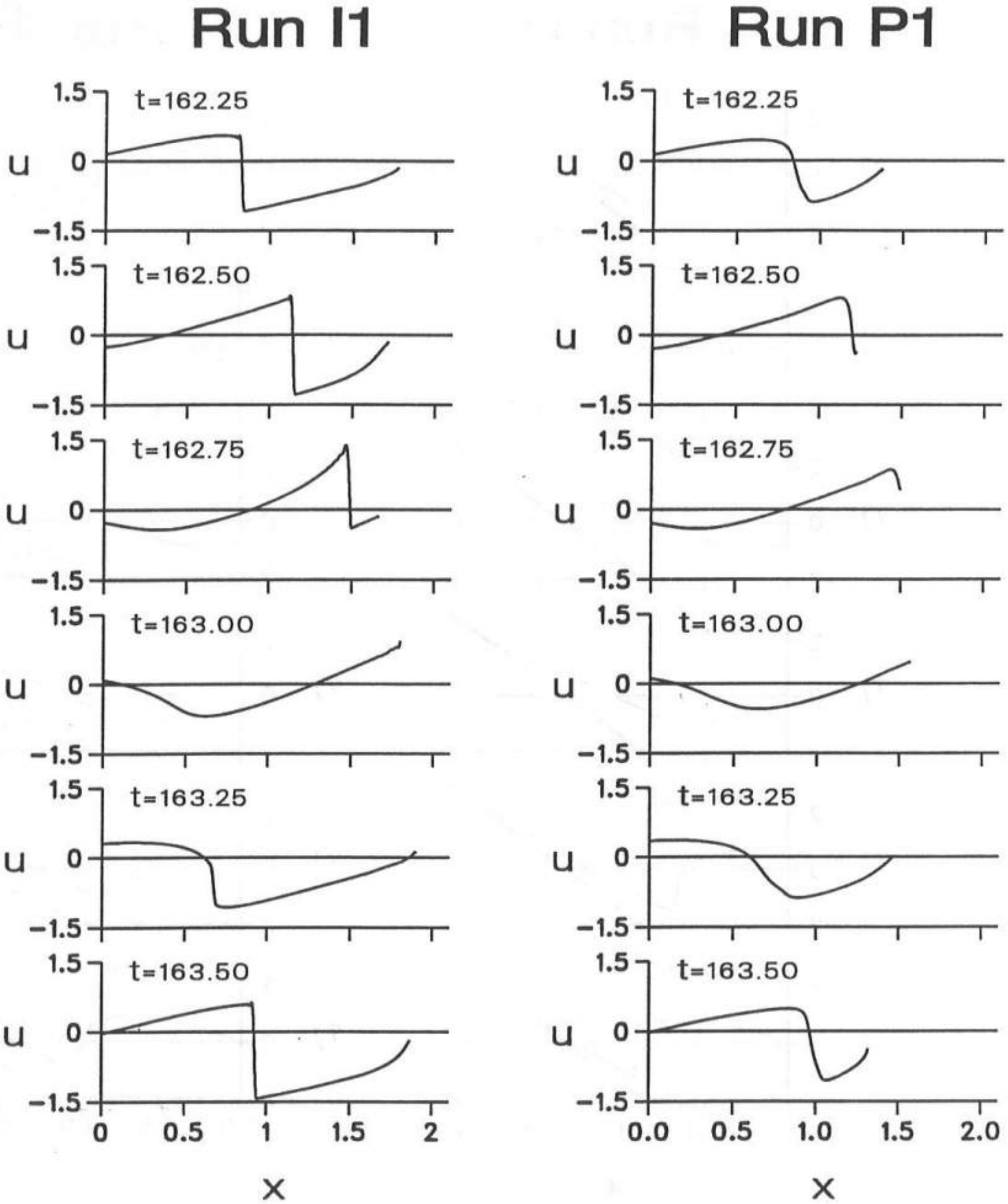

Figure 7.7: Instantaneous spatial variations of depth-averaged horizontal velocity u for Runs P1 and I1.

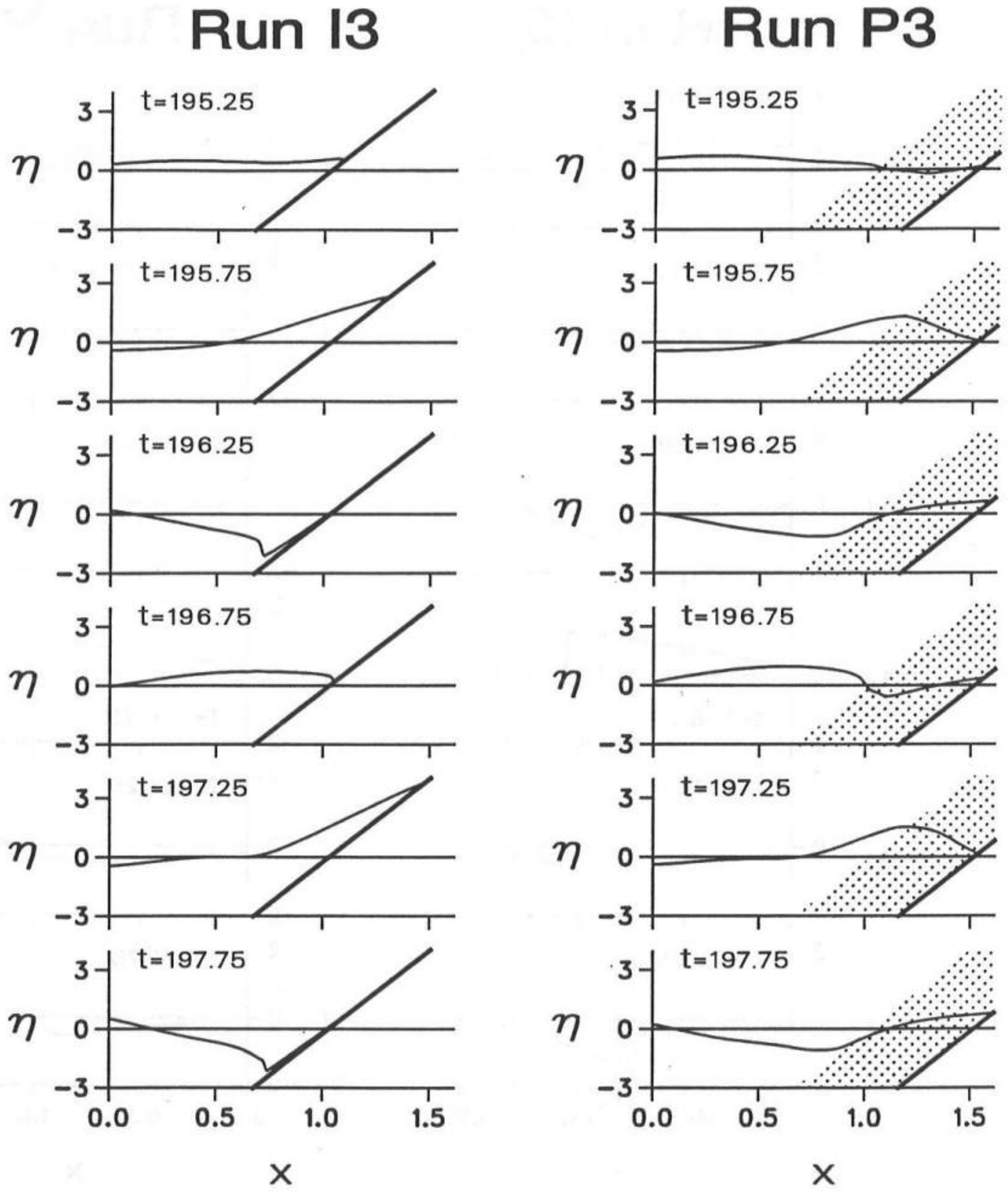

Figure 7.8: Instantaneous spatial variations of free surface elevation η for Runs P3 and I3.

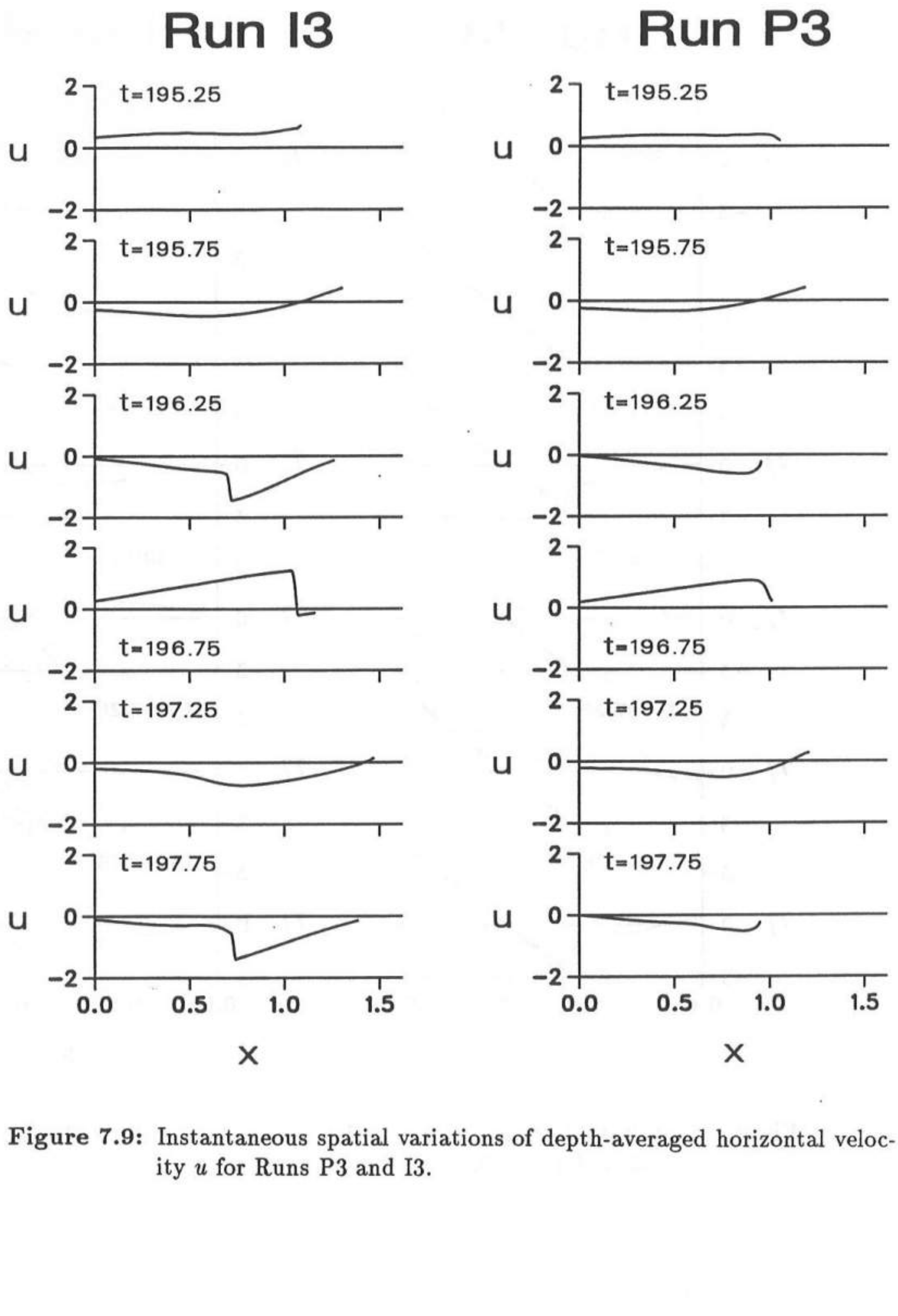

Figure 7.9: Instantaneous spatial variations of depth-averaged horizontal velocity u for Runs P3 and I3.

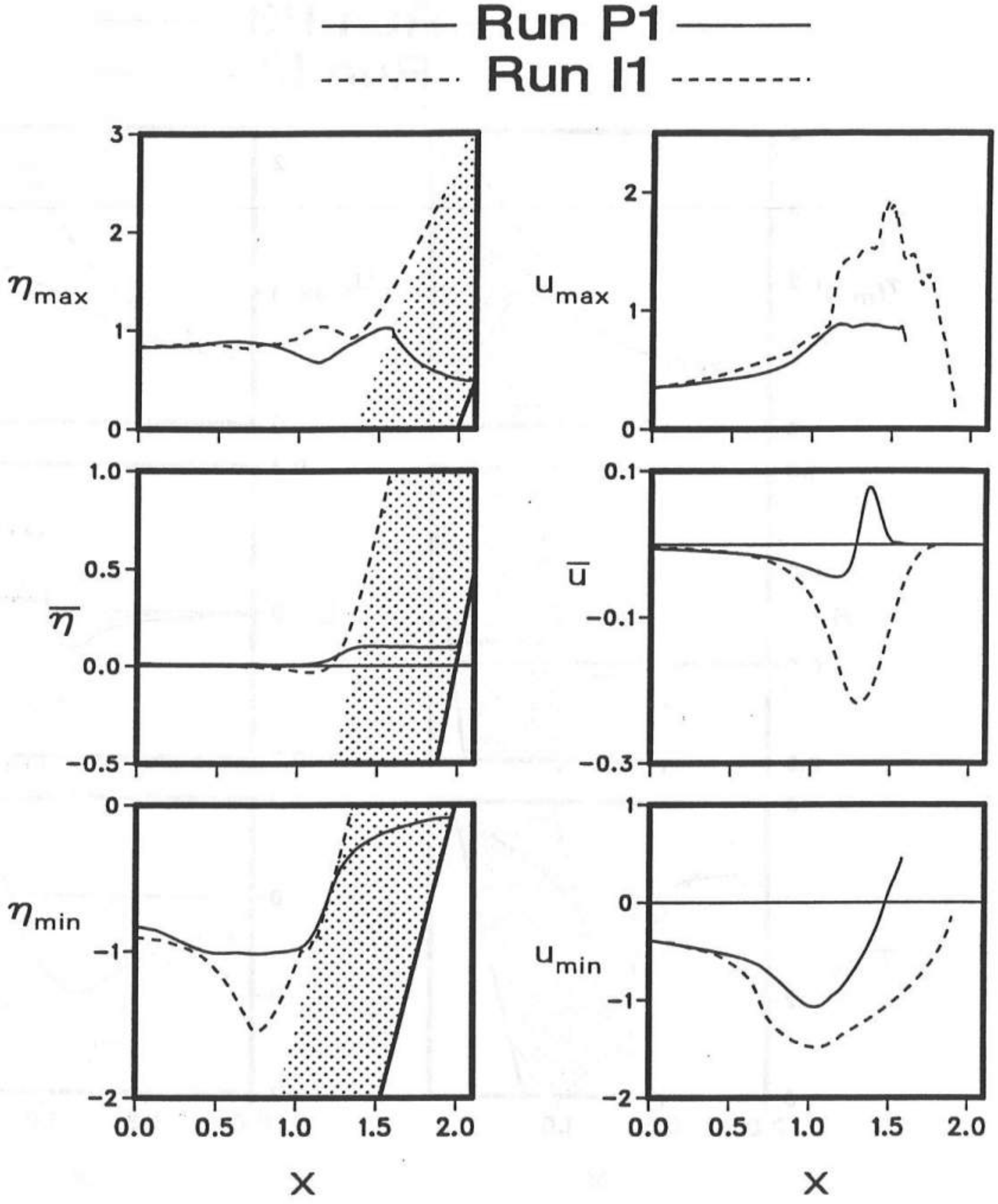

Figure 7.10: Mean, maximum, and minimum values of free surface elevation η and depth-averaged horizontal velocity u for Runs P1 and I1.

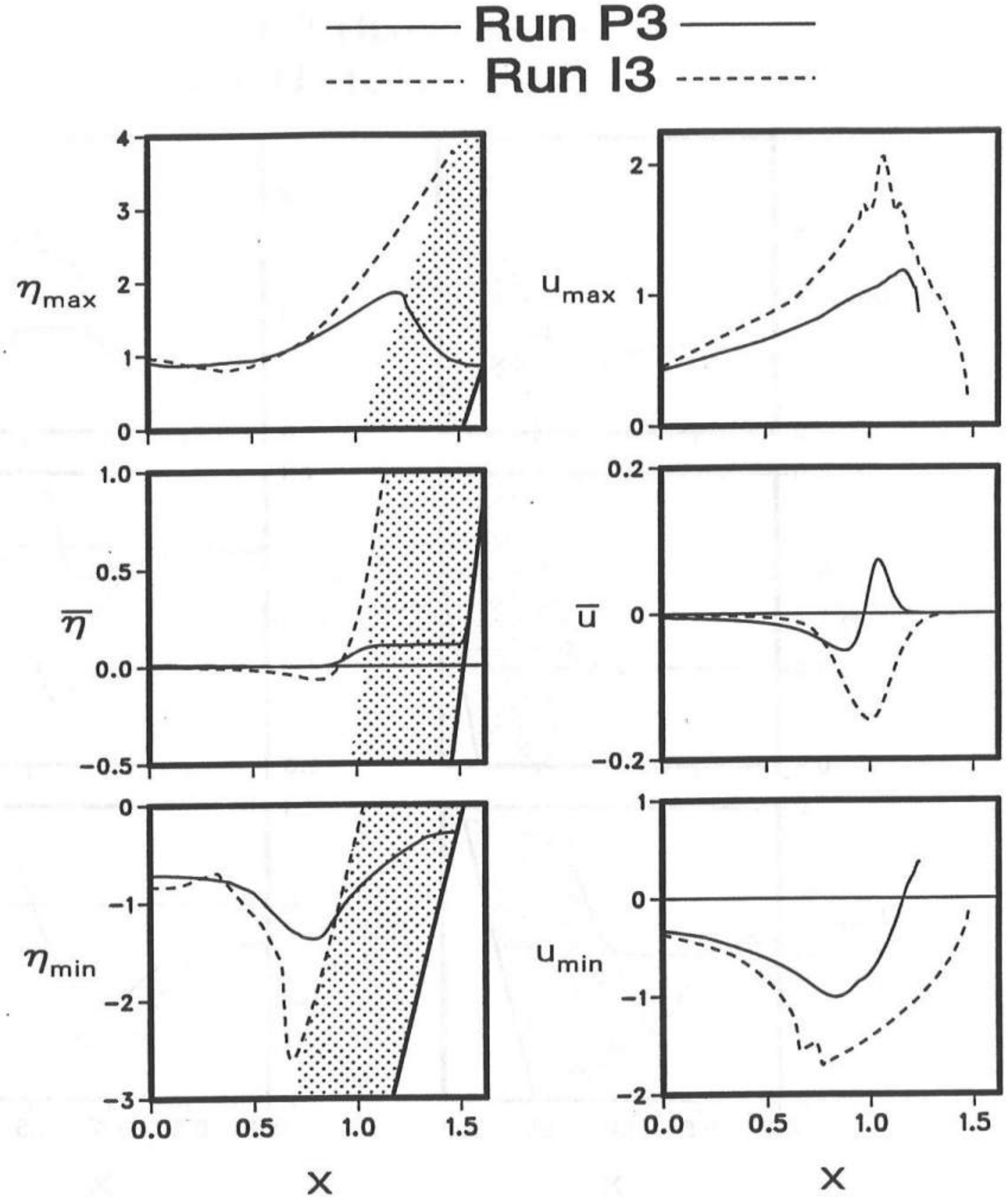

Figure 7.11: Mean, maximum, and minimum values of free surface elevation η and depth-averaged horizontal velocity u for Runs P3 and I3.

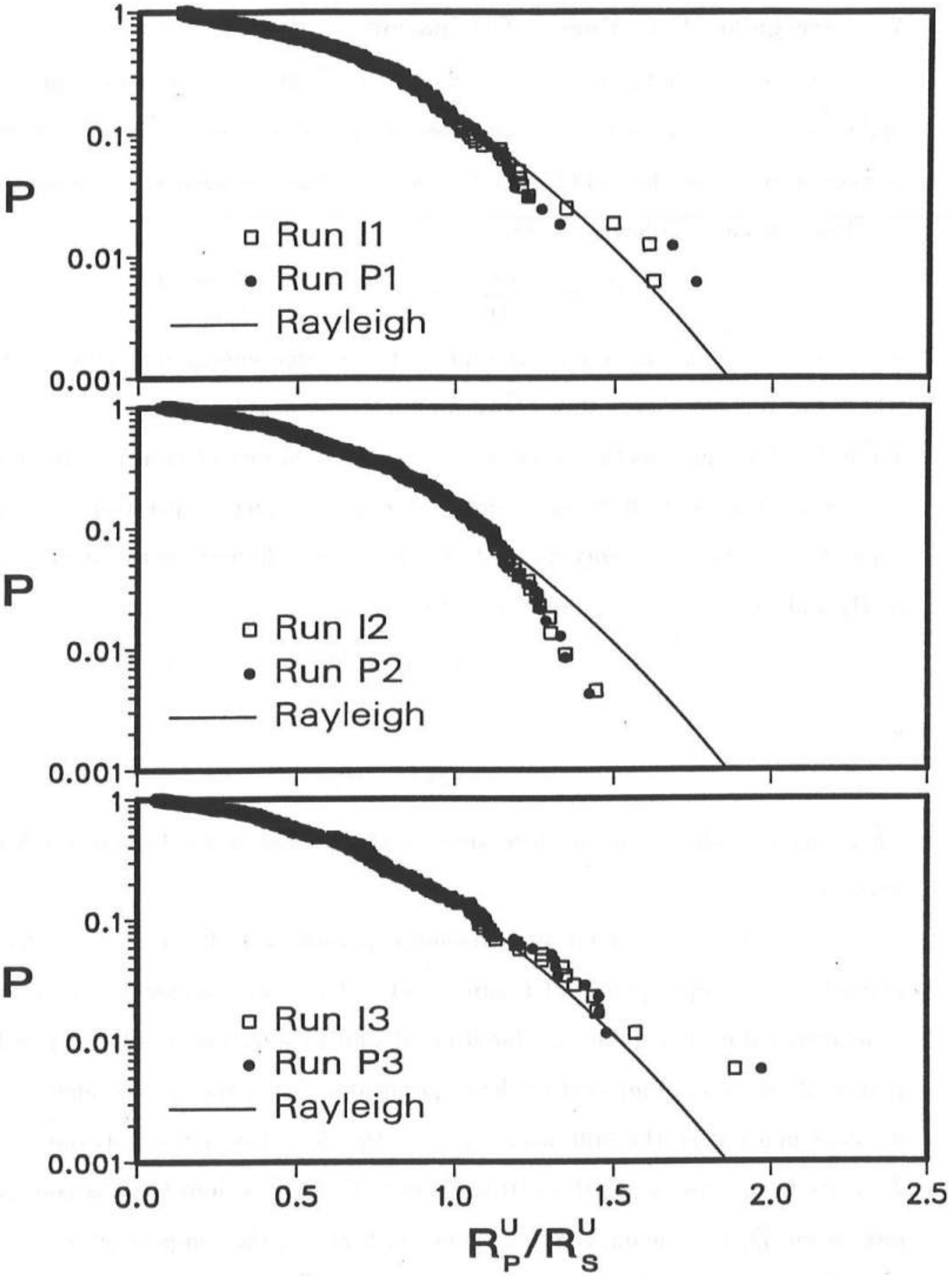

Figure 7.12: Computed exceedance probability of run-up as compared with Rayleigh distribution for six runs.

7.4 Irregular Wave Energy Dissipation

The energy equation for the flow over the rough permeable slope has been derived in Section 5.1 and the corresponding time-averaged energy quantities have been discussed in Section 6.7. For the impermeable slope, the time averaged energy equation is given by (Wurjanto and Kobayashi 1991)

$$\overline{D_B} = -\frac{d\overline{F}}{dx} - \overline{D_f} - \frac{E(t_{max}) - E(t_{min})}{t_{max} - t_{min}} \tag{7.1}$$

The symbols $\overline{F}$ and E in Eq. 7.1 represent the same energy quantities as in Eq. 5.30 where the vertical energy flux $\overline{D_p}$=0 for the impermeable slope. The symbols $\overline{D_f}$ and $\overline{D_B}$ in Eq. 7.1 represent the normalized time-averaged rate of energy dissipation per unit horizontal area due to bottom friction and wave breaking, respectively. The normalized time-averaged rate of energy dissipation, $\overline{D}$, in Eq. 5.30 may be assumed to be the sum of $\overline{D_f}$ and $\overline{D_B}$ (Kobayashi and Wurjanto 1992).

$$\overline{D} = \overline{D_f} + \overline{D_B} \tag{7.2}$$

with

$$\overline{D_f} = \overline{\tau_b\, u} \tag{7.3}$$

where the normalized bottom shear stress τ_b is expressed in the form of Eq. 3.19 together with Eq. 4.7.

The normalized time-averaged energy quantities for Region 1 for Runs P1 and P3 plotted on the upper panels of Figures 7.13 and 7.14 are similar unlike the normalized time-averaged energy quantities for Runs I1 and I3 shown on the lower panels. For the permeable slope as compared to the impermeable slope, the specific energy $\overline{E}$ does not increase much near the still waterline and the decrease of the horizontal energy flux $\overline{F}$ starts from x=0, while the vertical energy flux $\overline{D_p}$ is dominant as compared to the dissipation $\overline{D}$. For the impermeable slope with $\overline{D_p}$=0, the comparison of $\overline{D_f}$ and $\overline{D_B}$ for Runs I1, I2, and I3 indicates that $\overline{D_B}$ is dominant for mostly plunging waves observed in Run I1 and $\overline{D_f}$ is dominant for mostly surging waves observed in Run I3, while both are equally important for Run I2 which is not shown here. Consequently, the thick permeable underlayer modifies the time-averaged energy balance significantly.

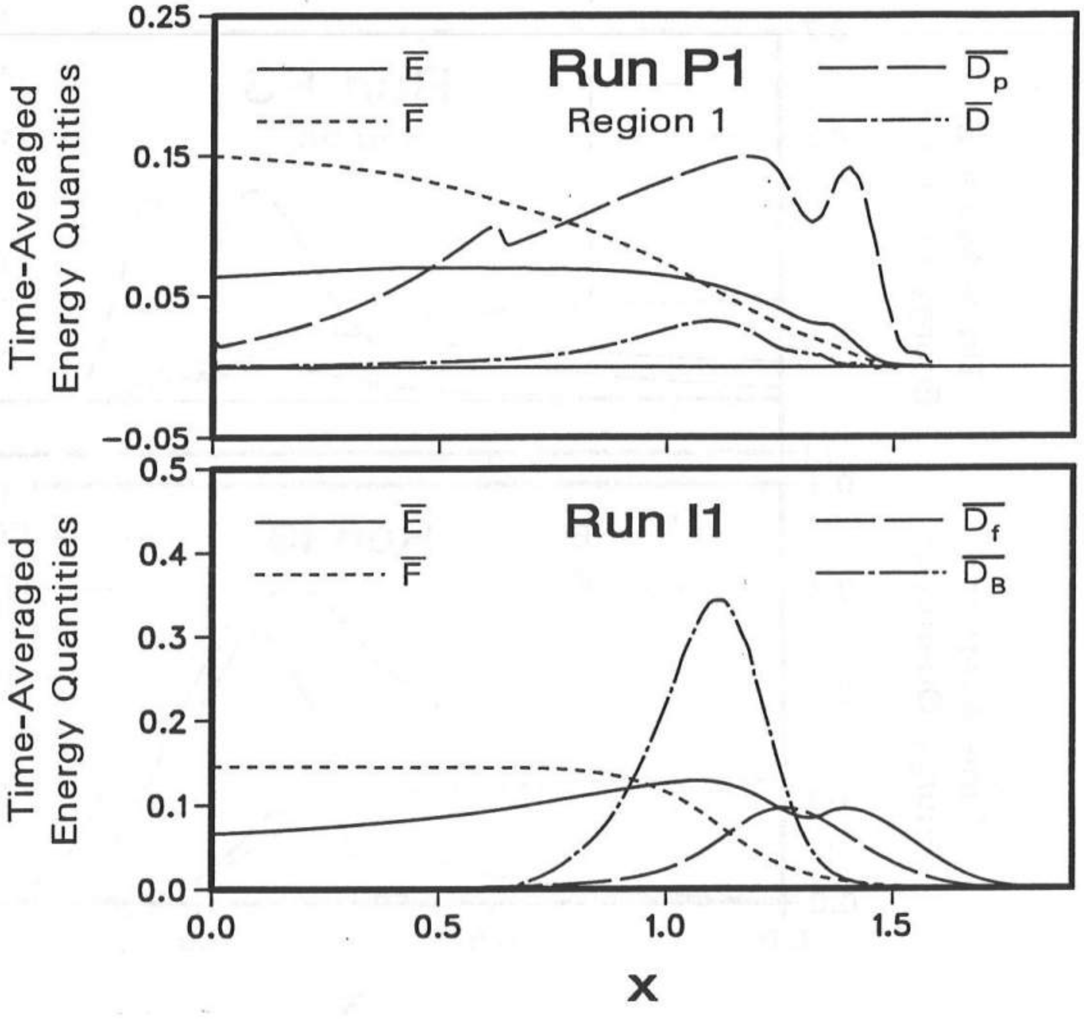

Figure 7.13: Time-averaged energy quantities for Runs P1 and I1.

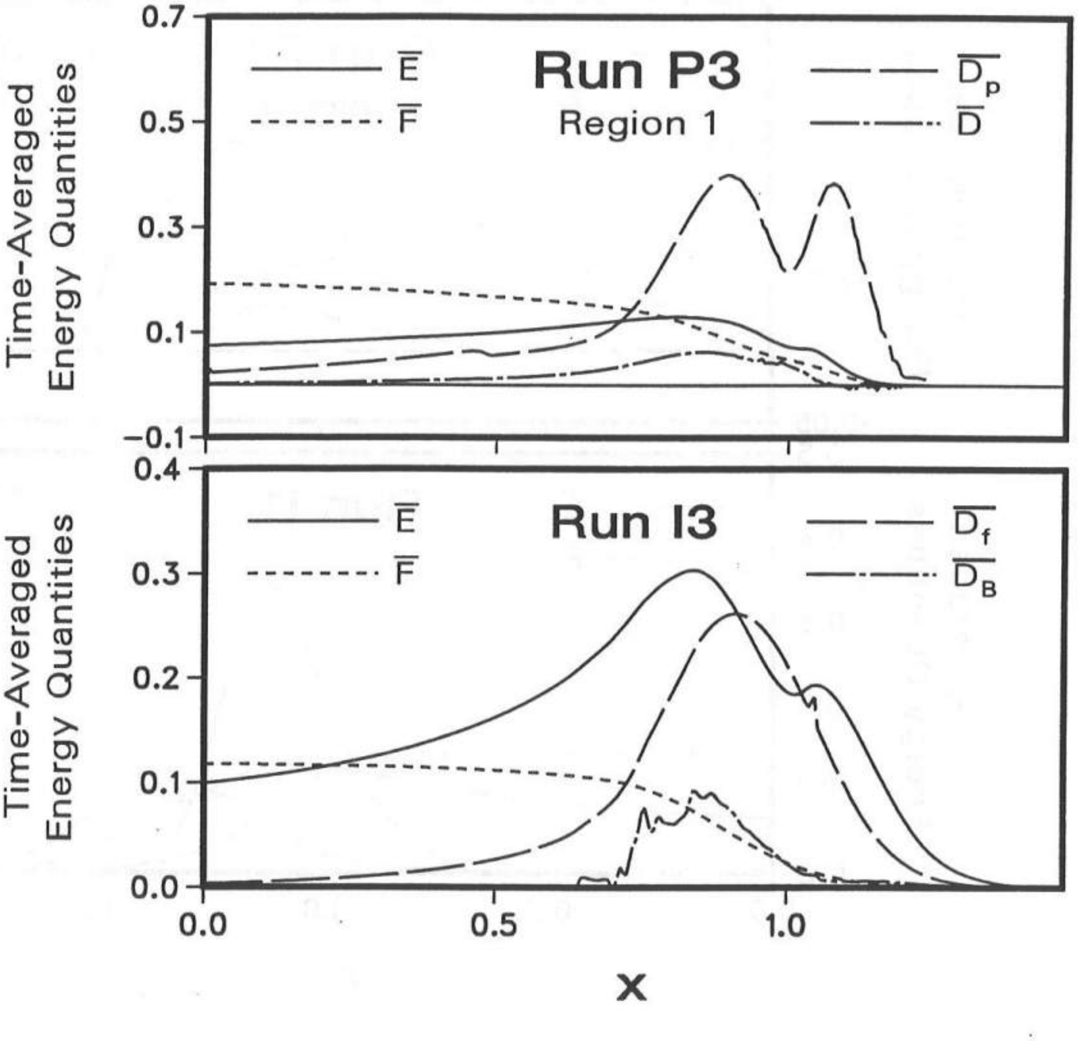

Figure 7.14: Time-averaged energy quantities for Runs P3 and I3.

7.5 Hydraulic Stability of Armor Units

The hydraulic stability of armor units is analyzed using the computed flow fields over the rough permeable and impermeable slopes. The computation procedure is the same as that of Kobayashi and Wurjanto (1990) for the case of a *thin* permeable underlayer. In the numerical model, the permeability affects armor stability in two ways. First, the expression for the fluid acceleration involves a term reflecting mass and momentum exchanges between the flows in Regions 1 and 2:

$$\frac{du}{dt} = \frac{\partial u}{\partial t} + u\frac{\partial u}{\partial x} = -\frac{\partial h}{\partial x} - \theta - \frac{f|u|u}{h} + \frac{p_q q_b(u-u_b)}{h} \tag{7.4}$$

where use is made of Eqs. 4.1 and 4.2. Second, the horizontal velocity u is also affected by the presence of the permeable underlayer since Eqs. 4.1 and 4.2 include the mass and momentum fluxes into and out of the thick permeable underlayer. The permeability effect on u has been shown and discussed in Section 7.3. No attempt has been made in this simplified approach to consider the direct effects of the water flowing in and out of the thick permeable underlayer. Consequently, the prediction of the armor stability by the present model may not be very accurate. For the impermeable slope, the armor stability computation in RBREAK (Wurjanto and Kobayashi 1991) follows essentially the same procedure as in the numerical model PBREAK as outlined in WK 92, excluding the permeability effects. The two procedures originated from Kobayashi, Otta, and Roy (1987).

In both numerical models, the hydraulic stability condition against sliding or rolling for an armor unit is expressed as

$$N_s = \frac{H'}{[W'/(\rho s_g)]^{1/3}(s_g-1)} \le N_R(t, z_b) \tag{7.5}$$

where

N_s = stability number

N_R = armor stability function varying with the normalized time t and the armor location represented by z_b, which is the normalized z-coordinate of the (upper) slope

H' = significant wave height used for the normalization of the governing equations

s_g = specific gravity of the armor unit whose unit mass is given by ρs_g

W' = median mass of the armor unit

For the gravel used in the experiment conducted by Cox (1989), s_g=2.7, W'=1.48x10^{-2} kg, and $(W'/\rho s_g)^{1/3}$ = 1.763x10^{-3}m.

The armor stability computation is performed for the entire computation duration $0 < t \leq t_{max}$ for the stretch of the slope from the seaward boundary where $z_b = -d_t$ to the landward location where the physical water depth h' equals δ'_a=0.021m, which is equal to the median diameter of the gravel assumed to be fully submerged. The local stability number $N_{sx}(z_b)$ is defined as the minimum value of the armor stability function $N_R(t, z_b)$ at given z_b during $0 < t \leq t_{max}$. The critical stability number N_{sc} is defined as the minimum value of the local stability number $N_{sx}(z_b)$ for $z_b \geq -d_t$.

The computed values of the critical stability number N_{sc} are given in Table 7.2 along with the values of the stability number N_s. Figure 7.15 shows the spatial variations of the local stability number $N_{sx}(z_b)$ for the six runs. The values of the stability number N_s are also plotted on this figure. The numerical model predicts that the gravel units in the region $N_{sx} < N_s$ should slide or roll. Cox (1989) observed that loose gravel units on the permeable slope remained at their initial locations whereas those on the impermeable slope were dislodged during the tests. Figure 7.15 indicates the intense movement of loose gravel units in the wide region of the impermeable slope and the limited movement of loose gravel units on the permeable slope. The improved stability of the gravel units due to the permeability as predicted by the numerical model is qualitatively consistent with the observations and the empirical formula of Van der Meer (1988). In relation with the test results of Cox (1989), the limited sliding or rolling of loose gravel units on the permeable slope predicted by the numerical model may not result in the dislodgement of the units from their initial locations.

Table 7.3: Computed values of critical stability number N_{sc}, time t_{sc}, and coordinates (x_{sc}, z_{sc}) of minimum stability for permeable (P) and impermeable (I) slopes, together with stability number N_s for each test run.

RUN NO.	PERMEABLE (P)				IMPERMEABLE (I)				N_s
	N_{sc}	t_{sc}	x_{sc}	z_{sc}	N_{sc}	t_{sc}	x_{sc}	z_{sc}	
(1)	(2)	(3)	(4)	(5)	(6)	(7)	(8)	(9)	(10)
1	1.155	163.434	1.049	−1.314	0.493	114.669	1.353	0.000	2.285
2	1.485	197.657	1.001	−1.346	0.377	91.829	1.135	−0.523	1.785
3	1.431	199.115	0.846	−1.575	0.454	72.880	0.974	−0.481	1.525

In Table 7.3, the normalized time when the critical stability number N_{sc} occurs is denoted by t_{sc}. The normalized coordinates of the (upper) slope where the critical stability number N_{sc} occurs are denoted by x_{sc} and z_{sc}. The flow conditions for Runs P1 and I1 as well as P3 and I3 at the time of the minimum armor stability t_{sc} are depicted in Figures 7.16 and 7.17. In these figures, the normalized surface elevation η, the depth-averaged horizontal velocity u, the horizontal acceleration $\frac{du}{dt}$, and the armor stability function N_R are shown as functions of z_b at $t{=}t_{sc}$. The computed results for Runs P2 and I2 show similar flow conditions at the time of the minimum armor stability. For the impermeable slope, the minimum armor stability occurs during wave up-rush when the landward fluid velocity and acceleration are large. For the permeable slope, on the contrary, the minimum armor stability occurs during wave down-rush when the seaward fluid velocity and acceleration are large.

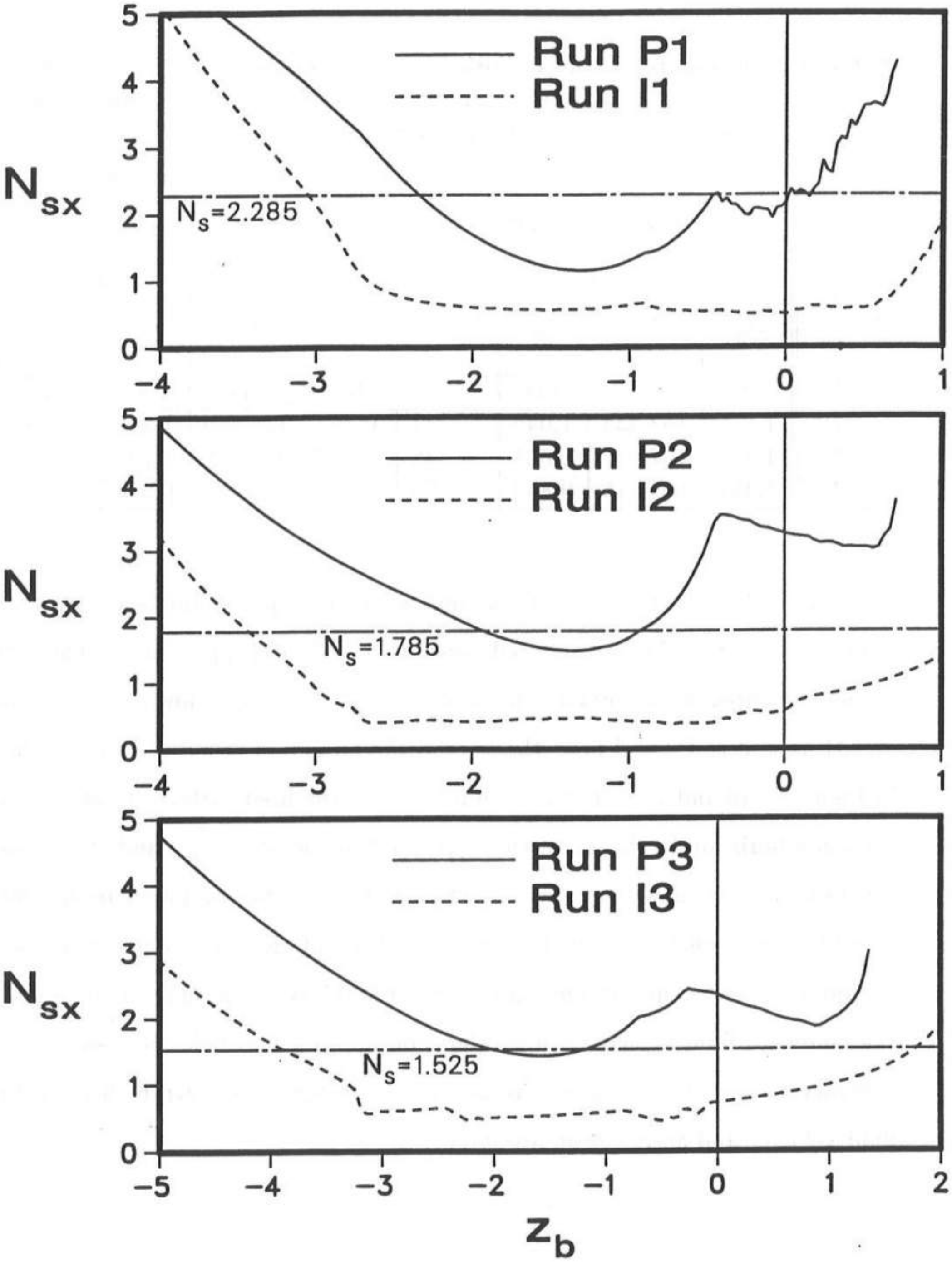

Figure 7.15: Spatial variations of local stability number N_{sx} for six runs.

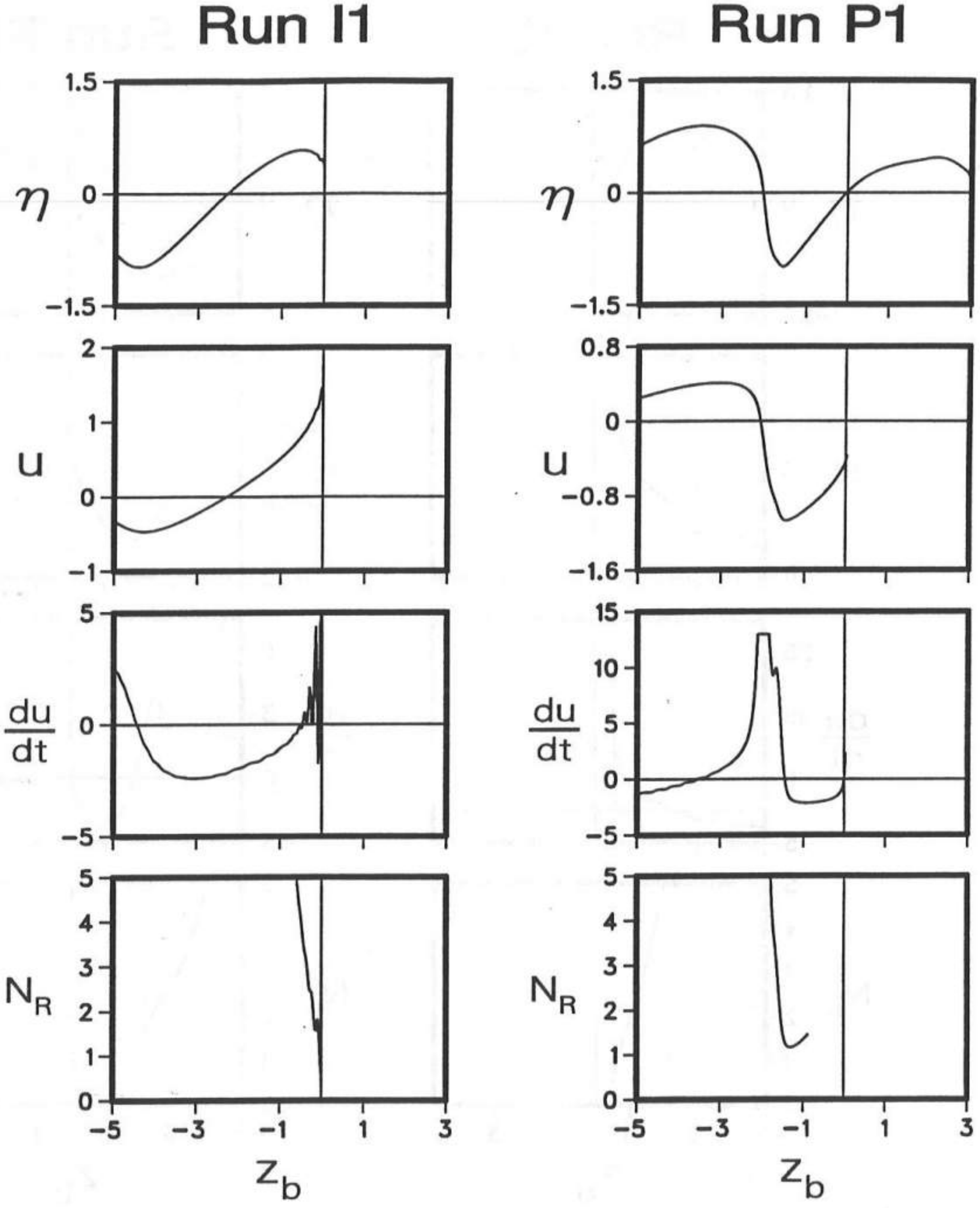

Figure 7.16: Flow conditions at time of minimum armor stability for Runs P1 and I1.

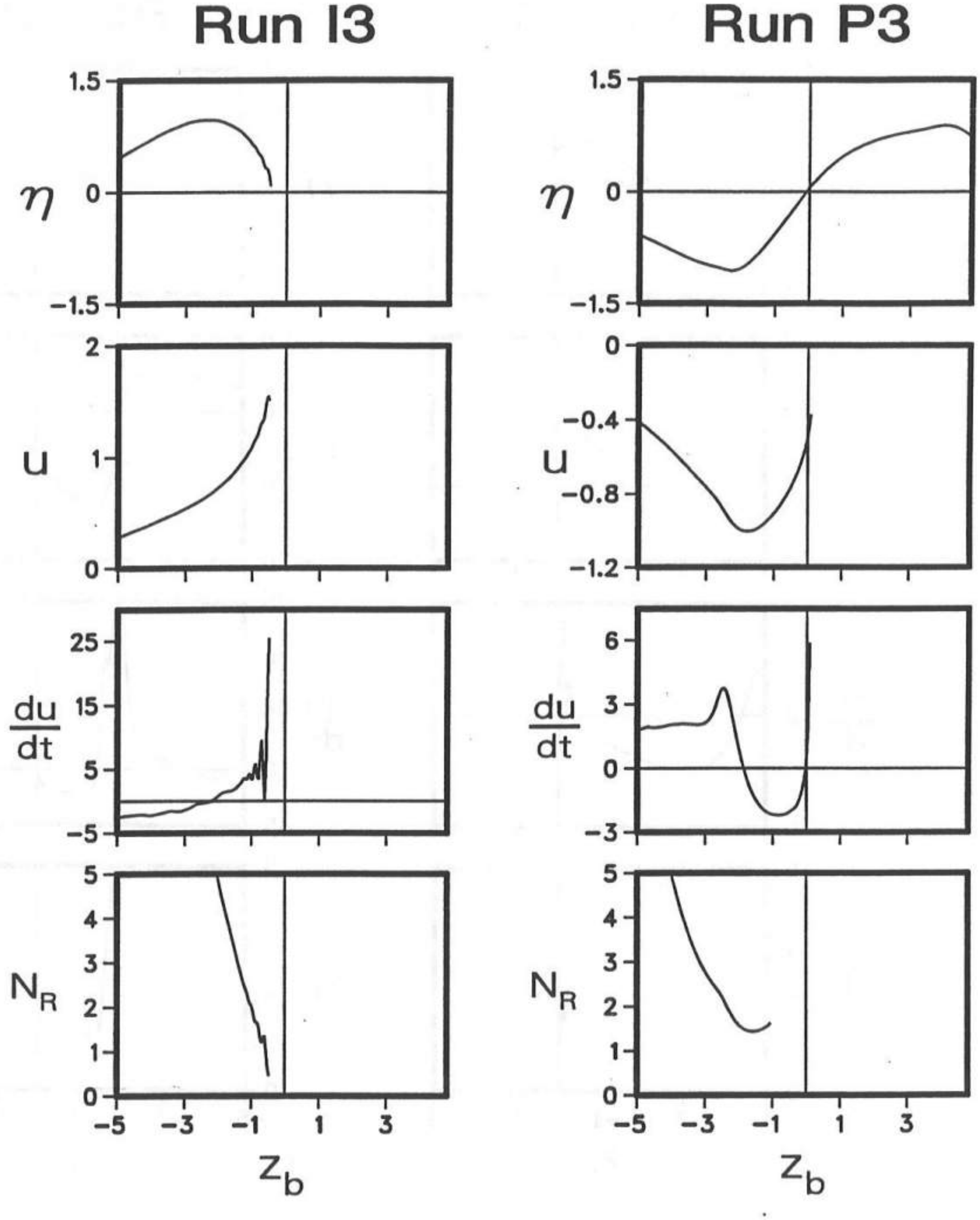

Figure 7.17: Flow conditions at time of minimum armor stability for Runs P3 and I3.

7.6 Spectral Evolution of Surface Elevation

Figures 7.18 and 7.19 for Runs P1 and I1 as well as P3 and I3 show the evolution of the normalized power spectral density $S_\eta(f_*)$ of the free surface elevation η over the slope. The four locations shown in each figure are equally spaced along the slope with the first being at the seaward boundary of the computation domain.

As expected in the light of the discussion regarding the spatial variations of the free surface elevations in Section 7.3, the spectral density S_η for the impermeable slope is generally larger in magnitude than that for the permeable slope. Since the free surface elevations over the slope were not measured in Cox (1989), these computed results for the permeable slope can not be verified. The numerical model RBREAK for the impermeable slopes, on the other hand, has been shown to be in agreement with the measured free surface elevations inside the surf zone on a laboratory beach by Cox, Kobayashi, and Wurjanto (1992).

It is noted that the generation of additional low-frequency wave components appears significant for Run I1 as shown in Figure 7.18, which might explain why the reflection coefficient $r(f_*)$ exceeds unity for the low frequency range as shown in Figure 7.2 in Section 7.2. However, the time-domain model for the impermeable slopes is unable to explain how and where the additional low-frequency wave components could be generated.

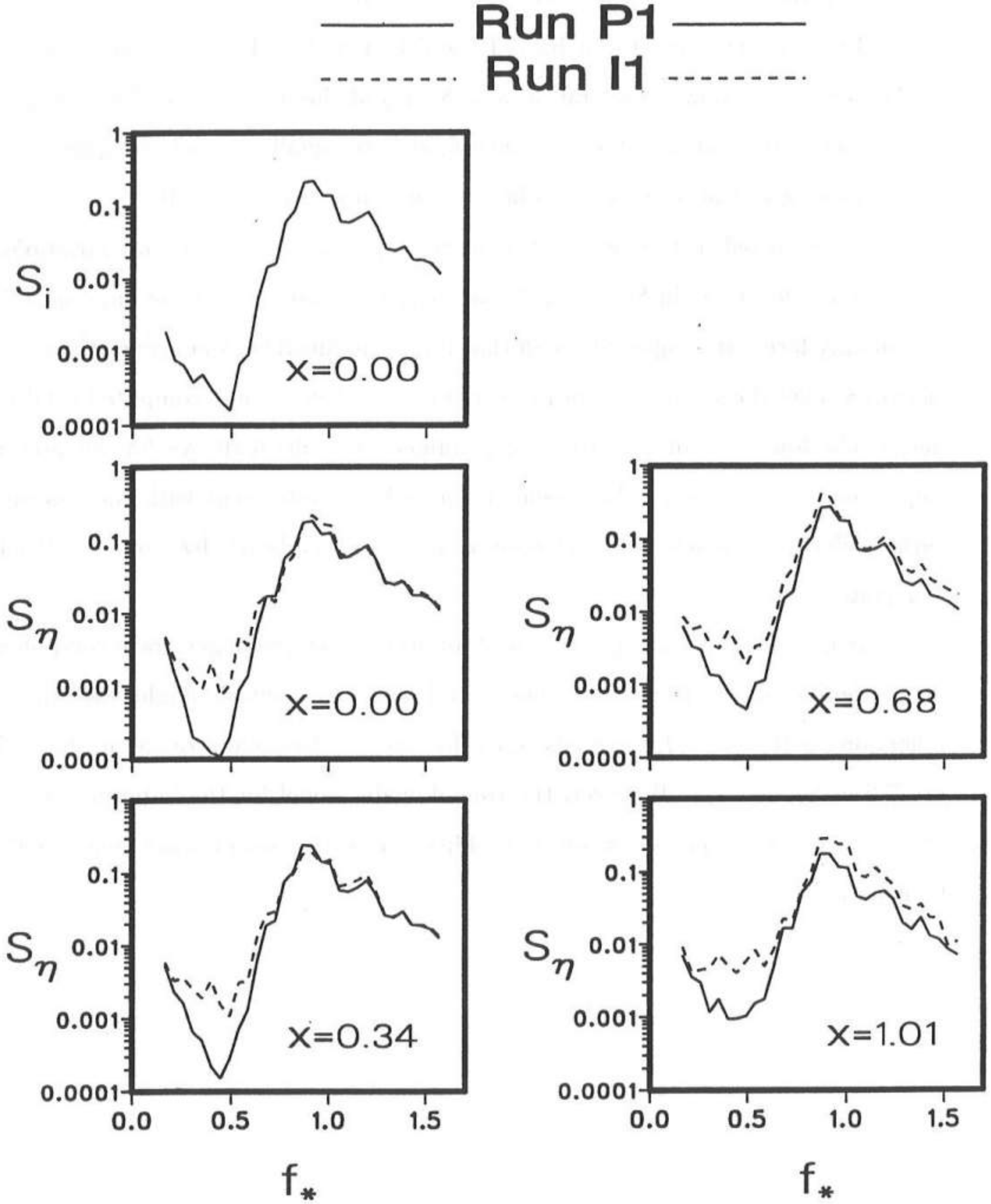

Figure 7.18: Evolution of spectra of surface elevation for Runs P1 and I1.

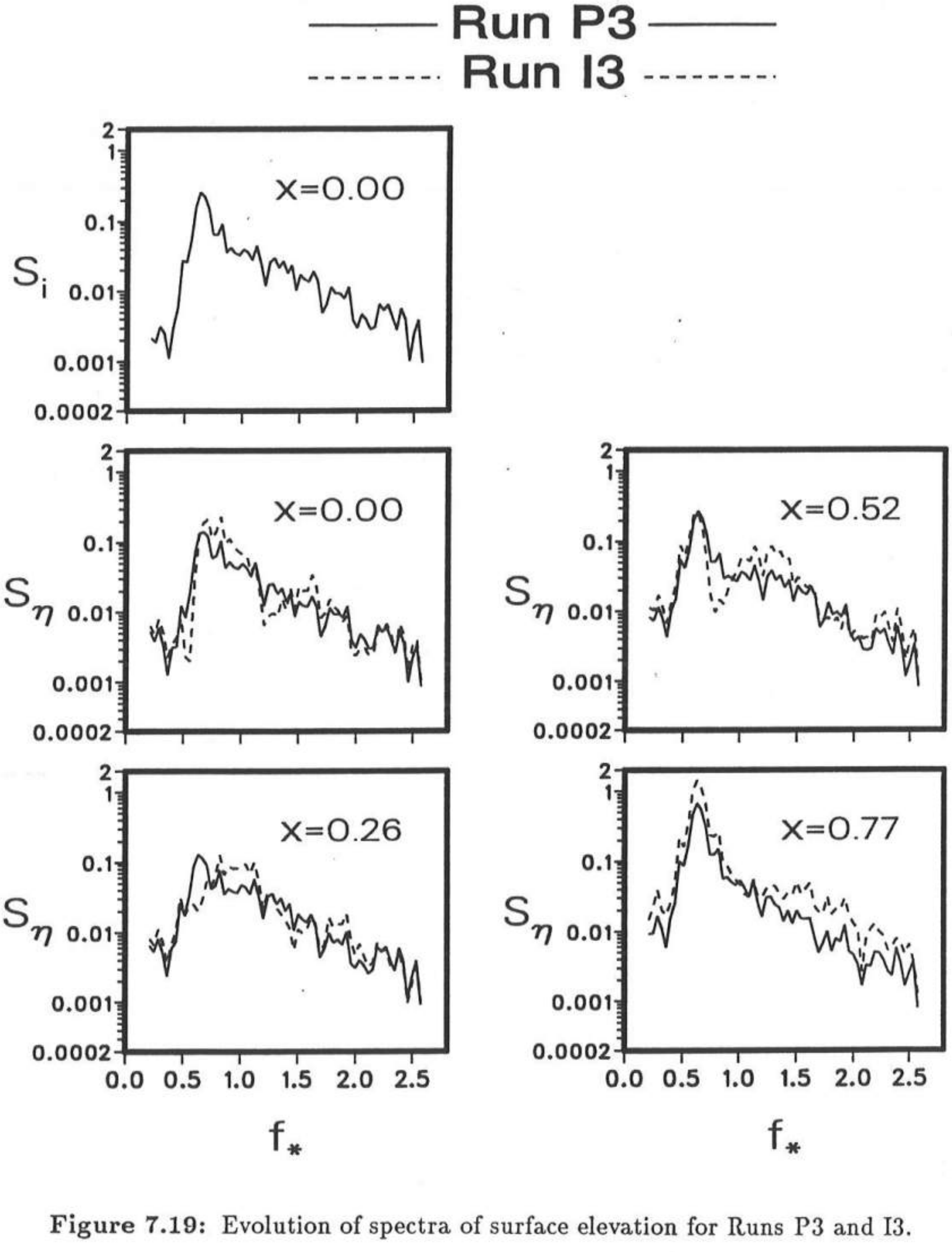

Figure 7.19: Evolution of spectra of surface elevation for Runs P3 and I3.

Chapter 8

CONCLUSIONS

The essential equations used in the one-dimensional, time-dependent numerical model with two layers have been derived in this study. The numerical model simulates the flow over a rough permeable slope of arbitrary geometry as well as the flow inside a permeable underlayer of arbitrary thickness for specified normally-incident irregular waves. Any incident wave train can be specified as input at the seaward boundary of the computation domain. The numerical model computes the reflected wave train at the seaward boundary from which the reflected wave spectrum can be calculated. It also computes the waterline oscillation on the permeable slope from which the run-up spectrum and exceedance probability can be calculated. In addition to the equations of mass and horizontal momentum used to compute the flow field, equations of energy are used to estimate the spatial variations of energy fluxes and dissipation rates.

The numerical model has been compared with three test runs to assess the capabilities and limitations of the numerical model for predicting the reflected waves and waterline oscillations on the rough permeable slope with a thick permeable underlayer. The agreement between the measured and computed results may be acceptable but could be improved by calibrating the empirical parameters included in the model. The computed results for the three runs have also been examined to elucidate the hydrodynamics involved in the interaction of irregular waves with the highly permeable slope. The wave propagation, attenuation, and setup inside the permeable underlayer reduce the intensity of wave breaking and resulting energy dissipation on the permeable slope. Most of the energy transmitted into the permeable underlayer is dissipated locally by the turbulent and viscous flow resistance. The time-averaged mass flux is into the permeable underlayer above SWL and out of the underlayer below SWL. Correspondingly, the time-averaged mass flux near the still waterline is landward above the slope and seaward inside the permeable underlayer. These computed results will need to be verified experimentally.

The computed results have also been compared with those for the corresponding impermeable slope to examine the differences caused solely by the presence of the thick permeable underlayer. The thick permeable underlayer has been shown to increase the armor stability considerably and reduce the wave reflection and run-up significantly. Most of the results from this comparison have been observed visually or described qualitatively by previous researchers.

The numerical model is capable of providing quantitative data with high spatial and temporal resolutions. It also allows one to perform sensitivity analyses easily by changing only one input parameter at a time. For example, it may be important for the design of berm breakwater to examine the sensitivity of the computed results to the thickness, porosity, and stone diameter of the permeable underlayer.

This numerical model is probably the simplest time-dependent model that can be applied for breaking and broken waves on a permeable slope. The limited verification presented herein indicates that the model may predict some quantities accurately but other quantities only marginally. As a result, correct interpretations of the output of this model are essential to avoid a misuse. It will eventually be necessary to develop unsteady two-dimensional and three-dimensional models to improve the accuracy of the predictions, although computational efforts will increase considerably.

REFERENCES

Abbott, M.B., McCowan, A., and Warren, I.R., 1981. Numerical modelling of free-surface flows that are two-dimensional in plan. In *Transport Models for Inland and Coastal Water* edited by H.B. Fischer. Academic Press, New York.

Ahrens, J.P., 1989. Stability of reef breakwaters. *J. Waterway, Port, Coastal, and Ocean Engineering*, ASCE, **115** (2), 221-234.

Ahrens, J.P., 1990. Dynamic revetments. *Proc. 22nd Coastal Engineering Conference*, ASCE, **2**, 1837-1850.

Ahrens, J.P., and Ward, D.L., 1991. Performance of bermed revetments. *J. Waterway, Port, Coastal, and Ocean Engineering*, ASCE, **117** (5), 534-540.

Anderson, D.A., Tannehill, J.C., and Pletcher, R.H., 1984. *Computational Fluid Mechanics and Heat Transfer.* Hemisphere, New York.

Arbhabhirama, A., and Dinoy, A.A., 1973. Friction factor and Reynolds number in porous media flow. *J. Hydraulic Division*, ASCE, **99** (HY6), 901-911.

Baird, W.F., and Hall, K.R., 1984. The design of breakwaters using quarried stones. *Proc. 19th Coastal Engineering Conference*, ASCE, **1**, 1024-1031.

Barends, F.B.J., and Holscher, P., 1988. Modelling interior process in a breakwater. *Breakwater '88.* Thomas Telford, London.

Battjes, J.A., 1974. Surf Similarity. *Proc. 14th Coastal Engineering Conference*, ASCE, **1**, 466-479.

Bear, J., 1979. *Hydraulics of Groundwater.* McGraw-Hill, New York.

Bendat, J.S., and Piersol, A.G., 1986. *Random Data: Analysis and Measurement Procedures*, Second Edition. Wiley, New York.

Bruun, P., 1992. Trends in phreatic surface motion in rubble-mound breakwaters. Discussion. *J. Waterway, Port, Coastal, and Ocean Engineering*, ASCE, **118** (3), 326-327.

Bruun, P., and Johannesson, P., 1976. Parameters affecting stability of rubble mounds. *J. Waterways, Harbors, and Coastal Engineering Division*, ASCE, **102** (WW2), 141-164.

Cox, D., 1989. Irregular wave reflection and run-up on rough, permeable slopes. *Master's Thesis.* Department of Civil Engineering, University of Delaware, Newark, Delaware.

Cox, D.T., Kobayashi, N., and Wurjanto, A., 1991. Computer programs for spectral and time series analyses for random waves. *Research Report No. CACR-91-06*, Center for Applied Coastal Research, University of Delaware, Newark, Delaware.

Cox, D.T., Kobayashi, N., and Wurjanto, A., 1992. Irregular wave transformation processes in surf and swash zones. *Proc. 23rd Coastal Engineering Conference*, ASCE (accepted).

Cunge, J., Holley, F.M., and Verwey, A., 1980. *Practical Aspects of Computational River Hydraulics.* Pitman, Boston.

Dalrymple, R.A., Losada, M.A., and Martin, P.A., 1991. Reflection and transmission from porous structures under oblique wave attack. *J. Fluid Mechanics*, **224**, 625-644.

Delmonte, R.C., 1972. Scale effects of wave transmission through permeable structures. *Proc. 13th Coastal Engineering Conference*, ASCE, **3**, 1867-1872.

Engelund, F., 1953. On the laminar and turbulent flows of groundwater through homogeneous sand. *Trans. Danish Academy of Technical Sciences*, **3** (4).

Fennema, R.J., and Chaudhry, M.H., 1986. Explicit numerical schemes for unsteady free-surface flows with shocks. *Water Resources Research*, **22** (13), 1923-1930.

Gabutti, B., 1983. On two upwind finite difference schemes for hyperbolic equations in non-conservative form. *Computers and Fluids*, **11** (3), 207-230.

Greenberg, M.D., 1988. *Advanced Engineering Mathematics.* Prentice Hall, Englewood Cliffs, New Jersey.

Guza, R.T., and Thornton, E.B., 1982. Swash oscillations on a natural beach. *J. Geophysical Research*, **87** (C1), 483-491.

Hall, K.R., 1991. Trends in phreatic surface motion in rubble-mound breakwaters. *J. Waterway, Port, Coastal, and Ocean Engineering*, ASCE, **117** (2), 179-187.

Hall, K.R., 1992. Trends in phreatic surface motion in rubble-mound breakwaters. Closure. *J. Waterway, Port, Coastal, and Ocean Engineering*, ASCE, **118** (3), 328-331.

Hannoura, A.A., and McCorquodale, J.A., 1985b. Rubble mounds: Numerical modeling of wave motion. *J. Waterway, Port, Coastal, and Ocean Engineering*, ASCE, **111** (5), 800-816.

Henderson, F.M., 1966. *Open Channel Flow.* Macmillan, New York.

Hibberd, S., 1977. Surf and run-up. *Ph.D. Dissertation.* School of Mathematics, University of Bristol, United Kingdom.

Hibberd, S., and Peregrine, D.H., 1979. Surf and run-up on a beach: a uniform bore. *J. Fluid Mechanics*, **95** (2), 323-345.

Holman, R.A., and Sallenger, A.H., Jr., 1985. Set-up and swash on a natural beach. *J. Geophysical Research*, **90** (C1), 945-953.

Holscher, P., and Barends, F.B.J., 1990. Finite-difference scheme for wave transmission in a rubble mound breakwater. *Int. J. Numerical Methods in Engineering*, **30**, 1129-1145.

Johnson, J.W., Kondo, H., and Wallihan, R., 1966. Scale effects in wave action through porous structures. *Proc. 10th Coastal Engineering Conference*, ASCE, **2**, 1022-1024.

Kobayashi, N., Cox, D.T., and Wurjanto, A., 1990. Irregular wave reflection and run-up on rough impermeable slopes. *J. Waterway, Port, Coastal, and Ocean Engineering*, ASCE, **116** (6), 708-726.

Kobayashi, N., Cox, D.T., and Wurjanto, A., 1991. Permeability effects on irregular wave run-up and reflection. *J. Coastal Research*, **7** (1), 127-136.

Kobayashi, N., DeSilva, G.S., and Watson, K.D., 1989. Wave transformation and swash oscillation on gentle and steep slopes. *J. Geophysical Research*, **94** (C1), 951-966.

Kobayashi, N., and Greenwald, J.H., 1988. Waterline oscillation and riprap movement. *J. Waterway, Port, Coastal, and Ocean Engineering*, ASCE, **114** (3), 281-296.

Kobayashi, N., and Otta, A.K., 1987. Hydraulic stability analysis of armor units. *J. Waterway, Port, Coastal, and Ocean Engineering*, ASCE, **113** (2), 171-186.

Kobayashi, N., Otta, A.K., and Roy, I., 1987. Wave reflection and run-up on rough slopes. *J. Waterway, Port, Coastal, and Ocean Engineering*, ASCE, **113** (3), 282-298.

Kobayashi, N., and Wurjanto, A., 1989a. Numerical model for design of impermeable coastal structures. *Research Report No. CE-89-75*, Center for Applied Coastal Research, University of Delaware, Newark, Delaware.

Kobayashi, N., and Wurjanto, A., 1989b. Armor stability on rough permeable slopes of marine structures. *Proc. 23rd Congress of International Association for Hydraulic Research*, Ottawa, Canada, **C**, 407-414.

Kobayashi, N., and Wurjanto, A., 1989c. Wave transmission over submerged breakwaters. *J. Waterway, Port, Coastal, and Ocean Engineering*, ASCE, **115** (5), 662-680.

Kobayashi, N., and Wurjanto, A., 1990. Numerical model for waves on rough permeable slopes. *J. Coastal Research*, Special Issue No. **7** on Rational Design of Mound Structures, 149-166.

Kobayashi, N., and Wurjanto, A., 1992. Irregular wave set-up and run-up on beaches. *J. Waterway, Port, Coastal, and Ocean Engineering*, ASCE, **118** (4) (to appear).

Kobayashi, N., Wurjanto, A., and Cox, D.T., 1990a. Irregular waves on rough permeable slopes. *J. Coastal Research*, Special Issue No. **7** on Rational Design of Mound Structures, 167-184.

Kobayashi, N., Wurjanto, A., and Cox, D.T., 1990b. Rock slopes under irregular wave attack. *Proc. 22nd Coastal Engineering Conference*, ASCE, 1306-1319.

Kondo, H, and Toma, S., 1972. Reflection and transmission for a porous structure. *Proc. 13th Coastal Engineering Conference*, ASCE, **3**, 1847-1866.

Lax, P., and Wendroff, B., 1960. Systems of Conservation Laws. *Communications on Pure and Applied Mathematics*, **XIII**, 217-237.

Lerat, A., and Peyret, R., 1973. *Comptes Rendus l'Academie des Sciences*, A **276**, 759-762.

Lerat, A., and Peyret, R., 1974. *Comptes Rendus l'Academie des Sciences*, A **277**, 363-366.

Lerat, A., and Peyret, R., 1975. In *Lecture Notes in Physics*, **35**, 251-256. Springer-Verlag, New York.

MacCormack, R.W., 1969. The effect of viscosity in hypervelocity impact cratering. *Paper No. 69-354*, American Institute of Aeronautics and Astronautics, 7 pages.

Madsen, O.S., 1974. Wave transmission through porous structures. *J. Waterways, Harbors, and Coastal Engineering Division*, ASCE, **100** (WW3), 169-188.

Madsen, O.S., Shusang, P., and Hanson, S.A., 1978. Wave transmission through trapezoidal breakwaters. *Proc. 16th Coastal Engineering Conference*, ASCE, **3**, 2140-2152.

Madsen, O.S., and White, S.M., 1976. Reflection and transmission characteristics of porous rubble mound breakwaters. *Miscellaneous Report 76-5.* U.S. Army Corps of Engineers Coastal Engineering Research Center.

Madsen, P.A., 1983. Wave reflection from a vertical permeable wave absorber. *Coastal Engineering*, **7**, 381-396.

Marino, M.A., and Luthin, J.N., 1982. *Seepage and Groundwater.* Elsevier, Amsterdam.

Massel, S.R., and Butowski, P., 1980. Wind waves transmission through porous breakwater. *Proc. 17th Coastal Engineering Conference*, ASCE, **1**, 333-346.

Mei, C.C., 1983. *The Applied Dynamics of Ocean Surface Waves.* Wiley, New York.

Moretti, G., 1979. The λ scheme. *Computers and Fluids*, **7**, 191-205.

Moretti, G., 1987. Computation of flows with shocks. *Ann. Rev. Fluid Mechanics*, **19**, 313-337.

Packwood, A.R., 1980. Surf and run-up on beaches. *Ph.D. Dissertation.* School of Mathematics, University of Bristol, United Kingdom.

Packwood, A.R., 1983. The influence of beach porosity on wave up-rush and back-wash. *Coastal Engineering*, **7**, 29-40.

Panton, R.L., 1984. *Incompressible Flow.* Wiley, New York.

Peyret, R., and Taylor, T.D., 1983. *Computational Methods for Fluid Flow.* Springer-Verlag, New York.

Richtmyer, R.D., and Morton, K.W., 1967. *Difference Methods for Initial-Value Problems*, Second Edition. Interscience, New York.

Roache, P.J., 1982. *Computational Fluid Dynamics*, Revised Printing. Hermosa, Albuquerque, New Mexico.

Scarlatos, P.D., and Singh, V.P., 1987. Long-wave transmission through porous breakwaters. *Coastal Engineering*, **11**, 141-157.

Scheidegger, A.E., 1960. *The Physics of Flow Through Porous Media.* Macmillan, New York.

Sollitt, C.K., and Cross, R.H., 1972. Wave transmission through permeable breakwaters. *Proc. 13th Coastal Engineering Conference*, ASCE, **3**, 1827-1846.

Sollitt, C.K., and Cross, R.H., 1976. Wave reflection and transmission at permeable breakwaters. *Technical Paper 76-8.* U.S. Army Corps of Engineers Coastal Engineering Research Center.

Sulisz, W., 1985. Wave reflection and transmission at permeable breakwaters of arbitrary cross section. *Coastal Engineering*, **9**, 371-386.

Svendsen, I.A., and Madsen, P.A., 1984. A turbulent bore on a beach. *J. Fluid Mechanics*, **148**, 73-96.

Todd, D.K., 1980. *Groundwater Hydrology.* Second Edition. Wiley, New York.

Van der Meer, J.W., 1988. Rock slopes and gravel beaches under wave attack. *Doctoral Dissertation.* Technische Universiteit Delft, The Netherlands.

Ward, J.C., 1964. Turbulent flow in porous media. *J. Hydraulic Division*, ASCE, **90** (HY5), 1-12.

Wilson, K.W., and Cross, R.H., 1972. Scale effects in rubble-mound breakwaters. *Proc. 13th Coastal Engineering Conference*, ASCE, **3**, 1873-1884.

Wise, R.A., Kobayashi, N., and Wurjanto, A., 1991. Cross-shore sediment transport under irregular waves in surf zones. *Proc. Coastal Sediments '91*, ASCE, 658-673.

Wurjanto, A., and Kobayashi, N., 1991. Numerical model for random waves on impermeable coastal structures and beaches. *Research Report No. CACR-91-05*, Center for Applied Coastal Research, University of Delaware, Newark, Delaware.

Wurjanto, A., and Kobayashi, N., 1992. Numerical model for random waves on permeable coastal structures. *Research Report No. CACR-92-02*, Center for Applied Coastal Research, University of Delaware, Newark, Delaware.